MICROWAVE SINTERING OF SILICON NITRIDE WITH ZIRCONIA AS A SECONDARY ADDITIVE

BY

SREEKUMAR CHOCKALINGAM

A THESIS

SUBMITTED TO THE FACULTY OF

ALFRED UNIVERSITY

IN PARTIAL FULFILLMENT OF THE REQUIREMENTS
FOR THE DEGREE OF

DOCTOR OF PHILOSOPHY

IN

CERAMICS

ALFRED, NEW YORK

APRIL, 2007

Alfred University theses are copyright protected and may be used for education or personal research only. Reproduction or distribution in part or whole is prohibited without written permission from the author.

Signature page may be viewed at Scholes Library, New York State College of Ceramics, Alfred University, Alfred, New York.

MICROWAVE SINTERING OF SILICON NITRIDE WITH ZIRCONIA AS A SECONDARY ADDITIVE

BY

SREEKUMAR CHOCKALINGAM

B.SC. PHYSICS (KERALA UNIVERSITY, INDIA, 1987)

M.SC. IN PHYSICS (KERALA UNIVERSITY, INDIA, 1990)

M.TECH. IN ELECTRONICS (CUSAT, INDIA, 1992)

SIGNATURE OF AUTHOR (Signature on File)

APPROVED BY (Signature on File)

DAVID A. EARL, ADVISOR

(Signature on File)

VASANTHA R. W. AMARAKOON, ADVISORY COMMITTEE

(Signature on File)

JAMES R. VARNER, ADVISORY COMMITTEE

(Signature on File)

WILLIAM M. CARTY, ADVISORY COMMITTEE

(Signature on File)

CHAIR, ORAL THESIS DEFENSE

ACCEPTED BY (Signature on File)

ALASTAIR N. CORMACK, DEAN
KAZUO INAMORI SCHOOL OF ENGINEERING

ACCEPTED BY (Signature on File)

WILLIAM M. HALL, ASSOCIATE PROVOST
FOR GRADUATE AND PROFESSIONAL PROGRAMS
ALFRED UNIVERSITY

ACKNOWLEDGMENTS

Thank you God for everything you gave to me.

I would like to express my deep gratitude, sincere thanks and appreciation to my advisor Dr. David A. Earl for his valuable guidance for the last five years time. You were more than an advisor to me. You offered me every help you can with out asking. You always supported me whenever I needed help. Sir, I thank you from my heart for all the help, encouragement, and support you generously extended to me during the last five years time. I also would like to thank Mrs. Earl for many family gatherings.

Dr. Vasantha R.W. Amarakoon, a great respectable Professor who provided me many opportunities to realize the real potential within me. You gave me constant encouragement and support for my research and education at Alfred University. Sir, I thank you sincerely for all the help and encouragement you gave to me. I also thank Mrs. Amarakoon who made me to feel Alfred another home away from home.

Thanks are also due to Dr. James R. Varner and Dr. William M. Carty for serving my graduate committee and many critical help without which I would not be able to complete my thesis in time.

I greatly appreciate and thank Dr. Jacob George, Corning Incorporated for teaching me numerical modeling which was part of Chapter-3 of this thesis. I also appreciate and thank Dr. Andrew A. Wereszczak, Metals and Ceramic Division, ORNL for plasma etching and mechanical properties measurements.

I also thank Mr. Gerald Wynick for SEM work. I would like to express my sincere thanks to Mrs. Patricia Lacourse for her patience and help without that I would not be able to finish my thesis in time.

I gratefully acknowledge Government of India, CEER and CACT at Alfred University for the financial support. I would like to express my sincere thanks to Mr. Gary Del Regno, Dr. Steve Arrasmith, Mrs. Marlene Wightmann, Dr. Licio Pennisi, Deb Chilson and Carnie Emilie for their support and encouragement throughout this period.

I would also like to thank Appa and Amma for their support. I am greatful to my wife Mrs. Raji for her support and encouragement during the five year period of time. I would also like to express my sincere thanks for Mr. Devarajan Sir for teaching the basics of Mathematics and English which helped me lot to complete this thesis.

Finally I dedicate this Ph. D thesis to my dearest son Sreejit S. Pillai. Thank you very much for your love and cooperation during the last five year time.

TABLE OF CONTENTS

Page

Acknowledgments i

Table of Contents iv

List of Tables vii

List of Figures xi

CHAPTER 1. INTRODUCTION 1

1.1 Silicon Nitride 1

1.2 Crystal Structure 2

1.3 Synthesis of Silicon Nitride Powder 4

1.4 Sintering of Silicon Nitride 6

1.4.1 Liquid Phase Sintering of Silicon Nitride 6

1.4.2 Selection of Sintering Additives 8

1.4.3 Liquid Phase Sintering Model 9

1.4.4 Microwave Sintering of Silicon Nitride 12

1.4.4.1 Microwave Processing of Materials 12

1.4.4.2 Conversion of Electromagnetic Energy to Heat 12

1.4.4.3 Microwave Material Interactions 14

1.4.4.4 "Microwave Effect" or Non-thermal Interaction 16

1.4.4.5 Conventional Heating Versus Microwave Heating 17

1.5 Microstructure and Mechanical Properties of Silicon Nitride 20

1.6 Previous Work on Microwave Sintering of Silicon Nitride 25

1.7 Objectives and Organization of the Thesis 27

1.8 References 28

CHAPTER 2. FDTD NUMERICAL SIMULATION 32

2.1 Introduction 32

2.2 Dielectric Properties Measurements 33

2.2.1 Sample Preparation 33

2.2.2 Dielectric Constant Measurements 34

2.2.3 Sample Holder Considerations 36

2.2.4 Measurement Results 37

2.3 The Coupled FDTD Numerical Model 41
2.4 Discussions 49
2.4.1 Complex Dielectric Properties of the Sintering Additives 49
2.4.2 Numerical Simulations 53
2.5 Conclusions 68
2.6 References 68
CHAPTER 3. DENSIFICATION AND ALPHA TO BETA PHASE TRANSFORMATION 70
3.1 Introduction 70
3.2 Experimental Procedure 72
3.3 Results and Discussion 76
3.3.1 Selection of Sintering Aids 76
3.3.2 Phase Identification 77
3.3.3 The $\alpha \rightarrow \beta$ Phase Transformation 86
3.3.4 Densification Behavior 87
3.4 Conclusions 91
3.5 References 92
CHAPTER 4. GRAIN BOUNDARY PHASE ANALYSIS 95
4.1 Introduction 95
4.2 Experimental Procedure 97
4.3 Results and Discussion 98
4.4 Conclusions 108
4.5 References 108
CHAPTER 5. GRAIN MORPHOLOGY AND MECHANICAL PROPERTIES...113
5.1 Introduction 113
5.2 Experimental Procedure 115
5.3 Results and Discussion 118
5.4 Conclusions 140
5.5 References 140
CHAPTER 6. CONCLUSIONS 142
6.1 Summary 142
6.2 Recommendations for Future Work 144

APPENDIX A. VICKERS HARDNESS AND FRACTURE TOUGHNESS RAW DATA OF MICROWAVE SINTERED SILICON NITRIDE 145

APPENDIX B. VICKERS HARDNESS AND FRACTURE TOUGHNESS RAW DATA OF CONVENTIONALLY SINTERED SILICON NITRIDE SAMPLES……. 151

APPENDIX C. GRAIN SIZE DISTRIBUTION RAW DATA OF GRAINS OF MICROWAVE SINTERED SILICON NITRIDE SAMPLES..... 154

APPENDIX D. GRAIN SIZE DISTRIBUTION RAW DATA OF GRAINS OF CONVENTIONALLY SINTERED SILICON NITRIDE SAMPLES……..... ..160

LIST OF TABLES

		Page
Table 1.I.	Crystallographic Data for Si_3N_4 Polymorphs	3
Table 1.II.	Properties of Commercially Available Silicon Nitride Powders.	5
Table 1.III.	Mechanical Properties of Structural Ceramics.	22
Table 2.I.	Dielectric Properties of 100% Si_3N_4	38
Table 2.II	Dielectric Properties of 90 wt% Si_3N_4 with 4 wt% MgO 6wt% Y_2O_3	39
Table 2.III.	Dielectric Properties of 87.5 wt% Si_3N_4 with 4 wt% MgO, 6 wt% Y_2O_3 and 2.5 wt% ZrO_2,	40
Table 2.IV.	Thermal Properties of Si_3N_4 with Sintering Aids	54
Table 3.I.	Chemical Composition of Starting Powder (weight%)	76
Table 3.II.	Phases in Microwave Sintered Si_3N_4-MgO-Y_2O_3 Systems as a Function of Sintering Temperature (°C) and ZrO_2 Content.	82
Table 3.III.	Phases in Conventionally Sintered Si_3N_4-MgO-Y_2O_3 Systems as a Function of Sintering Temperature (°C) and ZrO_2 Content	84
Table 3.IV.	XRD Intensity Ratios for α and β Si_3N_4 as a Function of Sintering Temperature (°C) and Zr O_2Content	86
Table 3.V.	Density of the Conventionally Sintered Samples as a Function of Sintering Temperature (°C) and ZrO_2 Content	91
Table 5.I.	Vickers hardness and fracture toughness of conventionally sintered silicon nitride samples	118
Table A.I.	Vickers Hardness and Fracture Toughness of Microwave Sintered Sample at 1650°C-0 wt% ZrO_2	144
Table A.II.	Vickers Hardness and Fracture Toughness of Microwave Sintered Sample at 1650°C-2.5 wt% ZrO_2	144

Table A.III. Vickers Hardness and Fracture Toughness of Microwave Sintered Sample at 1650°C- 4 wt% ZrO_2 145

Table A.IV. Vickers Hardness and Fracture Toughness of Microwave Sintered Sample at 1650°C- 5 wt% ZrO_2 145

Table A.V. Vickers Hardness and Fracture Toughness of Microwave Sintered Sample at 1700°C- 0 wt% ZrO_2 146

Table A.VI. Vickers Hardness and Fracture Toughness of Microwave Sintered Sample at 1700°C- 2.5 wt% ZrO_2 146

Table A.VII. Vickers Hardness and Fracture Toughness of Microwave Sintered Sample at 1700°C- 4 wt% ZrO_2 147

Table A.VIII. Vickers Hardness and Fracture Toughness of Microwave Sintered Sample at 1700°C- 5 wt% ZrO_2 147

Table A.IX. Vickers Hardness and Fracture Toughness of Microwave Sintered Sample at 1750°C- 0 wt% ZrO_2 148

Table A.X. Vickers Hardness and Fracture Toughness of Microwave Sintered Sample at 1750°C- 2.5 wt% ZrO_2 148

Table A.XI. Vickers Hardness and Fracture Toughness of Microwave Sintered Sample at 1750°C- 4 wt% ZrO_2 149

Table A.XII. Vickers Hardness and Fracture Toughness of Microwave Sintered Sample at 1750°C- 5 wt% ZrO_2 149

Table B.I. Vickers Hardness and Fracture Toughness of Conventionally Sintered Sample at 1650°C- 0 wt% ZrO_2 150

Table B.II. Vickers Hardness and Fracture Toughness of Conventionally Sintered Sample at 1650°C- 2.5 wt% ZrO_2 150

Table B.III. Vickers Hardness and Fracture Toughness of Conventionally Sintered Sample at 1700°C- 0 wt% ZrO_2 151

Table B.IV. Vickers Hardness and Fracture Toughness of Conventionally Sintered Sample at 1700°C- 2.5 wt% ZrO_2 151

Table B.V. Vickers Hardness and Fracture Toughness of Conventionally Sintered Sample at 1750°C- 0 wt% ZrO_2 152

Table B.VI. Vickers Hardness and Fracture Toughness of Conventionally Sintered Sample at 1750°C- 2.5 wt% ZrO_2 152

Table C.I. Length (L), Width (W) and Aspect Ratio (AR) of Grains of Microwave Sintered Sample at 1650°C- 0 wt% ZrO_2.....153

Table C.II. Length (L), Width (W) and Aspect Ratio (AR) of Grains of Microwave Sintered Sample at 1650°C- 2.5 wt% ZrO_2.....153

Table C.III. Length (L), Width (W) and Aspect Ratio (AR) of Grains of Microwave Sintered Sample at 1650°C- 4 wt% ZrO_2.....154

Table C.IV. Length (L), Width (W) and Aspect Ratio (AR) of Grains of Microwave Sintered Sample at 1650°C- 5 wt% ZrO_2.....154

Table C.V. Length (L), Width (W) and Aspect Ratio (AR) of Grains of Microwave Sintered Sample at 1700°C- 0 wt% ZrO_2.....155

Table C.VI. Length (L), Width (W) and Aspect Ratio (AR) of Grains of Microwave Sintered Sample at 1700°C- 2.5 wt% ZrO_2.....155

Table C.VII. Length (L), Width (W) and Aspect Ratio (AR) of Grains of Microwave Sintered Sample at 1700°C- 4 wt% ZrO_2.....156

Table C.VIII. Length (L), Width (W) and Aspect Ratio (AR) of Grains of Microwave Sintered Sample at 1700°C- 5 wt% ZrO_2.....156

Table C.IX. Length (L), Width (W) and Aspect Ratio (AR) of Grains of Microwave Sintered Sample at 1750°C- 0 wt% ZrO_2.....157

Table C.X. Length (L), Width (W) and Aspect Ratio (AR) of Grains of Microwave Sintered Sample at 1750°C- 2.5 wt% ZrO_2.....157

Table C.XI. Length (L), Width (W) and Aspect Ratio (AR) of Grains of Microwave Sintered Sample at 1750°C- 4 wt% ZrO_2.....158

Table C.XII. Length (L), Width (W) and Aspect Ratio (AR) of Grains of Microwave Sintered Sample at 1750°C- 5 wt% ZrO_2.....158

Table D.I. Length (L), Width (W) and Aspect Ratio (AR) of Grains of Conventionally Sintered Sample at 1650°C- 0 wt% ZrO_2.....159

Table D.II. Length (L), Width (W) and Aspect Ratio (AR) of Grains of Conventionally Sintered Sample at 1650°C- 2.5 wt% ZrO_2.....159

Table D.III. Length (L), Width (W) and Aspect Ratio (AR) of Grains of Conventionally Sintered Sample at 1700°C- 0 wt% ZrO_2.....160

Table D.IV. Length (L), Width (W) and Aspect Ratio (AR) of Grains of Conventionally Sintered Sample at 1700°C- 2.5 wt% ZrO_2.....160

Table D.V. Length (L), Width (W) and Aspect Ratio (AR) of Grains of Conventionally Sintered Sample at 1750°C- 0 wt% ZrO_2.....161

Table D.VI. Length (L), Width (W) and Aspect Ratio (AR) of Grains of Conventionally Sintered Sample at 1750°C- 2.5 wt% ZrO_2.....161

LIST OF FIGURES

Page

Figure 1.1. β-Si_3N_4 crystal structure showing AB layers…. .....……2

Figure 1.2. α-Si_3N_4 crystal structure showing AB and CD layers… ..... ……3

Figure 1.3 Flow chart for the preparation of Si_3N_4 powder by nonaqueous liquid reactions……. .....……5

Figure 1.4. Silicon vapor pressure in equilibrium with silicon nitride as a function of nitrogen temperature and pressure… ..... ……7

Figure 1.5. A plot of $-\Delta G_{[3]}$ against $-\Delta G_{[4]}$ for some metal oxides at 2000 K. $-\Delta G_{[1]}$ versus $-\Delta G_{[2]}$ at 2000K are also indicated by solid and broken lines. Shaded area is characterized by $\Delta G_{[3]} < \Delta G_{[1]}$, $\Delta G_{[2]}$ materials underlined are metal oxides that can be successfully used as a sintering aid for silicon nitrid ceramics……..… 9

Figure 1.6. Kingery model plot for sintering of Si_3N_4 ..... ……10

Figure 1.7. Schematic of Kingery's model for sintering of Si_3N_4…….. ……...…11

Figure 1.8. Relationship between the dielectric loss factor and the ability to absorb microwave power for some common materials …… .... ……..14

Figure 1.9. Relative dielectric constant (8 to 10 GHz) versus temperature …….. 15

Figure 1.10. Loss tangent (8 to 10 GHz) versus temperature.…….…...…15

Figure 1.11. SEM image of plasma etched section of Si_3N_4 showing the inter granular glassy phase (white region) and β-Si_3N_4 grain…. 21

Figure 1.12. Computer simulated 3D image of Si_3N_4 microstructure……...……21

Figure 1.13. Strength and fracture toughness of various Si_3N_4……22

Figure 1.14. Crack wake mechanisms operating in silicon nitride ……... ...23

Figure 1.15. SEM image showing crack deflection and branching by a β-Si_3N_4 grain …… .... ……24

Figure 1.16. SEM image showing elongated β-Si_3N_4 grain pullout ……..…24

Figure 1.17. SEM image of crack bridging and partial de-bonding by a β-Si_3N_4 grain ……24

Figure 2.1. The temperature dependent dielectric property measurements setup.....35

Figure 2.2. Microwave Sintering Configuration used for Simulating Temperature Distributions….....41

Figure 2.3. Model Spacing the Yee Cell Grids.....42

Figure 2.4. Temperature Dependent Complex Dielectric permittivity of Si_3N_4 Systems Measured while Heating Samples from Room Temperature to 1400°C in 0.1MPa of Nitrogen Pressure …….. . …… 50

Figure 2.5. Temperature Dependent Complex Dielectric permittivity of Si_3N_4 SystemsMeasured while Cooling Samples from 1400°C to Room Temperature in 0.1MPa of Nitrogen Pressure ……. ..52

Figure 2.6. TGA/DSC results from SN2. The endotherm beginning near 1000°C correlates to the rise in ε" shown in Figure 2.4.....……53

Figure 2.7. Power absorption of pure Si_3N_4 (SN) at 1650ºC. The yellow circle represents the perimeter of the sample pellet ..…….....…….. ……56

Figure 2.8. Temperature distribution of pure Si_3N_4 (SN) at 1550ºC. The yellow circle represents the perimeter of the sample pellet….....57

Figure 2.9. Temperature distribution of pure Si_3N_4 (SN) at 1600ºC. The yellow circle represents the perimeter of the sample pellet .....……58

Figure 2.10. Temperature distribution of pure Si_3N_4 (SN) at 1650ºC. The yellow circle represents the perimeter of the sample pellet……...……..... …59

..

Figure 2.11. Power absorption of Si_3N_4 +Y_2O_3+MgO (SN1) at 1650ºC……...60

Figure 2.12 Temperature distribution of Si_3N_4 +Y_2O_3+MgO (SN1) at 1550ºC. The yellow circle represents the perimeter of the sample pellet..... 61

Figure 2.13 Temperature distribution of Si_3N_4 +Y_2O_3+MgO (SN1) at 1600ºC. The yellow circle represents the perimeter of the sample pellet.....…… .62

Figure 2.14 Temperature distribution of Si_3N_4 +Y_2O_3+MgO (SN1) at 1650ºC. The yellow circle represents the perimeter of the sample pellet ……...…….63

Figure 2.15 Power absorption of Si_3N_4 +Y_2O_3+MgO+ZrO_2 (SN2) at 1650ºC ……...64

Figure 2.16 Temperature distribution of Si_3N_4 +Y_2O_3+MgO+ZrO_2 (SN2) at 1550ºC. The yellow circle represents the perimeter of the sample pellet. ….....…...65

Figure 2.17 Temperature distribution of Si_3N_4 +Y_2O_3+MgO+ZrO_2 (SN2) at 1600ºC. The yellow circle represents the perimeter of the sample pellet …..…..... 66

Figure 2.18 Temperature distribution of Si_3N_4 +Y_2O_3+MgO+ZrO_2 (SN2) at 1650ºC 67

Figure 3.1 Schematic of the microwave sintering set up used for sintering silicon nitride sample. ……73

Figure 3.2. Communication and power industries (CPI) 2.45 GHz automated industrial microwave furnace (A) and sintering set up showing on alumina fiber insulation box and a boron nitride crucible containing Si_3N_4 smples(B).....74

Figure 3.3. Centorr vacuum furnace (A) and sintering setup showing a tungsten heating element and a boron nitride crucible containing Si_3N_4 samples(B).....75

Figure 3.4a XRD patterns for microwave sintered Si_3N_4 with 4 wt% MgO and 6 wt% Y_2O_3 as a function of ZrO_2 content. Samples were sintered at 1650ºC for 15 min in 0.1 MPa of nitrogen pressure (α: α–Si_3N_4, β : β–Si_3N_4, ▼: ZrO_2, ♦: ZrN ■: $Y_2Si_3O_3N_4$). Numerical simulation results show a temperature of 50ºC higher in the sample which contains 2.5 wt% ZrO_2 than the sample without ZrO_2.Power absorption of Si_3N_4 +Y_2O_3+MgO+ZrO_2 (SN2) at 1650ºC ……..79

Figure 3.4b XRD patterns for microwave sintered Si_3N_4 with 4 wt% MgO and 6 wt% Y_2O_3 as a function of ZrO_2 content. Samples were sintered at 1700ºC for 15 min in 0.1 MPa of nitrogen pressure (α: α–Si_3N_4, β : β–Si_3N_4, ▼: ZrO_2, ♦: ZrN ■: $Y_2Si_3O_3N_4$). Numerical simulation results show a temperature of 50ºC higher in the sample which contains 2.5 wt% ZrO_2 than the sample without ZrO_2. …… 80

Figure 3.4c. XRD patterns for microwave sintered Si_3N_4 with 4 wt% MgO and 6 wt% Y_2O_3 as a function of ZrO_2 content. Samples were sintered at 1750ºC for 15 min in 0.1 MPa of nitrogen pressure (α: α–Si_3N_4, β : β–Si_3N_4, ▼: ZrO_2, ♦: ZrN ■: $Y_2Si_3O_3N_4$). Numerical simulation results show a temperature of 50ºC higher in the sample which contains 2.5 wt% ZrO_2 than the sample without ZrO_2..... …… 81

Figure 3.5a. XRD patterns for conventionally sintered Si_3N_4 with 4 wt% MgO and 6 wt% Y_2O_3 as a function of ZrO_2 content. Samples were sintered at 1650ºC for 15 min in 0.1 MPa of nitrogen pressure. (α: α–Si_3N_4, β : β–Si_3N_4, ▼: ZrO_2, ♦: ZrN ……....83

Figure 3.5b HTXRD pattern on the microwave sintered specimen containing Si_3N_4, 6 wt % Y_2O_3, 4 wt% MgO and 5 wt% ZrO_2 heated to 900°C from 20°C and cooled to room temperature.HTXRD pattern on the microwave sintered specimen containing Si_3N_4, 6 wt % Y_2O_3, 4 wt% MgO and 5 wt% ZrO_2 heated to 900°C from 20°C and cooled to room temperature ..... ……83

Figure 3.5c. XRD patterns for conventionally sintered Si_3N_4 with 4 wt% MgO and 6 wt% Y_2O_3 as a function of ZrO_2 content. Samples were sintered at 1750ºC for 15 min in 0.1 MPa of nitrogen pressure. (α: α–Si_3N_4, β : β–Si_3N_4, ▼: ZrO_2, ♦:ZrN.....……....84

Figure 3.6. HTXRD pattern for a microwave sintered specimen containing Si_3N_4, 6 wt % Y_2O_3, 4 wt% MgO and 5 wt% ZrO_2 heated to 900°C from 20°C and cooled to room temperature …… 85

Figure 3.7. HTXRD pattern for a microwave sintered specimen containing Si_3N_4, 6 wt % Y_2O_3, 4 wt% MgO and 5 wt% ZrO_2 heated to 900°C from 20°C and subsequently heat- treated for 24 hours.....……....85

Figure 3.8. Density of microwave sintered Si_3N_4-MgO-Y_2O_3 samples as a function of ZrO_2 content and sintering temperature in 0.1 MPa of nitrogen pressure.....88

Figure 3.9. SEM images of microwave sintered Si_3N_4 with MgO and Y_2O_3 as a function of ZrO_2 content. Samples were sintered at 1650ºC (A), 1700ºC (B) and 1750ºC (C) for 15min in 0.1 MPa of nitrogen pressure..... 89

Figure 3.10. SEM image of a microwave sintered sample consisting of 95 wt% Si_3N_4, 4 wt% MgO, 6 wt% Y_2O_3 and 5 wt% ZrO_2, showing residual porosity. The sample was sintered at 1750ºC for 15 min..... 90

Figure 3.11. SEM images of conventionally sintered Si_3N_4 with MgO and Y_2O_3, as a function of ZrO_2 content. Samples were sintered at 1650ºC (A), 1700ºC (B) and 1750ºC (C) for 15 min in 0.1 MPa of nitrogen pressure.wt% Y_2O_3 - 2.5 wt% ZrO_2 microwave sintered at 1750ºC for 15 min in 0.1 MPa of nitrogen .pressure.....90

Figure 4.1. Typical bright field transmission electron microscopy image of the microwave-sintered Si_3N_4.....99

Figure 4.2. Bright field image showing small ZrO_2 particulates embedded in a large Si_3N_4 grain and located on the grain boundary. The Si_3N_4 grain is the β phase, as confirmed by the selected-area electron diffraction pattern inset on the bottom-left corner; (b) energy-dispersive X-ray spectrometer spectrum for the embedded ZrO_2 grain 100

Figure 4.3. Bright field image exhibiting a large ZrO_2 particulate dispersed in the Si_3N_4 matrix. Incommensurate diffraction spots are observed in the selected-area electron diffraction pattern of the ZrO_2 grain. The Miller indices refer to cubic fluoride. (b) Energy-dispersive X-ray `spectrometer (EDS) spectrum for the areas labeled ‘‘A’’ and ‘‘B’’ in (a). The inset EDS spectra were collected at a beam energy of 80 keV..... .101

Figure 4.4. Bright field image showing a Zr-rich grain. It is cubic, as confrmed by the inset selected-area electron diffraction pattern. (b) Energy-dispersive X-ray spectrometer (EDS) spectrum of the Zr-rich grain. The inset EDS spectrum was collected at a beam energy of 80 keV..... 102

Figure 4.5. Bright field image showing a crystallized multigrain junction phase labeled ‘‘N.’’ It is N-Melilite, as identifed by the selected-area electron diffraction inset in this Figure. The grain labeled ‘‘S’’ is Si_3N_4. (b) Diffused dark field image of (a). (c) Energy-dispersive X-ray spectrometer (EDS) spectra of the area labeled ‘‘N.’’ The inset EDS spectrum was collected at a beam energy of 80 keV..... 103

Figure 4.6. Bright field image showing the distribution of the remnant glassy phase. Enlargement of the ‘‘core-rim’’ structure is displayed in a square inset on the top-left corner; (b) Energy-dispersive X-ray spectrometer point-by-point analysis for areas in (a). The appearances of Y/Si and Zr/Si in areas labeled ‘‘D’’ and ‘‘E’’ were from the background noise.....105

Figure 4.7. Diffused dark field image of typical homophase boundaries oriented edge-on with respect to the electron beam..... 107

Figure 5.1. Example of a SEM micrograph (85 wt% Si_3N_4 with 4 wt% MgO, 6 wt% Y_2O_3 and 5 wt% ZrO_2 microwave sintered at 1750°C for 15 minutes) used for grain size analysis..... 116

Figure 5.2. Grain size parameters as determined from specific grain sections 117

Figure 5.3. Vickers hardness of microwave sintered silicon nitride samples 118

Figure 5.4. Fine grain microstructure (85 wt% Si_3N_4 with 4 wt% MgO, 6 wt% Y_2O_3,and 5 wt% ZrO_2 microwave sintered at 1750°C for 15 minutes.....118

Figure 5.5. Fracture toughness of microwave sintered silicon nitride samples.....119

Figure 5.6. SEM images showing crack path of microwave sintered Si_3N_4 with MgO and Y_2O_3 as a function of ZrO_2 content (0 % ZrO_2 = SN1; 2.5 wt% ZrO_2 = SN2; 4 wt% ZrO_2 = SN3; and 5 wt% ZrO_2 = SN4) sintered at 1650ºC (A), 1700ºC (B) and 1750ºC (C) for 15 min in 0.1 MPa of nitrogen pressure.igure 5.5. Fracture toughness of microwave sintered silicon nitride samples..... 121

Figure 5.7. SEM images of conventioal sintered Si_3N_4 with MgO and Y_2O_3 as a function of ZrO_2 content (0 wt% ZrO_2 = SN1; 2.5 wt% ZrO_2 = SN2) sintered at 1650ºC (A), 1700ºC (B) and 1750ºC (C) for 15 min in 0.1 MPa of nitrogen pressure.....122

Figure 5.8. Grain length distributions of Si_3N_4 samples microwave sintered at 1650ºC, 1700ºC and 1750ºC. 124

Figure 5.9. Grain width distribution of Si_3N_4 samples microwave sintered at 1650ºC, 1700ºC and 1750ºC..... 125

Figure 5.10. Aspect ratios of Si_3N_4 samples microwave sintered at 1650ºC, 1700ºCand 1750ºC..... 126

Figure 5.11. Grain length distributions of Si_3N_4 samples conventional sintered at 1650ºC, 1700ºC and 1750ºC.....128

Figure 5.12. Grain width distributions of Si_3N_4 samples conventional sintered at 1650ºC, 1700ºC and 1750ºC. 129

Figure 5.13. Aspect ratios of Si_3N_4 samples conventional sintered at 1650ºC, 1700ºC and1750°C 130

Figure 5.14. Grain length distributions of microwave (MW) versus conventional(CON) sintered Si_3N_4 sample containing 0 wt% ZrO_2..... 133

Figure 5.15. Grain width distributions of microwave (MW) versus conventional (CON) sintered Si_3N_4 samples containing 0 wt ZrO2 134

Figure 5.16. Aspect ratios of microwave (MW) versus conventional (CON) sintered Si_3N_4 samples containing 0 wt% ZrO_2..... 135

Figure 5.17. Grain length distributions of microwave (MW) versus conventional(CON) sintered Si_3N_4 sample containing 2.5 wt% ZrO_2.....136

Figure 5.18. Grain width distributions of microwave (MW) versus conventional (CON) sintered Si_3N_4 samples containing 2.5 wt %ZrO_2.....137

Figure 5.19. Aspect ratios of microwave (MW) versus conventional (CON) sintered Si_3N_4 samples containing 2.5 wt% ZrO_2..... 138

Abstract

The effect of 3 mol % Y_2O_3 stabilized ZrO_2 in microwave sintered Si_3N_4 was investigated in the present study. A Finite Difference Time Domain (FDTD) numerical technique was used to estimate the microwave power absorption and temperature distribution within Si_3N_4 samples with MgO and Y_2O_3 sintering aids and different levels of ZrO_2 during microwave sintering. Higher temperatures were developed in the sample containing the highest dielectric loss additive (4 wt% MgO, 6 wt% Y_2O_3 and 2.5 wt% ZrO_2) when compared to the lower loss additive (4 wt% MgO and 6 wt% Y_2O_3) or pure Si_3N_4. The numerically calculated temperatures within the samples were used to correct the values experimentally measured by an optical pyrometer, which were 75-125 ºC lower.

Isothermal densification and $\alpha \rightarrow \beta$ phase transformation rates of Si_3N_4 containing 4 wt% MgO, 6 wt% Y_2O_3 and between 0 and 5 wt% ZrO_2 were examined. An addition of 2.5 wt% ZrO_2 enhanced the densification rate during microwave sintering. Complete $\alpha \rightarrow \beta$ phase transformation occurred at a lower temperature during microwave sintering than conventional sintering. Grain boundary phases of microwave sintered samples were characterized by transmission electron microscopy (TEM). Small ZrO_2 grains ($d<200$ nm) were remained dispersed in the matrix. Both tetragonal and cubic Zr-rich phases were identified by selected-area electron diffraction. Additions of ZrO_2 improved the hardness of Si_3N_4. However, no variation in fracture toughness was observed despite differences in microstructures. The strong bonding between the grains and grain boundary phase resulted in predominantly transgranular crack propagation paths.

CHAPTER 1

Introduction

1.1 Silicon Nitride

Silicon nitride (Si_3N_4) ceramics are light weight and exhibit excellent high-temperature mechanical properties and thermal shock resistance. Silicon nitride's outstanding high-temperature properties and processing versatility have enabled it to be used in a variety of demanding applications over the past decade. These applications include cutting tools, bearings, and selected components for diesel engines. Recently, silicon nitride has emerged as a modern high-performance ceramic which combines carefully controlled chemistry and deliberately designed microstructures capable of enhancing the performance of many engineering systems. Future application for this material includes a broad range of reciprocating and gas turbine engine components, and electronic components.

Silicon nitride does not occur in nature.[1] However, particles of meteoritic rock have been shown to contain α-Si_3N_4, which is evidence for the natural existence of silicon nitride in the galaxy having its possible origins in supernovae.[2] A process for the production of Si_3N_4 by carbothermal reduction of SiO_2 was patented by H. Melner in Germany in 1896.[3] Silicon nitride was recognized as a refractory material in the early 1950s. Patents[4] were filed in 1952 by the Carborundum Company for mechanically strong silicon nitride made by the carbothermal reduction of SiO_2, followed by direct nitridation of silicon. Reaction-bonded Si_3N_4 (RBSN) was developed in 1955-1964 in the United Kingdom.[1] The development of Si_3N_4 ceramics as a potential high-temperature structural engine component material was markedly accelerated in the early 1960s.[1] This outcome was the result of a deliberate search for new materials with good high-temperature properties, of which, resistance to thermal shock was of paramount importance. This work led to the development of a wide range of Si_3N_4 components for internal combustion engines. In 1961 a fully dense silicon nitride was developed by hot-pressing Si_3N_4 powder in the presence of small amounts of a metal oxide, MgO.[1] Thirteen years later this development led to the production of dense, pressure-less

sintered silicon nitride. Development work on Si_3N_4 materials was started in the 1970s in the United States.[5] Microwave sintering of silicon nitride was initiated early 1990s, and research in this area is still at an early stage.[6]

1.2 Crystal Structure

The Si atom in Si_3N_4 is in a hybridized state sp^3 configuration producing a tetrahedral arrangement of valence orbital electrons bonding covalently with four N atoms.[7] The bonding between atoms is about 70% covalent and 30% ionic. Silicon nitride has two polymorphs, α and β forms. Based on x-ray powder diffraction (XRD) it was determined (Hardie and Jack, 1957; Ruddleston and Popper, 1969)[7] that α and β forms both have a hexagonal crystal structure. α-Si_3N_4 was assigned the space group P31c and β- Si_3N_4 was assigned the space group $P6_3/m$. For β-Si_3N_4 the unit cell is Si_6N_8, while for α-Si_3N_4, the unit cell is $Si_{12}N_{16}$. Both α and β Si_3N_4 can be considered to be built up of SiN_4 tetrahedra joined in a three-dimensional network by sharing corners; each nitrogen corner is common to three tetrahedra. The structures can be regarded as consisting of layers of silicon and nitrogen atoms in the sequence ABAB, or ABCDABCD. along the c-axis for the β (Figure 1.1.) and α (Figure 1.2.) modifications, respectively.

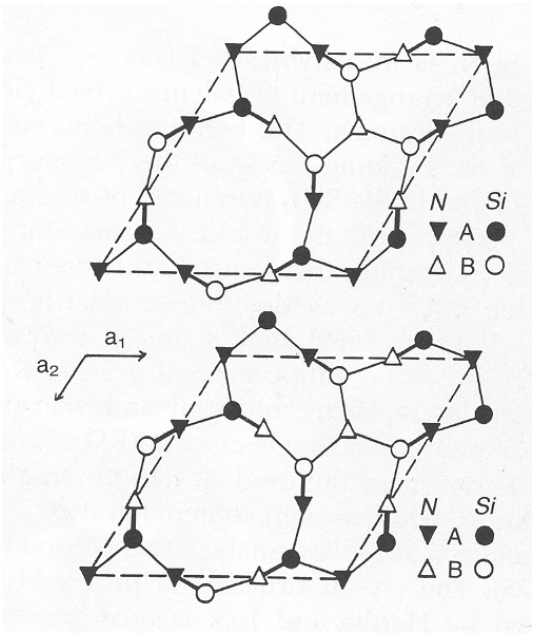

Figure 1.1. β-Si_3N_4 crystal structure showing AB layers.[7]

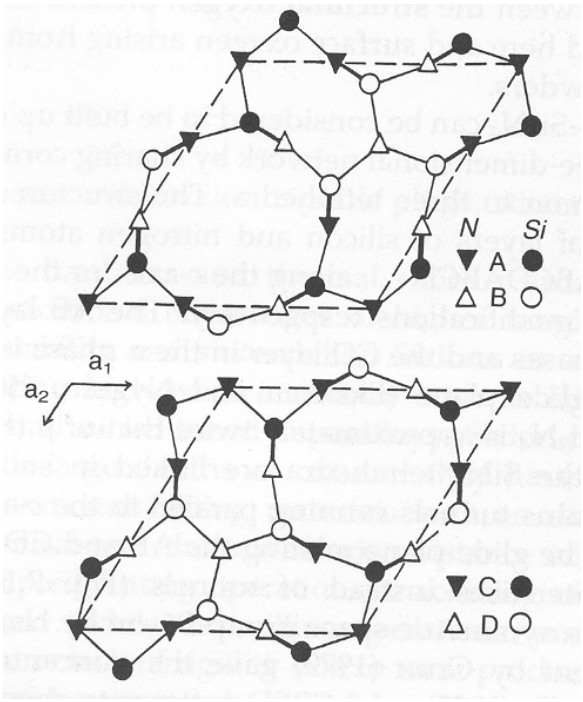

Figure 1.2. α-Si_3N_4 crystal structure showing AB and CD layers.[7]

The AB layer is the same in the α and β phases, and the CD layer in the α phase is related to the AB layer by a c-glide plane so that the c spacing of α-Si_3N_4 is approximately twice that of β (Figure 1.2.). In β-Si_3N_4 the SiN_4 tetrahedra are linked in such a way that the structure contains tunnels running parallel to the c-axis of the unit cell. The glide plane relating the AB and CD layers means that α contains interstices instead of tunnels. Crystallographic data for Silicon nitride polymorphs are summarized in Table 1.I

Table 1.I. Crystallographic Data for Si_3N_4 Polymorphs.[7]

Polymorph	Space group	Lattice parameters (A^o)	JCPDS card
α-Si_3N_4	P31c	a=7.753 c=5.618	41-360
β-Si_3N_4	$P6_3/m$	a=7.595 c=2.9023	33-1160

1.3 Synthesis of Silicon Nitride Powder

Silicon nitride powder can be synthesized through several routes. A widely used method for the synthesis of Si_3N_4 powder is direct nitridation of Si particles at temperatures between 1200°C and 1400°C for 10-30 hours.[8] The synthesis reaction of silicon nitride powder may be written as:

$$3Si + 2N_2 \rightarrow Si_3N_4 \qquad (1.1)$$

This method is used by H. C. Starck (Germany) for producing commercial grades of Si_3N_4 powder. Generally 5 % H_2 is mixed with N_2 to volatilize the SiO_2 thin coating on Si particles, which severely reduces the rate of the reaction. Silicon nitride powder is also produced by the carbothermal reduction of SiO_2 and C powders followed by nitridation at 1200 to 1400°C in N_2. This process is used industrially by Toshiba (Japan). The overall reaction may be written as[8]

$$3SiO_2 + 6C + 2N_2 \rightarrow Si_3N_4 + 6CO \qquad (1.2)$$

The above two methods produce a strongly agglomerated Si_3N_4 powder that requires comminution, washing and classification. Impurities introduced during these processes severely affect the high-temperature mechanical properties of the sintered bodies. The reaction between $SiCl_4$ and NH_3 is used commercially by Toya Soda (Japan) for the production of Si_3N_4 powder. The reactions may be written as[9]

$$SiCl_4\,(l) + NH_3\,(g) \rightarrow Si\,(NH)_2 + 4NH_4Cl \qquad (1.3)$$

$$3Si\,(NH)_2 \rightarrow Si_3N_4 + N_2 + 3H_2 \qquad (1.4)$$

The formed amorphous powder is crystallized to α-Si_3N_4 after prolonged heating between 1200°C and 1400°C. All the experiments conducted in this work used UBE-SN-E10 Silicon Nitride powder produced by UBE Industries (Japan). UBE uses a nonaqueous liquid reaction route. The advantage of this method is higher purity and finer particle size on the order of 200 nanometers compared with aforementioned methods that involve grinding of the solid product. The reaction between liquid $SiCl_4$ and liquid NH_3 has been used on an industrial scale by UBE Industries. A schematic of the sequence of operations is shown in Figure 1.3. Table 1.II summarizes the properties of commercially available silicon nitride powders.[8]

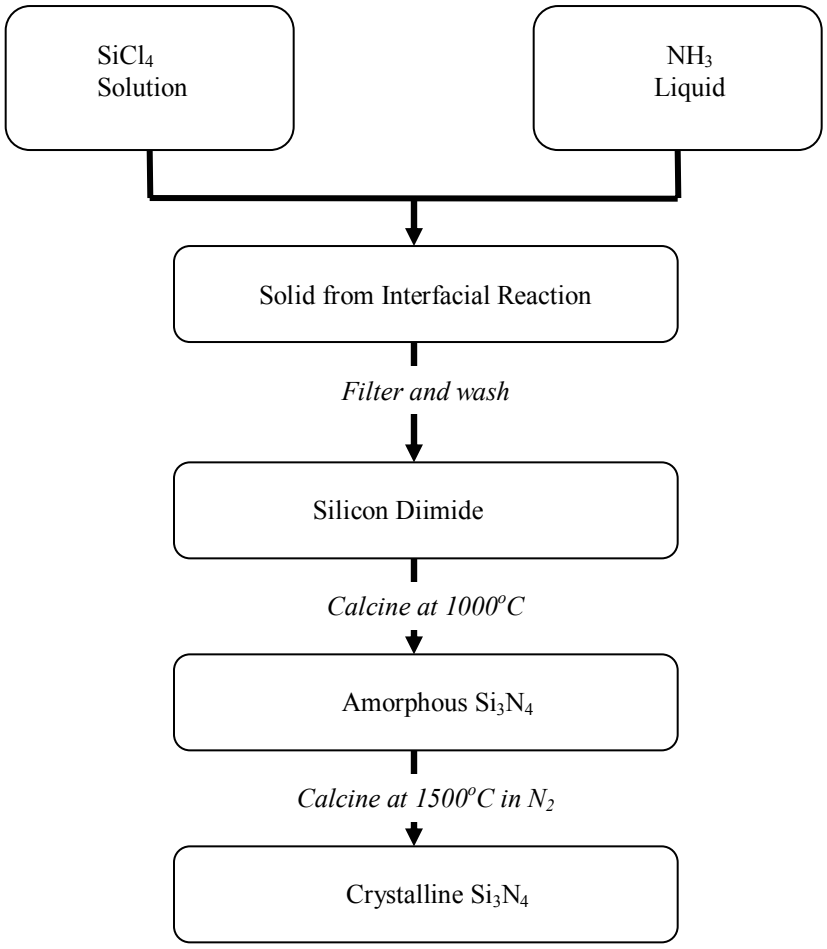

Figure 1.3. Flow chart for the preparation of Si_3N_4 powder by nonaqueous liquid reactions.[8]

Table 1.II. Properties of Commercially Available Silicon Nitride Powders.[8]

Manufacturer	**UBE**	**H. C. Starck**	**Toshiba**	**ToyaSoda**
Grade	SN-E10	H1		TSK TS-7
Metallic impurities (wt%)	0.02	0.1	0.1	0.01
Nonmetallic impurities (wt%)	2.2	1.7	4.1	1.2
α-Si_3N_4 (wt%)	95	92	88	90
β-Si_3N_4 (wt%)	5	4	5	10
SiO_2 (wt%)	2.5	2.4	5.6	
Surface area(m^2/g)	11	9	5	12
Average particle size (μm)	0.2	0.8	1	0.5

1.4 Sintering of Silicon Nitride

1.4.1 Liquid-Phase Sintering of Silicon Nitride

The need for a fully dense silicon nitride, which can be readily formed to near net shape by mass production processes, has long been recognized as a key technological requirement if silicon-nitride-based ceramics are to become true engineering materials. The basic problem associated with sintering silicon nitride is that the compound dissociates into silicon vapor and nitrogen gas at temperatures high enough to achieve the necessary atomic mobility for sintering to occur due to the covalent nature of the atomic bonds in Si_3N_4.[1] Two of the main fabrication processes which can be used to form dense silicon nitride bodies are hot pressing (HP) and hot isostatic pressing (HIP).[8] These techniques generally operate up to 2500ºC with 75 to 200 MPa pressure. Si_3N_4 can be densified to greater than 99% of the theoretical density by hot-pressing at 15-30 MPa in graphite dies inductively heated to 1550-1800ºC for 1 to 4 hours in a nitrogen atmosphere. A BN coating is applied to the graphite die to prevent reaction with Si_3N_4. The hot-pressed product is so hard that the final shape must be finished by expensive diamond machining. However, this process is limited to simple shapes. Complex shaped parts can be produced in large number by HIP. Although this route is expensive, it has the advantage of requiring lower additive contents so that high-temperature properties may be improved.

Early attempts to pressure-less sinter silicon nitride were not successful in achieving full density and strength due to the low lattice mobility of silicon and nitrogen and the high-temperature volatility of Si_3N_4. This led to microstructural coarsening and reduced density. The decomposition of Si_3N_4 into silicon vapor and nitrogen gas prevented the tendency for pore shrinkage. Terwilliger and Lange[5] first reported in 1976 that Si_3N_4 ceramics could be sintered to full density from Si_3N_4 powder without applying high nitrogen pressure. Giachello *et al*.[9] reported that packing silicon nitride samples into a suitable powder bed could avoid the use of high nitrogen pressure. This technique prevented pore growth by avoiding evaporation of silicon vapor and nitrogen gas.

Greskovich and his coworkers suggested the following conditions for successful sintering of silicon nitride.[9]

(1) Use ultra-fine powders of the order of 200 nanometers. This increases both the thermodynamic driving force for sintering and reduces diffusion distances and time for sintering.

(2) Apply high nitrogen pressure to keep the system to the right of the solid-liquid coexistence boundary, as shown in Figure 1.4

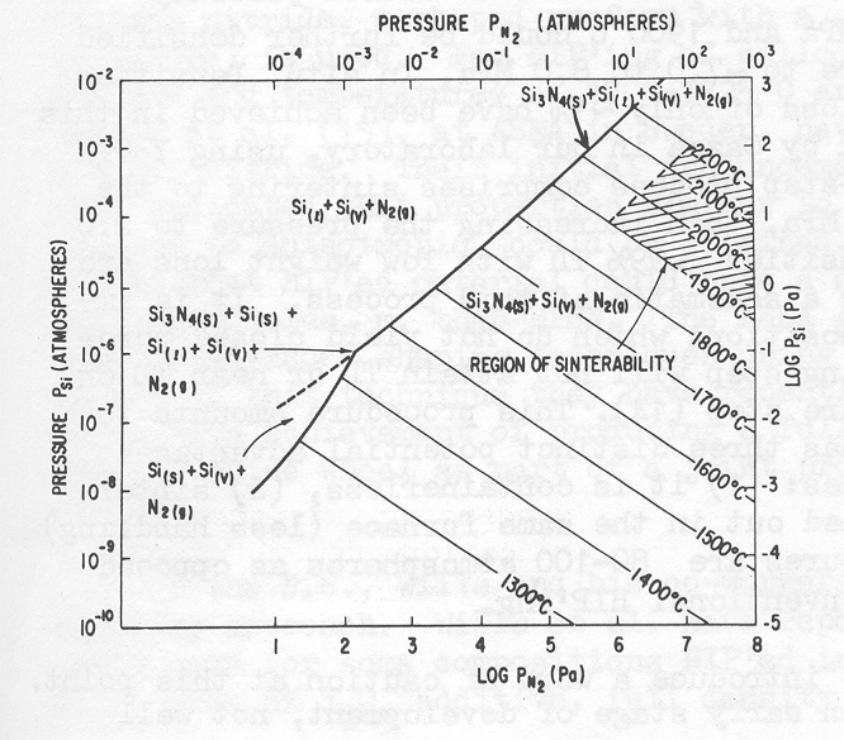

Figure 1.4. Silicon vapor pressure in equilibrium with silicon nitride as a function of nitrogen temperature and pressure.[9]

(3) Prevent silicon vapor loss from the system. This condition is automatically met when sintering in a closed system.

(4) Keep the oxygen level in the Si_3N_4 powder at a minimum.

1.4.2 Selection of Sintering Additives

The critical thermodynamic condition for choosing effective sintering additives is that they do not decompose Si_3N_4 to nitrogen and SiO_2 or SiO gas in the sintering process. This condition is met by the following equation.[40]

$$\Delta G_{[3]} < \Delta G_{[1]}, \Delta G_{[2]} \quad (1.5)$$

$$\Delta G_{[4]} < \Delta G_{[1]}, \Delta G_{[2]} \quad (1.6)$$

$\Delta G_{[1]}$ represents the standard free energy of reaction of Si_3N_4 with O_2 to form SiO_2 below 1877ºC, and $\Delta G_{[2]}$ is the standard free energy of reaction of Si_3N_4 with O_2 to form SiO above 1877ºC. The standard free energy for oxidation of the metal oxides is represented as $\Delta G_{[3]}$. $\Delta G_{[4]}$ is the standard free energy of oxidation reaction of metal nitrides. Si_3N_4 reacts with oxygen present in the environment gas, metal oxide sintering additives, or oxide impurities in silicon nitride powder according to the reactions given below.[40]

$$\frac{1}{3}Si_3N_4(s) + O_2(g) \rightarrow SiO_2(s,l) + \frac{2}{3}N_2(g) \quad (1.7)$$

$$\frac{2}{3}Si_3N_4(s) + O_2(g) \rightarrow 2SiO(g) + \frac{4}{3}N_2(g) \quad (1.8)$$

The standard free energy changes for these reactions at 1727ºC are $\Delta G_{[1]}$ = -126.9 kcal mol^{-1} and $\Delta G_{[2]}$ = -113.1 kcal mol^{-1}. The standard free energies for oxidation of metal oxides MgO, Y_2O_3 and ZrO_2, are -153.3, -198.1 and -173.1 kcal mol^{-1} respectively. The additive system is selected based on the lower value of standard free energy for oxidation values, $\Delta G_{[3]}$ compared to silicon nitride's value of $\Delta G_{[1]}$ = -126.9 kcal mol^{-1} at 1727ºC. The values of $-\Delta G_{[3]}$, compared with those of $-\Delta G_{[4]}$ at 2000K of some metal oxides are plotted with $-\Delta G_{[1]}$ and $-\Delta G_{[2]}$ at 2000K is shown in Figure 1.5. The area which satisfies equation (1.5) and (1.6) are shaded in this figure. Metal oxides which are in this region include MgO, Al_2O_3, Y_2O_3 and ZrO_2.

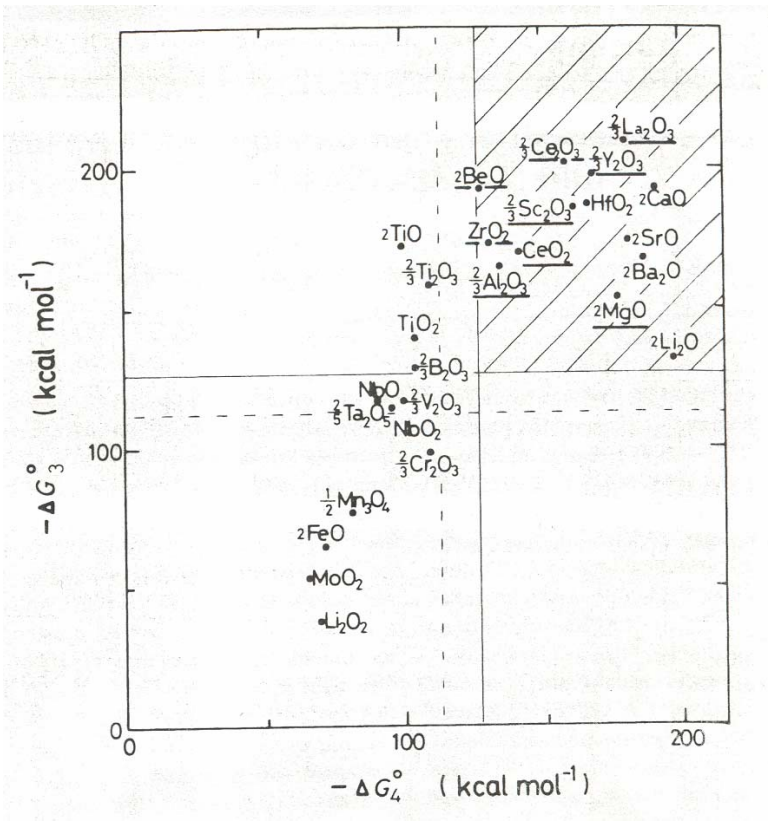

Figure 1.5 A plot of $-\Delta G_{[3]}$ against $-\Delta G_{[4]}$ for some metal oxides at 2000 K. $-\Delta G_{[1]}$ against $-\Delta G_{[2]}$ at 2000K are also indicated by solid and broken lines. Shaded area is characterized by $\Delta G_{[3]} < \Delta G_{[1]}$, $\Delta G_{[2]}$ Materials underlined are metal oxides that can be successfully used as a sintering aid for silicon nitride ceramics.[45]

1.4.3 Liquid-Phase Sintering Model

Kingery,[10] described a three-stage model for liquid-phase sintering:

(i) Particle rearrangement caused by initial formation of liquid.

(ii) Solution-precipitation process in which material is dissolved away from particle contact points, causing their centers to approach each other.

(iii) Ostwald ripening

At sufficiently high temperature, the particles in a consolidated body will rearrange themselves under the action of surface tension. The liquid will redistribute itself between the particles and into the pores. The rate of shrinkage during this rearrangement stage will depend upon the viscosity and volume of the liquid phase, as well as the sintering time according to

$$\Delta L/L_o \approx t^{1+y} \qquad (1.9)$$

where L is the length at time t, L_o is initial length, y is some small fraction, and

$$\Delta L = (L_o - L)$$

After the rearrangement of the particles, densification slows down and solution precipitation starts to dominate. The solid dissolves at the solid-liquid interfaces with a higher chemical potential, diffuses through the liquid, and is precipitated on the particles at other sites with a lower chemical potential. Shrinkage during this stage is interpreted by

$$\Delta L/L_o \approx t^{1/n} \qquad (1.10)$$

where the n depends on the mechanism of material transfer. If diffusion is the rate-controlling parameter during solution precipitation, then n= 3. If the phase boundary reaction is controlling, then n = 2. The third stage of liquid phase sintering is the coalescence process. Densification becomes very slow due to the large diffusion distance in the coarsened structure. Microstructural coarsening by Ostwald ripening dominates in this final stage. It is accompanied by grain-shape accommodation, which allows more efficient packing of the grain. Isolated pores will be closed due to the flow of liquid from the more efficiently packed region, leading to densification. The three stages of liquid-phase sintering can be identified on plots of log L/L_o versus log sintering time by the regions of different slope. Figure 1.6 is a plot of the Kingery model for the sintering of silicon nitride. Figure 1.7 shows a schematic representation of Kingery's model for sintering of Si_3N_4.

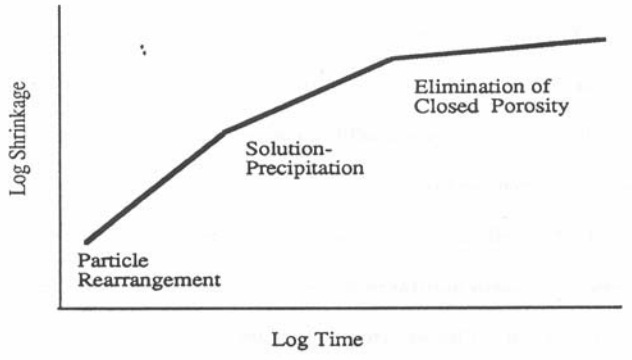

Figure 1.6. Kingery model plot for sintering Si_3N_4.[10]

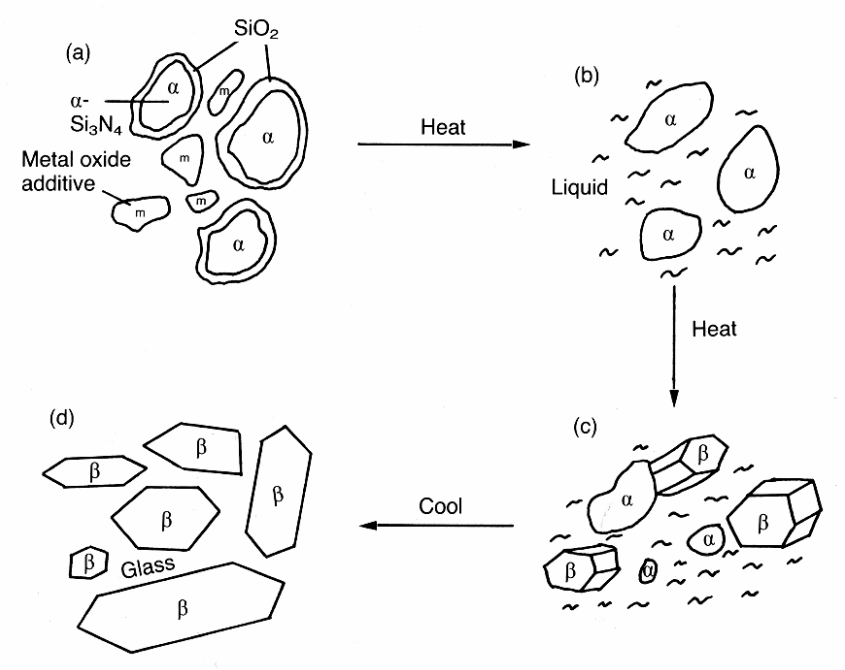

Figure 1.7. Schematic of Kingery's model for sintering Si_3N_4.[11]

During the sintering process, oxide sintering additives react with silica impurities present on the surface of Si_3N_4 powder and form a low-melting-point eutectic melt. The melt solidifies when cooling to yield an amorphous or crystalline grain-boundary phase, depending on the nature of the additives and processing conditions. The general reaction for liquid formation is described as[8]

$$Si_3N_4 + \text{additives} + SiO_2 + \text{impurities} \rightarrow Si_3N_4(s) + \text{liquid}$$

The amount and distribution of the sintering aid controls the properties of the sintered body. A greater liquid content produces a less porous body, although a large amount of grain boundary-phase is produced, which deteriorates high-temperature mechanical properties. Thus achieving both densification and high-temperature properties at the same time are a most challenging task. Practically, a compromise must be reached between the two.

1.4.4 Microwave Sintering of Silicon Nitride

1.4.4.1 Microwave Processing of Materials

Microwave processing of materials is a relatively new approach for improving the properties of the materials. Microwave frequency ranges from 300 MHz to approximately 300 GHz. Microwaves have been used for many applications, including satellite communications, radar, cellular phones, and heating. Domestic microwave ovens use 2.45 GHz for heating; industrial and laboratory microwave ovens range mostly from 915 MHz up to 30 GHz. Microwaves came of age with the development of radar during World War II. At that time it was discovered that microwave energy from radar could dry large ceramic bodies. However, serious efforts to process ceramics with microwave energy did not emerge until the late 1960's and early 1970's.[12] In recent years, many researchers have studied high-temperature processing of ceramics such as firing, sintering, joining, and melting.[13-14] The initial stimuli for their efforts were the unique benefits microwave heating could provide in comparison to conventional heating. These benefits include more precise, controlled and uniform volumetric heating, faster ramp-up to temperature, lower energy consumption, and improved material quality and properties. The sintering of Al_2O_3 30 wt% TiC composites using nitrogen pressures of about 1 MPa in a microwave field was reported.[14] Composite rods were rapidly and uniformly heated to 1850°C and were sintered to 95% of theoretical density without cracking. These composites are difficult to densify using conventional sintering methods.

1.4.4.2 Conversion of Electromagnetic Energy to Heat

Microwave energy is transferred to materials by the interaction of electromagnetic fields at the molecular level. The material property which dictates the interaction is best described by the material's complex permittivity.

Complex permittivity is defined as[14]

$$\varepsilon^{*} = \varepsilon' - j\varepsilon'' = \varepsilon_o(\varepsilon_r' - j\varepsilon_{eff}'') \qquad (1.11)$$

where ε' is the dielectric constant, ε'' is the dielectric loss factor, ε_o is the permittivity of free space, ε_r' is the relative dielectric constant and ε_{eff}'' is the relative dielectric loss factor.

The loss tangent is defined as[14]

$$\tan \delta = \varepsilon''/\varepsilon' \qquad (1.12)$$

At microwave frequencies, dipole polarization is the most important mechanism for energy transfer at the molecular level. The dielectric properties of materials in combination with an applied electromagnetic field result in the conversion of electromagnetic energy into heat.

The power absorbed per unit volume is given by[14]

$$P = 2\pi f \varepsilon_o \varepsilon_r' \tan \delta |E|^2 \qquad (1.13)$$

Where E is the magnitude of the internal electric field and f is the frequency.

The penetration depth is given by[14]

$$d = c\, \varepsilon_o / 2\pi f \varepsilon'' \qquad (1.14)$$

where c is the speed of light

Equations (1.11) and (1.12) give an insight into which dielectric materials are suitable for microwave processing. Materials with a high conductance and low capacitance (such as metals) have high dielectric loss factors. As the dielectric loss factor increases, the penetration depth approaches zero. Materials with low dielectric loss factors have a very large penetration depth. As a result, very little of the energy is absorbed in the material, and the material is transparent to microwave energy such as alumina (Figure 1.8). As a result, materials that have dielectric loss factors in the middle of the conductivity range convert electromagnetic energy into heat energy efficiently. The dielectric properties depend on the mobility of the dipoles within the structure, and are therefore functions of temperature and frequency.

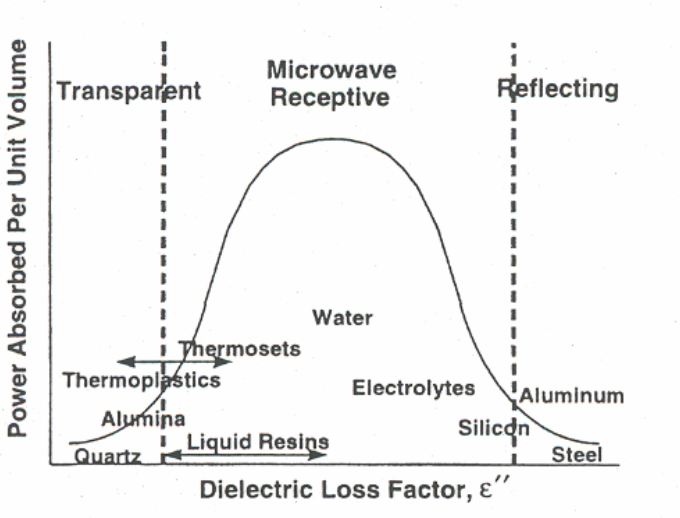

Figure 1.8. Relationship between the dielectric loss factor and the ability to absorb microwave power for some common materials.[15]

1.4.4.3 Microwave Material Interactions

Many ceramics, such as silicon carbide SiC and β-alumina have dielectric properties (high loss tangent) that are suitable for microwave processing at relatively low temperatures (e.g., below 1000°C). Other materials, such as silicon nitride (Si_3N_4) and α-alumina (Al_2O_3), are transparent to microwaves at room temperature. During heating, the dielectric constant and loss tangent change. At temperatures above a critical temperature, the dielectric loss factor begins to increase, and the material begins to couple with microwaves.[14] Figure 1.9 and Figure 1.10 show the interaction of Al_2O_3 with 8-10 GHz microwaves. 97% pure Al_2O_3 couples with microwaves about 800°C. However, 99% pure Al_2O_3 is not as good a coupler as 97% Al_2O_3.

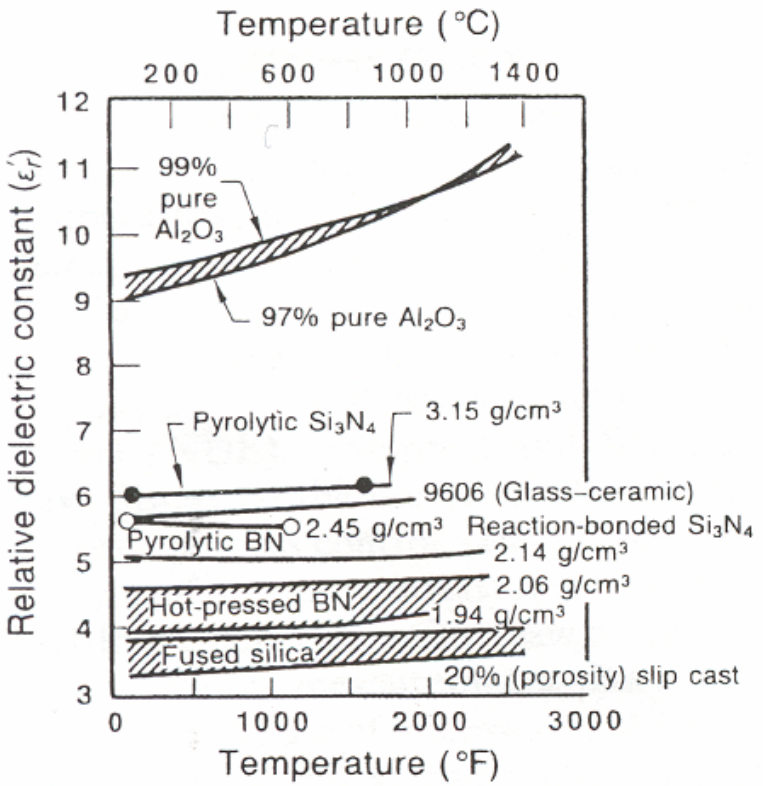

Figure 1.9. Relative dielectric constant (8 to 10 GHz) versus temperature.[14]

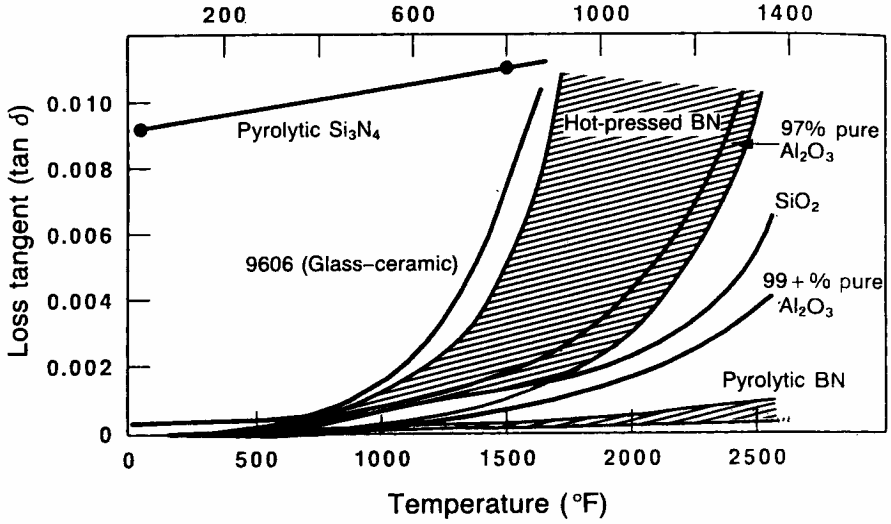

Figure 1.10. Loss tangent (8 to 10 GHz) versus temperature.[14]

When ceramics are processed in non-uniform electromagnetic fields, the local temperature may vary within the material. If a local volume reaches the critical temperature before the rest of the material, that area begins to heat more rapidly, and the temperature begins to increase at an even higher rate. This can result in localized thermal runaway that can cause stresses high enough to fracture the material.[14] Hybrid heating can be used to process materials which exhibit this behavior. Before the critical temperature is reached, the ceramic is heated through traditional heat transfer. When the material begins to heat, its loss factor increases, and as a result, the material more readily absorbs the microwaves.

In addition to increased heating rates, microwave sintering often results in enhanced mechanical properties. Due to the reduced thermal gradients realized during microwave sintering processes, there are lower induced stresses. Also, the uniformity of the ceramic microstructure can be improved with microwave heating. Because of the shorter sintering cycles and reduced thermal gradients, finer grain sizes can be obtained, and there is greater uniformity in the grain size and shape factor.[14] Greater uniformity in the microstructure results in reduced scatter in the mechanical properties.

1.4.4.4 "Microwave Effect" or Non-thermal Interaction

Recent reports suggest that microwave heating of ionic crystalline solids (e.g. ceramics) leads to enhanced mass transport rates when compared to conventional heating at the same temperature.

Densification and the mass transport rates have sometimes been enhanced by an order of magnitude. Process times and temperatures have been significantly lowered. Specific observations exist for pure and blended alumina,[16, 17] blends of zirconia,[18] and other ceramics such as hydroxyapatites,[19] and nitrides.[20-21]

In addition to sintering, many other thermally activated processes have been studied in microwave furnaces and compared to conventional processing. Several research groups have reported microwave-enhanced joining of ceramic parts.[22] Other processes studied span a wide range of nucleation and crystallization,[23] grain growth,[24] annealing[25] and other solid-state reactions.[26] More fundamental studies of tracer diffusion of O^{18} in alumina and chemical diffusion in glasses[27] and ceramics[28] have, in

some cases, shown microwave-enhanced surface penetration by the diffusing species. Investigators at Oak Ridge National Laboratories have reported faster densification rates for Al_2O_3 and ZrO_2. Their grain-growth studies with Al_2O_3 yielded activation energies of 480 kJ/mole (microwave) compared to 590 kJ/mole (conventional).[24]

Direct comparisons of different studies are difficult to make due to varying conditions between research facilities. The studies have involved different microwave field strengths, field orientations and patterns, processing temperature, ramp-up rates, materials, etc. Some comparisons between microwave and conventional thermal processing have been performed with identical heating schedules, while many others used dissimilar schedules. Nonetheless, the bulk of the evidence showing microwave enhancements suggest that a non-thermal interaction (s) may indeed exist.

1.4.4.5 Conventional Heating versus Microwave Heating

Microwave heating is fundamentally different from conventional heating. In the microwave process, heat is generated internally within the material.[14] As a result of this internal and volumetric heating, the thermal gradients and flow of heat in microwave processed materials are the reverse of those in materials processed by conventional heating. Consequently, microwave processing makes it possible to heat both small and large shapes very rapidly and uniformly to efficiently remove volatile constituents (binders, moisture) from thick sections, and to reduce thermal stresses that cause cracking during processing.[14] Since the absorption of microwave energy varies with the composition and structure of different phases, selective heating is also possible and presents new opportunities. Conventional heating in dielectric ceramics is a combined function of the thermal conductivities of the specific material.

In ceramics, the conduction process for heat transfer under the influence of a temperature gradient depends on the energy concentration present per unit volume, its velocity of movement, and it's rate of dissipation with the surroundings. There are two mechanisms by which heat conduction is effected: phonon conduction, the predominant mechanism, and photon conduction.[28] The conduction of heat in dielectric solids may be considered either as the propagation of inharmonic elastic waves through a continuum or as the interaction between quanta of thermal energy called phonons. Thus, the thermal

conductivity of dielectric ceramics can be attributed to phonon and photon processes. In polycrystalline and poly-phase ceramics the conductivity is fixed by the compositions of the phases present, and by the shape and distribution of phases including the pore phase. When these parameters are known, the overall conductivity can be predicted. Although phonon conduction processes are known to be predominant, at higher temperatures photon conduction processes assume importance, and contribute to the overall conductivity. Photons are scattered by even small amounts of porosity. Hence in most polycrystalline ceramics, which contain a few percent porosity, the photon contribution to energy transfer does not become significant until very high temperatures (e.g., 1500°C) are reached.[28]

The conduction of heat in dielectric ceramics, can be expresses as

$$q = \left(\frac{dQ}{dt}\right) = -k\,A\frac{dT}{dx} \tag{1.15}$$

where "q" is the amount of heat; "dQ" flowing in time dt which is normal to the area "A"

This heat flow is proportional to the temperature gradient in the direction of heat flow $-\left(\frac{dT}{dx}\right)$, and the proportionality constant is the thermal conductivity (k).

Fourier's law explains the heat flow in three dimensions as

$$\frac{\partial T}{\partial t} = \alpha \nabla^2 T \tag{1.16}$$

where α (thermal diffusivity) $= \left(\frac{k}{\rho C_P}\right)$ and (1.17)

$$\nabla^2 T = \left[\frac{\partial^2 T}{\partial x^2} + \frac{\partial^2 T}{\partial y^2} + \frac{\partial^2 T}{\partial z^2}\right] \tag{1.18}$$

is the temperature gradient.

From Equations 1.16 and 1.17, we have,

$$\rho C_P \left(\frac{\partial T}{\partial t} \right) = -\nabla \overset{\rho}{J}_q \tag{1.19}$$

$$\text{where the heat flux } \overset{\cup}{J}_q = \left(-k \cdot \nabla T \right) \tag{1.20}$$

Equation (1.19) may also be written as the divergence of the heat flux div J_q

Therefore equation (1.19) can be re-written as

$$\left[\rho C_P \left(\frac{\partial T}{\partial t} \right) \right]_{CONV.} = -div\, J_q \tag{1.21}$$

This denotes the rate of accumulation of heat in the ceramic fired by conventional heating.

For microwave heating, the rate of accumulation of heat is a function of microwave/material interaction, and therefore, the ceramic's dielectric properties. Hence we can write,

$$\rho\, C_P \left(\frac{\partial T}{\partial t} \right) = \dot{q} = \frac{dQ}{dt} = P \tag{1.22}$$

where P is the microwave power dissipated, and

$$P = \sigma \left| E \right|^2 = 2\pi f\, \varepsilon_0\, \varepsilon_r^{'} \tan\delta \left| E \right|^2 \tag{1.23}$$

Therefore, for microwave heating of ceramics we have,

$$\left[\rho\, C_P \left(\frac{\partial T}{\partial t} \right) \right]_{MW} = 2\pi f\, \varepsilon_0\, \varepsilon_r^{'} \tan\delta \left| E \right|^2 \tag{1.24}$$

For microwave hybrid heating of ceramics, a combination of conventional heating (thermal conductivity) and microwave/material interaction (dielectric properties) can be written (from equations 1.21 and 1.22) as

$$\left[\rho C_P \left(\frac{\partial T}{\partial t} \right) \right]_{MHH} = \left[-div\, J_q \right]_{CONV.} + \left[\dot{q} \right]_{MW} \tag{1.25}$$

The divergence of the heat flux J_q may also be expressed alternatively as

$$-div\ J_q = -\nabla\left(-k\nabla T\right) = k\nabla^2 T \qquad (1.26)$$

Therefore, the local rate of rise in temperature in a ceramic heated by microwave hybrid heating (from equations 1.24, 1.25 and 1.26) may be given

$$\left(\frac{\partial T}{\partial t}\right)_{MHH} = \frac{1}{\rho C_P}\left\{\left(k\nabla 2\, T\right)_{CONV.} + \left(2\,\pi\, f\,\varepsilon_0\,\varepsilon'_r\,\tan\delta|E|^2\right)_{MW}\right\} \qquad (1.27)$$

1.5 Microstructure and Mechanical Properties of Silicon Nitride

Although, silicon nitride has a high specific strength at elevated temperatures, its use for a wide range of applications has still not been realized due to the high cost of components and the large scatter in the property data such as strength, fracture toughness reliability and reproducibility. The difficulty in reproducibility can be attributed to the relatively complex microstructure developed during densification by liquid-phase sintering and the complicated interrelationships between the size and shape of the silicon nitride grains, distribution of the grain boundary phase, and the mechanical properties. The multi-phase microstructure, consisting of silicon nitride embedded in an amorphous or partially crystalline grain-boundary phase, provides a great opportunity to optimize material properties for specific applications.[1] Thus, a detailed understanding of the microstructural development is necessary in order to achieve the best properties required for demanding applications.[1] Figure 1.11 shows the microstructure of a polished and plasma-etched silicon nitride sample. The multiphase microstructure consists of β-Si_3N_4 grains, embedded in an amorphous or partially crystalline matrix. Figure 1.12 shows a computer-simulated 3D microstructure of silicon nitride.

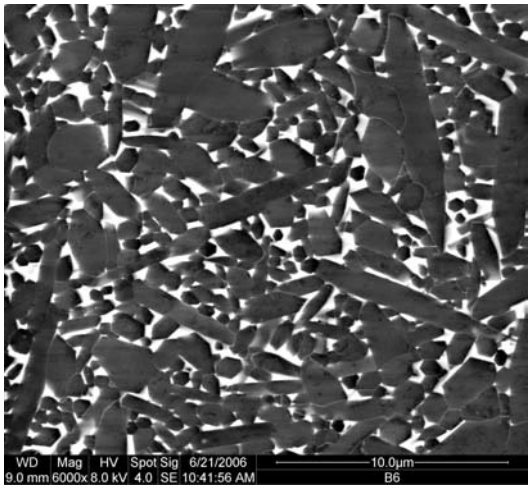

Figure 1.11 SEM image of plasma etched Si_3N_4 showing the inter-granular glassy phase (white region) and β-Si_3N_4 grains.

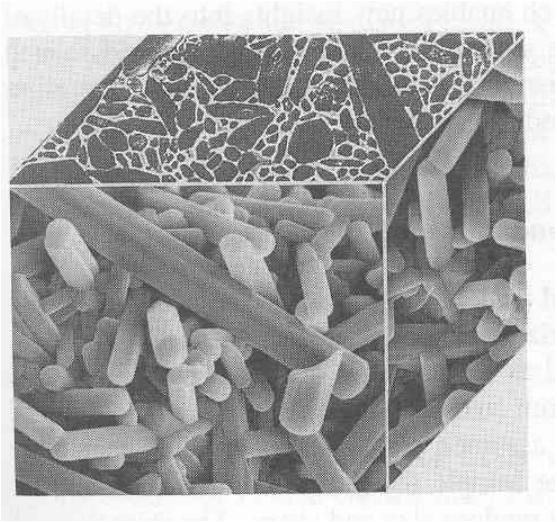

Figure 1.12 Computer simulated 3D image of a Si_3N_4 microstructure.[29]

The key to obtaining a high-strength silicon nitride is a nearly defect-free fine grain microstructure with a specific grain size distribution and aspect ratio.[1] Figure 1.13 shows the fracture toughness-strength relations for the silicon nitride ceramics that are commercially available.[30] Attempts to improve these properties have resulted in two distinctive patterns, as shown in Figure 1.13: higher strength and higher fracture toughness. Large elongated grains are preferred for high-toughness materials, since crack bridging is the major toughening mechanism. Large grains are a necessary, but

insufficient condition for high toughness. An interfacial bonding force is another key factor, and thus the chemistry of grain boundary phases is also an important consideration. One needs to choose appropriate starting powders, compositions and sintering methods to optimize the manufacturing conditions. For instance, grain growth is promoted by high-temperature sintering (gas pressure sintering) and selecting suitable sintering additives which promote grain growth. Conversely, during low-temperature sintering and hipping, a grain-growth inhibitor is necessary to obtain high-strength materials. The materials currently used for real applications have fracture toughnesses in the order of 5-7 MPa·$m^{1/2}$ and flexural strengths of 700-1100 MPa.[30] Table 1.III compares the mechanical properties of silicon nitride with selected advanced structural ceramics.

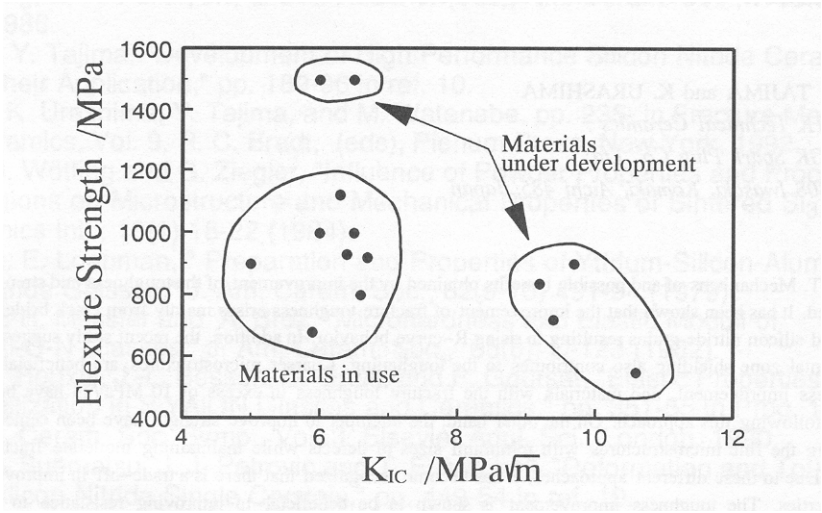

Figure 1.13 Strength and fracture toughness of various Si_3N_4.[30]

Table 1.III. Mechanical Properties of Structural Ceramics.[31]

	Oxides		Nitrides	Carbides	
	Al_2O_3	ZrO_2	Si_3N_4	SiC	B_4C
Density, gm/cc	3.9	6.1	3.2	3.1	2.5
Flexural Strength, MPa, RT	300-600	900-1200	800-1100	400-600	300-400
Fracture Toughness, MPa-$m^{1/2}$	3–4	6–10	5–7	3–4	2–3
Thermal Coef.Exp. (x 10^{-6}/°K)	7–8	9–11	2–3	4–5	5–6
Hardness, HV (10 kg load)	15–18	11–13	15–17	25–27	27–29

Figure 1.14 shows the toughening mechanisms operative in silicon nitride ceramics. They are (a) crack bridging by larger elongated grains, (b) frictional translation of partially separated grains, (c) frictional pull out of elongated grains, and (d) inclined reinforcement bending. Figure 1.15 shows the role of elongated β-Si_3N_4 grains in crack deflection and branching leading to improved fracture toughness. Figure 1.16 shows pullout of elongated β-Si_3N_4.

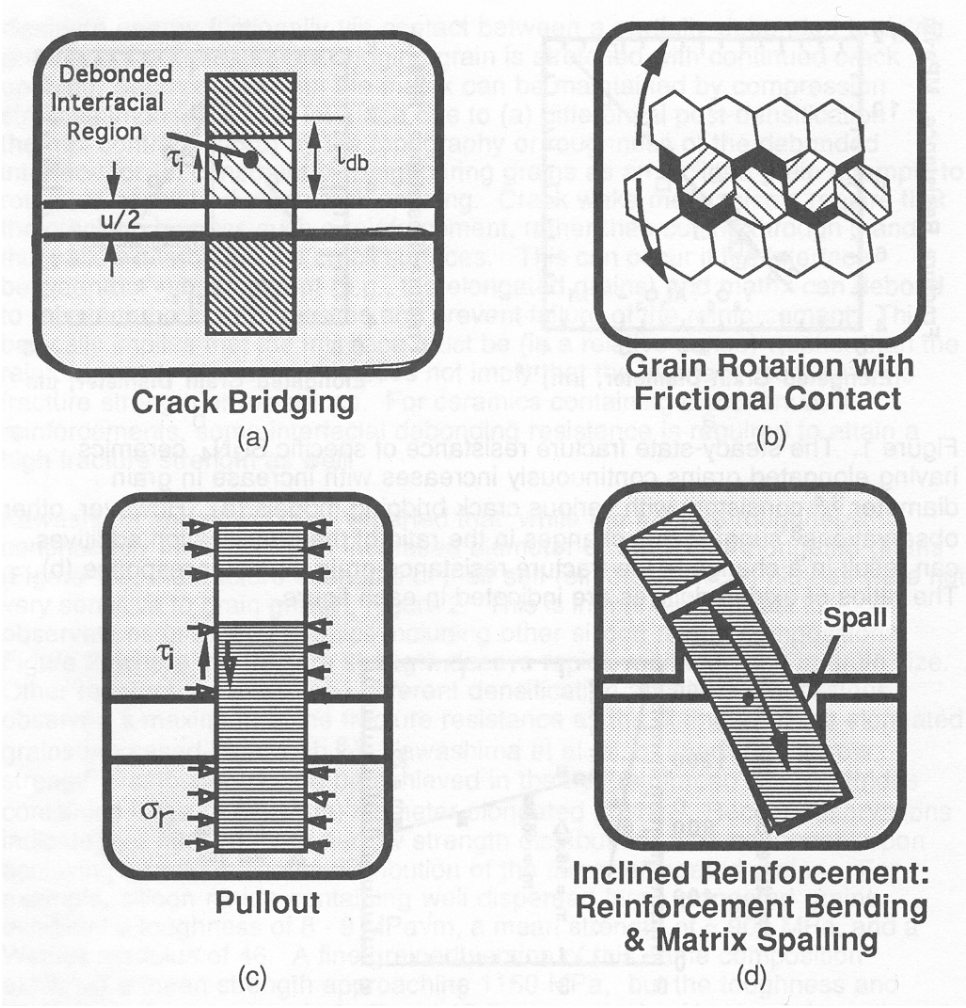

Figure 1.14. Crack wake mechanisms operating in silicon nitride.[32]

Crack bridging and partial debonding of elongated β-Si_3N_4 grains are shown in Figure 1.17.

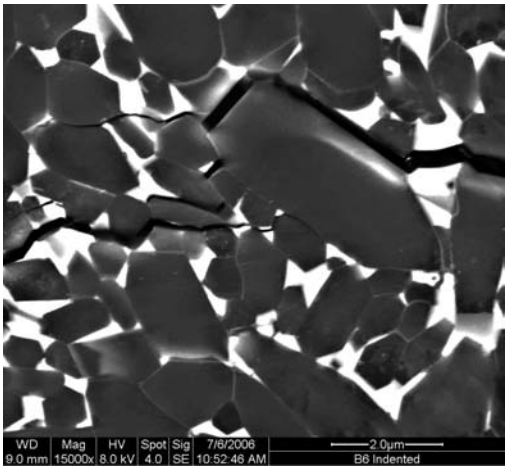

Figure 1.15. SEM image showing crack deflection and branching by a β-Si_3N_4 grain.

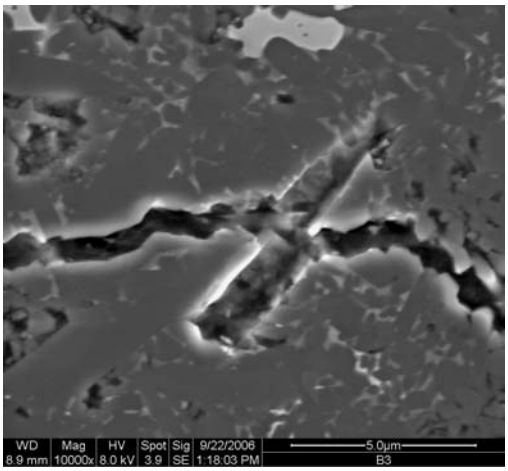

Figure 1.16. SEM image showing elongated β-Si_3N_4 grain pullout.

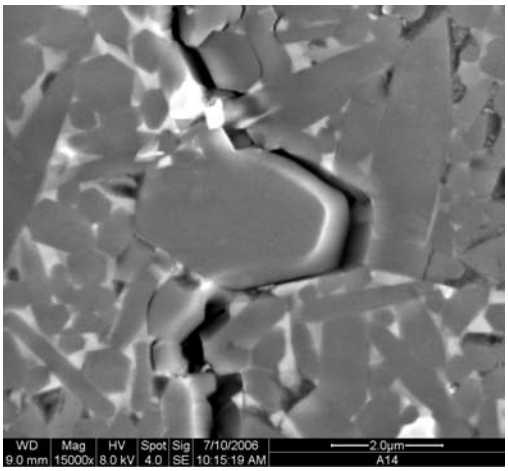

Figure 1.17. SEM image shows crack bridging and partial de-bonding by a β-Si_3N_4 grain.

By changing the angle where the crack plane intercepts the longitudinal surface of the β-Si_3N_4 whisker, one can measure the distance the crack propagates along the interface (debond length). It is easier to deflect the crack further up the interface as the angle of incidence decreases.[33] The relative energy to de-bond the interface is related to the structure and chemistry of the interfaces as affected by the composition of the oxynitride glass matrix. The maximum angle of crack-plane incidence for interfacial debonding increases with a decrease in N_2 content of an oxynitride glass with ratio of Al_2O_3 to Y_2O_3 of one. This reflects a decrease in the energy for interfacial debonding with the decrease in N_2 content of this oxynitride glass. Decreasing the Al_2O_3-Y_2O_3 ratio of the glass decreases the interfacial debonding energy in oxynitride glass with a fixed N_2 content.

The second set of studies involved tailoring the additives used for liquid-phase sintering of Si_3N_4 to alter the thermal expansion coefficient and Young's modulus of the glassy grain boundary phase. With the relatively low thermal expansion coefficient of β-Si_3N_4, the grain boundary glass phase is subjected to residual tensile stresses at room temperature. As a result, fracture in the glass near the interface may be promoted, leading to the development of bridging of elongated β-Si_3N_4 grains. The fracture toughness of Si_3N_4 ceramics is increased with an increase in the thermal expansion coefficient of the grain boundary phase represented by the selection of the additive composition.[33] Fine-grain Si_3N_4 ceramics have reduced fracture toughness, and their fracture strengths can be exceptionally high, reaching 1000-1500 MPa. With grain growth, increases in the size of the elongated grains increases the fracture toughness but the fracture strength decreases. Further improvement of fracture toughness in Si_3N_4 can be attained by the alignment of large elongated β-Si_3N_4 by tape casting the raw powders seeded with rod-like β-Si_3N_4 particles. A fracture toughness of 12 MPa $m^{1/2}$ and a bending strength of 1.4 GPa were achieved in the direction perpendicular to the grain alignment. [34]

1.6 Previous Work on Microwave Sintering of Si_3N_4

Early in the 1990s, Oak Ridge National Laboratory (ORNL) researchers developed a microwave sintering method for making silicon nitride parts for advanced

engines for transportation.[35] The ORNL technique produced silicon nitride parts that were cost effective and denser than parts made by conventional heating processes. Applications of these include components for engines operated at high temperatures, such as turbocharger rotors, valves and valve parts, and pump seals. Others include tools to cut metals and dies for forming aluminum beverage cans. Some silicon nitride parts that meet the requirements for use in engine applications have been made with different processes, but these components were more expensive than metal parts. The ORNL process using microwave heating produced ceramic parts that were economically competitive with metal components. The chief reasons were that ORNL used a combination of low-cost raw materials (about one-fourth that of the materials used in other processes) and a simplified sintering route, made possible by the microwave heating. This process was developed by Terry Tiegs and James Kiggans, both of ORNL's Metals and Ceramics Division, and Cressie Holcombe, a researcher in the Development Division of the ORNL Y-12 Plant.[44] In ORNL's process, silicon powder mixed with additives in a preformed shape is reacted with a nitrogen-containing gas as the ceramic part is heated to 1200 to 1400ºC by microwave power. As a result, nitridation of the silicon (Si) to silicon nitride (Si_3N_4) occurred. Without removing the parts from the microwave furnace or cooling them down, the parts are then heated at 1750 to 1825°C, making them extremely dense. With conventional heating, the nitridation and densification steps are done in two different furnaces. By using microwave heating to accomplish both tasks, the fabrication times and labor costs were significantly reduced. According to the developers,[35] microwave heating offers several advantages over conventional heating. Nitridation begins at a lower temperature and occurs at a faster rate. Nitridation and sintering (heating) are accomplished in one continuous process. Densification rates are increased. Finally, thicker parts can be made because nitridation proceeds from the inside out.

K. P. Plucknett and S. D. Wilkinson[36] microwave sintered silicon nitride in air with a typical sintering time of 90 minutes, although longer cycle times were used for larger batches (1Kg). Y_2O_3 and Al_2O_3 were used as sintering additives, and a density of 3.10 (94% of theoretical density) was achieved. M. C. L. Patterson et al.[6] microwave sintered 1kg of silicon nitride with 5 wt% each of Y_2O_3 and Al_2O_3; full density was

achieved by hipping at 1800ºC for 60 minutes. They reported energy savings up to 78% with microwave sintering. ORNL successfully conducted microwave sintering of silicon nitride with 12 wt% Y_2O_3 and 4 wt% Al_2O_3; after sintering at 1750ºC for 1 hour, a density of 96% was obtained.[37] They also added secondary additives that couple well with microwaves such as SiC and TiN, and observed enhanced densification.[38] M. Hirota et al.[39] sintered silicon nitride using 28 GHz frequency and reported 97% theoretical density and fracture toughness of 9 $MPa \cdot m^{1/2}$.

1.7 Objectives and Organization of the Thesis

The main objective of this study was to determine the effects of ZrO_2 as a secondary additive on the $\alpha \rightarrow \beta$ phase transformation, densification behavior, microstructural development and mechanical properties of microwave sintered Si_3N_4. ZrO_2 was selected as the additive of interest because it couples with microwaves at a lower temperature than Si_3N_4 and exhibits a high fracture toughness. Y_2O_3 and MgO were used as primary sintering additives in all of the formulations. SEM microstructural analysis was performed to understand the structure property interrelationships. TEM analysis was conducted to gain insight in the grain boundary phase. Results of dielectric the properties of Si_3N_4 with additives from room temperature to 1450ºC are presented. Conventional sintering was performed in similar conditions for the critical review of the benefits of microwave sintering. Temperature measurement uncertainties involved with the optical radiation pyrometer during microwave sintering were addressed with Finite Difference Time Domain (FDTD) numerical modeling of temperature and power distribution within the sample and the surroundings. The modeling was based on temperature-dependent dielectric properties of Si_3N_4 samples measured using resonant-cavity perturbation techniques.

This thesis contains five chapters. The first chapter is a general introduction, which includes an abridged literature survey of silicon nitride and microwave sintering. In Chapter 2, details of the Finite Difference Time Domain (FDTD) numerical modeling of temperature and power distribution within the sample and surroundings during microwave heating are given. Chapter 2 also provides dielectric properties of Si_3N_4 with and without sintering additives versus temperature. In Chapter 3, $\alpha \rightarrow \beta$ phase

transformation and densification behavior of microwave sintered Si_3N_4 samples in comparison with conventionally sintered samples is discussed. Chapter 4 give details of TEM grain boundary analysis of microwave sintered samples. Chapter 5 critically examines the effect of ZrO_2 on grain morphology on mechanical properties of the microwave samples and compares the results with conventionally sintered samples.

1.8 References

1. F.L. Riley, "Silicon Nitride and Related Materials," *J. Am. Ceram. Soc.,* **83** [2] 245-65 (2000).

2. L.R. Nittler, R. Strebel, R.M. Walker, and E. Zinner," Silicon Nitride from Supernovae*," J. Astrophys.*, **453** [1] L25-28 (1995).

3. H. Melner, "Verfahren Zur Darstellung Von Nitriden," Germ. Pat. 88999, 1896.

4. Carborundum Co., "Silicon Nitride Bonded Articles," U.S. Pat. 2618565, 1952.

5. G.R. Terwilliger and F.F. Lange, "Pressureless Sintering of Silicon Nitride," *J. Mater. Sci.,* **10** [7] 1169-74 (1975).

6. M.C.L. Patterson, P.S. Apte, R.M. Kimber, and R. Roy, "Batch Process for Microwave Sintering of Si_3N_4," Mat. Res. Soc. Symp. Proc. Vol. **269**, 291-300 (1992).

7. D. Hardie and K.H. Jack, "Crystal structures of silicon nitride," *Nature (London)*, **180** [8] 332-33 (1957).

8. M. N. Rahaman, *Ceramic Processing and Sintering*, pp.80-86. Marcel Dekker, New York, 1995.

9. C. Greskovich, S. Prochazka and J.H. Rosolowski, "The Sintering Behavior of Covalently Bonded Materials," *Nitrogen Ceramics*. Edited by F.L. Riley. Noordhoff International, Leyden, UK, (1977).

10. W.D. Kingary, "Densification During Sintering in the Presence of a Liquid Phase: I. Theory," J. Appl. Phys., **30** [3] 301-06 (1959).

11. W.E. Lee and W.M. Rainforth, *Ceramic Microstructures Property Control by Processing.* Chapman & Hall, London, UK, (1994).

12. W.H. Sutton, "Microwave Firing of High Alumina Castables," Microwave Processing of Materials, *Matls. Res. Symp. Proc.*, **124**, 287-95 (1988).

13. J.F. MacDowell, "Microwave Heating of Nepheline Glass-Ceramics," *Am. Ceram. Soc. Bull*., **63** [2] 282-86 (1984).

14. W.H. Sutton, "Microwave Processing of Ceramics," *Am. Ceram. Soc. Bull*., **68** [2] 376-86 (1989).

15. E.T. Thostenson and T.W. Chou, "Microwave Processing: Fundamentals and Applications," *Composites, Part A*, **30** [2] 1055-71 (1999).

16. M.A. Janney and H.D. Kimrey, "Diffusion-Controlled Processes in Microwave-Fired Oxide Ceramics,**"** *Mater. Res. Soc. Proc.,* **189,** 215-27 (1990).

17. J. Samuels and J.R. Brandon, "Effect of Composition on the Enhanced Microwave Sintering of Alumina Based Ceramic Composites," *J. Mater. Sci*., **27** [12] 3259-65 (1992).

18. M.A. Janney, C.L. Calhoun, and H.D. Kimrey, "Microwave Sintering of Zirconia 8 Mole % Yittria," pp. 311-18 in Ceramic Transactions, Vol. 21, *Microwaves: Theory and Application in Materials Processing.* Edited By D.E. Clark, F.D. Gac, and W.H. Sutton. American Ceramic Society, Westerville, OH, 1991.

19. Y. Fang, D.K. Agrawal, D.M. Roy, and R. Roy, "Rapid Sintering of Hydroxyapatite Ceramics by Microwave Processing," pp. 349-56 in Ceramic Transactions, Vol. 21, *Microwaves: Theory and Application in Materials Processing.* Edited by D.E. Clark, F.D. Gac, and W.H. Sutton. American Ceramic Society, Westerville, OH, 1991.

20. J. Zhang, L. Cao, and F. Xia, "Microwave Sintering of Si_3N_4 Ceramics," *Mater. Res. Symp. Proc*., **269,** 329-34 (1992).

21. Y.C. Kim, S.C. Koh, D.K. Kim, and C.H. Kim, "Effect of Microwave Heating on the Sintering of Silicon Nitride-Doped with Al_2O_3 and Y_2O_3," pp. 415-22 in Ceramic Transactions, Vol. 59, *Microwaves: Theory and Application in Materials Processing III,* Edited by D.E. Clark, D. Folz, S.J. Oda, and R. Silberglitt, . American Ceramic Society, Westerville, OH, 1995.

22. S. Al-Assafi and D.E. Clark, "Microwave Joining of Ceramics: A Study on Joining Alumina both Directly and with Alumina Gel," *Mater. Res. Symp. Proc.,* **269**, 335-40 (1992).

23. A. Boonyapiwat and D.E. Clark, "Nucleation and Crystal Growth of Li_2O - $2SiO_2$ in a Microwave Field," pp. 505-10 in Ceramic Transactions, Vol. 59, *Microwaves: Theory and Application in Materials Processing III,* Edited by D.E. Clark, D. Folz, S.J. Oda, and R. Silberglitt, . American Ceramic Society, Westerville, OH, 1995.

24. M.A. Janney and H.D. Kimrey, M.A. Schmidt, and J.O. Kiggans, "Grain Growth in Microwave-Annealed Alumina," *J. Am. Ceram. Soc*., **74** [7] 1675-81 (1991).

25. T.N. Tiegs, M.K. Ferber, J.O. Kiggans, K.L. More, C.M. Hubbard, and D.W. Coffey, "Microstructure Development During Microwave Annealing of Dense Silicon Nitride," pp. 411-20 in Ceramic Transactions, Vol. 21, *Microwaves: Theory and Application in Materials Processing*. Edited by D.E. Clark, F.D. Gac, and W. H. Shutton. American Ceramic Society, Westerville, OH, 1991.

26. I. Ahmad and D.E. Clark, "Effect of Microwave Heating on Solid State Reactions of Ceramics," pp. 605-12 in Ceramic Transactions, Vol. 21, *Microwaves: Theory and Application in Materials Processing*. Edited by D.E. Clark, F.D. Gac, and W. H. Shutton. American Ceramic Society, Westerville, OH, and1991.

27. Z. Fathi, I.Ahmad, J.H. Simmons, and D.E. Clark, "Surface Modification of Sodium Aluminosilicate Glasses Using Microwave Energy," pp. 623-29 in Ceramic Transactions, Vol. 21, *Microwaves: Theory and Application in Materials Processing*. Edited by D.E. Clark, F.D. Gac, and W. H. Shutton. American Ceramic Society, Westerville, OH, 1991.

28. W.D. Kingery, "The Thermal Conductivity of Dielectric Ceramics," pp. 182-35 in *Progress in Ceramic Science* Vol. 2. Edited by J.E. Burke. The Pergamon Press, New York, (1962).

29. F.M.J. Ohser, "3D Characterization of Sintered Microstructure with Prismatic Grains," pp. 73-86 in *Tailoring of Mechanical Properties of Silicon Nitride Ceramics*, Vol. 276. Edited by M. J. Hoffmann and G. Petzow. Kluwer Academic, Boston, MA, 1994.

30. Y. Tajima and K. Urashima, "Improvement of strength and toughness silicon nitride ceramics", pp. 101-109 in *Tailoring of Mechanical Properties of Silicon Nitride Ceramics*, Vol. 276. Edited by M. J. Hoffmann and G. Petzow. Kluwer Academic, Boston, MA, 1994.

31. "Ceramic Materials and Bearing Compatibility" (2002) Saint Gobain Cermics. Accessed on: May 2007. Available at <www. cerbec.com>.

32. P.F. Becher, S.L. Hwang, H.T. Lin, and T.N. Tiegs, "Microstructural Contributions to the Fracture Resistance of Silicon Nitride Ceramis," pp. 87-100 in *Tailoring of Mechanical Properties of Si_3N_4 Ceramics,* Vol. 276. Edited by M. J. Hoffmann and G. Petzow. Kluwer Academic, Boston, MA, 1994.

33. P.F. Becher, S.L. Hwang, and C.H. Hsueh, "Using Microstructure to Attack the Brittle Nature of Silicon Nitride Ceramics," *Mater. Res. Bull*., **20** [2] 23-27 (1995).

34. K. Hirao and S. Kanzaki, "Processing Strategy for Producing Highly Anisotropic Silicon Nitride," *J. Am. Ceram. Soc*., **78** [6] 1687-90 (1995).

35. J.O. Kiggans, Jr., T.N. Tiegs, C.C. Davisson, M.S. Morrow, and G.J. Garvey, "Scale-up of the Nitridation and Sintering of Silicon Performs Using Microwave Heating," *Mater. Res. Symp. Proc*., **430**, 3-8 (1996).

36. K.P. Plucknett and D. Wilkinson, "Microstructural Characterization of Microwave Sintered Silicon Nitride Cermics," *Mater. Res. Symp. Proc*., **245**, 289-94 (1993).

37. T.N. Tiegs, J.O. Kiggans, and H.D. Kimrey, "Microwave Processing of Silicon Nitride," *Mater. Res. Symp. Proc*., **189**, 267-72 (1990).

38. T.N. Tiegs, J.O. Kiggans, and H.D. Kimrey, "Microwave Sintering of Silicon Nitride," *Ceram. Eng. Sci. Proc*., **12** [9-10] 1981-92 (1991).

39. M. Hirota, M.E. Brito, K. Hirao, K. Watari, M. Toriyama, and T. Nagaoka, "Microwave Sintering of Silicon Nitride With Rare Earth Sesquioxide Additions," pp. 515-22 in *Microwaves: Theory and Application in Materials Processing IV,* Vol. 80. Edited. By D.E. Clark, W. H. Sutton, and D. A. Lewis. Materials Research Society, Pittsburgh, PA, 1997.

40. K. Negita, "Effective Sintering Aids for Si_3N_4," *J. of Mater. Sci. Letters*, **4** [1] 755-58 (1985).

CHAPTER 2

FDTD Numerical Simulation

Abstract

Accurate measurements of the temperature distribution in materials during microwave sintering are difficult to obtain using an optical pyrometer and other traditional methods. This chapter discusses simulations of microwave power absorption and the resulting temperature evolution in silicon nitride samples and the surroundings based on predictions from Finite Difference Time Domain (FDTD) electromagnetic tool coupled to a thermal solver. The simulation was used to better explain results from real Si_3N_4 sintering trials that utilized a similar microwave setup. Microwave power absorption was calculated from temperature-dependent dielectric properties measured from 25°C to 1400°C using a conventional cavity perturbation technique. Three different compositions were prepared for this study. i) Si_3N_4 without sintering additives, ii) 90 wt% Si_3N_4 with 4 wt% MgO and 6 wt% Y_2O_3, and iii) 87.5 wt% Si_3N_4 with 4 wt% MgO, 6 wt% Y_2O_3 and 2.5 wt% ZrO_2. It was observed that higher temperatures were developed in samples containing a higher dielectric loss sintering additive (4 wt% MgO, 6wt% Y_2O_3 and 2.5 wt% ZrO_2) when compared against similar samples with; i) a low dielectric loss sintering additive (4 wt% MgO and 6 wt% Y_2O_3), and ii) no sintering additives. Moreover, all the silicon nitride samples showed a reverse thermal gradient. Temperatures within the samples, as predicted by the FDTD simulation, were much higher than temperatures indicated by the optical pyrometer.

2. 1 Introduction

Silicon nitride ceramic is considered as one of the most promising high-temperature structural materials by virtue of its excellent thermal, wear resistance and mechanical properties.[1] Densification of Si_3N_4 by solid-state sintering is difficult because of its covalent bonding and low diffusion coefficients.[2] Hot iso-static pressing and gas-pressure sintering are the common fabrication methods utilized for the production of full dense Si_3N_4 components.[3] However, these methods are very expensive. In recent years, many reports have suggested that microwave sintering is an alternative method, that and has advantages over conventional sintering such as reduced sintering time, temperature, and the capability of producing unique microstructures.[4-7]

The effective use of microwave energy for the high-temperature sintering of ceramic materials requires knowledge of the dielectric properties of the material, as well as its dependence on temperature.[8] During the microwave sintering process, the

microwave power absorbed by a sample is proportional to the electrical field distribution within the sample; and is determined by the complex dielectric permittivity of the material. The imaginary part of the permittivity determines the attenuation or absorption of the electric field as electromagnetic energy propagates through the material. Si_3N_4, in its pure form, is a poor microwave absorber due to its low dielectric loss over the entire temperature range of interest.[8] Tiegs et al.[9] reported that the efficiency of microwave power absorption of low-loss materials can be improved by the addition of high-dielectric-loss secondary particulates. In the presence of these additives, sintering of Si_3N_4 takes place as a consequence of preferential coupling of microwaves to the oxide additives. The resulting liquid phase created at the grain boundary assists the densification of Si_3N_4 well below its decomposition temperature at 1840^oC at 0.1 MPa of nitrogen pressure.[9]

The objectives of this research were to measure the temperature-dependent dielectric properties of Si_3N_4 samples, containing high-lossy secondary particulates and use this information to simulate the microwave power absorption and temperature during microwave sintering using FDTD numerical tool. Three samples were considered in the study; i) pure Si_3N_4, ii) Si_3N_4 with MgO and Y_2O_3 and iii) Si_3N_4 with MgO, Y_2O_3, and ZrO_2. The numerically predicted surface temperature of the crucible, which contained the silicon nitride samples, was compared with corresponding experimentally measured temperature, using optical radiation pyrometer for the purpose of benchmarking the model. Profiles of microwave power absorption and temperature distribution of three different samples were presented and used to gain better understanding of the microwave material interactions.

2.2 Dielectric Properties Measurement

2.2.1 Sample Preparation

Three silicon nitride sample compositions were prepared for this study. The first set of samples contained no sintering additives. The second set of samples contained 90 wt% α-Si_3N_4 powder (E10 grade, UBE Industries Ltd., Japan) with 6 wt% Y_2O_3 (Aldrich Chemical Company, Inc, 99.99%), and 4 wt% MgO (Aldrich Chemical Company, Inc,

99.99%). The third sample set contained 87.5 wt% α-Si_3N_4 powder (E10 grade, UBE Industries Ltd., Japan) with 6 wt % Y_2O_3 (Aldrich Chemical Company, Inc, 99.99%), 4 wt% MgO (Aldrich Chemical Company, Inc, 99.99%), and 2.5 wt% of a 3 mol% Y_2O_3 stabilized ZrO_2, 99.99% (Tosoh Corporation, Japan). The samples were prepared by ball milling the α-Si_3N_4 powder containing the additives and dispersed in de-ionized water, for 12 hours. The powders were dried, ground, and sieved through a 75-micron mesh. Five grams of the mixed powders were uniaxially die-pressed at 30 MPa and then cold isostatically pressed at 200 MPa into a cylindrical pellet having green dimensions of 23mm diameter and 5 mm thickness. From these prepared green samples cylindrical pieces 4 mm diameter and 12 mm length were cut for dielectric measurements. This measurement technique requires that the sample be loaded into a long, slim, high-purity, amorphous silica tube having dimension of 12 mm length and 4 mm inner diameter.

2.2.2 Dielectric Constant Measurements

The temperature-dependent dielectric property measurement system consists of a TM_{ono} resonator (Figure 2.1.) which is a 580 mm (23") diameter, 50 mm long right cylindrical cavity (fundamental mode at 400 MHz) which, with a 12 mm long, 4 mm diameter sample inserted along the central axis, and which has clearly separated modes up to n=6 at 2970 MHz. The cavity is a furnace-brazed, thick-walled OFHC copper structure with cooling channels machined into the central axial region which is exposed to the high temperature sample and sample holder. The unloaded Q of this cavity is approximately 10,000 at 400 MHz and increases to over 30,000 for the n= 6 mode. The thermal transient produced by inserting the hot sample produces small shifts in frequency; the effect of these shifts are minimized by performing hot empty sample holder measurements having the same time delays and frequency sequences used during measurements with samples.

$\chi_e = \chi_e' - j\,\chi_e''$ may be determined from resonant-cavity perturbation measurements using the following equation

$$\frac{\Delta f}{f_E} + j\left(\frac{1}{2Q_{L,S}} - \frac{1}{2Q_{L,E}}\right) = \frac{-\chi_e}{(1 + F_{sh} * \chi_e)} \frac{V_s}{V_c} A \qquad (2.1)$$

where f_E, $Q_{L,E}$ are the cavity frequency and loaded Q, with the empty holder,

Δf is the frequency shift produced by the sample,

$Q_{L,S}$ is the loaded cavity Q, with the holder and sample,

F_{sh} is a real number dependent only on the sample shape,

V_s and V_c are the sample and cavity volumes,

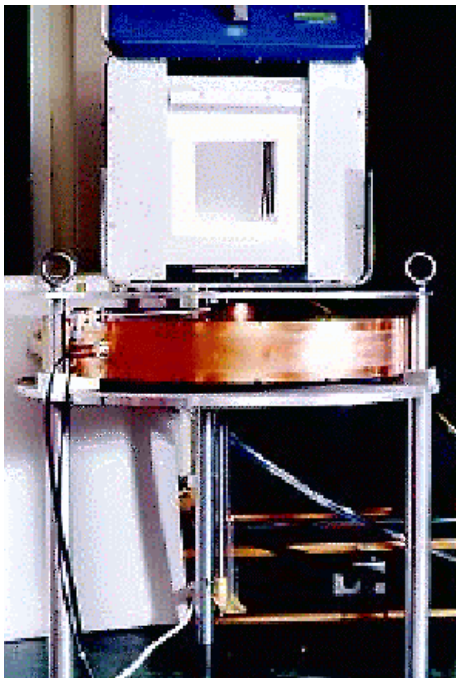

Figure 2.1. The temperature-dependent dielectric property measurements setup.

"A" is a real calibration constant dependent only on the shape of the electric fields in the absence of the sample. The two calibration constants in the formula, A and F_{sh} can be determined either by comparison with computer simulations or by comparison with known samples. For solid calibrators, single-crystal, high-purity sapphire ($\varepsilon_r' = 11.54$ with electric field parallel to the C-axis, $\varepsilon_r' = 9.34$ perpendicular to C-axis) may be used for the second calibration point, with teflon ($\varepsilon_r' = 2.07$) used as a reference check at lower dielectric constant values. The error of this calibration technique for the present sample length-diameter ratio (≈ 3.5) was shown to be less than $\pm$ 3% for $\varepsilon_r \leq 30$ and $\tan \delta \leq 1$ by comparing the results of Equation 2.1 with numerical calculations.

The initial dimensions were determined, and the initial mass of each sample was obtained by weighing the holder before and after loading the sample. A "run" consisted of flushing the holder for 30 minutes with high-purity nitrogen, and then leaving a 15

sccm flow of nitrogen flowing up past the sample during the measurements. The furnace temperature was increased in 200°C, then 100°C, then 50°C steps up to 1450°C, holding after each step for a 6-minute soak in order to allow the temperature of each sample to stabilize and become uniform. After reaching 1450°C, the temperature was reduced, and the resonant frequency and loaded Q of the cavity were measured with a Hewlett-Packard-8753 network analyzer. Measurements were also done at a few temperatures on the return to room temperature and stored for off-line analysis which included subtraction of hot empty sample holder effects. At the end of the run, the sample dimensions and the mass of the final sample holder plus sample were determined. The sample was removed from the holder and the dielectric properties of the empty holder, re-measured, to determine the high-temperature empty sample-holder contamination contribution.

The data analysis uses the general formalism of resonant cavity frequency shift theory, in which the real and imaginary parts of the complex electric susceptibility, $\chi = \varepsilon_r - 1$, are related, through functions dependent on sample shape, to the change in cavity resonant frequency and Q. The fundamental numbers, determined by the measurement, are the real and imaginary parts of the complex dielectric constant, denoted by ε' and ε''. The secondary number, derived from the values of ε' and ε'', is $\tan\delta = \varepsilon''/\varepsilon'$, which is an indicator of how well the material will absorb the microwaves, assuming the microwaves penetrate the material.

2.2.3 Sample Holder Considerations

Rapid movement of the sample in and out of a high-temperature furnace requires the sample holder to be relatively insensitive to temperature gradients and to high cooling and heating rates. High-purity amorphous silica by virtue of its superior thermal shock resistance can tolerate these conditions, as well as being inert in air up to 1600°C. Thus, the sample holders for high-temperature measurements are made from amorphous silica tubes, having one mille-meter wall thickness, and 6.0 mm and 4.0 mm inner diameters for the low and high frequency cavities, respectively. A one mille meter thick flat bottom is fused into the tube to support the sample. Teflon sample holders are used for low-temperature studies. High purity, low-OH-content amorphous silica has $\varepsilon_r' = 3.8$ and $\tan\delta = 10^{-4}$ at room temperature. However at high-temperatures (>1000°C), both ε_r' and the

losses increase significantly, and their contribution to the cavity frequency and Q shift value must be included. Before a measurement with a sample, the empty holder values are measured at 100°C intervals up to the maximum planned temperature. They are later subtracted from the sample measurements assuming the sample and empty holder shifts add linearly. The use of the amorphous silica holder is limited by two effects: 1) the gradual nucleation and recrystallization to cristoballite above 1000°C, and 2) chemical and physical interaction with the sample, particularly if the sample contains mobile or reactive metal ions. The former effect results in heavy "frosting" of the surface of the tube due to the formation of crystabolite, and, although there is very little change in the dielectric properties, embrittlement and cracking of the holder will eventually occur.

2.2.4 Measurement Results

Tables 2.I, 2.II and 2.III show the the temperature-dependent dielectric properties of the samples measured from room temperature to 1450°C:

i) 100 wt% Si_3N_4 (without sintering additives)

ii) 90 wt% Si_3N_4 with 4 wt% MgO, 6 wt% Y_2O_3,

iii) 87.5 wt% Si_3N_4 with 4 wt% MgO, 6 wt % Y_2O_3 and 2.5 wt % ZrO_2 respectively.

Table 2.I Dielectric Properties of 100% Si_3N_4

Temperature°C	Density	ε'	ε''	tanδ
24	1.691	3.27	0.002	0.000
161	1.689	3.27	0.001	0.000
359	1.686	3.27	0.002	0.001
566	1.683	3.28	0.002	0.001
671	1.681	3.29	0.005	0.001
774	1.679	3.3	0.003	0.001
876	1.678	3.31	0.006	0.002

985	1.676	3.33	0.010	0.003
1080	1.675	3.34	0.013	0.004
1181	1.673	3.35	0.020	0.006
1276	1.672	3.39	0.024	0.007
1323	1.671	3.41	0.023	0.007
1372	1.67	3.42	0.023	0.007
1419	1.669	3.42	0.018	0.005
1417	1.669	3.43	0.010	0.003
1176	1.673	3.39	0.004	0.001
977	1.676	3.37	0.004	0.001
24	1.691	3.27	0.000	0.000

Table 2.II Dielectric Properties of 90 wt% Si_3N_4 with 4 wt% MgO and 6 wt% Y_2O_3.

Temperature°C	Density	ε'	ε''	tanδ
24	1.746	3.49	0.007	0.002
124	1.744	3.48	0.005	0.001
213	1.743	3.44	0.002	0.001
308	1.741	3.43	0.003	0.001
407	1.74	3.36	0.002	0.001
511	1.738	3.36	0.005	0.001
619	1.736	3.35	0.006	0.002
724	1.734	3.36	0.008	0.002
827	1.733	3.37	0.015	0.004
932	1.731	3.38	0.027	0.008
1032	1.73	3.45	0.046	0.013
1131	1.728	3.5	0.050	0.014
1230	1.726	3.59	0.062	0.017
1323	1.725	3.75	0.108	0.029
1359	1.784	4.69	0.393	0.084
1201	1.786	4.31	0.100	0.023
1026	1.789	4.21	0.030	0.007
820	1.792	4.12	0.016	0.004
24	1.805	3.96	0.004	0.001

Table 2.III Dielectric Properties of 87.5 wt% Si_3N_4 with 4 wt% MgO, 6 wt% Y_2O_3 and 2.5 wt% ZrO_2, Respectively.

Temperature°C	Density	ε'	ε''	tanδ
24	1.684	3.43	0.014	0.004
177	1.682	3.38	0.003	0.001
273	1.68	3.37	0.003	0.001
368	1.679	3.32	0.003	0.001
464	1.677	3.32	0.003	0.001
572	1.676	3.32	0.007	0.002
677	1.674	3.33	0.013	0.004
780	1.672	3.35	0.025	0.007
879	1.671	3.37	0.040	0.012
986	1.669	3.44	0.067	0.020
1032	1.668	3.49	0.076	0.022
1079	1.668	3.54	0.085	0.024
1131	1.667	3.58	0.063	0.018
1180	1.666	3.55	0.032	0.009
1229	1.665	3.57	0.028	0.008
1275	1.665	3.61	0.036	0.010
1322	1.683	3.69	0.060	0.016
1371	1.7	4.1	0.252	0.061
1417	1.718	4.53	0.549	0.121
1418	1.737	4.53	0.498	0.110
1247	1.74	4	0.060	0.015
1073	1.743	3.89	0.017	0.004
870	1.746	3.82	0.019	0.005
24	1.759	3.67	0.001	0.000

2.3 The Coupled FDTD Numerical Model

The three-dimensional heat-generation term, resulting from the microwave material interaction, is obtained by solving Maxwell's equations, based on the Finite Difference Time Domain (FDTD) method. Based on this method, the geometry of the microwave furnace shown in Figure 2.2 is approximated into a finite difference mesh made up of Yee cells which defines the problem space as uniform cell and locate them by I, J, K in 3D.[10] On each cell, all of the electric and magnetic field components (Ex, Ey, Ez, and Hx, Hy, and Hz) are calculated for the current time step explicitly with an initial condition of zero, as shown in Figure 2.3.

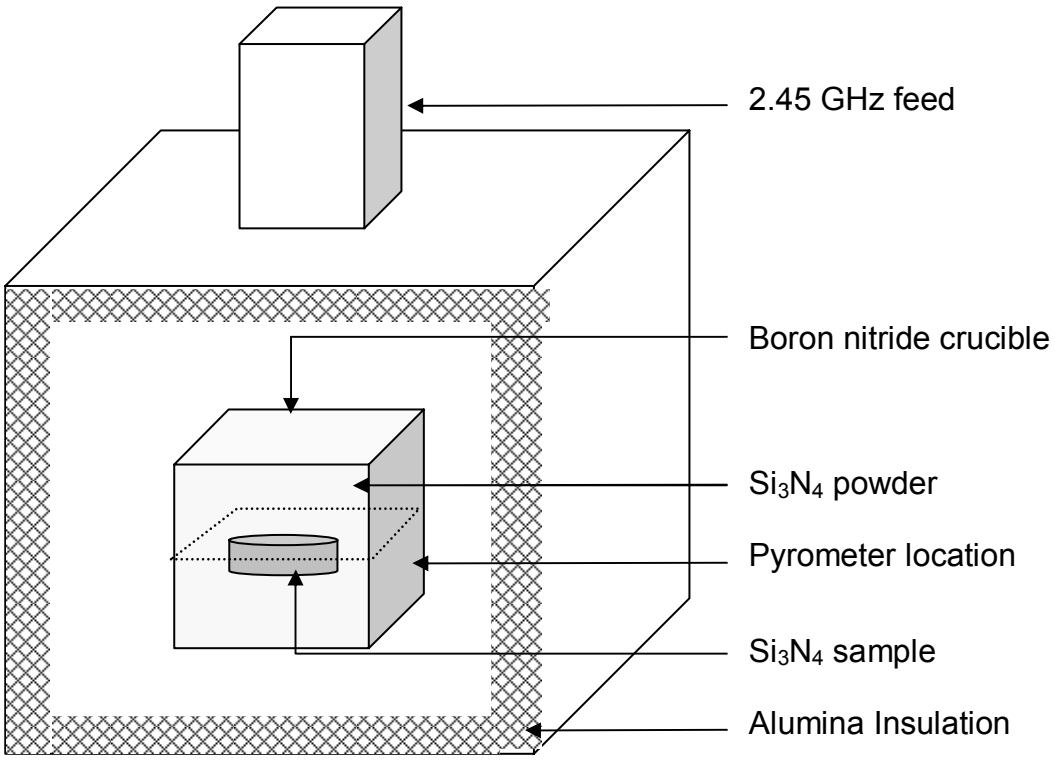

Figure 2.2. Microwave sintering configuration used for simulating temperature distributions.

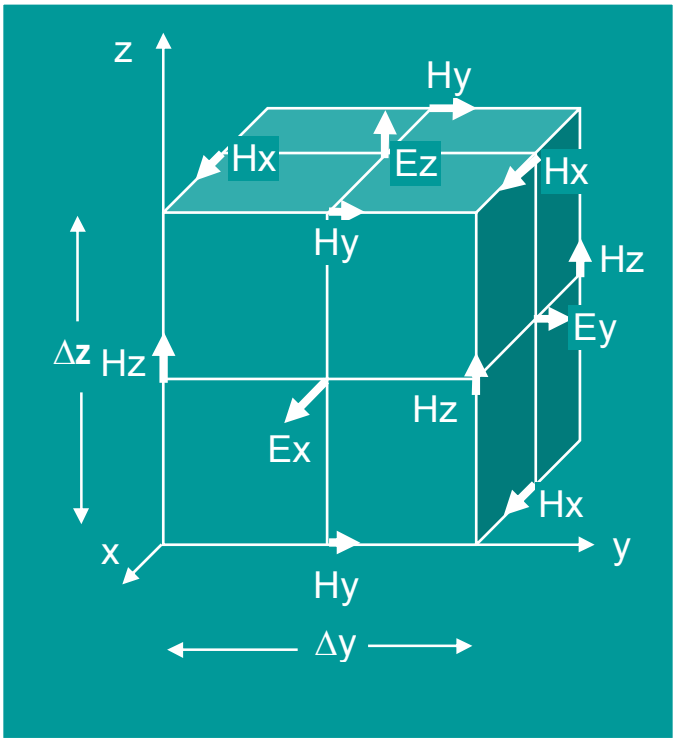

Figure 2.3. Model spacing the Yee cell Grids

The Maxwell curl equations can be expressed in vector differential form in terms of the electric E (Vm^{-1}) and magnetic H (Am^{-1}) fields as

$$\nabla \times H = \sigma E + j\omega\varepsilon_o \varepsilon E \tag{1.2}$$

$$\nabla \times E = -j\omega\mu_o H \tag{1.3}$$

where σ is the electrical conductivity, μ is the magnetic permeability and ε is the electrical permittivity. In rectangular coordinates, the curl equations can be expressed as a set of six coupled scalar partial differential equations.

$$\frac{\partial H_x}{\partial t} = \frac{1}{\mu_o}\left[\frac{\partial E_y}{\partial z} - \frac{\partial E_z}{\partial y}\right] \tag{2.4}$$

$$\frac{\partial H_y}{\partial t} = \frac{1}{\mu_o}\left[\frac{\partial E_z}{\partial x} - \frac{\partial E_x}{\partial z}\right] \tag{2.5}$$

$$\frac{\partial H_z}{\partial t} = \frac{1}{\mu_o}\left[\frac{\partial E_x}{\partial y} - \frac{\partial E_y}{\partial x}\right] \tag{2.6}$$

$$\frac{\partial E_x}{\partial t} = \frac{1}{\varepsilon_o \varepsilon}\left[\frac{\partial H_z}{\partial y} - \frac{\partial H_y}{\partial z} - \sigma E_x\right] \tag{2.7}$$

$$\frac{\partial E_y}{\partial t} = \frac{1}{\varepsilon_o \varepsilon}\left[\frac{\partial H_x}{\partial z} - \frac{\partial H_z}{\partial x} - \sigma E_y\right] \tag{2.8}$$

$$\frac{\partial E_z}{\partial t} = \frac{1}{\varepsilon_o \varepsilon}\left[\frac{\partial H_y}{\partial x} - \frac{\partial H_x}{\partial y} - \sigma E_z\right] \tag{2.9}$$

According to Yee, a space lattice point is defined as

$$(i, j, k) = (i\delta, j\delta, k\delta) \tag{2.10}$$

Discretization of the function in space and time domain yield

$$F^n_{(i,j,k)} = F_{(i\delta, j\delta, k\delta, n\delta t)} \tag{2.11}$$

where $\delta = \delta_x = \delta_y = \delta_z$ represent space increment, δt represent time increment and i, j, k, n are integers.

The FDTD formulation is obtained by approximating temporal and spatial derivatives using central differencing.

$$\frac{\partial F^n_{(i,j,k)}}{\partial x} = \frac{\partial F^n_{(i+1/2,j,k)} - \partial F^n_{(i-1/2,j,k)}}{\delta} + O(\delta^2) \tag{2.12}$$

$$\frac{\partial F^n_{(i,j,k)}}{\partial t} = \frac{\partial F^{n+1/2}_{(i,j,k)} - \partial F^{n-1/2}_{(i,j,k)}}{\delta t} + O(\delta t^2) \tag{2.13}$$

The **E** and **H** fields evaluated at alternate half-time steps and, the resulting finite difference equations for the system of equation (2.4) - (2.9) are obtained as

$$H_x^{n+1/2}(i,j+1/2,k+1/2) = H_x^{n-1/2}(i,j+1/2,k+1/2) + \frac{\delta t}{\mu_o(i,j+1/2,k+1/2)\delta}\begin{bmatrix} E_y^n(i,j+1/2,k+1) - E_y^n(i,j+1/2,k) + \\ E_z^n(i,j,k+1/2) - E_z^n(i,j+1,k+1/2) \end{bmatrix} \quad (2.14)$$

$$H_y^{n+1/2}(i+1/2,j,k+1/2) = H_x^{n-1/2}(i+1/2,j,k+1/2) + \frac{\delta t}{\mu_o(i+1/2,j,k+1/2)\delta}\begin{bmatrix} E_z^n(i+1,j,k+1/2) - E_z^n(i,j,k+1/2) + \\ E_x^n(i+1/2,j,k) - E_x^n(i+1/2,j,k+1) \end{bmatrix} \quad (2.15)$$

$$H_z^{n+1/2}(i+1/2,j+1/2,k) = H_x^{n-1/2}(i+1/2,j+1/2,k) + \frac{\delta t}{\mu_o(i+1/2,j+1/2,k)\delta}\begin{bmatrix} E_x^n(i+1/2,j+1,k) - E_x^n(i+1/2,j,k) + \\ E_y^n(i,j+1/2,k) - E_y^n(i+1,j+1/2,k) \end{bmatrix} \quad (2.16)$$

$$E_x^{n+1}(i+1/2,j,k) = \left[1 + \frac{\sigma(i+1/2,j,k)\delta t}{\varepsilon_o\varepsilon(i+1/2,j,k)}\right]E_x^n(i+1/2,j,k) + \frac{\delta t}{\varepsilon_o\varepsilon(i+1/2,j,k)\delta}\begin{bmatrix} H_z^{n+1/2}(i+1/2,j+1/2,k) - E_x^n(i+1/2,j,k) + \\ H_y^{n+1/2}(i,j+1/2,k) - H_y^{n+1/2}(i+1,j+1/2,k) \end{bmatrix} \quad (2.17)$$

$$E_y^{n+1}(i,j+1/2,k) = \left[1 + \frac{\sigma(i,j+1/2,k)\delta t}{\varepsilon_o\varepsilon(i,j+1/2,k)}\right]E_y^n(i,j+1/2,k) + \frac{\delta t}{\varepsilon_o\varepsilon(i,j+1/2,k)\delta}\begin{bmatrix} H_x^{n+1/2}(i,j+1/2,k+1/2) - H_x^{n+1/2}(i,j+1/2,k-1/2) + \\ H_z^{n+1/2}(i-1/2,j+1/2,k) - H_y^{n+1/2}(i+1/2,j+1/2,k) \end{bmatrix}$$

(2.18)

$$E_z^{n+1}(i,j,k+1/2)=\left[1+\frac{\sigma(i,j,k+1/2)\delta t}{\varepsilon_o\varepsilon(i,j,k+1/2)}\right]E_Z^n(i,j,k+1/2)+$$
$$\frac{\delta t}{\varepsilon_o\varepsilon(i,j,k+1/2)\delta}\left[\begin{matrix}H_y^{n+1/2}(i+1/2,j,k+1/2)-H_y^{n+1/2}(i-1/2,j,k+1/2)+\\ H_z^{n+1/2}(i,j-1/2,k+1/2)-H_y^{n+1/2}(i,j+1/2,k+1/2)\end{matrix}\right] \tag{2.19}$$

where (*i, j, k*) represents the index of the Yee cell, *n* represents the number of the time step, *E* stands for the electric field and *H* stands for the magnetic field. The subscripts *x*, *y*, and *z* indicate the orientation of the corresponding field components. δt is the FDTD time step size, δ is uniform spatial Yee cell size, ε_0 is the permittivity of free space, ε the dielectric constant of the material volume enclosed by the Yee cell.

Electromagnetic excitation at a frequency of 2.45 GHz is launched into the waveguide feed using the transparent source condition, as described by L. Ma *et.al.*[10] Back end of the waveguide was terminated by a second-order Mur's absorbing boundary conditions.[16] All the six field components are determined at different instances of time using a leap-frog approach untill the steady state is reached. At steady state,[10] the time-averaged power dissipation at the middle of each Yee cell (P_{mw}) is calculated by using an interpolated value of the electric field (E_{rms}) obtained from all the 12 electric field components located at the edges of the Yee cell. The power dissipation can be written as[10]

$$P_{mw}=2\pi f\,\varepsilon_0\,\varepsilon_r^{''}\left|E_{rms}\right|^2 \tag{2.20}$$

The temperature distribution inside the sample can be obtained by substituting microwave power dissipation P_{MW} obtained from equation (2.20) and numerically solving the heat conduction equation given below.[10]

$$\frac{\partial T}{\partial t}=\frac{\kappa}{\rho\,c}\nabla^2T+\frac{P_{mw}}{\rho\,c} \tag{2.21}$$

where *T* is the temperature, κ is the thermal conductivity, P_{mw} is the microwave heat generation term obtained from equation, (ρ is the mass density and *c* is the specific heat).

$$\frac{\partial T}{\partial t} = \frac{\kappa}{\rho\, c}\left[\nabla^2 T + P_{MW}\right] \tag{2.22}$$

$$\frac{\partial T}{\partial t} = \frac{T^{n+1} - T^n}{\partial t} \tag{2.23}$$

$$\frac{T^{n+1} - T^n}{\partial t} = \frac{\kappa}{\rho\, c}\left[\frac{\partial^2 T}{\partial x^2} + \frac{\partial^2 T}{\partial y^2} + \frac{\partial^2 T}{\partial z^2}\right] + \frac{P_{MW}}{\rho\, c} \tag{2.24}$$

$$T^{n+1} = \frac{\kappa\, \partial t}{\rho\, c}\left[\frac{\partial^2 T}{\partial x^2} + \frac{\partial^2 T}{\partial y^2} + \frac{\partial^2 T}{\partial z^2}\right] + \frac{P_{MW}\partial t}{\rho\, c} + T^n \tag{2.25}$$

$$T^{n+1} = T^n + \frac{k\,\partial t}{\rho\, c}\left\{\begin{array}{l}\left[\dfrac{T(i-1,j,k) - 2T(i,j,k) + T(i+1,j,k)}{\partial x^2}\right] + \\ \left[\dfrac{T(i,j-1,k) - 2T(i,j,k) + T(i,j+1,k)}{\partial y^2}\right] + \\ \left[\dfrac{T(i,j,k-1) - 2T(i,j,k) + T(i,j,k+1)}{\partial z^2}\right] + \dfrac{P_{MW}\partial t}{\rho\, c}\end{array}\right\} \tag{2.26}$$

$$T^{n+1} = T^n + \frac{k\,\partial t}{\rho\, c\left(\partial x^2\right)}\left[\begin{array}{l}T^n_{(i-1,j,k)} + T^n_{(i+1,j,k)} + T^n_{(i,j-1,k)} + \\ T^n_{(i,j+1,k)} + T^n_{(i,j,k-1)} + T^n_{(i,j,k+1)} - 6T^n_{(i,j,k)}\end{array}\right] + \frac{P_{MW}\partial t}{\rho\, c}$$

where i, j, k are node positions

$$T^{n+1} = T^n + F_o\left[\begin{array}{l}T^n_{(i-1,j,k)} + T^n_{(i+1,j,k)} + T^n_{(i,j-1,k)} + T^n_{(i,j+1,k)} + \\ T^n_{(i,j,k-1)} + T^n_{(i,j,k+1)} - 6T^n_{(i,j,k)}\end{array}\right] + \frac{P_{MW}\partial t}{\rho\, c} \tag{2.28}$$

$$where \quad F_o = \frac{k\,\partial t}{\rho\, c\left(\partial x^2\right)}$$

$$T^{n+1} = F_o \begin{bmatrix} T^n_{(i-1,j,k)} + T^n_{(i+1,j,k)} + T^n_{(i,j-1,k)} + T^n_{(i,j+1,k)} + T^n_{(i,j,k-1)} + \\ T^n_{(i,j,k+1)} \end{bmatrix} + \quad (2.29)$$
$$(1 - 6F_o)\, T^n_{(i,j,k)} + \frac{P_{MW}\partial t}{\rho c}$$

Temperature rise in all the nodes, except the boundary nodes, are solved using the above explicit finite difference formulation of the heat conduction equation.[10] The superscript *n* refers to the time step and the indices *(i, j, k)* refers to the node positions and δt is the time step for the thermal solver.

$$T^{n+1} = T^n + F_o\, T^n_{(i+1,j+k)} + F_o \begin{bmatrix} T^n_{(i-1,j,k)} + T^n_{(i,j-1,k)} + T^n_{(i,j+1,k)} + \\ T^n_{(i,j,k-1)} + T^n_{(i,j,k+1)} - 6T^n_{(i,j,k)} \end{bmatrix} + \frac{P_{MW}\partial t}{\rho c} \quad (2.30)$$

$$T^{n+1} = T^n + F_o \left[T^n_{(i+1,j,k)} - T^n_{(i,j,k)} + T^n_{(i,j,k)}\right] +$$
$$F_o \begin{bmatrix} T^n_{(i-1,j,k)} + T^n_{(i,j-1,k)} + T^n_{(i,j+1,k)} + T^n_{(i,j,k-1)} + \\ T^n_{(i,j,k+1)} - 6T^n_{(i,j,k)} \end{bmatrix} + \frac{P_{MW}\partial t}{\rho c} \quad (2.31)$$

$$T^{n+1} = T^n + F_o \left[T^n_{(i+1,j,k)} - T^n_{(i,j,k)}\right] +$$
$$F_o \begin{bmatrix} T^n_{(i,j,k)} + T^n_{(i-1,j,k)} + T^n_{(i,j-1,k)} + T^n_{(i,j+1,k)} + T^n_{(i,j,k-1)} + \\ T^n_{(i,j,k+1)} - 6T^n_{(i,j,k)} \end{bmatrix} + \frac{P_{MW}\partial t}{\rho c} \quad (2.32)$$

$$T^{n+1} = T^n + \frac{k\,\partial t}{\rho c\ \partial x^2}\left[T^n_{(i+1,j,k)} - T^n_{(i,j,k)}\right] + F_o\begin{bmatrix} T^n_{(i,j,k)} + T^n_{(i-1,j,k)} + T^n_{(i,j-1,k)} + T^n_{(i,j+1,k)} + \\ T^n_{(i,j,k-1)} + T^n_{(i,j,k+1)} - 6\,T^n_{(i,j,k)} \end{bmatrix} + \frac{P_{MW}\partial t}{\rho c} \tag{2.33}$$

For the boundary nodes, there exists heat loss due to convection as well as radiation. In our simulations we used a combined convective/radiation boundary condition to account for these losses.[10] According to this method, the heat-transfer rate q from a boundary cell is given by;

$$q = h\,A\,(T_s - T_{amb}) \tag{2.34}$$

where h is the convection heat transfer coefficient, A is the surface area, T_s is the surface temperature of the heat load and T_{amb} is the temperature of the surrounding air.
Substituting

$\left[T^n_{(i+1,j+k)} - T^n_{(i,j,k)}\right] k\,\partial x = \left[T_{air} - T^n_{(i,j,k)}\right] h\,\partial x^2$ into equation 2.32 yield

$$T^{n+1} = T^n + \frac{h\ \delta t\ \partial x^2}{\rho c\ \partial x^3}\left[T_{air} - T^n_{(i,j,k)}\right] + F_o\begin{bmatrix} T^n_{(i,j,k)} + T^n_{(i-1,j,k)} + T^n_{(i,j-1,k)} + T^n_{(i,j+1,k)} + T^n_{(i,j,k-1)} + \\ T^n_{(i,j,k+1)} - 6\,T^n_{(i,j,k)} \end{bmatrix} + \frac{P_{MW}\partial t}{\rho c} \tag{2.35}$$

$$T^{n+1} = T^n + \frac{k\,h\ \delta t\ \partial x^2}{k\,\rho c\ \partial x^3}\left[T_{air} - T^n_{(i,j,k)}\right] + F_o\begin{bmatrix} T^n_{(i,j,k)} + T^n_{(i-1,j,k)} + T^n_{(i,j-1,k)} + T^n_{(i,j+1,k)} + T^n_{(i,j,k-1)} + \\ T^n_{(i,j,k+1)} - 6\,T^n_{(i,j,k)} \end{bmatrix} + \frac{P_{MW}\partial t}{\rho c} \tag{2.36}$$

$$T^{n+1} = T^n + B_i\,F_o\left[T_{air} - T^n_{(i,j,k)}\right] + F_o\begin{bmatrix} T^n_{(i,j,k)} + T^n_{(i-1,j,k)} + T^n_{(i,j-1,k)} + T^n_{(i,j+1,k)} + T^n_{(i,j,k-1)} + \\ T^n_{(i,j,k+1)} - 6\,T^n_{(i,j,k)} \end{bmatrix} + \frac{P_{MW}\partial t}{\rho c} \tag{2.37}$$

where $B_i = \frac{h\,\partial x}{k}$

$$T^{n+1} = T^n + B_i F_o T_{air} - B_i F_o T^n_{(i,j,k)} + F_o\left[\begin{array}{l} T^n_{(i,j,k)} + T^n_{(i-1,j,k)} + T^n_{(i,j-1,k)} + T^n_{(i,j+1,k)} + T^n_{(i,j,k-1)} + \\ T^n_{(i,j,k+1)} - 6T^n_{(i,j,k)} \end{array}\right] + \frac{P_{MW}\,\partial t}{\rho c} \tag{2.38}$$

$$T^{n+1} = F_o\left[T^n_{(i-1,j,k)} + T^n_{(i,j-1,k)} + T^n_{(i,j+1,k)} + T^n_{(i,j,k-1)} + T^n_{(i,j,k+1)}\right] + \left[1 - 6F_o - F_o(B_i - 1)\right]T^n_{(i,j,k)} + F_o B_i T_{air} + \frac{P_{MW}\,\partial t}{\rho c} \tag{2.39}$$

By including the loss mechanisms in the heat conduction equation given in (2.21) for all of the boundary cells, the explicit finite difference equation would obtained. For the numerical stability of the thermal solver, the time step for the thermal solutions satisfying the following condition must be met.[10]

$$\delta t' < \frac{\delta_x^2}{6\alpha\left(1 + B_i\right)} \tag{2.40}$$

2.4 Discussion

2.4.1 Complex Dielectric Properties of the Sintering Additives

Knowledge of the complex temperature dependent-dielectric properties of the Si_3N_4 sample with and without the additives is critical for gaining a meaningful insight into the microwave sintering behavior. Figure 2.4 shows the measured real and imaginary parts of the complex dielectric constants of the three samples. All three samples, namely i) pure Si_3N_4, ii) Si_3N_4 with MgO and Y_2O_3, and iii) Si_3N_4 with MgO, Y_2O_3 and ZrO_2, exhibit the need for preheating before microwave treatment. These samples are labeled SN, SN1, and SN2, respectively, in Figures 2.4 and 2.5. The preheating is necessary due to the fact that at lower temperatures these ceramic materials exhibit relatively low loss at microwave frequencies (represented by the imaginary part of the complex dielectric constant). From Figure 2.4, it is clear that the dielectric properties

of all the samples, with the exception of pure Si_3N_4, increase favorably at temperatures above 1000°C. This rapid increase in the dielectric loss at higher temperatures, commonly observed in polycrystalline ceramics, is associated with the softening of inter-granular amorphous phase resulting in an increased localized electrical conductivity.[11]

From Figure 2.4 it should also be noted that the maximum measured temperature for the dielectric properties is 1400°C. Measurements beyond this temperature were not possible with the conventional measurement technique used for this study. However, since the objective was to assess the relative differences between the heating patterns within the three samples, it was assumed that the properties at 1650°C would have similar relative differences as those measured up to 1400°C. Measured dielectric constants (ε′) and loss factors (ε") for the three different compositions are plotted as a function of temperature in Figure 2.4. The dielectric constant and loss factor of the sample SN (Si_3N_4 with no additives) is relatively low and increases monotonically as temperature increases, suggesting that the sample is essentially transparent to microwave radiation throughout the range of temperatures of interest. Conversely, SN1 and SN2 show an increase in ε′ and ε′′ beginning near 800ºC; this is the critical temperature where microwaves begin to couple with the material. Therefore, the sintering additives couple with microwave energy and thus facilitate a more rapid heating. The sample with ZrO_2 (SN2) exhibits the strongest coupling behavior between approximately 800°C and 1100°C.

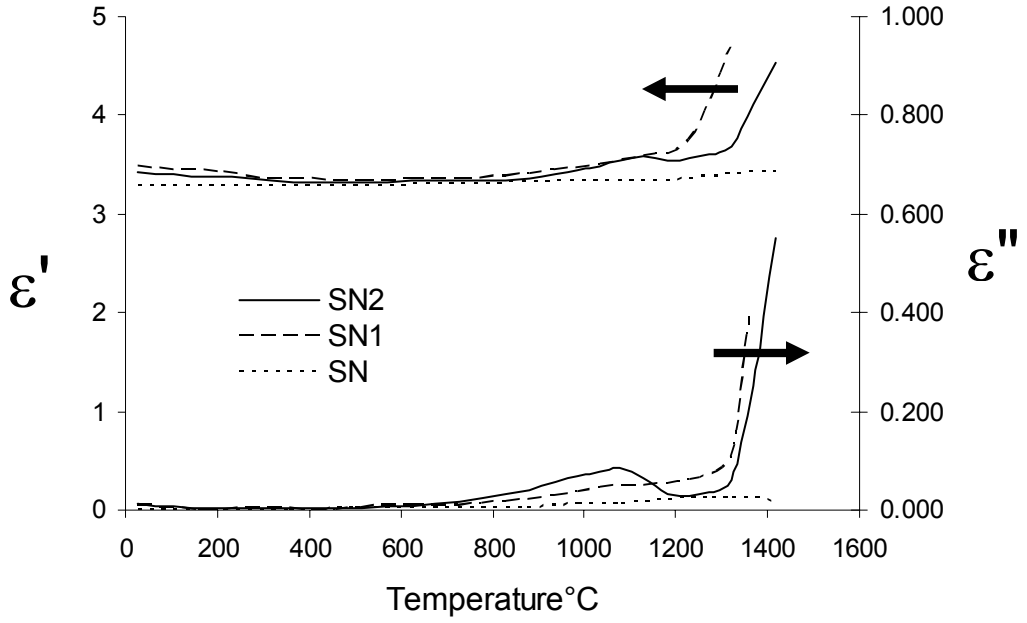

Figure 2.4. Temperature-dependent complex dielectric permittivity of Si_3N_4 systems measured while heating samples from room temperature to 1400ºC in 0.1 MPa of nitrogen pressure.

The sharp increases of ε′ and ε″ observed above 1350ºC for the two samples with sintering aids indicate a thermal runaway condition. This results from the continuous conducting percolation path from the formation of the inter-granular liquid phase at 1350°C, which increases mobility of ions, and which results in an increased localized ionic conductivity. The higher value of ε″ for SN2 is attributed to the enhanced ionic conductivity of ZrO_2 at higher temperature.[33] The dielectric data clearly reflect the critical role of sintering additives and the requirement of external susceptors to bring the temperature of the sample to its critical microwave coupling temperature of 800ºC. Moreover, it highlights the need to control the microwave power input to avoid thermal runaway.

C. J. P. Calame *et al.*[12] reported that increases in the dielectric properties in a material during sintering may be due to an increase in density. In order to verify this, we measured the density of each sample, before and after the dielectric measurements. Our results indicate that the initial density of SN2 is 1.68 g/cm^3 and its final density is 1.70 g/cm^3 after performing the dielectric measurements. There was no significant change in

density observed in SN2 or SN1. Therefore, it is clear that strong temperature dependence observed for complex permittivity is not due to the densification of the compacted powder samples.

The data presented in Figure 2.4 show a peak in ε" at approximately at 1100°C in the case of SN2, which is completely absent during cooling as shown in Figure 2.5. A similar observation was previously reported by L.P. Martin *et al.*[13] in the case of ZnO, who argued that the observed anomalous temperature dependence of ε" was due to the desorption of chemisorbed water from the surface of the ZnO powder. This hypothesis was confirmed based on mass spectrometer measurements. D. Gershon *et al.*[14] used TGA as alternative technique to measure the amount of water adsorbed on the surface of alumina particles, from 140°C to 1000°C in order to explain the observed increase in the measured value of ε". The porous alumina had chemisorbed water present in the contact region of alumina particles.

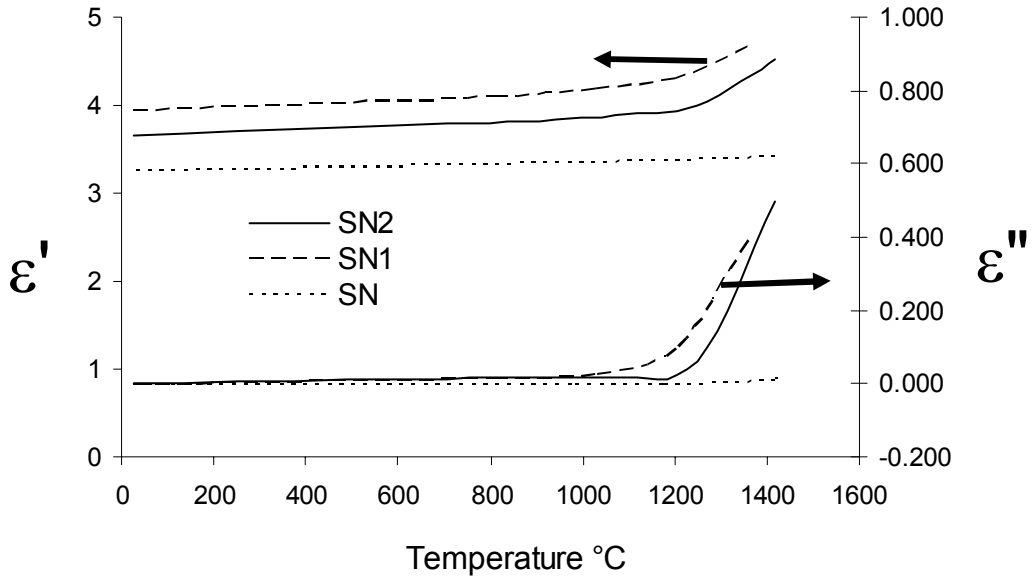

Figure 2.5. Temperature dependent complex dielectric permittivity of Si_3N_4 systems measured while cooling samples from 1400ºC to room temperature in 0.1 MPa of nitrogen pressure.

TGA/DSC of SN2 was performed from room temperature to 1400°C at 10°C/min in a nitrogen atmosphere, in order to explain the observed peak in ε" at approximately at

1100°C. A significant mass loss near 1100°C is shown in the TGA/DSC results presented in Figure 2.6. Thus, the anomalous temperature dependence of ε" is related to desorption of chemisorbed water present in the contact region of Si_3N_4 particles.

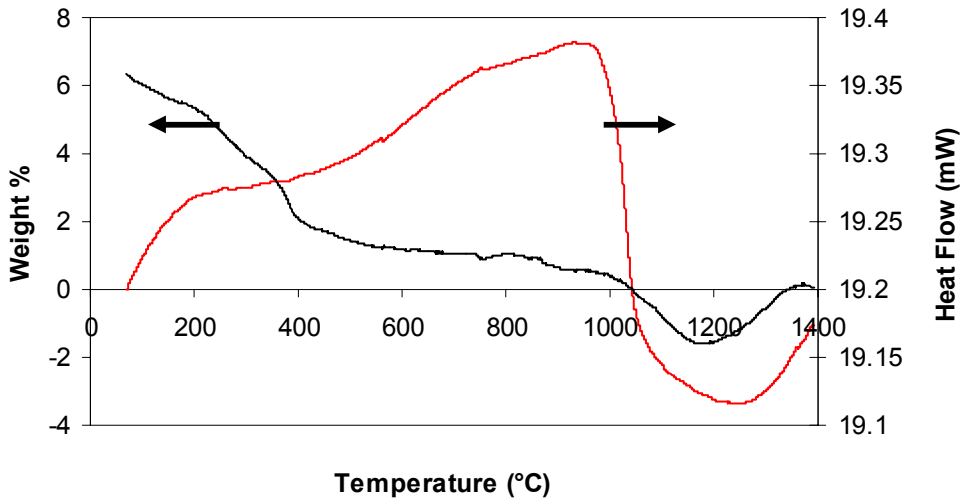

Figure 2.6. TGA/DSC results from SN2. The endotherm beginning near 1000°C correlates to the rise in ε" shown in Figure 2.4.

2.4.2 Numerical Simulations

The microwave power absorption and resulting temperature evolution during sintering process were simulated for the three samples SN, SN1, and SN2. The dimension of the cubical microwave heating cavity used was 22 x 22 x 22 cm^3. The dimensions of the crucible used was 5 x 5 x 2.5 and the sample was a pellet with 2.5 cm diameter and 0.5 cm height. The thickness of the thermal insulation pack inside the cavity is 2.5 cm on all the walls. The cavity also had a WR340 (8.6 x 4.3 cm^2 as the cross-sectional area) wave guide to feed in microwave power at 2.45 GHz rated for a maximum of 3 kW output power.

The preliminary objective of this simulation was to obtain a greater insight into the temperature evolution within the three samples, at the measured hold temperature during the sintering process. The hypothesis tested was that the temperature measurements at the outside wall of the crucible did not accurately represent the actual temperatures developed at the center of the sample. To prove this hypothesis, the

maximum available measured dielectric property of the samples at 1400°C was assumed. Extrapolation of dielectric properties at higher temperatures was not performed due to the fact that the number of available data points in the steeper high-temperature regime of the dielectric properties (Figure 2.3). The dielectric properties of the samples at 1650°C used in the FDTD electromagnetic simulation are; (3.25 – j0.03) for SN, (4.7– j0.4) for SN1, and (4.7 – j0.55) for SN2. The corresponding properties used for the thermal insulation is (1.7 – j0.001). Thermal simulations were performed for three starting temperatures of 1550°C, 1600°C and 1650°C and ran for 15 minutes, the same as the hold time used during sintering.

The 3D electromagnetic power dissipation data obtained above was fed into the thermal solver to obtain the temperature evolution inside the samples. The thermal solver was run only for the sample and the crucible. Radiation and convection boundary conditions were used at all the boundaries. The thermal properties of SN, SN1, SN2, and the silicon nitride filling inside crucible at 1600°C are given in Table 2.IV. Variations in these properties, which are not significant, with respect to further temperature rise were not considered in the simulations. It was believed that since the objective of these simulations was to provide a comparative study among the three samples, such an assumption is valid.

Table 2.IV. Thermal Properties of Silicon Nitride with Sintering Aids.[15]

Code	Composition	Thermal Conductivity ($W\ m^{-1}\ K^{-1}$)	Specific heat ($J\ kg^{-1}\ K^{-1}$)	Density ($kg\ m^{-3}$)
SN	Si_3N_4	30	680	3190
SN1	$Si_3N_4 + MgO + Y_2O_3$	20	1255.2	3190
SN2	$Si_3N_4 + MgO + Y_2O_3 + ZrO_2$	20	1255.2	3450

Figure 2.7 shows the 3D and 2D image of microwave power absorption of pure Si_3N_4 (SN) without sintering additives. From a total of 1000 watts of input power, only 8 mille watts was absorbed by the sample due to the low dielectric loss factor (0.03) of the pure silicon nitride sample at the sintering temperature. Figures 2.8, 2.9 and 2.10 show the temperature profiles of the samples SN at three different experimentally measured temperatures 1550°C, 1600°C and 1650°C respectively. The temperature difference between the center of the sample and surface of the crucible is approximately

50 – 75°C. Figure 2.11 show the results of the power dissipation 4 wt% MgO and 6 wt% Y_2O_3 were added to silicon nitride as sintering additives (SN1). Non-uniform power absorption can be clearly seen in the work load. The maximum power absorption at the center of the sample is 37 mille watts and edge is 25 mille watts. It is of particular interest to note that the non uniformities in power absorption get smoothed out when the sample's maximum temperature of the sample is 1550°C. However, this trend is not continued when the sample attained a higher sintering temperature (Figure 2.13 and 2.14). The temperature difference between the center of the sample and surface of the crucible is approximately 75-125°C. This difference in temperature is clearly caused by changes in the value of the dielectric loss of the surrounding silicon nitride powder relating to the silicon nitride sample containing the lossy sintering additives. Figure 2.15 shows the microwave power distribution for the sample SN2. Power dissipation at the center of the pellet is 46 mille watts and 12 watts at the edges. The difference in the dissipated power between edge and center is 21 watts higher compared to the sample SN1. The difference in the temperature between the center and edge of the samples SN2 sintered at all the temperature (1550°C, 1600°C and 1650°C) was 20°C. The temperature difference between the center of the sample and surface of the crucible is approximately 150°C.

In each of the previously discussed cases, it should be noted that the silicon nitride powder filling the crucible shows very little coupling with the microwave power because of its inherently low loss nature. It is evident from the above argument that the microwave power dissipation of the sample with the highest dielectric loss, SN2, is the maximum. From the above discussion, it is clear that for the same measured temperature of 1650°C at the crucible surface, the actual sample temperatures were higher in the case of SN, SN1 and SN2. This estimated temperature difference strongly suggests that the sample SN2 was originally sintered at a higher temperature than the measured surface temperature of 1650°C.

The accuracy of the temperature prediction was further confirmed by considering the Si_3N_4 decomposition temperature of 1780 °C at ambient nitrogen pressure described in Figure 1.4. In our case Si_3N_4 never decomposed during sintering indicating the fact that the maximum sintering temperatures never exceed 1780 °C.

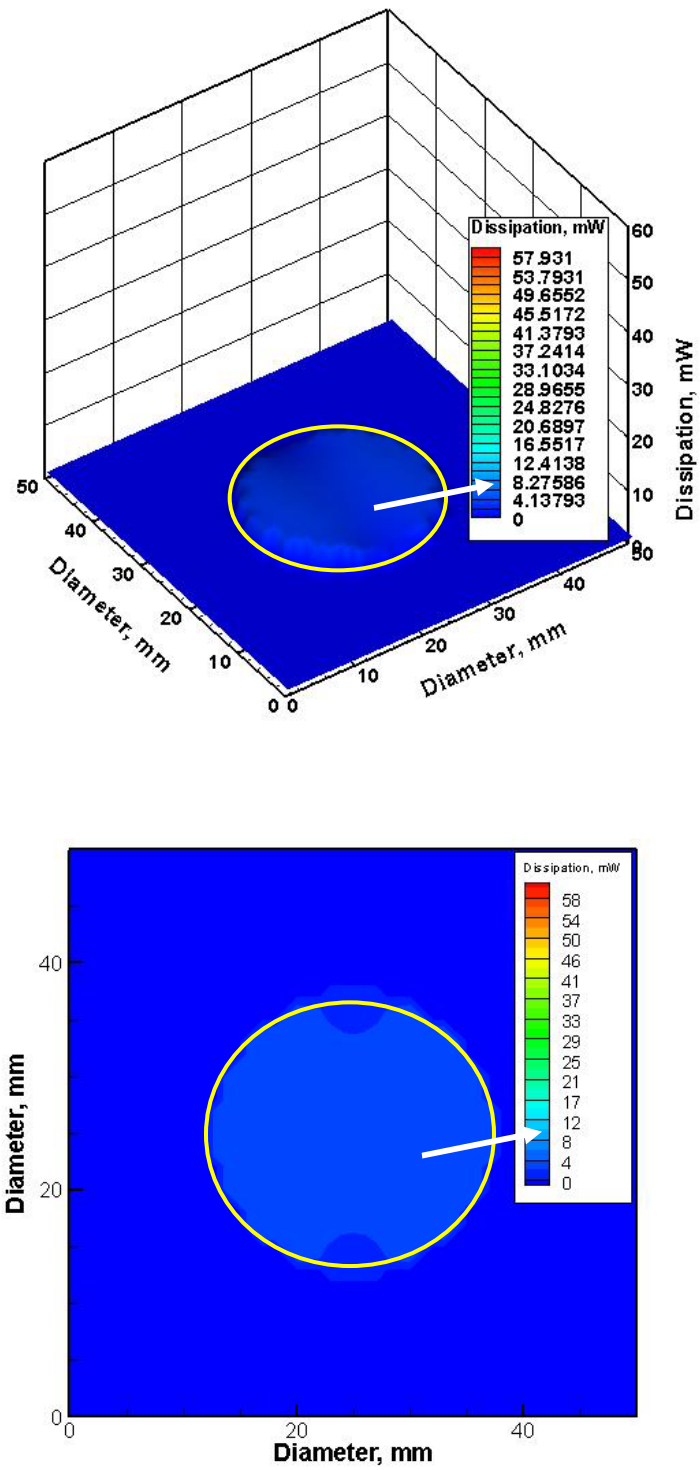

Figure 2. 7. Power absorption of pure SN at 1650ºC. The yellow circle represents the perimeter of the sample pellet.

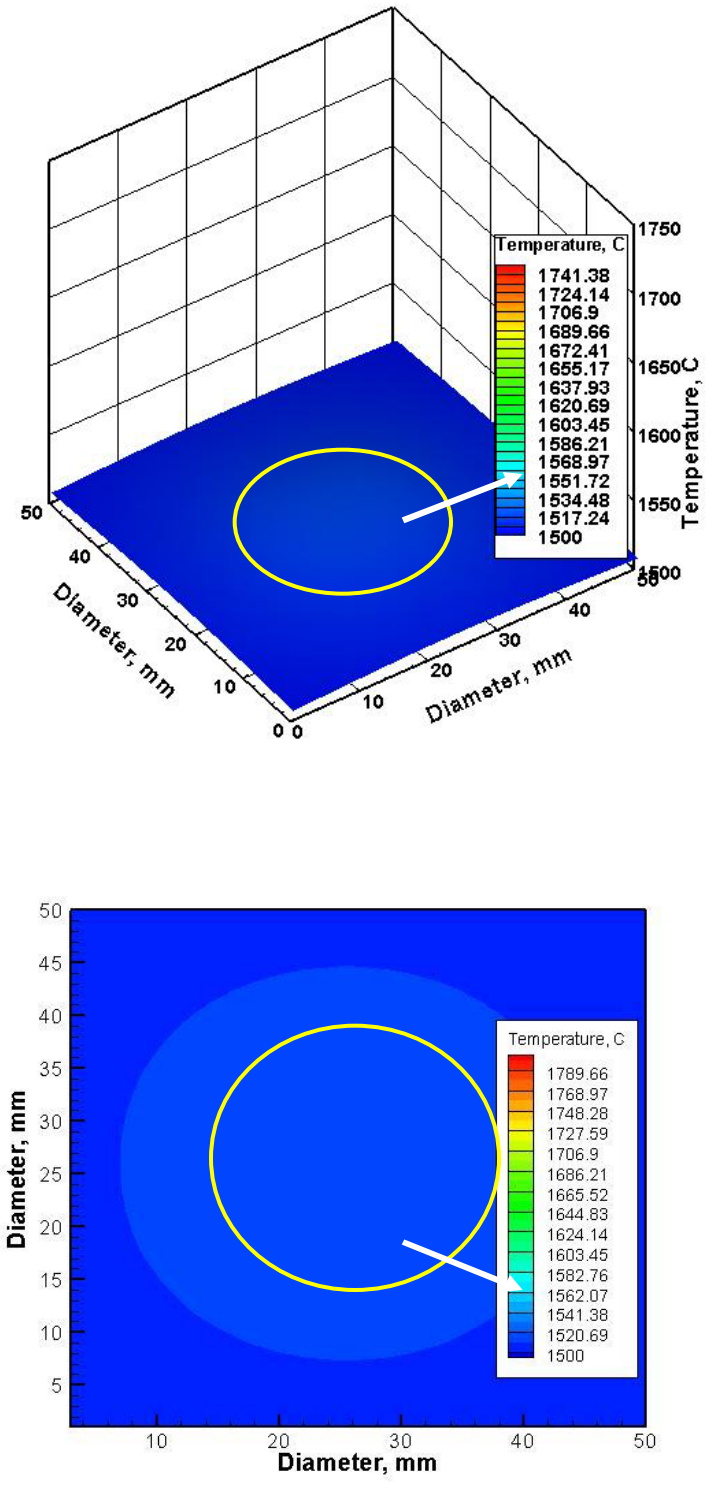

Figure 2.8. Temperature distribution of pure SN at 1550ºC. The yellow circle represents the perimeter of the sample pellet.

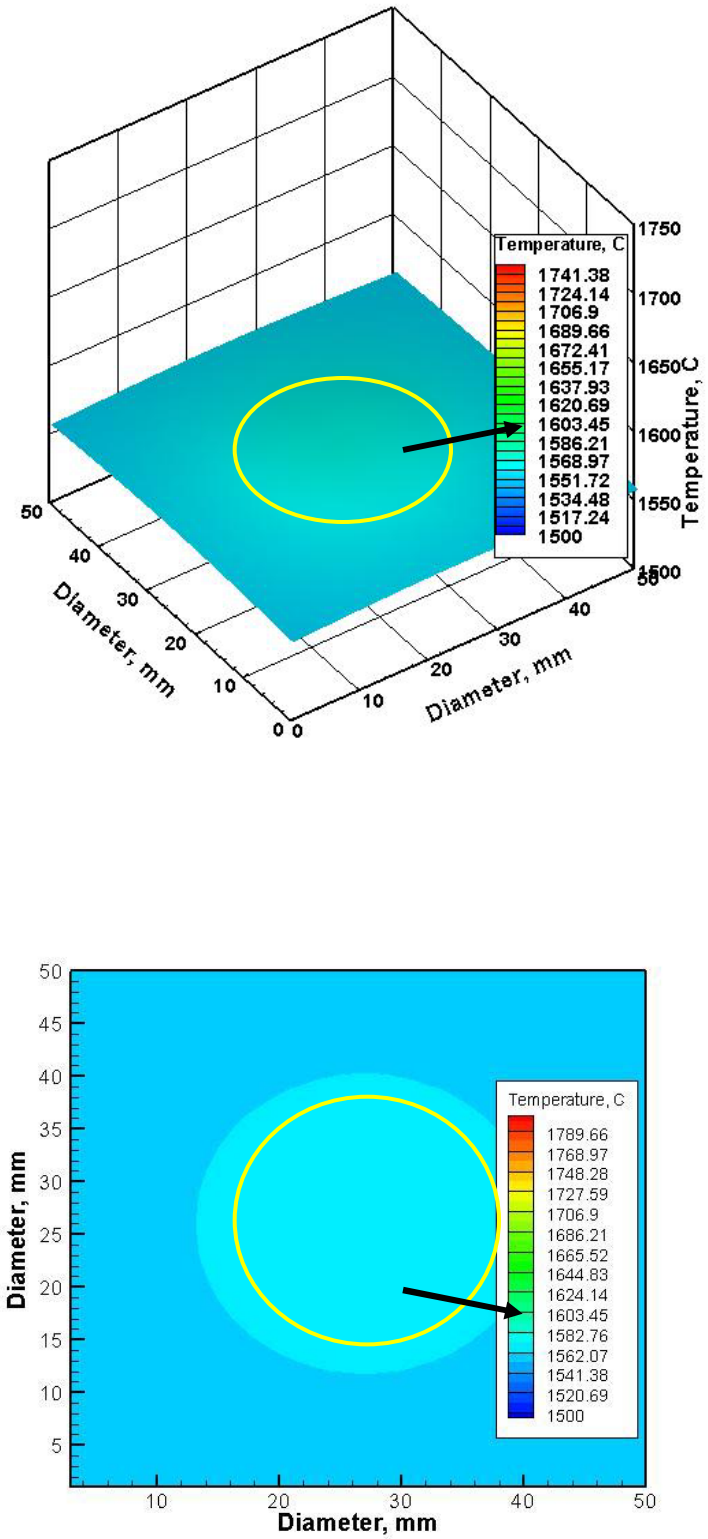

Figure 2.9. Temperature distribution of pure SN at 1600ºC. The yellow circle represents the perimeter of the sample pellet.

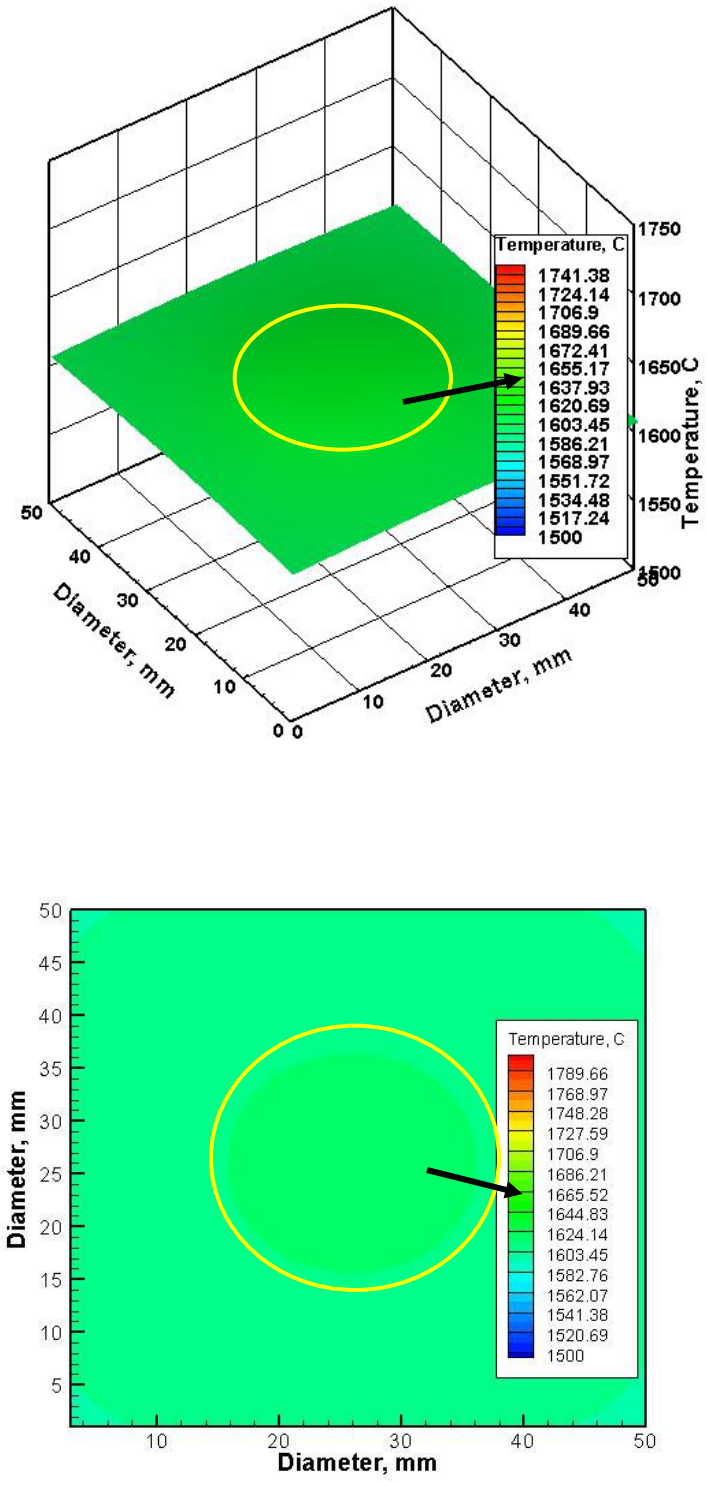

Figure 2.10. Temperature distribution of pure SN at 1650ºC. The yellow circle represents the perimeter of the sample pellet.

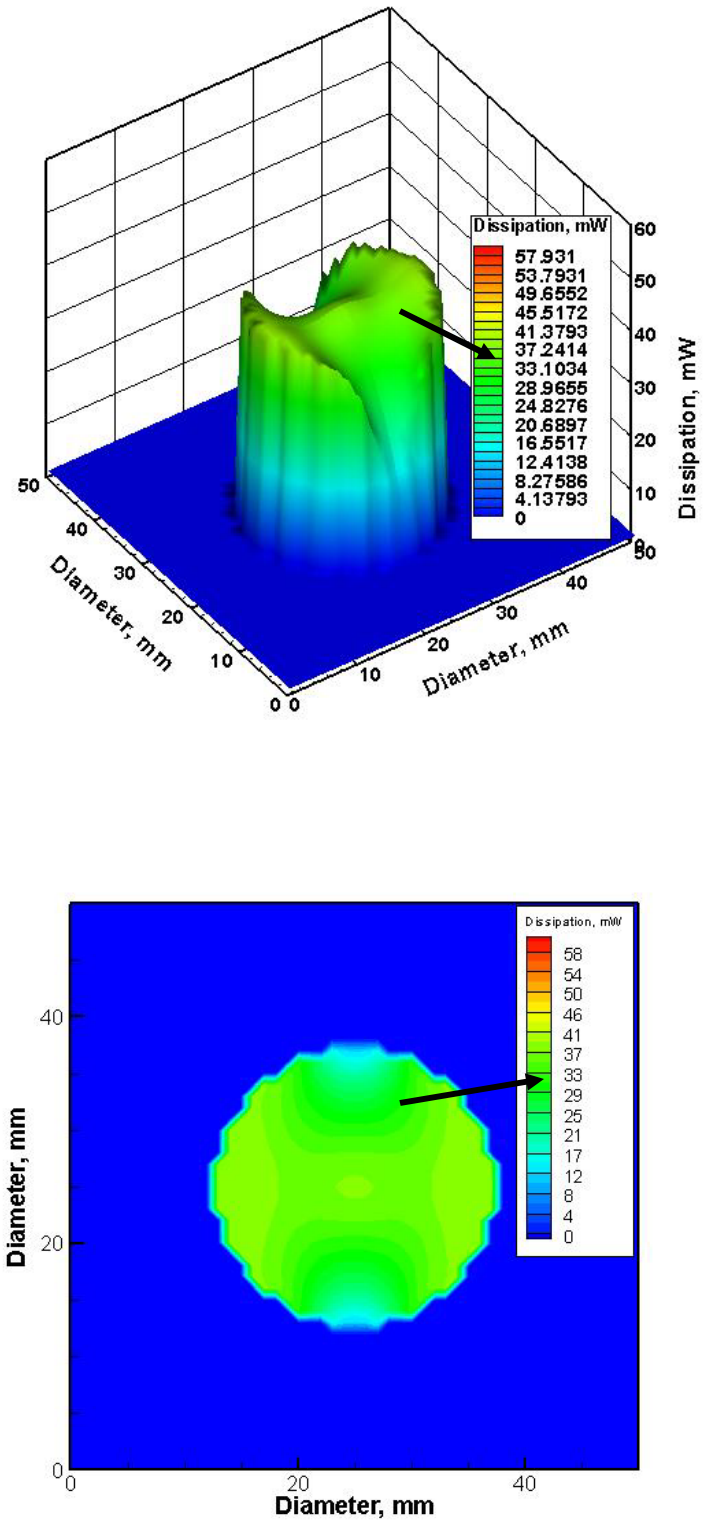

Figure 2.11. Power absorption of SN1 at 1650ºC.

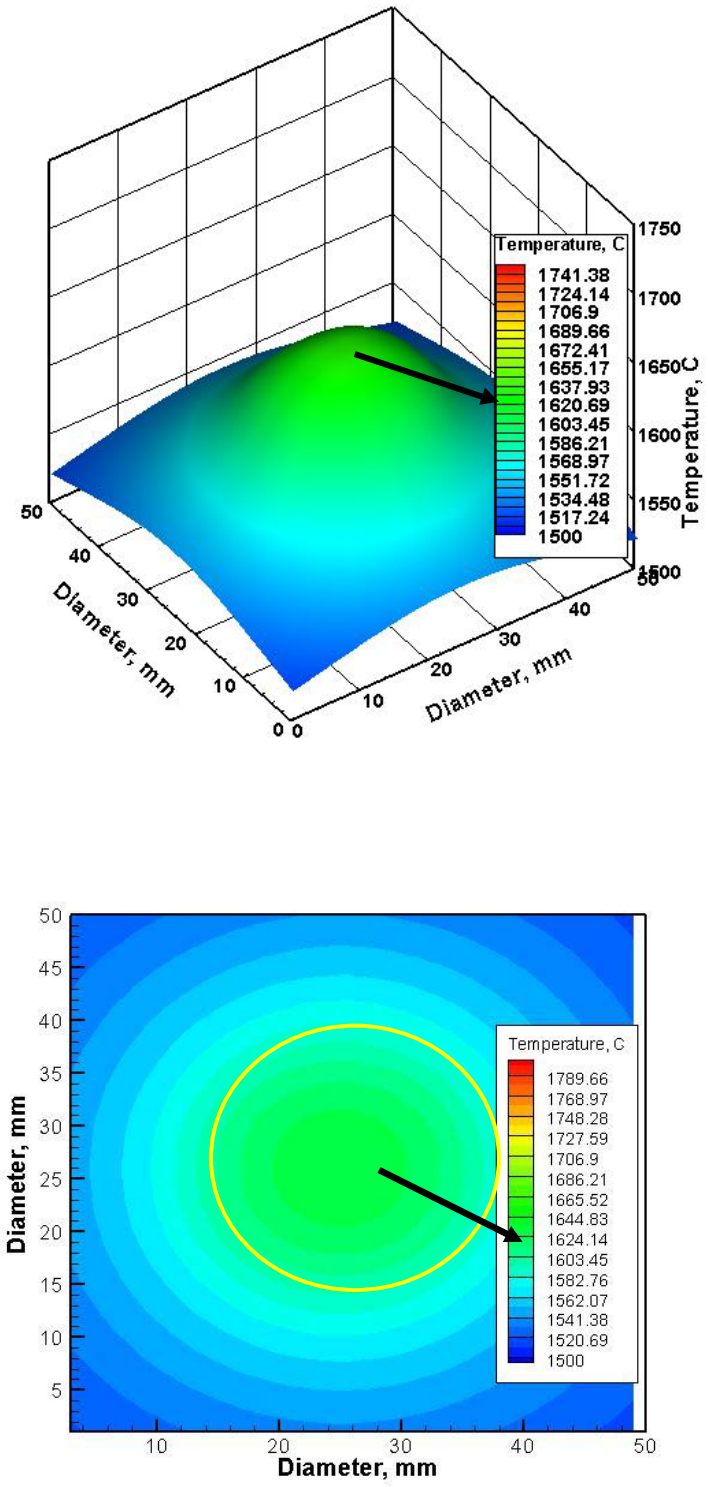

Figure 2.12. Temperature distribution of SN1 at 1550ºC. The yellow circle represents the perimeter of the sample pellet.

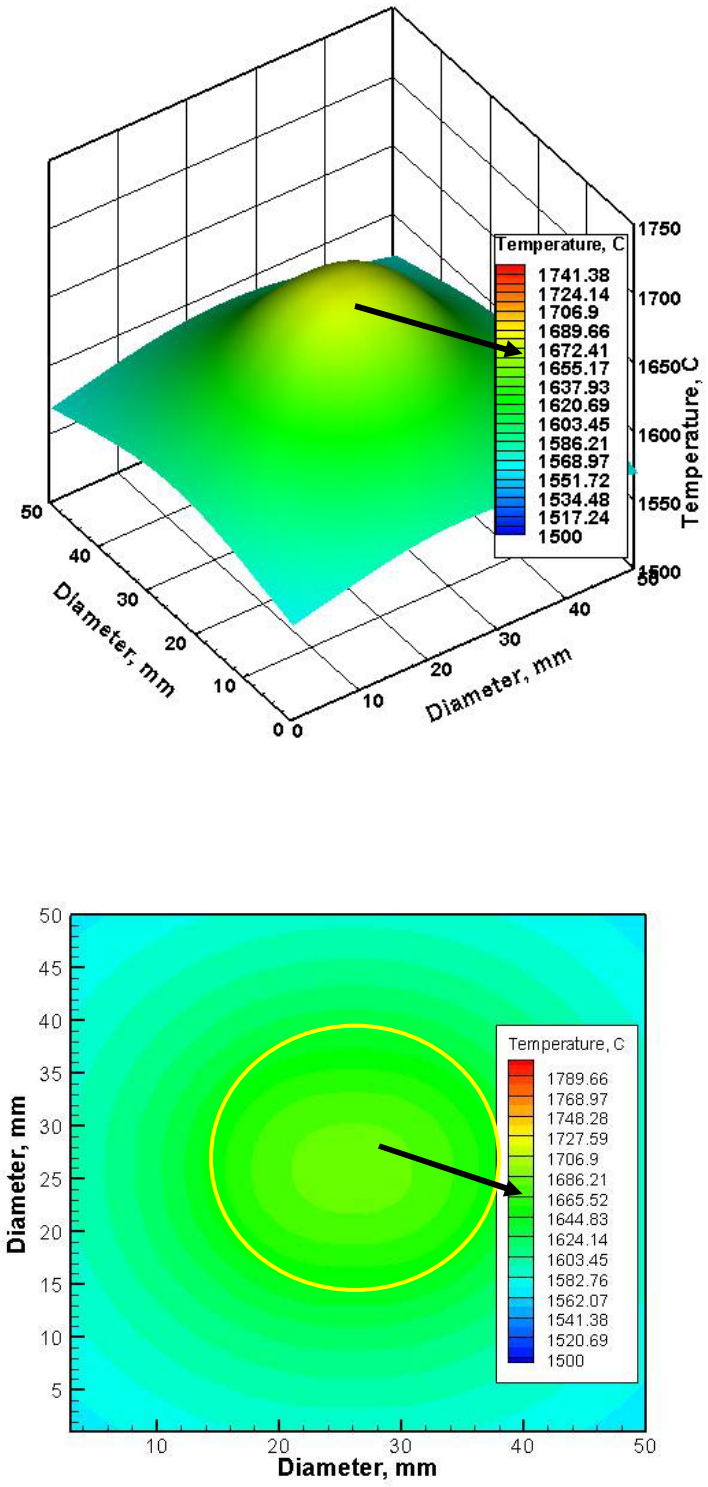

Figure 2.13. Temperature distribution of SN1 at 1600ºC. The yellow circle represents the perimeter of the sample pellet.

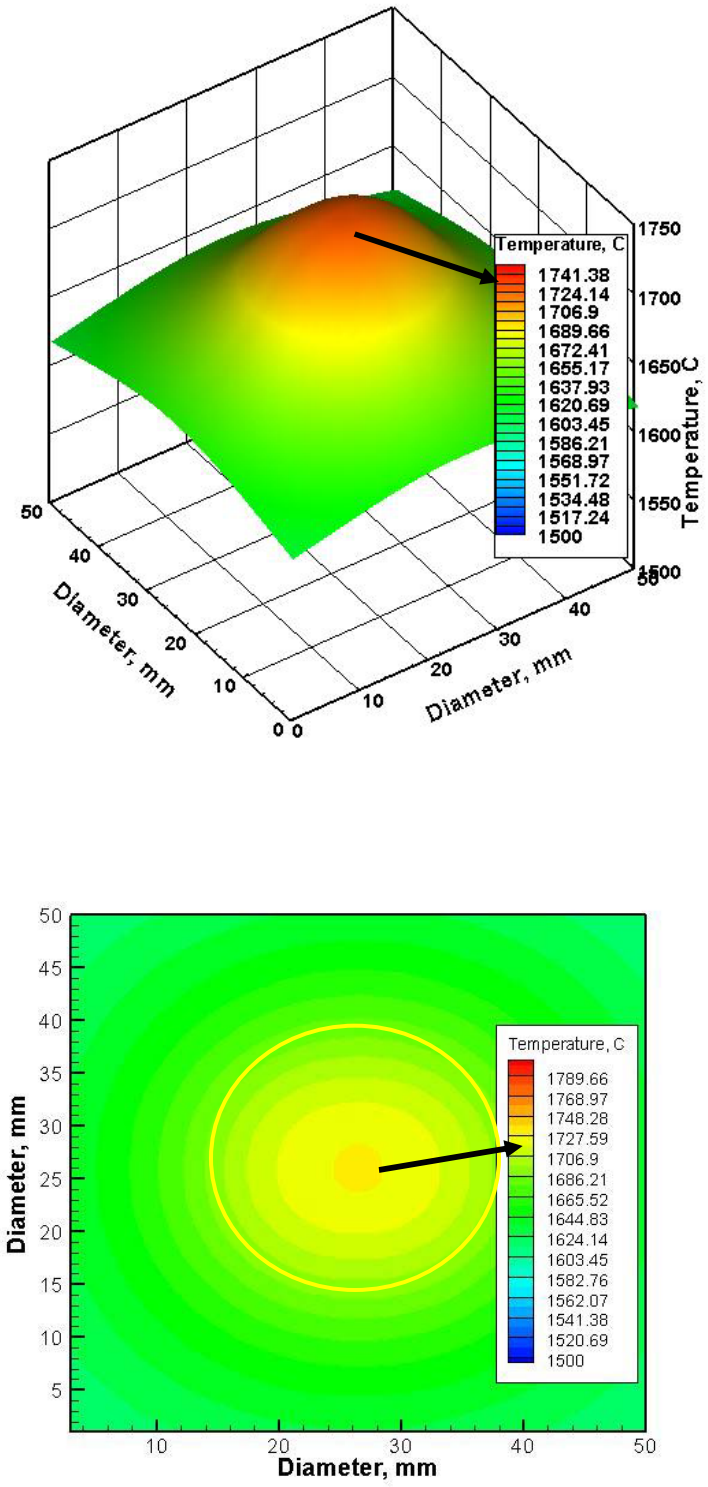

Figure 2.14. Temperature distribution of SN1 at 1650ºC. The yellow circle represents the perimeter of the sample pellet.

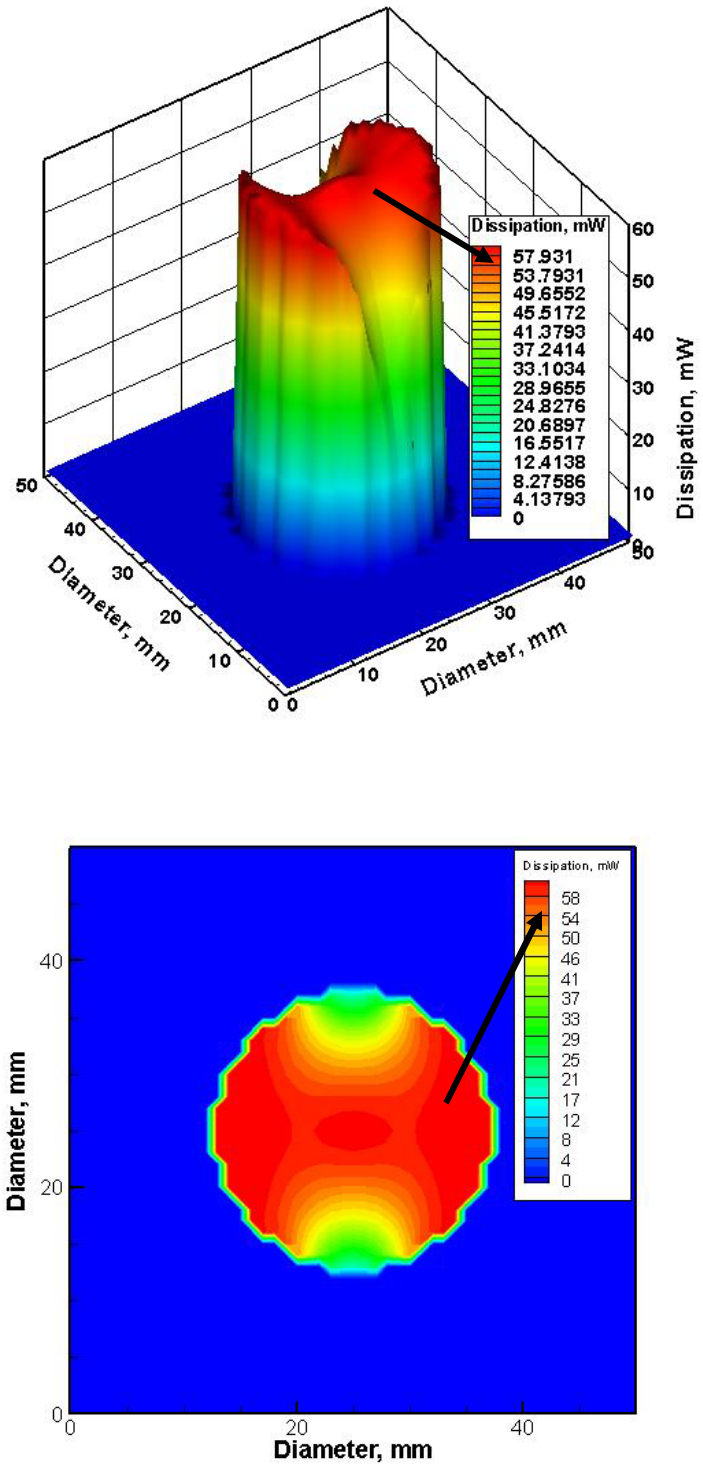

Figure 2.15. Power absorption of SN2 at 1650ºC.

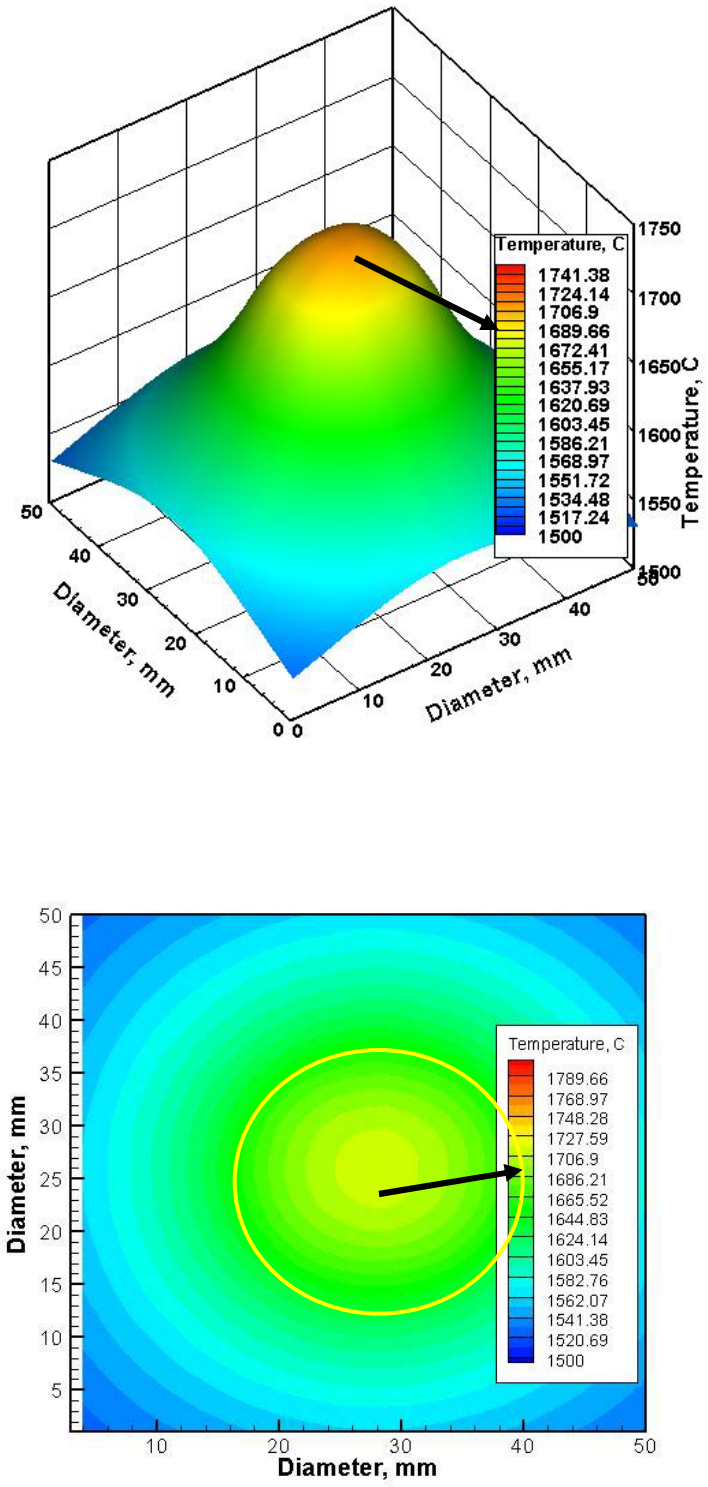

Figure 2.16. Temperature distribution of SN2 at 1550ºC. The yellow circle represents the perimeter of the sample pellet.

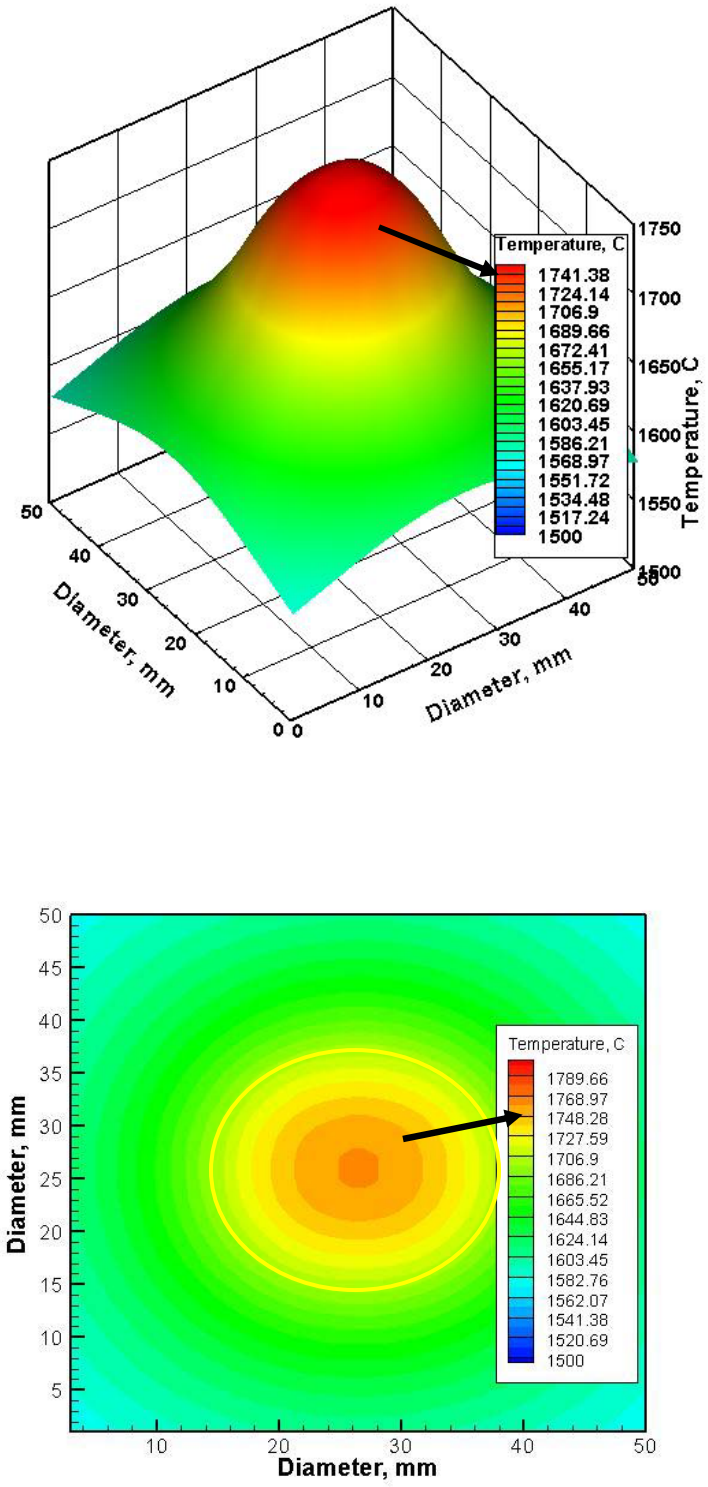

Figure 2.17. Temperature distribution of SN2 at 1600ºC. The yellow circle represents the perimeter of the sample pellet.

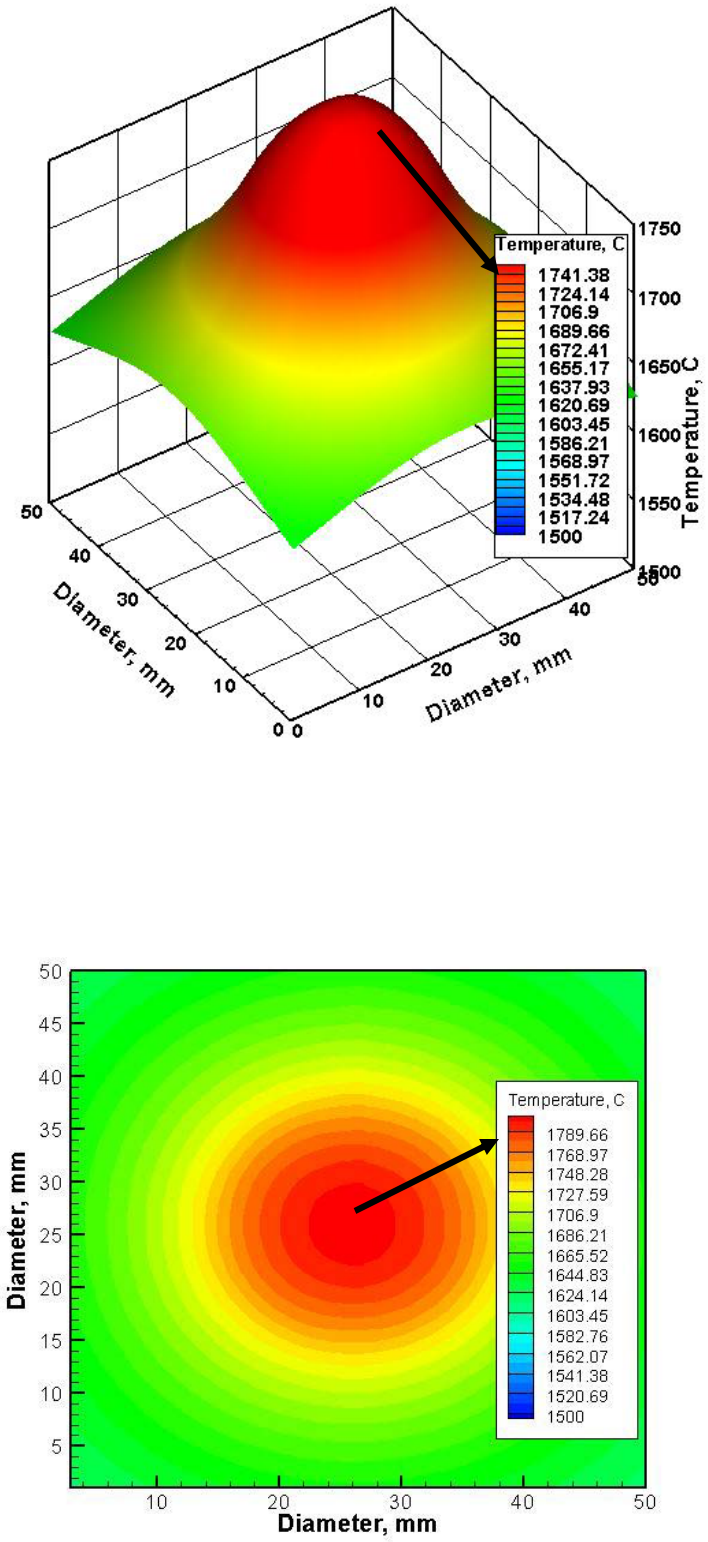

Figure 2.18. Temperature distribution of SN2 at 1650ºC.

2.5 Conclusions

Coupled electromagnetic and thermal simulations were used to study microwave power absorption and temperature distribution within samples of Si_3N_4 and the surroundings. The dielectric properties of the samples were measured from room temperature to 1450^oC and used in the electromagnetic simulations. The simulated electromagnetic power dissipation terms were further used in a thermal solver to predict the temperature evolution within the samples during microwave heating. The simulation results indicated an increase in microwave power absorption within the silicon nitride samples, which in turn resulted in an increase in sintering temperatures experienced by the sample in the presence of the higher dielectric loss additives. The numerical simulations predicted a 50-150^oC higher temperature than the value measured experimentally using an optical radiation pyrometer. From these results, it may be concluded that pure silicon nitride without sintering additives is poor coupler of 2.45 GHz microwaves at all of the temperatures of interest. The dielectric properties of oxide sintering additives dictate the temperature generation inside silicon nitride samples. In the case of 2.45 GHz microwave sintered silicon nitride, it was demonstrated through numerical simulation studies that the required temperature profiles for the successful sintering could be generated by tailoring the dielectric properties of sintering additives.

2.6 References

1. F.L. Riley, "Silicon Nitride and Related Materials," *J. Am. Ceram. Soc.,* **83** [2] 245–65 (2000).

2. D. Hardie and K.H. Jack, "Crystal Structures of Silicon Nitride," *Nature (London)*, **180** [8] 332–33 (1957).

3. G.R. Terwilliger and F.F Lange, "Pressureless Sintering of Si_3N_4," *J. Mater. Sci*., **10** [7] 1169–74 (1975).

4. T.N. Tiegs, M.K. Ferber, J.O. Kiggans, K.L. More, C.M. Hubbard, and D.W. Coffey, "Microstructure Development During Microwave Annealing of Dense Silicon Nitride," pp. 411-20 in Ceramic Transactions, Vol. 21, *Microwaves: Theory and Applications in Materials Processing*. Edited By D.E. Clark, F.D. Gac, and W.H. Sutton. American Ceramic Society, Westerville, OH, (1991).

5. J. Zhang, L. Cao, and F. Xia: "Microwave Sintering of Si_3N_4 Ceramics," *Mater. Res. Symp. Proc*., **269**, 329-34 (1992).

6. T. N. Tiegs, J. O. Kiggans, H. T. Lin, and C. A. Willkens, "Comparison of Properties of Sintered and Reaction-Bonded Silicon Nitride Fabricated by Microwave and Conventional Heating," *Mater. Res. Symp. Proc*., **347**, 501-56 (1994).

7. Y.C. Kim, S.C. Koh, D.K. Kim, and C.H. Kim, "Effect of Microwave Heating on the Sintering of Silicon Nitride-Doped with Al_2O_3 and Y_2O_3," pp. 415-22 in Ceramic Transactions, Vol. 59, *Microwaves: Theory and Applications in Materials Processing III*. Edited by D.E. Clark, D. Folz, S. Joda, and R. Siberglitt. American Ceramic Society, Westerville, OH, (1995).

8. W.H. Sutton, "Microwave Processing of Ceramic Materials," *Am. Ceram. Soc. Bull*., **68** [2] 376-86 (1989).

9. T.N. Tiegs, J.O. Kiggans, and H.D. Kimrey, "Microwave Sintering of Silicon Nitride," *Ceram. Eng. Sci. Proc*., **12** [9-10] 1981-92 (1991).

10. L. Ma, D.L. Paul, N. Pothecary, C. Railton, J. Bows, L. Barrat. J. Mullin, and D. Simons, "Experimental Validation of a Combined Electromagnetic and Thermal FDTD Model of a Microwave Heating Process," *IEEE Trans. Microwave. Theory. Tech.,* **43** [11] pp. 2565-72 (1995).

11. Y.V. Bykov, K.I. Rybakov, and V.E. Semenov, "High Temperature Microwave Processing of Materials (Topical Review)," *J. Phys. D: Appl. Phys*. **34** [13] R55-75 (2001).

12. J.P. Calame, A. Birman, Y. Carmel, D. Gershon, B. Levush, A.A. Sorokin, V. E. Semenov, D. Dadon, L.P. Martin, and M. Rosen, "A Dielectric Mixing Law for Porous Ceramics Based on Fractal Boundaries," *J. Appl. Phys***. 80** [7**]** 3992-4000 (1996).

13. L.P. Martin, D. Dadon, M. Rosen, D. Gershon, K.I. Rybakov, A. Birman, J.P. Calame, B. Levush, Y. Carmel, and R. Hutcheon, "Effect of Anomalous Permittivity on the Microwave Heating of Zinc Oxide," *J. Appl. Phys*. **83** [1] 432-37 (1998).

14. D. Gershon, J.P. Calame, and A. Birnboim, "Complex Permittivity Measurements and Mixings Laws of Alumina Composites," *J. Appl. Phys*. **89** [12] 8117-20 (2001).

15. M. Kitayama, K. Hirao, M. Toriyama, and S. Kanzaki, "Thermal Conductivity of β-Si_3N_4: I, Effects of Various Microstructural Factors," *J. Am. Ceram. Soc.,* **82** [11] 3105–12 (1999).

CHAPTER 3

Densification and α → β Phase Transformation

Abstract

A 2.45 GHz microwave-sintered Si_3N_4 - Y_2O_3 - MgO system with ZrO_2 additions has been investigated. The isothermal densification and α → β phase transformation rate of Si_3N_4 were examined. Results from microwave and conventional sintering were compared. The α → β phase transformation was completed at a lower temperature in microwave sintered samples compared to conventionally-sintered samples. The enhanced phase transformation from microwave sintering is attributed to selective localized volumetric heating of the dielectrically lossy grain-boundary glass phase. In addition, the coupling of microwaves with glassy liquid grain-boundary phase increased the vibration rate and amplitude of the liquid molecules, resulting in a decreased viscosity of the oxynitride glassy phase and enhanced α → β phase transformation. Additions of ZrO_2 to the Y_2O_3 and MgO sintering aids produced a higher sintered density, irrespective of the heating method, most likely due to the development of a lower viscosity glassy phase. High-temperature X-ray diffraction (HTXRD) analysis was performed to study in situ the phase stability of Si_3N_4 at high temperatures. Si_3N_4 specimens with 4 wt % ZrO_2 were exposed to air at temperature between 25°C and 900°C for up to 24 hours. The microwave-sintered sample showed no variations in phases as a function of temperature. It was demonstrated that α → β transformation and densification of the Si_3N_4 - Y_2O_3 - MgO system could be enhanced through microwave sintering and tailoring of the amount of ZrO_2 additive, sintering temperature and time.

3.1 Introduction

Silicon nitride is one of the most promising high-temperature structural materials due to its excellent wear resistance, thermal and mechanical properties.[1] Densification of Si_3N_4 without high pressure or sintering additives is difficult due to the Si-N covalent bonding and low self-diffusion coefficient.[2] Hot isostatic pressing and gas pressure sintering are the common fabrication methods for producing a fully dense Si_3N_4; but these methods are expensive.[3] Full densification can also be achieved by pressure-less sintering with suitable additives, such as MgO, Y_2O_3 and Al_2O_3.[3-5] In recent years, many reports have suggested that sintering by use of microwave energy is another alternative.[6-10] Microwave sintering of ceramic materials has received much attention, since there are several advantages over conventional sintering techniques, such as reduced sintering time and temperature, and its capability of producing unique microstructures that cannot be achieved by conventional methods.[11-21] Various structural ceramics and composites have

achieved by conventional methods.[11-21] Various structural ceramics and composites have also been sintered successfully by microwave energy, including ZrO_2 and TiB_2.[22]

When the microwave sintering technique is applied, the power absorbed by the sample is determined by the complex dielectric permittivity of the material, which is a function of the temperature and frequency. Lossy ceramic materials like SiC and NiO couple readily with 2.45 GHz microwaves at room temperature. Low-loss ceramic materials such as Al_2O_3 and SiO_2 never couple with microwaves at room temperature.[22] However, these materials will begin to couple with microwaves above a critical temperature, as a function of the increase in their complex dielectric properties. The coupling of microwave power with a low-loss ceramic can be improved by either using a hybrid heating scheme or adding lossy conductive or magnetic materials in the form of secondary phases.[22-23] The lossy secondary additives couple microwave power more efficiently than the low-loss matrix material, and, hence, can be heated selectively and rapidly at ambient temperature. Si_3N_4, in its pure form, is a poor microwave absorber due to its low dielectric loss.[23] Heating Si_3N_4-based material takes place by selective coupling of microwaves at the grain boundary phases, which helps to form a liquid phase. Since diffusion through the liquid is the rate-controlling mechanism, higher densification can be achieved by adding lossy secondary additives that couple well with microwaves. Tiegs et al. reported improved densification in the Si_3N_4-Y_2O_3-Al_2O_3 system with the addition of 2 wt% SiC or TiN.[23]

Adding Y_2O_3 and ZrO_2 to Si_3N_4 promoted densification and formed a refractory grain-boundary phase.[24-25] F. F. Lange *et al.*[26] reported increased fracture toughness for a composite system consists of Si_3N_4/ZrO_2 (+Y_2O_3) with increased ZrO_2 content. ZrO_2 has also been used as a densification aid for Si_3N_4.[27] Although ZrO_2 has been previously used as a sintering additive for conventionally sintered Si_3N_4 by many researchers, there are no detailed studies existing in the literature regarding the use of ZrO_2 as a secondary additive in the context of microwave sintering.

The objective of the present work was to study the effect of ZrO_2 secondary additives on $\alpha \rightarrow \beta$ phase transformation and densification behavior of microwave-sintered Si_3N_4. Results of dielectric properties of Si_3N_4 with additives from room temperature to 1450ºC are presented. X-ray diffraction (XRD) phase analysis and

scanning electron microscope (SEM) microstructural analysis were performed. Microwave sintering results were compared with data from conventional sintering.

3.2 Experimental Procedure

Silicon nitride samples were prepared by ball milling α-Si_3N_4 powder (E10 grade, UBE Industries Ltd., Yamaguchi, Japan) with 6 wt% Y_2O_3 (Aldrich Chemical Company Inc., Milwaukee, WI, 99.99%), 4 wt% MgO (Aldrich Chemical Company Inc., Milwaukee, WI, 99.99%), and varying amounts (0-5 wt%) of TZ3Y (3 mole% Y_2O_3 stabilized ZrO_2, (Tosoh Corporation, Tokyo, Japan, 99.99%). The powders were ball milled in de-ionized water for 12 hours using high-wear-resistant ZrO_2 milling media (YTZ Grinding Media, Tosoh Corporation, Tokyo, Japan). Milled powders were dried, ground and sieved through a 75 micron mesh. Five grams of mixed powder were uniaxially die-pressed at 30 MPa and then cold isostatically pressed at 200 MPa to form cylindrical green pellets of diameter 23 mm and thickness of 5 mm.

Microwave sintering was performed in a 2.45 GHz, industrial microwave furnace having variable output power of 3 kW maximum. The microwave sintering setup consisted of an alumina fiber-board insulation box, BN crucible and SiC susceptor, as shown in Figure 3.1. A green pellet was embedded in a Si_3N_4 powder bed contained in a BN crucible. A photograph of the microwave sintering set up is shown in Figure 3.2. Microwave sintering was performed at 0.1 MPa nitrogen pressure. The heating rate was manually controlled with the aid of a computer, at 50°C/min, prior to the holding period at the peak temperature. Samples were allowed to cool to ambient temperature in the applicator. Measurement of the sample surface temperature with a pyrometer focused through a hole in the BN crucible was not successful due to the high radiation loss at the sintering temperature of 1750°C. Rodger Black and Thomas Meek reported similar observations while measuring the surface temperature through a small hole in the reaction cavity during microwave sintering of ceramic composite materials at 1800ºC.[28] The approach used was to measure the surface temperature of the BN crucible containing the sample using a computer-controlled two-color pyrometer. Then, a correction for the experimentally measured value based on the numerically calculated temperature from complex dielectric properties of the sample was made.

Conventional sintering of the samples was performed in a Centorr vacuum furnace with tungsten heating elements at 1650°C, 1700°C and 1750°C, with a heating rate of 10°C/min. A photograph of the conventional sintering set-up is shown in Figure 3.3. A green pellet was embedded in a Si_3N_4 powder bed contained in a BN crucible and sintered in continuously flowing nitrogen gas at 0.1 MPa.

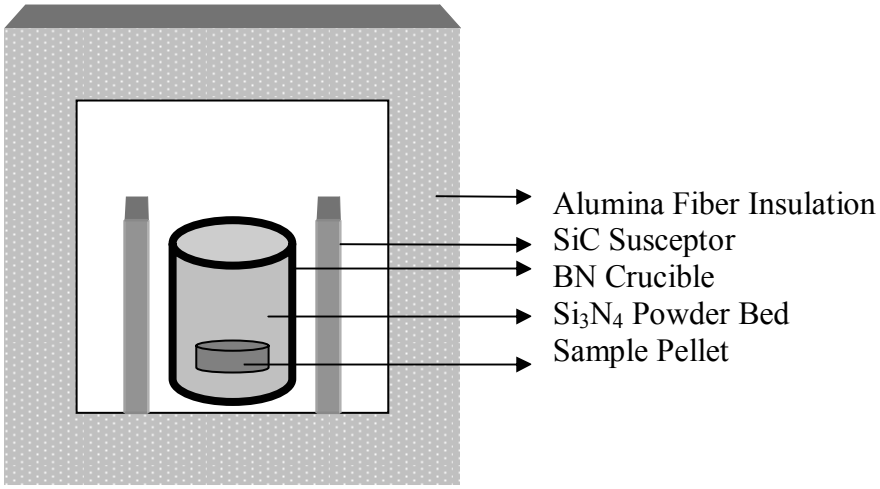

Figure 3.1. Schematic of the microwave sintering setup used for sintering silicon nitride samples.

The sintered sample densities were determined using Archimedes principle, with de-ionized water. The samples were diamond polished and CF_4 plasma etched using Ceramic and Metal Division, ORNL, Oak Ridge, TN's facilities. The microstructures were evaluated using a FEG 200 (FEI Company, Hillsboro, OR) environmental SEM (ESEM) with a field emission gun (FEG) operating at 10 kV. Phases in sintered samples were identified using x-ray diffraction (Philips, XRG 3100 X-ray generator). The generator was set to 40 kV and 20 mA utilizing Cu-Kα radiation. X-ray diffraction patterns were analyzed using a software package JADE 7 (Materials Data, Livermore, CA). The relative amounts of α and β-Si_3N_4 were determined by the method described by Gazzara and Messier.[29] Along with sinterability, high temperature phase stability was another important property to be understood in the case of Si_3N_4 ceramics, since there were many implications regarding its application at high-temperatures. Phase stability as a function of temperature was studied in-situ using an automated Siemen's High Temperature X-ray Diffractometer (HTXRD) using Co-Kα radation equipped with a θ-θ

Goniometer. Data were collected using a position sensitive detector from 20° to 70° (2θ), and step size of 0.02° while a continuous scan rate of 5°/min was employed. The analysis was performed every 50°C from 20°C to 900°C with a heating rate of 1K/sec, then the samples were held at 900°C for 24 hours. HTXRD ensured that the true evolution of phases with temperature could be followed, as cooling of heated samples could potentially induce artifacts.

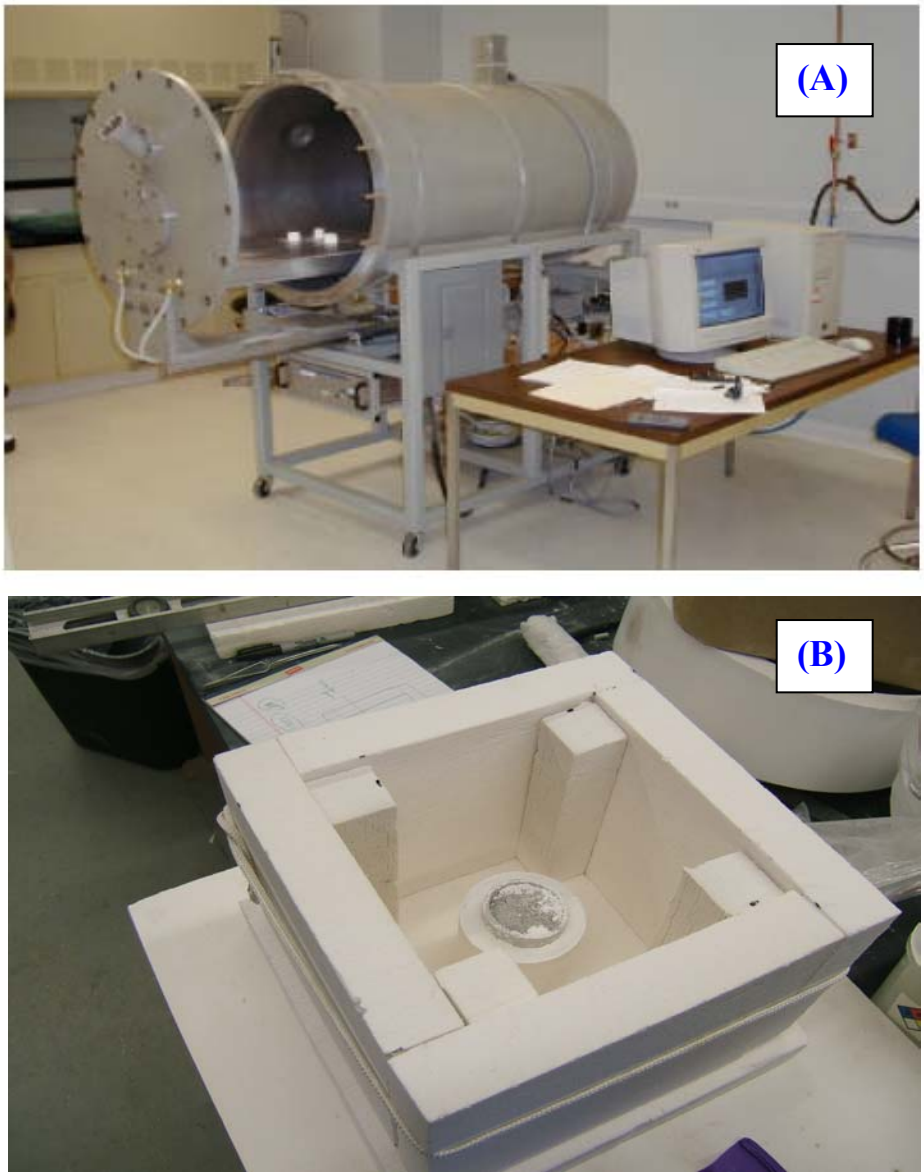

Figure 3.2. Communication and Power Industries (CPI) 2.45 GHz automated industrial microwave furnace (A) and sintering setup showing an alumina fiber insulation box and a boron nitride crucible containing Si_3N_4 samples (B).

Figure 3.3. Centorr vacuum furnace (A) and sintering setup showing a tungsten heating element and a boron nitride crucible containing Si_3N_4 samples (B).

3.3 Results and Discussion

3.3.1 Selection of Sintering Aids

Sintering aids such as MgO, Y_2O_3 and Al_2O_3, or some combination of them with other rare earth oxides, are commonly used in pressure-less sintering of Si_3N_4 to promote densification due to the covalent nature of Si-N bonds and their low self diffusivity. During the sintering process, these rare earth oxides react with silica impurities present on the surface of Si_3N_4 powder to form a low-melting-point eutectic melt. The melt solidifies when cooling to yield an amorphous or crystalline grain boundary phase depending on the nature of the additives and processing conditions. The general reaction for liquid formation is described as[30]

Si_3N_4 + additives + SiO_2 + impurities $\rightarrow$ $Si_3N_4(s)$ + grain boundary phases

The details of the compositions prepared for the present study are given in Table 3.I.

Table 3.I. Chemical Composition of Starting Powder (weight %).

Sr. No	Sample. ID	α-Si_3N_4	MgO	Y_2O_3	ZrO_2
1	SN1	90.0	4	6	0.0
2	SN2	87.5	4	6	2.5
3	SN3	86.0	4	6	4.0
4	SN4	85.0	4	6	5.0

The critical thermodynamic condition for choosing effective sintering additives is that reactions between Si_3N_4 and metal oxide should not proceed. This condition is met by the following equation.[31]

$$\Delta G_{[3]} < \Delta G_{[1]} \qquad (3.1)$$

$$\Delta G_{[3]} < \Delta G_{[2]} \qquad (3.2)$$

Where $\Delta G_{[1]}$ represents the standard free energy of reaction of Si_3N_4 with O_2 to form SiO_2 below 1727ºC and $\Delta G_{[2]}$ is the standard free energy of reaction of Si_3N_4 with O_2 to form SiO above 1727ºC. The standard free energy for oxidation of the metal is represented as $\Delta G_{[3]}$. Si_3N_4 reacts with oxygen present in the environment gas, metal oxide sintering additives and oxide impurities in silicon nitride powder according to the reactions given below.[31]

$$\frac{1}{3}S_3N_4(s) + O_2(g) \rightarrow SiO_2(s,l) + \frac{2}{3}N_2(g) \qquad (3.3)$$

$$\frac{2}{3}S_3N_4(s) + O_2(g) \rightarrow 2SiO(g) + \frac{4}{3}N_2(g) \qquad (3.4)$$

The standard free energy changes for these reactions at 1727ºC are $\Delta G_{[1]}$ = -126.9 kcal mol^{-1} and $\Delta G_{[2]}$ = -113.1 kcal mol^{-1}. The additive system is selected based on the lower value of standard free energy for oxidation, $\Delta G_{[3]}$ compared to $\Delta G_{[1]}$ or $\Delta G_{[2]}$. The value of $\Delta G_{[3]}$ of metal oxides MgO, Y_2O_3 and ZrO_2, are -153.3, -198.1 and -173.1 kcal mol^{-1} respectively.

3.3.2 Phase Identification

Figures 3.4a, 3.4b and 3.4c show XRD profiles for samples composed of Si_3N_4,with 6 wt% Y_2O_3 and 4 wt% MgO and varying amounts of ZrO_2. The samples were microwave sintered for 15 minutes in flowing nitrogen atmosphere at 1650ºC, 1700ºC and 1750ºC, respectively. Details of temperature, composition and phases identified are summarized in Table 3.II. The major crystalline phase identified in the microwave sintered samples is β-Si_3N_4, matching with PDF card 00-033-1160 with lattice parameters a =7.604 Å, b =7.604 Å and 2.908 Å. The minor phases are ZrO_2, ZrN and $Y_2Si_3O_3N_4$. The peak intensity for β-Si_3N_4 increases with higher ZrO_2 content at 1650ºC, although there is no variation in intensity at higher sintering temperatures. The peaks that appear in the ZrO_2 diffraction pattern fit best with the tetragonal phase corresponding to PDF card 01-089-6976, with lattice parameters a =3.640 Å, b =3.640 Å and c = 5.270 Å. The [101] (2θ = 29º) diffraction peak of the ZrO_2 phase overlaps with [201] (2θ = 29º) peak of the $Y_2Si_3O_3N_4$. The [111] (2θ = 39º) and [200] (2θ = 39º) peaks of the ZrN overlap with [101] (2θ = 33º) and [111] (2θ = 33º) peaks of β-Si_3N_4 and best fit with the cubic phase corresponding to PDF card 03-065-0961, with lattice parameters a = 4.600 Å,b = 4.600 Å and c = 4.600 Å. ZrO_2 reacted with Si_3N_4 form ZrN and SiO_2. The PDF card 00-045-0249 matched with the XRD profile of $Y_2Si_3O_3N_4$. The compatibility of $Y_2Si_3O_3N_4$ with Si_3N_4 is clearly evident on the Si_3N_4-Y_2O_3 side of the Si_3N_4-Y_2O_3-SiO_2 phase diagram.[31]

Figures 3.5a, 3.5b, and 3.5c show XRD patterns for conventionally sintered samples of Si_3N_4 with 6 wt% Y_2O_3, 4 wt% MgO, and 0 to 2.5 wt% of ZrO_2. The samples were sintered for 15 minutes in flowing nitrogen atmosphere at 1650ºC, 1700ºC and 1750ºC, respectively. These temperatures are corrected from the original pyrometer readings, based on numerical modeling results discussed in Chapter 2. A list of the phases identified with XRD is shown in Table 3.III. In contrast to microwave-sintered samples, the conventionally sintered samples contain both α-Si_3N_4 and β-Si_3N_4 phases, indicating that the $\alpha \rightarrow \beta$ phase transformation is incomplete. This is readily observable in Figures 3.5a, 3.5b and 3.5c, even for samples sintered at 1750ºC for 30 minutes. In addition to α-Si_3N_4 and β-Si_3N_4 peaks, weak tetragonal ZrO_2 and cubic ZrN peaks are also identifiable. It is interesting to note that, unlike microwave sintered samples, the formation of $Y_2Si_3O_3N_4$ was completely absent in conventionally sintered samples. Additionally, there are no detectable magnesium peaks because all of the magnesium is incorporated into the grain boundary glassy phase.

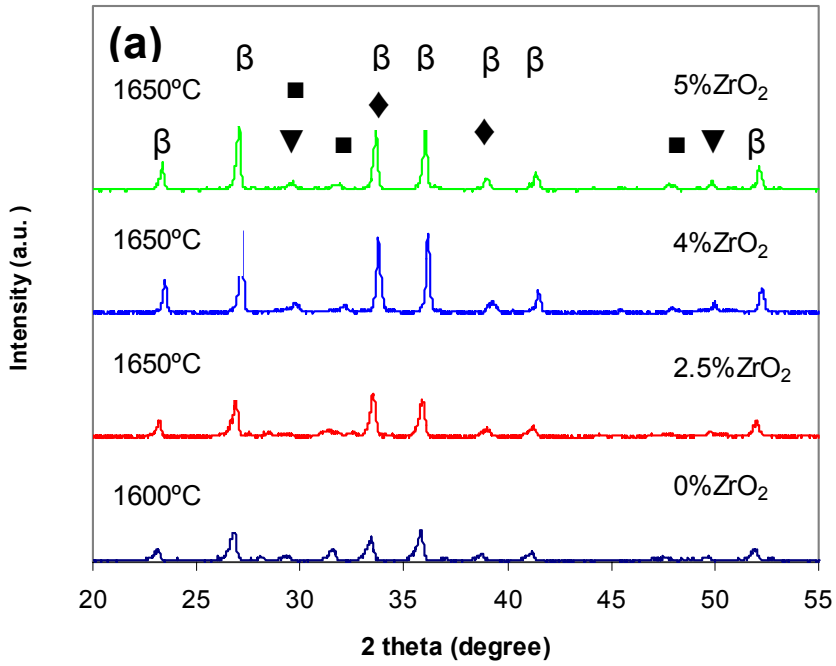

Figure 3.4a. XRD patterns for microwave-sintered Si_3N_4 with 4 wt% MgO and 6 wt% Y_2O_3 as a function of ZrO_2 content. Samples were sintered at 1650ºC for 15 min in 0.1 MPa of nitrogen pressure (**α:** α–Si_3N_4, **β** : β–Si_3N_4, ▼: ZrO_2, ♦: ZrN ■: $Y_2Si_3O_3N_4$). Numerical simulation results show a temperature of 50ºC higher in the sample which contains 2.5 wt% ZrO_2 than the sample without ZrO_2.

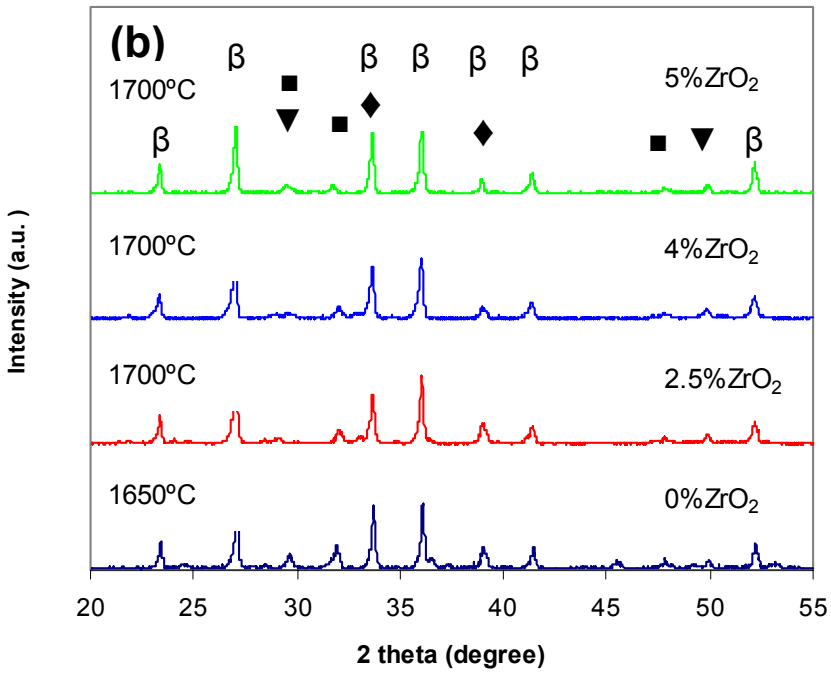

Figure 3.4b. XRD patterns for microwave-sintered Si_3N_4 with 4 wt% MgO and 6 wt% Y_2O_3 as a function of ZrO_2 content. Samples were sintered at 1700ºC for 15 min in 0.1 MPa of nitrogen pressure (**α:** α–Si_3N_4, **β** : β–Si_3N_4, ▼: ZrO_2, ♦: ZrN ■: $Y_2Si_3O_3N_4$). Numerical simulation results show a temperature of 50ºC higher in the sample which contains 2.5 wt% ZrO_2 than the sample without ZrO_2.

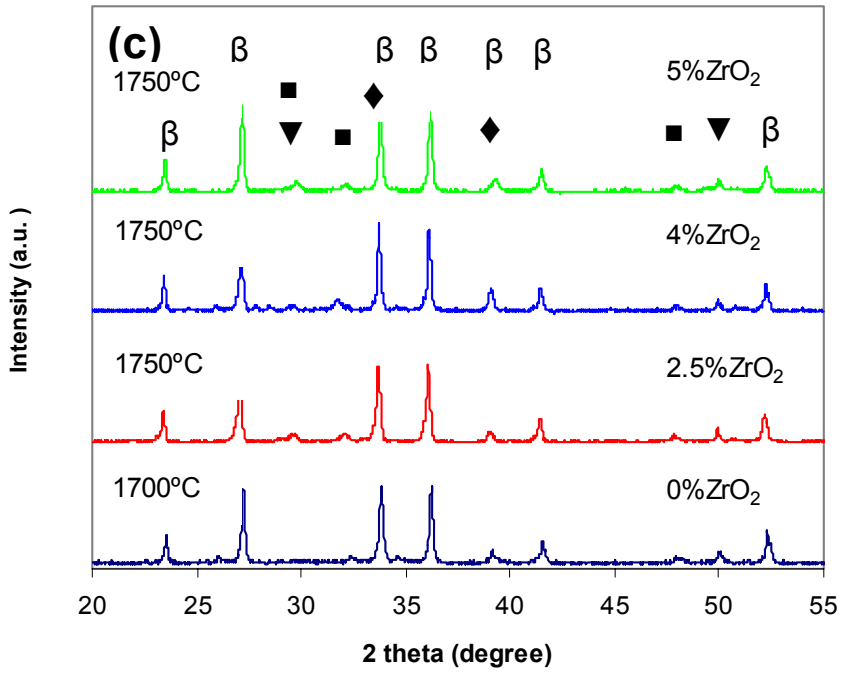

Figure 3.4c. XRD patterns for microwave-sintered Si_3N_4 with 4 wt% MgO and 6 wt% Y_2O_3 as a function of ZrO_2 content. Samples were sintered at 1750ºC for 15 min in 0.1 MPa of nitrogen pressure (**α:** α–Si_3N_4, **β** : β–Si_3N_4, ▼: ZrO_2, ♦: ZrN ■: $Y_2Si_3O_3N_4$). Numerical simulation results show a temperature of 50ºC higher in the sample which contains 2.5 wt% ZrO_2 than the sample without ZrO_2.

Table 3.II. Phases in Microwave-Sintered Si_3N_4-MgO-Y_2O_3 Systems as a Function of Sintering Temperature (ºC) and ZrO_2 Content.

T ºC	ZrO_2%	Sample. ID	Phases identified
1650	0	SN1	β-Si_3N_4, $Y_2Si_3O_3N_4$
1650	2.5	SN2	β-Si_3N_4, $Y_2Si_3O_3N_4$, ZrN, ZrO_2(t)
1650	4	SN3	β-Si_3N_4, $Y_2Si_3O_3N_4$, ZrN, ZrO_2(t)
1650	5	SN4	β-Si_3N_4, $Y_2Si_3O_3N_4$, ZrN, ZrO_2(t)
1700	0	SN1	β-Si_3N_4, $Y_2Si_3O_3N_4$,
1700	2.5	SN2	β-Si_3N_4, $Y_2Si_3O_3N_4$, ZrN, ZrO_2(t)
1700	4	SN3	β-Si_3N_4, $Y_2Si_3O_3N_4$, ZrN, ZrO_2(t)
1700	5	SN4	β-Si_3N_4, $Y_2Si_3O_3N_4$, ZrN, ZrO_2(t)
1750	0	SN1	β-Si_3N_4, $Y_2Si_3O_3N_4$
1750	2.5	SN2	β-Si_3N_4, $Y_2Si_3O_3N_4$, ZrN, ZrO_2(t)
1750	4	SN3	β-Si_3N_4, $Y_2Si_3O_3N_4$, ZrN, ZrO_2(t)
1750	5	SN4	β-Si_3N_4, $Y_2Si_3O_3N_4$, ZrN, ZrO_2(t)

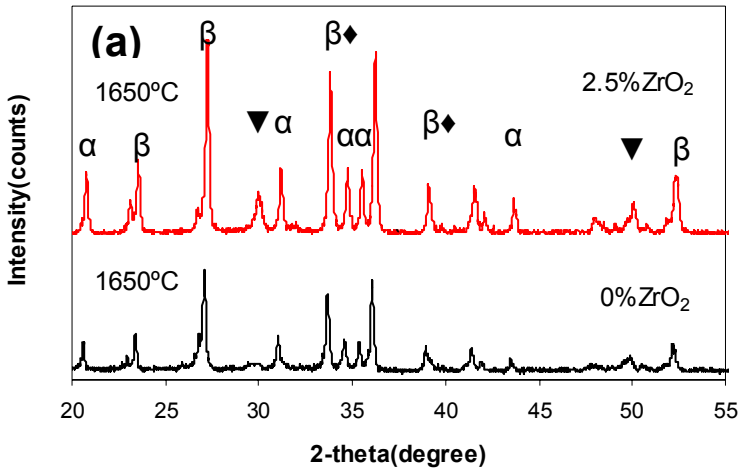

Figure 3.5a. XRD patterns for conventionally-sintered Si_3N_4 with 4 wt% MgO and 6 wt% Y_2O_3 as a function of ZrO_2 content. Samples were sintered at 1650ºC for 15 min in 0.1 MPa of nitrogen pressure. (**α:** α–Si_3N_4, **β** : β–Si_3N_4, ▼: ZrO_2, ♦: ZrN).

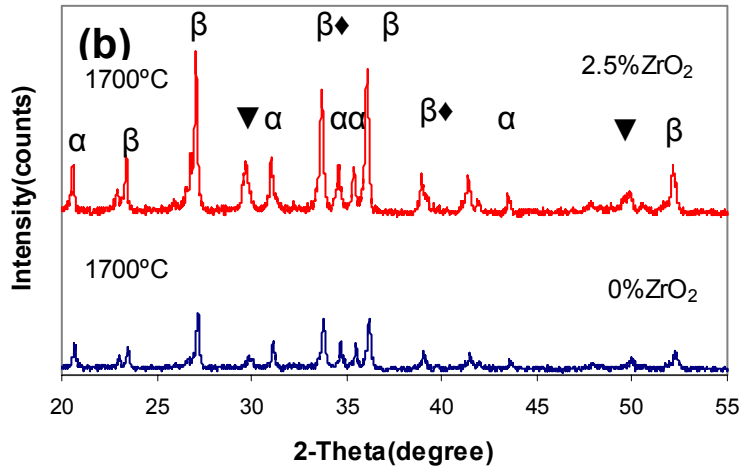

Figure 3.5b. XRD patterns for conventionally-sintered Si_3N_4 with 4 wt% MgO and 6 wt% Y_2O_3 as a function of ZrO_2 content. Samples were sintered at 1700ºC for 15 min in 0.1 MPa of nitrogen pressure. (**α:** α–Si_3N_4, **β** : β–Si_3N_4, ▼: ZrO_2, ♦: ZrN).

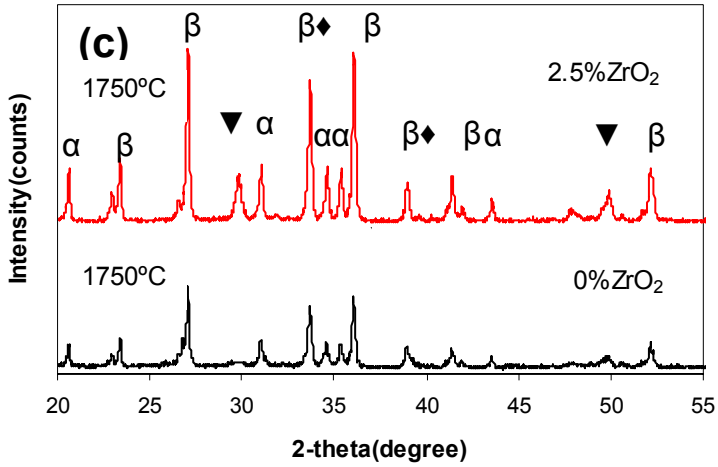

Figure 3.5c. XRD patterns for conventionally-sintered Si_3N_4 with 4 wt% MgO and 6 wt% Y_2O_3 as a function of ZrO_2 content. Samples were sintered at 1650ºC, 1700ºC and 1750ºC for 15 min in 0.1 MPa of nitrogen pressure. (**α:** α–Si_3N_4, **β** : β–Si_3N_4, ▼: ZrO_2, ♦: ZrN).

Table 3.III. Phases in Conventionally Sintered Si_3N_4-MgO-Y_2O_3 Systems

T ºC	ZrO_2%	Sample ID	Phases present
1650	0	SN1	β-Si_3N_4, α-Si_3N_4
1650	2.5	SN2	β-Si_3N_4, α-Si_3N_4, ZrN, ZrO_2(t)
1700	0	SN1	β-Si_3N_4, α-Si_3N_4,
1700	2.5	SN2	β-Si_3N_4, α-Si_3N_4, ZrN, ZrO_2(t)
1750	0	SN1	β-Si_3N_4, α-Si_3N_4
1750	2.5	SN2	β-Si_3N_4, α-Si_3N_4, ZrN, ZrO_2(t)

The high-temperature XRD patterns of the microwave-sintered specimen containing Si_3N_4, 6 wt% Y_2O_3, 4 wt% MgO and 4 wt% ZrO_2 at various temperatures are shown in Figure 3.6. The samples were heated to 900°C from 20°C and subsequently cooled down to room temperature. Diffraction measurements were performed at room temperature, then from 600°C to 900°C at 50°C intervals. The samples were then held at 900°C for 24 hours and the XRD patterns, were recorded for every 2 hours, as shown in Figure 3.7. No variation was observed in the case of β Si_3N_4 and ZrO_2 diffraction patterns with respect to temperature as well as aging time.

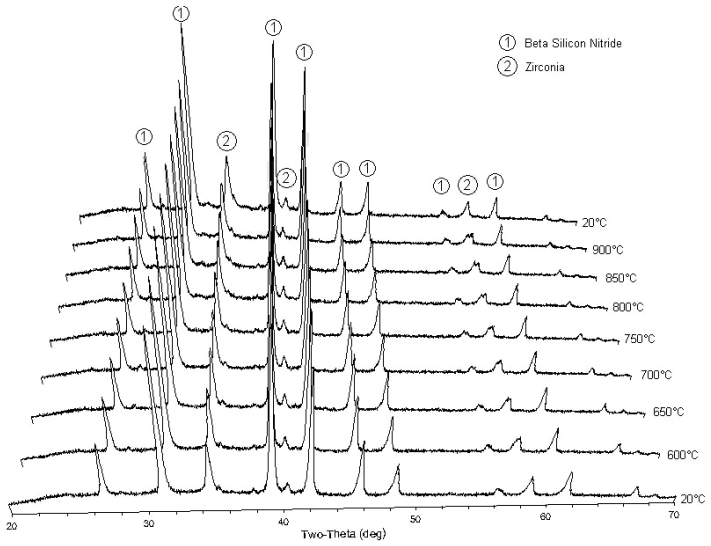

Figure 3.6. HTXRD pattern for a microwave-sintered specimen containing Si_3N_4, 6 wt % Y_2O_3, 4 wt% MgO and 5 wt% ZrO_2 heated to 900°C from 20°C and cooled to room temperature.

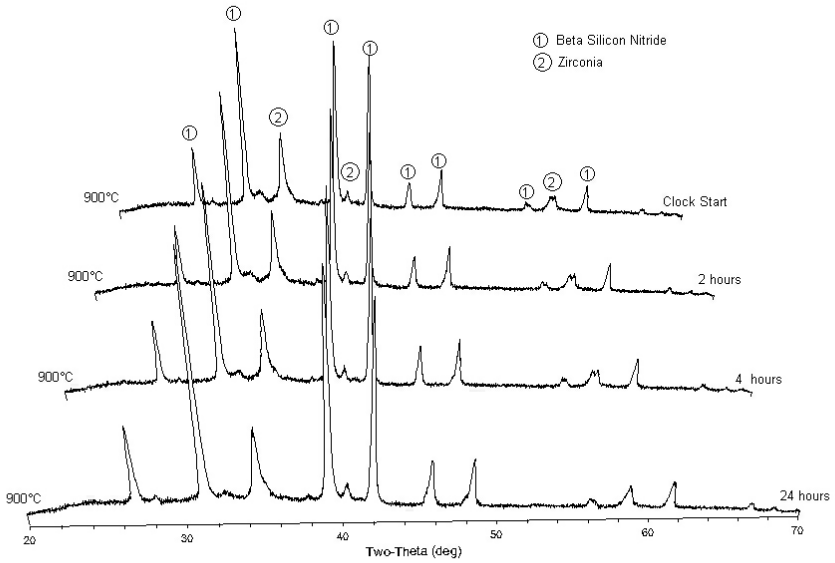

Figure 3.7. HTXRD pattern for a microwave-sintered specimen containing Si_3N_4, 6 wt % Y_2O_3, 4 wt% MgO and 5 wt% ZrO_2 heated to 900°C from 20°C and subsequently heat-treated for 24 hours.

3.3.3 The α → β Phase Transformation

The XRD peak intensities of [210] (2θ = 35.5) β-Si_3N_4 and [210] (2θ = 36) α-Si_3N_4 were compared to quantitatively estimate the relative amounts of α-Si_3N_4 and β Si_3N_4, following the method previously described by Gazzara and Messier.[29] This technique reduces the effects of preferred orientation and particle size, thereby lowering common sources of errors associated with XRD measurements. Table 3.IV shows the XRD intensity ratios which estimate the portions of α-Si_3N_4 and β-Si_3N_4 in microwave and conventionally-sintered samples. The X-ray results indicate the α → β phase transformation is completed in microwave-sintered samples, while in conventional sintered samples the transformation has been not completed even at 1750ºC. However, the experimental results demonstrated that the addition of ZrO_2 enhances α → β transformation during both microwave and conventional sintering. The complete transformation observed in microwave sintered samples may be attributed to the localized heating within the grain-boundary phase. This in turn increases the rates of dissolution of the α-Si_3N_4 phase into a low-viscosity oxynitride liquid phase and re-precipitated as β-Si_3N_4 crystals.[31-33]

Table 3.IV. XRD Intensity Ratios for α and β Si_3N_4 as a Function of Sintering Temperature (ºC) and ZrO_2 Content

TºC	ZrO_2%	Sample ID	$\beta_{(210)}/(\beta_{(210)}+\alpha_{(210)})$ Microwave	$\beta_{(210)}/(\beta_{(210)}+\alpha_{(210)})$ Conventional
1650	0	SN1	1	0.67
1650	2.5	SN2	1	0.73
1700	0	SN1	1	0.74
1700	2.5	SN2	1	0.75
1750	0	SN1	1	0.76
1750	2.5	SN2	1	0.81

Mark *et al.*[34] reported that the α → β transformation of Si_3N_4 with Y_2O_3, Al_2O_3, MgO sintering additives was completed after 1 hour of microwave heating at 28 GHz anda temperature of 1450ºC. Y. C. Kim *et al.*[35] also observed complete α → β transformation of Si_3N_4 with Y_2O_3 and Al_2O_3 after 30 minutes of microwave heating at 1750ºC using a multimode cylindrical cavity applicator with 2.45 GHz frequency. The

enhanced α → β phase transformation observed in microwave-sintered samples may also be related to the non-thermal action of microwaves on mass transfer in crystalline solids.[36]

3.3.4 Densification Behavior

The densities of the microwave-sintered Si_3N_4 samples are shown in Figure 3.8 as a function of ZrO_2 content for sintering temperatures of 1650ºC, 1700ºC and 1750ºC, respectively. As expected, the data indicates that density increases with increasing temperature. Samples with 2.5 wt%, ZrO_2 exhibit higher densities at all sintering temperatures, with the highest density (95.06%) occurring at 1750ºC. No further densification appears to have resulted from ZrO_2 levels above 2.5 wt%, suggesting densification was accompanied by increasing decomposition due to the localized selective overheating caused by microwaves.

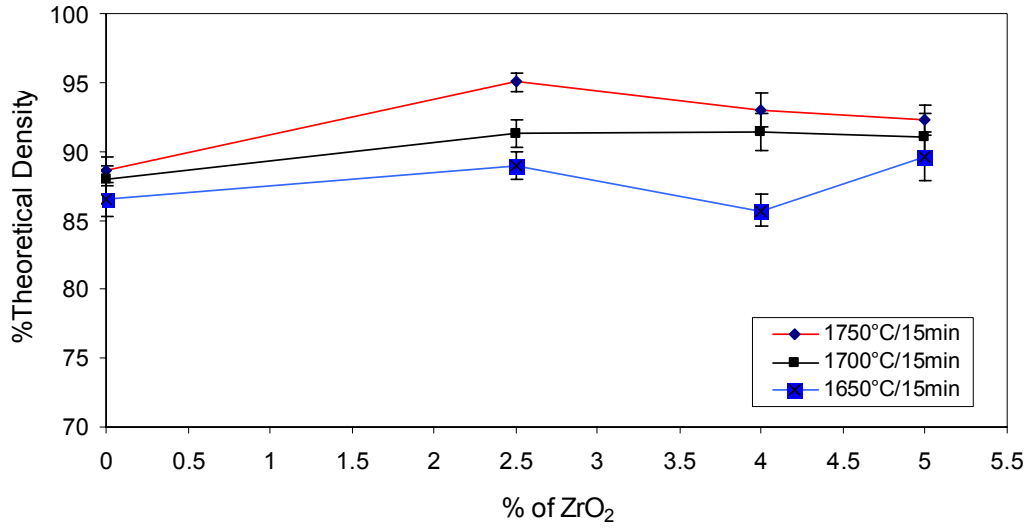

Figure 3.8 Density of microwave-sintered Si_3N_4-MgO-Y_2O_3 samples as a function of ZrO_2 content and sintering temperature in 0.1 MPa of nitrogen pressure.

Figure 3.9 shows microstructures of microwave-sintered samples with varying amounts of ZrO_2 sintered at 1650ºC, 1700ºC and 1750ºC. The microstructures of samples sintered at 1650ºC have open porosity irrespective of ZrO_2 content, in agreement with the lower density values displayed in Figure 3.8. This suggests the viscosity of the oxynitride

liquid phase was not low enough to allow for filling of the pores.[37] The sample which contains 2.5 wt% ZrO_2 sintered at 1750ºC exhibits the lowest porosity, again in agreement with the density values. In samples sintered at 1750ºC with 4-5 wt% of ZrO_2, the lower density most likely was due to residual porosity caused by the thermal decomposition from localized microwave heating. Residual porosity due to the decomposition of Si_3N_4 is clearly visible in the SEM micrograph of the acid etched silicon nitride sample (Figure 3.10) consisting of 4 wt% MgO, 6 wt% Y_2O_3 and 5 wt% ZrO_2, and microwave sintered at 1750ºC.

Figure 3.11 shows microstructures of the conventionally-sintered samples and Table 3.V compares the densities of microwave and conventionally-sintered samples. The results suggest the increase in density associated with ZrO_2 additions, as observed for both sintering techniques, is due to the lower viscosity glassy phase developed in the presence of ZrO_2. Moreover, nitrogen as an additional component may have further lowered the eutectic temperature, thereby enhancing diffusion.[38]

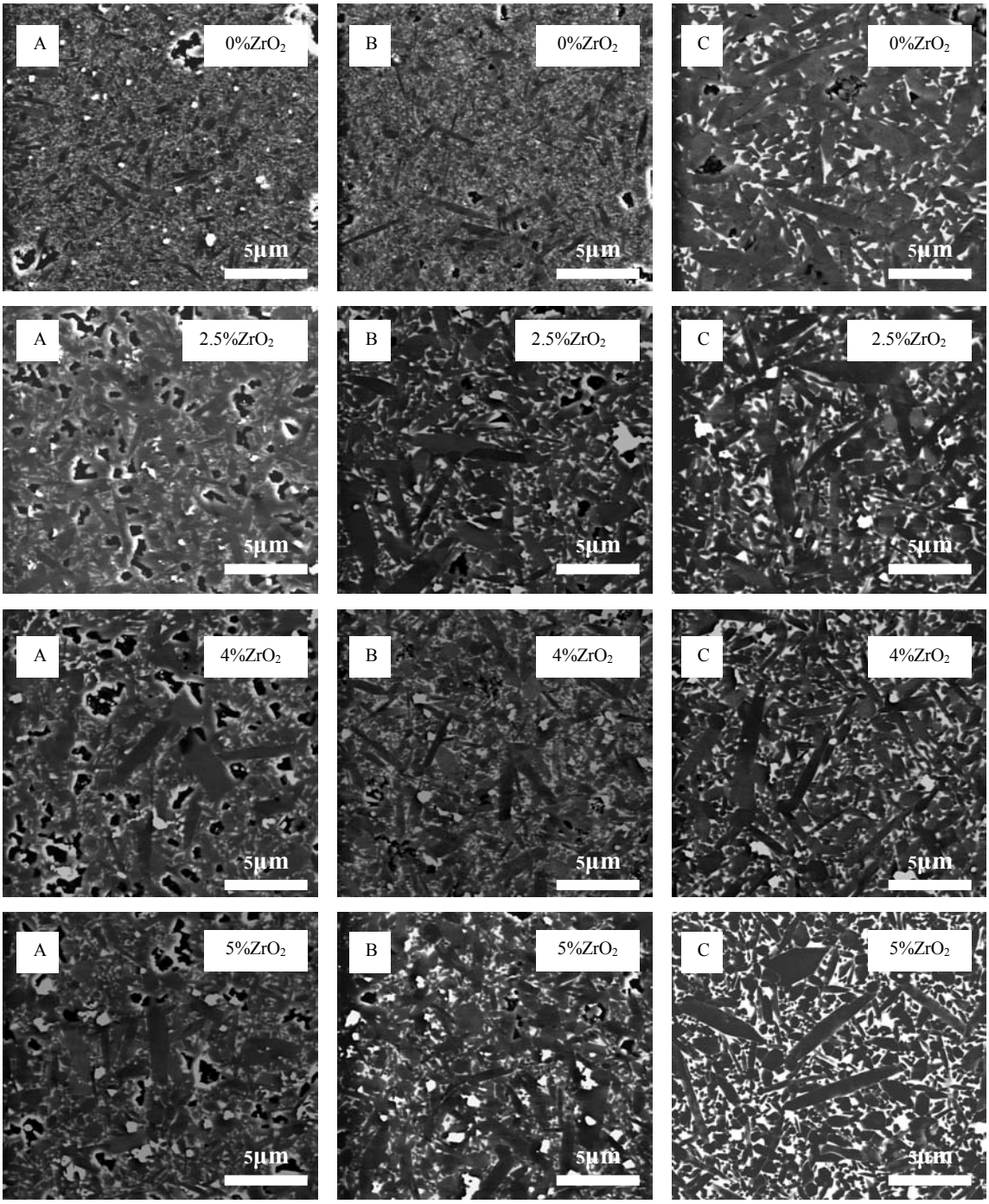

Figure 3.9. SEM images of microwave-sintered Si_3N_4 with MgO and Y_2O_3 as a function of ZrO_2 content. Samples were sintered at 1650ºC (A), 1700ºC (B) and 1750ºC (C) for 15 min in 0.1 MPa of nitrogen pressure.

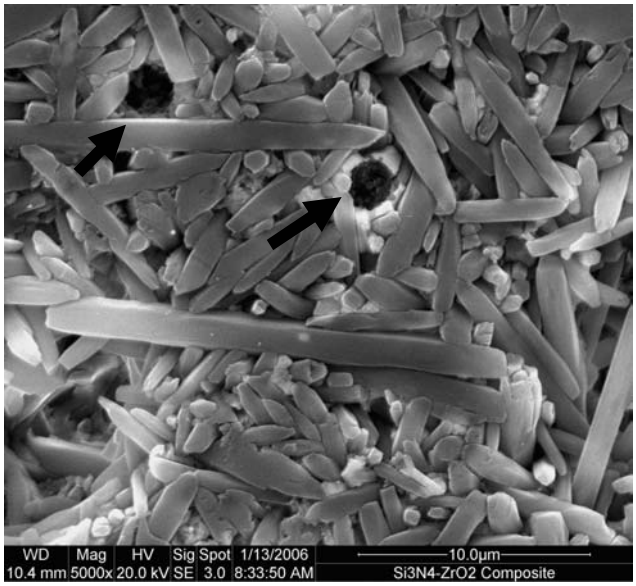

Figure 3.10. SEM image of a microwave-sintered sample consisting of 95 wt% Si_3N_4, 4 wt% MgO, 6 wt% Y_2O_3 and 5 wt% ZrO_2, showing residual porosity due to the decomposition of Si_3N_4. The sample was sintered at 1750ºC for 15 min.

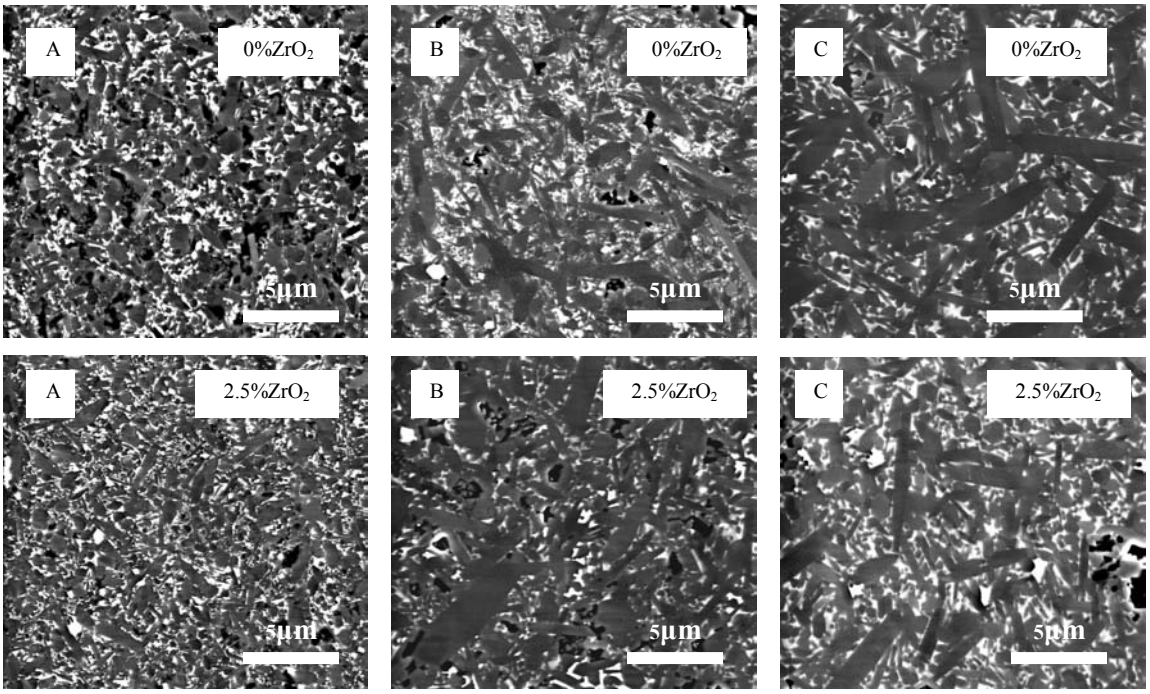

Figure 3.11. SEM images of conventionally-sintered Si_3N_4 with MgO and Y_2O_3, as a function of ZrO_2 content. Samples were sintered at 1650ºC (A), 1700ºC (B) and1750ºC (C) for 15 min in 0.1 MPa of nitrogen pressure.

Table 3.V. Density of the Conventionally-Sintered Samples as a Function of Sintered Temperature (ºC) and ZrO_2 Content.

T ºC	ZrO_2 (wt %)	Sample ID	Density Conventional (% Theoretical)	Density Microwave (% Theoretical)
1650	0	SN1	90.6 ±1.4	86.5±1.2
1650	2.5	SN2	93.4±1.9	89.0±1.0
1700	0	SN1	92.9±1.0	87.9±1.0
1700	2.5	SN2	94.1±1.1	91.4±1.0
1750	0	SN1	93.9±1.4	88.6±1.1
1750	2.5	SN2	94.4±1.0	95.1±0.6

In the case of conventional sintering, the density always increased with increasing sintering temperature and ZrO_2 level, and densification was more rapid than the $\alpha \rightarrow \beta$ phase transformation.. In contrast, the present experimental results with microwave sintered samples show that phase transformation is more rapid than densification. The above results suggest two competing phenomena affect the densification, namely pore growth by decomposition as evident from the weight losses of the sintered samples and pore shrinkage by liquid-phase sintering as seen in the microstructures. The results herein show the $\alpha \rightarrow \beta$ phase transformation and densification of silicon nitride can be enhanced by sintering with microwave energy and optimizing the amount of ZrO_2 additive, sintering temperature and time.

3.4 Conclusions

Densification and $\alpha \rightarrow \beta$ phase transformation during microwave sintering of Si_3N_4 - Y_2O_3 - MgO systems containing various amounts of ZrO_2 have been studied. The $\alpha \rightarrow \beta$ transformation in microwave sintered samples is completed much earlier than densification, whereas a significant amount of α-Si_3N_4 remains in conventionally sintered samples even after heating to 1750ºC for 30 minutes. The enhanced $\alpha \rightarrow \beta$ phase transformation during microwave sintering is most likely due to the coupling of microwave power with the dielectrically lossy grain boundary glassy phase

volumetrically, which promotes dissolution of α–Si_3N_4 and nucleation of β-Si_3N_4. ZrO_2 additions in Si_3N_4 -Y_2O_3 - MgO systems promoted densification during both microwave- and conventional sintering. However, densification appears to be limited in microwave sintered samples containing more than about 2.5 wt% ZrO_2, as surface porosity results from selective localized overheating and decomposition of ZrO_2-containing phases. This investigation demonstrated that it is possible to maximize the density by adjusting the amount of ZrO_2 additive and the microwave sintering temperature and time. Thus, microwave sintering can be used to simultaneously enhance α → β phase transformation and densification.

3.5 References

1. F.L. Riley, "Silicon Nitride and Related Materials," *J. Am. Ceram. Soc.,* **83** [2] 245-65 (2000).

2. D. Hardie and K.H. Jack, "Crystal Structures of Silicon Nitride," *Nature (London)*, **180** [8] 332-33 (1957).

3. G.R. Terwilliger and F.F. Lange, "Pressureless Sintering of Si_3N_4," *J. Mater. Sci*., **10** [7] 1169-74 (1975).

4. Y. Goto and G. Thomas, "Phase Transformation and Microstructural Changes of Si_3N_4 During Sintering," *J. Mater. Sci*., **30** [9] 2194-2200 (1995).

5. W.D. Kingery, "Densification During Sintering in the Presence of a Liquid Phase: I. Theory," *J. Appl. Phys*., **30** [3] 301-06 (1959).

6. T.N. Tiegs, M.K. Ferber, J.O. Kiggans, K.L. More, C.M. Hubbard, and D.W. Coffey, "Microstructure Development During Microwave Annealing of Dense Silicon Nitride," pp. 411-20 in Ceramic Transactions, Vol. 21, *Microwaves: Theory and Applications in Materials Processing*. Edited by D.E. Clark, F.D. Gac, and W.H. Shutton. American Ceramic Society, Westerville, OH, 1991.

7. J. Zhang, L. Cao, and F. Xia: "Microwave Sintering of Si_3N_4 Ceramics," *Mater. Res. Symp. Proc*., **269**, 329-34 (1992).

8. T.N. Tiegs, J.O. Kiggans, H.T. Lin, and C.A. Willkens, "Comparison of Properties of Sintered and Reaction-Bonded Silicon Nitride Fabricated by Microwave and Conventional Heating," *Mater. Res. Symp. Proc*., **347**, 501-56 (1994).

9. Y.C. Kim, S.C. Koh, D.K. Kim, and C.H. Kim, "Effect of Microwave Heating on the Sintering of Silicon Nitride-Doped with Al_2O_3 and Y_2O_3," pp. 415-22 in Ceramic Transactions, Vol. 59, *Microwaves: Theory and Applications in Materials Processing III*. Edited by D.E. Clark, D. Folz, S. Joda, and R. Siberglitt. American Ceramic Society, Westerville, OH, 1995.

10. W.H. Sutton, "Microwave Firing of High Alumina Castables," *Mater. Res. Symp. Proc.* **124**, 287-95 (1988).

11. J. F. MacDowell, "Microwave Heating of Nepheline Glass-Ceramics," *Am. Ceram. Soc. Bull.*, **63** [2] 282-86 (1984).

12. H. Fukushima, T. Yamaka, and M. Matsui, "Microwave Heating of Ceramics and Its Application to Joining," *J. Mater. Res.*, **5** [2] 397-405 (1990).

13. M.A. Janney and H.D. Kimrey, "Diffusion-Controlled Processes in Microwave-Fired Oxide Ceramics," *Mater. Res. Symp. Proc.*, **189**, 215-27 (1990).

14. J. Samuels and J.R. Brandon, "Effect of Composition on the Enhanced Microwave Sintering of Alumina- Based Ceramic Composites," *J. Mater. Sci.*, **27** [12] 3259-65 (1992).

15. M.A. Janney, C.L. Calhoun, and H.D. Kimrey, "Microwave Sintering of Zirconia-8 Mole % Yittria," pp. 311-18 in Ceramic Transactions, Vol. 21, *Microwaves: Theory and Applications in Materials Processing*. Edited by D.E. Clark, F.D. Gac, and W.H. Shutton. American Ceramic Society, Westerville, OH, 1991.

16. Y. Fang, D.K. Agrawal, D.M. Roy, and R. Roy, "Rapid Sintering of Hydroxyapatite Ceramics by Microwave Processing," pp. 349-56 in Ceramic Transactions, Vol. 21, *Microwaves: Theory and Applications in Materials Processing*. Edited by D.E. Clark, F.D. Gac, and W.H. Shutton. American Ceramic Society, Westerville, OH, 1991.

17. J. Cai, C.Y. Song, B.S. Li, X.X. Huang, J.K. Guo, and Y.L. Tian, "Microwave Sintering of Zirconia Toughened Mullite (ZTM)," *Mater. Res. Symp. Proc.*, **347**, 545-51 (1994).

18. P. Boch, N. Lequeux, and P. Piluso, "Reaction Sintering of Ceramic Materials by Microwave Heating," *Mater. Res. Symp. Proc.*, **269**, 211-16 (1992).

19. J. Cheng Y. Fang, D.K. Agrawal, and R. Roy, "Microwave Synthesis of Lead-Barium Titanate," *Mater. Res. Symp. Proc.*, **347**, 513-22 (1994).

20. S.A. Assafi and D.E. Clark, "Microwave Joining of Ceramics: A Study on Joining Alumina both Directly and with Alumina Gel," *Mater. Res. Symp. Proc*., **269**, 335-40 (1992).
21. M.A. Janney, H.D. Kimrey, M.A. Schmidt, and J.O. Kiggans, "Grain Growth in Microwave-Annealed Alumina," *J. Am. Ceram. Soc*., **74** [7] 1675-81 (1991).

22. W.H. Sutton, "Microwave Processing of Ceramics," *Am. Ceram. Soc. Bull*., **68** [2] 376-86 (1989).

23. T.N. Tiegs, J.O. Kiggans, and H.D. Kimrey, "Microwave Sintering of Silicon Nitride," *Ceram. Eng. Sci. Proc*., **12** [9-10] 1981-92 (1991).

24. R.W. Rice and W.J. McDonough, "Hot-Pressed Si_3N_4 with Zr-Based Additions," *J. Am. Ceram. Soc*, **58** [5] 264-67 (1975).

25. N. Claussen and C.P. Lahmann, "Fracture Behavior of Some Hot-Pressed Si_3N_4 Ceramics at High Temperatures," *Power Metall. Int*., **7** [3] 133-37 (1975).

26. F.F. Lange, L.K.L. Falk, and B.I. Davis, "Structural Ceramics Based on Si_3N_4-ZrO_2 (Y_2O_3) Compositions," *J. Mater. Res*. **2** [1] 66-76 (1987).

27. T. Vasilos, R.M. Cannon, Jr., and B.J. Wuensch, Final National Aeronautics and Space Administration Report No. NASA-CR-159585, 30 March 1979.

28. R.D. Blake and T.T. Meek, "Microwave Processed Composite Materials." *J. Mater. Sci. Lett.* **5** [11] 1097-98 (1986).

29. C.P. Gazzara and D.R. Messier, "Determination of Phase Content of Si_3N_4 by X-Ray Diffraction Analysis," *Am. Ceram. Soc. Bull*., **56** [9] 777-80 (1977).

30. M.N. Rahaman, *Ceramic Processing and Sintering*, pp.571-72. Marcel Dekker, New York, 1995.

31. M.I. Jones, M.C. Valecillos, K. Hirao and M. Toriyama, " Densification Behavior in Microwave -Sintered Silicon Nitride at 28 GHz," *J. Am. Ceram. Soc.*, **84** [10] 2424-26 (2001).

32. T. Ekstrom, L.K.L. Falk, and E.M.K. Wedel " Si_3N_4 –ZrO_2 Composites with Small Al_2O_3 and Y_2O_3 Additions Prepared by HIP," *J. Mater. Sci*., **26** [16] 4331-40 (1991).

33. Q. Feng, S. Chockalingam, and D. A. Earl, "Microstructures of Microwave Sintered Silicon Nitride with Zirconia as Secondary Particulates," *J. Am. Ceram. Soc.*, **89** [12] 3770-77 (2006).

34. M.I. Jones, M.C. Valecillos, K. Hirao and Y. Yamauchi, "Grain Growth in Microwave Sintered Si_3N_4 Ceramics Sintered from Different Starting Powders," *J. Eur. Ceram. Soc.*, **22** [16] 2981-88 (2002).

35. Y.C. Kim, C.H. Kim, and D.K. Kim, "Effect of Microwave Heating on Densification and $\alpha \rightarrow \beta$ Phase Transformation of Silicon Nitride," *J. Eur. Ceram. Soc.,* **17** [13] 1625-30 (1997).

36. J.H. Booske, R.F. Cooper, S.A. Freeman, B. Meng, K.I. Rybakov, and V.E. Semenov, "Thermal and Nonthermal Interactions Between Microwave Fields and Ceramics," pp.143-51 in Ceramic Transactions, Vol. 80, *Microwaves: Theory and Applications in Materials Processing IV*. Edited by D.E. Clark, W.H. Shutton, D.A. Lewis. American Ceramic Society, Westerville, OH, 1991.

37. F.C.R. Wroe and A.T. Rowley, "Microwave Enhanced Sintering of Ceramics," pp.69-76 in Ceramic Transactions, Vol. 59, *Microwaves: Theory and Applications in Materials Processing III*. Edited by D.E. Clark, D. Folz, S. Joda, and R. Siberglitt. American Ceramic Society, Westerville, OH, 1995.

38. S.M. Castanho, J.S. Blugan and M.J. Reece, "Si_3N_4-Al_2O_3/Si_3N_4-Y_2O_3 Couple Diffusion System," *Acta. Mater.*, **44** [3] 1001-10 (1996).

CHAPTER 4

Grain Boundary Phase Analysis

Abstract

Grain-boundary phases of microwave-sintered Si_3N_4-Y_2O_3-MgO system containing ZrO_2 particulates were characterized by transmission electron microscopy (TEM). Although the starting powder was α-Si_3N_4 with Y_2O_3, MgO, and ZrO_2 dopants, the sintered crystalline phases, analyzed by TEM, show that the N-Melilites are distributed at the multigrain junctions, suggesting they are formed by crystallization from a liquid phase. TEM analysis shows that Si_3N_4 grains are interlocked with each other. A large amount of a secondary phase (13 vol%), containing Si-Y-Mg-O-N elements as identified by energy-dispersive x-ray spectrometry, is present in the multigrain junctions and grain boundaries. TEM analysis also found that small ZrO_2 grains (d<200 nm) are dispersed in the matrix. The addition of ZrO_2 as a susceptor for microwave sintering increases the heating rate. However, there appeared to be very minor dissolution of ZrO_2 in the oxynitride liquid during sintering. Both tetragonal and cubic Zr-rich phases were identified by selected-area electron diffraction, which supports the existence of N-stabilizing ZrO_2. Microwave sintering favored the formation of the Si-Mg-Y oxynitride liquid phase and thus enhanced the dissolution of α-Si_3N_4.

4.1 Introduction

With many exceptional properties such as high strength and fracture toughness, silicon nitride is recognized as one of the leading candidates for structural applications at a high temperature. It has been shown that materials in which elongated β-Si_3N_4 particles are dispersed in a fine matrix with a bimodal grain-size distribution possess higher fracture toughness than those with equiaxed β-Si_3N_4 grain.[1] These self-reinforced β-Si_3N_4 materials are analogous to whisker-reinforced ceramics where crack deflection, bridging, and grain pullout are observed.[1] Preferential c-axis growth of β-Si_3N_4 grains results in elongated β-Si_3N_4 morphologies.[2-4] Besides grain morphology, grain boundary chemistry and intergranular film thickness are other important factors that can affect fracture toughness.[5] The occurrence of intergranular films favors the release of residual stresses at the grain boundaries, and thus supports debonding along the interfaces.[6] Grain-boundary chemistry influences the glass network structure of films on the atomic level, which governs mechanisms involved with transgranular fracture or intergranular fracture. Inter-granular film thickness is also dependent on the film chemistry.[7] For example, the intergranular film in undoped Si_3N_4 was about one nm,[8] while the thickness varied from

0.7 to 1.5 nm with calcium concentration.[9] It was reported that materials with different grain morphology exhibit similar fracture toughness if they are predominantly transgranular.[10] The results indicate that a bimodal grain distribution is a pre-requisite but not sufficient by itself to obtain high fracture toughness in β-Si_3N_4 materials. In addition to affecting the toughness at room temperature, variations of grain-boundary chemistry can significantly change high-temperature mechanical properties such as creep.[11] Presence of the halogenides significantly lowers the viscosity of the residual glass and creep temperatures,[12] and is thus detrimental to high-temperature applications.

A post-sintering heat treatment of silicon nitride materials is a feasible approach to improve mechanical properties.[13] A post-sintering heat treatment induces crystallization of the matrix glassy phases and changes the residual intergranular stress distribution, thereby influencing the mechanical properties.[14] For example, Kleebe *et al*.[5] found that a high degree of crystallization at the triple pockets of Sc_20_3-doped material can favor intergranular crack debonding and crack deflection. Microstructural characterizations showed that a post-sintering heat treatment changes dislocation density within β-Si_3N_4 grains and can cause crystallization from glassy phases at the grain boundary.[15] Extensive experimental data confirm that Si_3N_4 properties are directly related to the microstructure, and control of microstructural design is a feasible means to obtain extraordinary properties.[16]

Pure Si_3N_4 is difficult to sinter due to its covalent bonding and low self-diffusivity. Densification can be achieved by a solution-reprecipitation process with additions of Al_2O_3, SiO_2, Y_2O_3, MgO, and other oxides to form liquid phases. Currently, hot isostatic pressing and gas-pressure sintering are normally used to obtain dense Si_3N_4 ceramics. However, microwave sintering is attracting more attention for fabricating Si_3N_4 components. Microwave processing has been observed to enhance densification and accelerate the Si_3N_4 α → β phase transformation.[17] Pure Si_3N_4 is transparent to microwaves up to a critical temperature of approximately l350°C because of its low dielectric loss factor. However, liquid-phase additives and secondary particulates that couple well with microwaves are believed to improve the heating efficiency.[18] For example, ZrO_2 begins to rapidly heat with microwaves close to 800°C.

In the present study, Si_3N_4 with additions of yttria stabilized ZrO_2 as well as Y_2O_3 and MgO was sintered using microwave energy. Both stabilized and unstabilized ZrO_2 have been widely used as additives in conventional sintered Si_3N_4. Claussen and Jahn[19] reported that a dispersion of monoclinic ZrO_2 enhances the fracture toughness of hot-pressed Si_3N_4 in the same way that it does with $A1_2O_3$. If ZrO_2 takes part in the formation of a liquid phase, the high-temperature mechanical properties are expected to be improved, because ZrO_2 increases the transition temperature of the resulting glassy phase. Metal oxides such as Y_2O_3 and MgO function not only as sintering additives but also stabilize ZrO_2 if they enter the ZrO_2 lattice during sintering.

Although microwave sintering of Si_3N_4 has been previously researched by several groups,[20-22] a detailed microstructural analysis is not commonly found in the literature. The purpose of this work was to characterize microwave-sintered Si_3N_4 with ZrO_2 as secondary particulates, primarily using Transmission Electron Microscopy (TEM).

4.2 Experimental Procedure

Samples were prepared from α-Si_3N_4 powder (Grade E-l0, UBE Industries Ltd., Yamaguchi, Japan), with additions of 6 wt% Y_2O_3 (Aldrich Chemical Company Inc., Milwaukee, WI, 99.99%), 4 wt% MgO (Aldrich Chemical Company Inc., Mil-waukee, WI, 99.99%), and 2.5 wt% TZ3Y (3 mole% Y_2O_3 stabilized ZrO_2, Tosoh Corporation, Tokyo, Japan, 99.99%). The powders were ball milled in de-ionized water for 12 h using ZrO_2 milling media, dried, and sieved through a 75 μm screen. Cylindrical green pellets with a 23 mm diameter and 5 mm thickness were formed by dry pressing at 30 MPa and then cold isostatically pressing at 200 MPa. Samples were sintered in a Si_3N_4 powder bed at l650°C using a 2.45 GHz microwave oven with a variable power output of 3 kW maximum, using 0.1 MPa nitrogen gas pressure. The microwave setup included an alumina fiber-board insulation box, a BN crucible, and SiC susceptor. The sintering cycle involved a heating rate of 50°C/min and a hold for 15 minute l650°C. Following the holding period, the oven was shut off and samples were allowed to cool slowly. The sample surface temperature was automatically recorded using a computer-controlled two-color pyrometer. The sintered density was determined using the Archimedes principle, with deionized water.

Specimens for TEM analysis were made using a tripod polishing procedure. The microwave-sintered Si_3N_4 materials were cut, mechanically ground, and polished until optical fringes could be observed by reflected optical microscopy (Reichert Jung Polyvar-Met, Wien, Austria), and were then Ar ion milled to electron transparency using a Gatan 600 Dual Ion Beam Mill (Gatan Inc., Pleasanton, CA). Sample microstructures were analyzed using a JEOL JEM-2000FX TEM (JEOL, Tokyo, Japan) with a LaB_6 filament, operating at 200 kV. Phase identifications were made by selected area diffraction (SAD), and chemical information was obtained using a Princeton Gamma-Tech energy-dispersive X-ray spectrometer PGT, (Princeton, NJ). In order to better identify low atomic number elements such as O and N, a manual variation of accelerating voltages (200 and 80 kV) was used. The defaulted EDS spectra in the TEM were collected at an accelerating of voltage of 200 kV. The relative concentrations of additives were evaluated using the intensity ratio of the Y (Lα), Zr (Lα), and Mg (Kα) peaks to the Si (Kα) peak without background subtraction.

4.3 Results and Discussion

A typical bright-field TEM image of the microwave sintered Si_3N_4 is shown in Figure 4.1. Elongated grains with high aspect ratio are randomly distributed in the fine-grain matrix, showing a duplex microstructure. The diameter of the fine grains is about 500 nm, while the elongated grains reached up to several micrometers in length. Secondary phases are located at the multigrain junction points and grain boundaries. Phase inclusions, as indicated by arrows, are also present. Owing to their high atomic numbers, ZrO_2 particulates (as indicated by "Z" in Figure 4.1) show dark contrast among the fine Si_3N_4 grain matrix and on the grain boundaries, which has been confirmed by further analysis.

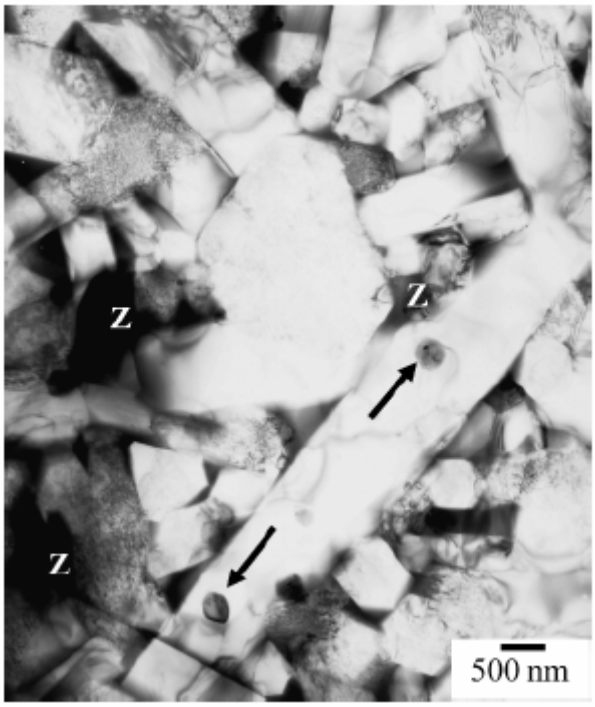

Figure 4.1. Typical bright field transmission electron microscopy image of the microwave-sintered Si_3N_4.

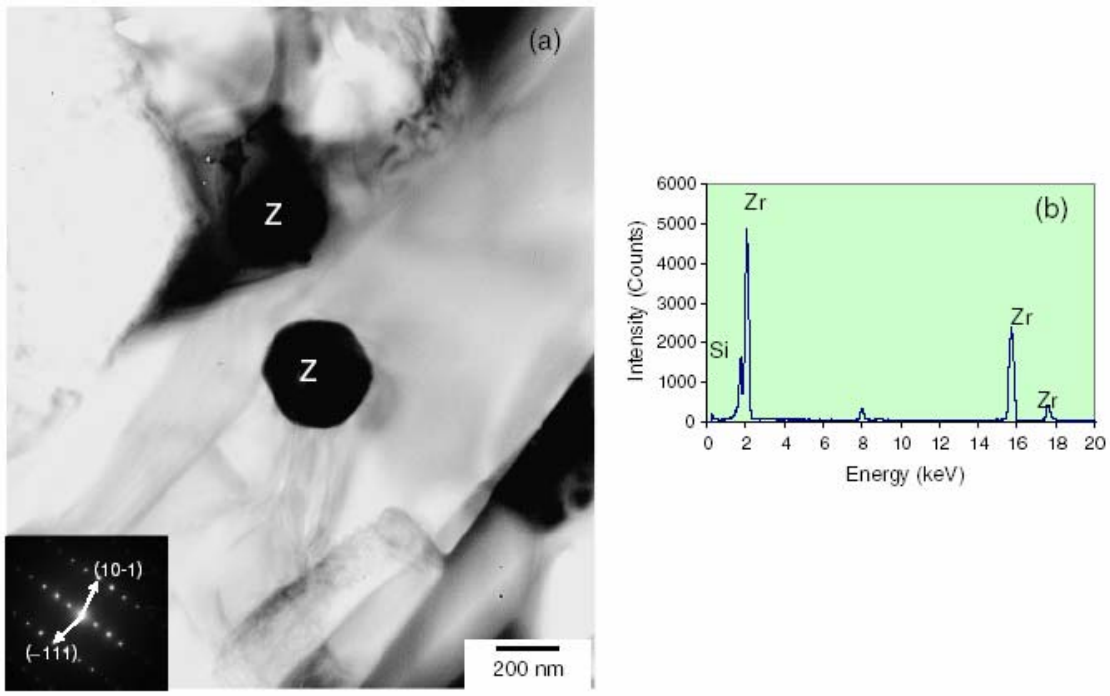

Figure 4.2a. Bright field image showing the β-Si_3N_4 grain confirmed by the selected-area electron diffraction pattern inset on the bottom-left corner; (b) energy-dispersive X-ray spectrometer spectrum for the dispersed ZrO_2 grain.

Figure 4.2a shows a typical second phase included in an elongated Si_3N_4 grain. The grain size of the second phase is about 200 nm. The chemical composition of the inclusion analyzed by EDS mainly includes Zr and Si, as shown in Figure 4.2b. The Si peak might be generated from the Si_3N_4 grain. Another Zr-rich particulate surrounded by the glassy phase is located at a triple-junction point. The crystallite with Zr-rich inclusions is β-Si_3N_4, as confirmed by the SAD pattern along the [101] zone axis inset in Figure 4.2a. Based on the above analysis, it is deduced that the addition of ZrO_2 as secondary particulates improves the microwave heating efficiency when sintering Si_3N_4.

It has been extensively researched that ZrO_2 particulates function as toughening and strengthening agents in hot-pressed, hot-isostatic-pressed, and pressureless-sintered Si_3N_4. One of the objectives of the present work was to determine whether a dispersion of ZrO_2 particulates would toughen microwave-sintered Si_3N_4. Figure 4.3a displays a BF-TEM image showing a typical Zr-rich particle in the Si_3N_4 matrix. The SAD pattern of the Zr-rich grain is inset on the bottom-left comer of Figure 4.3a. The Miller indices in this pattern refer to the cubic fluorite structure as indicated by an arrow in the BF

image. The chemical constituents of the grain, as analyzed by EDS, are shown in Figure 4.3b. The areas used for EDS analysis are indicated by letters "A" and "B" in Figure 4.3a. As expected, the particulate is a Zr-rich grain with small amounts of impurities such as Si and Mg. As the grain was much larger than the electron beam's spot size (about 20 nm), the Si peak was unlikely to be generated from the Si_3N_4 matrix.

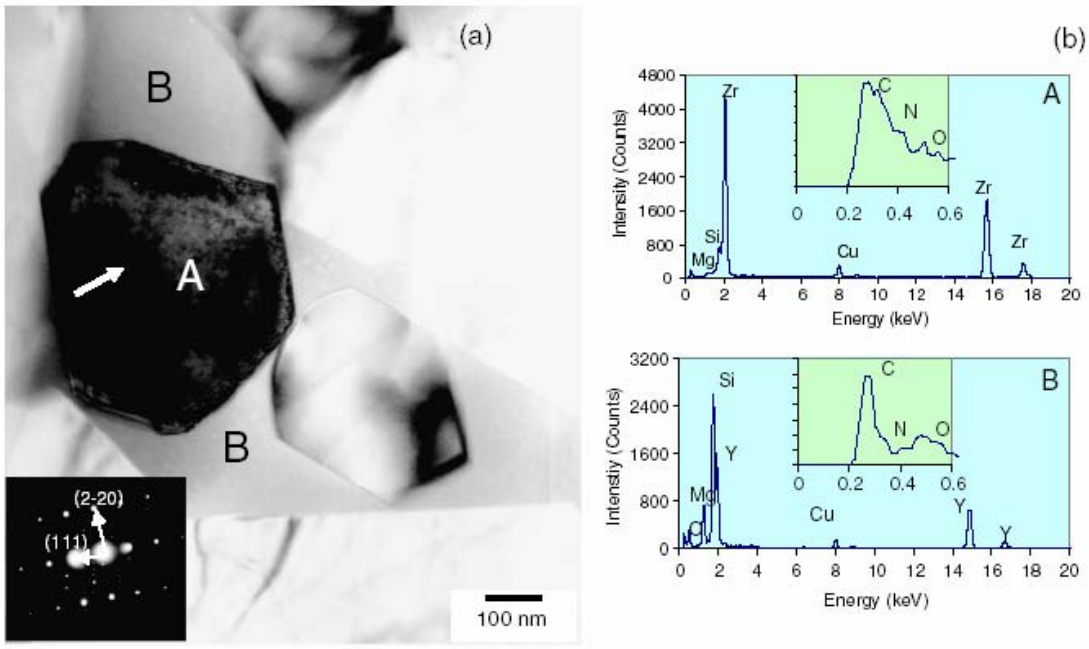

Figure 4.3a. Bright field image exhibiting a large ZrO_2 particulate dispersed in the Si_3N_4 matrix. Incommensurate diffraction spots are observed in the selected-area electron diffraction pattern of the ZrO_2 grain. The Miller indices refer to cubic fluoride. (b) Energy-dispersive X-ray spectrometer (EDS) spectrum for the areas labeled ‘‘A’’ and ‘‘B’’ in (a). The inset EDS spectra were collected at a beam energy of 80 keV.

The areas indicated by "B" are glassy phases containing elements Si-Mg-Y, as shown in Figure 4.3b. Yttria is another type of stabilizing agent for ZrO_2, but no detectable amount was found in the Zr-rich grain, as shown in Figure 4.3b even though it is surrounded by a Si-Mg-Y glassy phase. The small inset EDS spectra in Figure 4.3b were collected at 80 kV. Both N and O peaks show up in these spectra from both areas A and B. The incommensurate spots in the SAD pattern and N and Si peaks in the EDS spectrum strongly suggest that the grain is a tetragonal Zr- oxynitride phase, which was formed by the reaction of ZrO_2 with Si_3N_4 or the oxynitride glassy phases. Figure 4.4a shows a BF TEM image showing another Zr-rich grain. No incommensurate diffraction

spots are observed in the SAD pattern inset in Figure 4.4a. It is a cubic phase. The elements in the grain as detected by EDS are Zr-Si-O-N; as shown in Figure 4.4b.

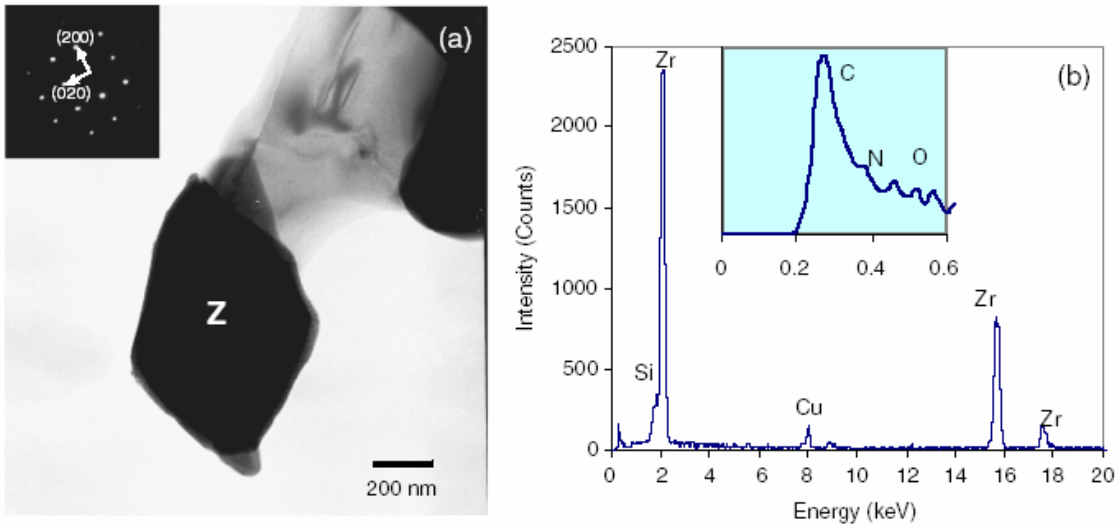

Figure 4.4a. Bright field image showing a Zr-rich grain. It is cubic, as confrmed by the inset selected-area electron diffraction pattern. (b) Energy-dispersive X-ray spectrometer (EDS) spectrum of the Zr-rich grain. The inset EDS spectrum was collected at a beam energy of 80 keV.

It is interesting to find that, unlike the Zr-rich grain in Figure 4.3a, no Mg was detected. It was apparent that the Si peak always shows up in the Zr-rich grains in this work. The detected Si in Zr-rich grains was also reported by several other research groups studying conventionally-sintered systems. Kleebe *et al.*[23] assumed that these precipitates represented a solid solution of $Zr_{1-x}Si_xO_2$. In the present study, the results suggest that the Si peak is not artificial. Although the starting ZrO_2 particulates were monoclinic phases, they appear to have been partially or fully stabilized by N or Mg dependent on the degree of the reaction. The cubic Zr-rich phase (Figure 4.4) with the absence of cation (such as Mg) substitution most likely arose from nitrogen stabilization. On the other hand, the theory of N-stabilizing ZrO_2 can be used to interpret that the Zr-rich grain (Figure 4.5)

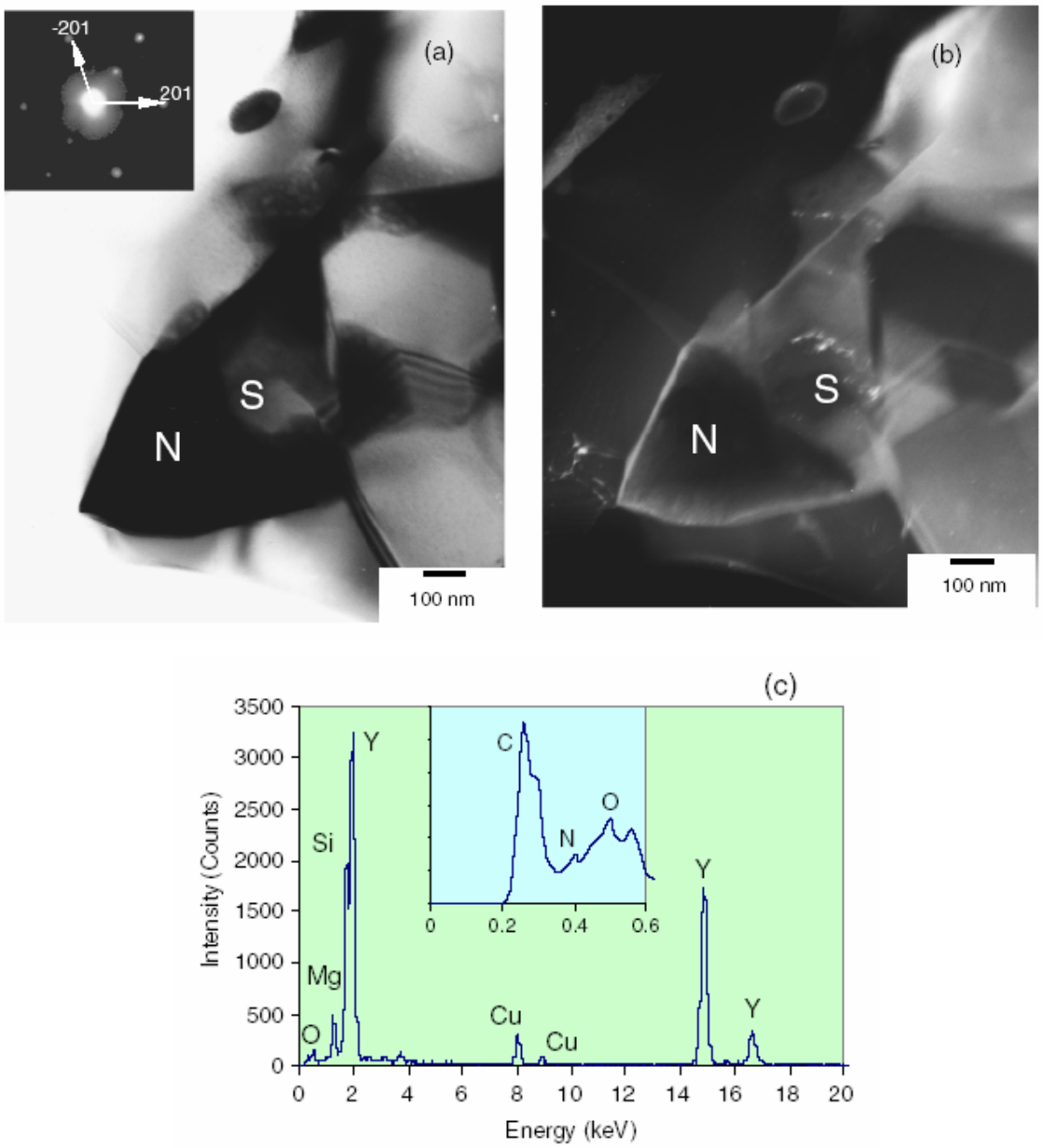

Figure 4.5a. Bright field image showing a crystallized multigrain junction phase labeled ''N.'' It is N-Melilite, as identifed by the selected-area electron diffraction inset in this Figure. The grain labeled ''S'' is Si_3N_4. (b) Diffused dark field image of (a). (c) Energy-dispersive X-ray spectrometer (EDS) spectra of the area labeled ''N.'' The inset EDS spectrum was collected at a beam energy of 80 keV.

with a cation stabilizer is a tetragonal phase instead of cubic. Lange *et al.*[24] showed that pre-existence of anion vacancies caused by aliovalent cation substitutions could preclude or decrease the influence of nitrogen in stabilizing zirconia. N-stabilizing ZrO_2 has been reported by many research groups.[25] Claussen claimed that monoclinic ZrO_2 is stabilized

as a cubic phase at room temperature when ZrO_2 is reacted with various metallic nitrides in a nitrogen atmosphere. However, N_2 is too stable to function as a vehicle for the supply of atomic nitrogen, because no cubic phase is found when un-doped ZrO_2 is annealed in a nitrogen environment. Non-transformable tetragonal ZrO_2 was also observed in hot-pressed Si_3N_4-ZrO_2 ceramics.[25] However, un-stabilized ZrO_2 appeared as a monoclinic phase at room temperature in the sintered reaction-bonded Si_3N_4.[26] Based on the experimental data, the ZrO_2 phase transformation toughening of Si_3N_4 is not expected in this system because of the reaction with Si_3N_4. The addition of ZrO_2 to Si_3N_4 in the samples analyzed for this work was found to improve the toughness moderately. Moderate improvement is most likely associated with other mechanisms, such as crack bridging and weak interfaces.

Finally, residual secondary phases at the grain boundaries and triple pockets were analyzed using TEM-EDS. A crystallized second phase labeled "N" at the triple pocket is shown in the BF TEM image Figure 4.5a. Figure 4.5b shows the diffused dark-field (DDF) image of the same area. The SAD pattern inset in Figure 4.5a confirmed that the second phase has an N-Melilite ($Y_2Si_3N_4O_3$) structure. The BF and DDF images indicate that the N-Melilite phase was formed by precipitation or crystallization from glassy phases on cooling. The chemistry of the N-Melilite phase as analyzed by EDS, shown in Figure 4.5c, is Y-Si-Mg-O-N. Figure 4.6a is a BF TEM image showing the distribution of residual glassy phases. Figure 4.6b displays results from EDS point-by-point analysis, corresponding to areas (or points) displayed in Figure 6a. As displayed in Figure 4.6b the area labeled "A" mainly contains Si-Mg-Y oxynitride, similar to the area labeled "B" in Figure 6a except that Zr peaks have been detected in area "B." It is apparent that both Y_2O_3 and MgO have formed liquid phases and filled into the intergranular gaps during the sintering process, and that Si_3N_4 has dissolved into these liquid phases.

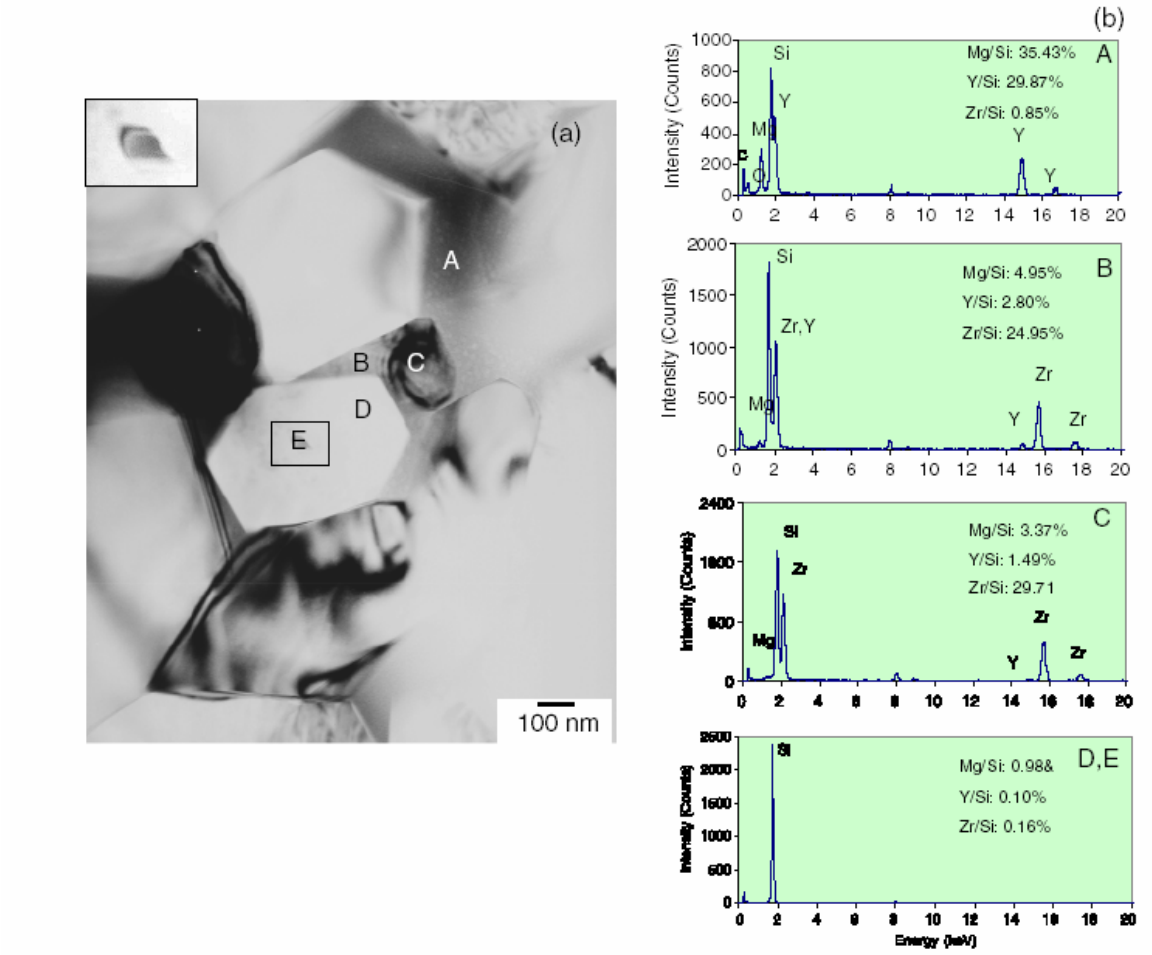

Figure 4.6a. Bright field image showing the distribution of the remnant glassy phase. Enlargement of the ‘‘core-rim’’ structure is displayed in a square inset on the top-left corner; (b) Energy-dispersive X-ray spectrometer point-by-point analysis for areas in (a). The appearances of Y/Si and Zr/Si in areas labeled ‘‘D’’ and ‘‘E’’ were from the background noise.

A non-isothermal microwave effect due to preferential heating of Y_2O_3 and MgO could be responsible for the enhanced densification. As shown in Figure 4.6b, these Si-rich glassy phases suggest that microwave heating enhanced the dissolution of α-Si_3N_4. However, not all of the high-temperature liquid phases devitrified to form β-Si_3N_4 rims during the cooling process, and thus may lead to the fine grains observed in this system. Microwave sintering that, results in a fine grain size has been reported.[27] Previous research reported that the α→β phase transformation in microwave-sintered Si_3N_4 was completed at a much earlier stage than observed for conventionally-sintered samples,[18]

but the absolute quantities of β-Si_3N_4 in both samples are still uncertain. Further research is needed to determine whether microwave processing enhances the formation of β-Si_3N_4. The grain labeled "C" in Figure 4.6a is Zr rich. Zr peaks found in the area labeled "B" are absent in the region labeled "A," indicating that ZrO_2 was dissolved only in the local area. Unlike Y_2O_3 and MgO, ZrO_2 particulates were not fully vitrified in the matrix, because they are more refractory. The results show that the addition of ZrO_2 improved densification but was not abundant in the glassy phase, unlike Y_2O_3 and MgO. ZrO_2 has played a similar role in the densification of hot-pressed Si_3N_4 systems.

The grain labeled "D" in Figure 4.6a shows a "core-rim" structure. The enlargement of the core is displayed as a square inset on the top-left corner of the figure. The chemical compositions of the core and rim are similar, as shown in Figure 4.6b. No artificial peaks such as Y-Mg-O have been detected, because EDS in TEM has a higher spatial resolution. The thin amorphous intergranular films between Si_3N_4 grains (homophase boundaries) were examined using DDF imaging. Figure 4.7 shows typical homophase boundaries oriented edge on with respect to the electron beam, revealing a thin film of about 3.4 nm. Using the same imaging technique, Cinibulk *et al*.[8] showed an average value of 3 nm for the intergranular film width in a gas-pressure-sintered Si_3N_4 with Y_2O_3 and MgO. It is very important to consider the formation of liquid phases during the sintering of S_3N_4-based materials. The conventional opinion is that liquid phases are formed due to the reaction of additives with SiO_2, and the SiO_2 is invariably introduced as a surface oxidation layer. This may be true; however, the availability of SiO_2 in the present system was limited, because the starting powders contained less than 1.4 wt% oxygen, and the green pellets were sintered in a N_2 atmosphere.

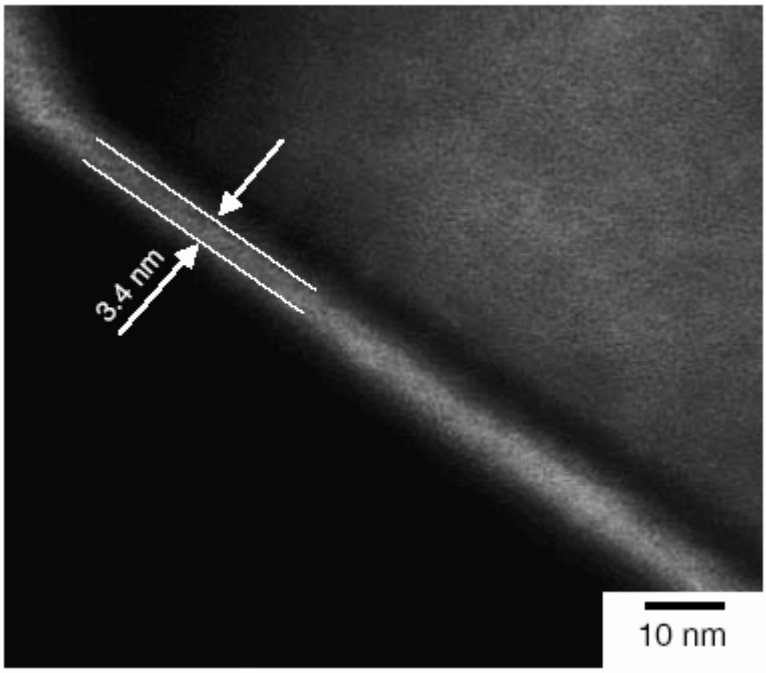

Figure 4.7. Diffused dark field (DDF) image of typical homophase boundaries oriented edge-on with respect to the electron beam.

The Si species found in the residual glassy phases most likely derived from β-Si_3N_4. Moreover, the final crystal phases are β-Si_3N_4, N-Melilite ($Y_2Si_3O_3N_4$), as well as Zr-rich phases. The compatibility of Si_3N_4 with N-Melilite is shown on the Si_3N_4-Y_2O_3 side of the SiO_2-Si_3N_4-Y_2O_3 phase triangle.[29] No other binary phases, such as $Y_2Si_2O_7$ and Si_2N_2O or ternary phases, such as ($4Y_2O_3$-SiO_2-Si_3N_4), were identified in this system, suggesting that the effect of silica on the formation of glassy phases is negligible. Based on the above analysis, the liquid phases are mainly formed through the reaction of MgO, Y_2O_3, and α-Si_3N_4. With more and more α-Si_3N_4 dissolving into the liquid phase, β-Si_3N_4 would be the first precipitated crystalline phase. On cooling, β-Si_3N_4 and N-Melilite phases appeared to have co-precipitated until the melts solidified. It is noteworthy that the residual glassy phases have a higher Si/Y ratio than the N-Melilite phase, as shown in Figure 4.5c and 4.6b.

4.4 Conclusions

The microstructure of a microwave-sintered Si_3N_4-Y_2O_3-MgO system with ZrO_2 as secondary particulates was analyzed using TEM-EDS. TEM shows that the final crystalline phases are mainly β-Si_3N_4 with a minor amount of N-Melilite. N-Melilite was formed by crystallization at the multigrain junctions. TEM micrographs reveal about 13 vol% Si-Y-Mg-O-N secondary phases located on the grain boundaries or multigrain junctions. The existence of ZrO_2 particulates improved the microwave heating efficiency and enhanced densification. However, there appeared to be minor dissolution of ZrO_2 in the oxynitride liquid during sintering. Both tetragonal and cubic Zr-rich phases were identified by SAD, which supports the existence of N-stabilized ZrO_2. Moreover sintering favored the formation of the Si-Mg-Y oxynitride liquid phase and thus enhanced the dissolution of α-Si_3N_4. The thickness of a homophase boundary is 3.4 nm as observed by DDF imaging.

4.5 References

1. P.F. Becher, "Microstructural Design of Toughened Ceramics," *J. Am. Ceram. Soc.*, **74** [2] 255-69 (1991).

2. M. Krämer, M.J. Hoffmann, and G. Petzow, "Grain Growth Studies of Silicon Nitride Dispersed in an Oxynitride Glass." *J. Am. Ceram. Soc.*, **76** [11] 2778-84 (1993).

3. L.L Wang, T.Y Tien, and I.W Cheng, "Morphology of Silicon Nitride Grown from a Liquid Phase," *J. Am. Ceram. Soc.*, **81** [10] 2677-86 (1998).

4. M. Kitayama, K. Hirao, M. Toriyama, and S. Kanzaki, "Comment on "Morphology of Silicon Nitride Grown from a Liquid Phase," *J. Am. Ceram. Soc.*, **83** [3] 675-76 (2000).

5. J. Kleebe, G. Pezzotti, and G. Ziegler, "Microstructure and Fracture Toughness of Si_3N_4 Ceramics: Combined Roles of Grain Morphology and Secondary Phase Chemistry," *J. Am. Ceram. Soc.*, **82** [7] 1857-67 (1999).

6. D.R. Clarke, "On the Equilibrium Thickness of Intergranular Glass Phases in Ceramic Materials," *J. Am. Ceram. Soc.*, **70** [1] 15-22 (1987).

7. H.J. Kleebe, M.K. Cinibulk, R.M. Cannon, and M. Rimle, "Statistical Analysis of the Intergranular Film Thickness in Silicon Nitride Ceramics," *J. Am. Ceram. Soc.,* **76** [8] 1969-77 (1993).

8. M.K. Cinibulk, H.J. Keebe, and M. Rimle, "Quantitative Comparison of TEM Techniques for Determining Amorphous Intergranular Film Thickness," *J. Am. Ceram. Soc.,* **76** [2] 426-32 (1993).

9. R. Tanaka, H.J. KIeebe, M.K. Cinibulk, J. Bruley, D.R. Clarke, and M. Rimle, "Calcium Concentration Dependence of the Intergranular Film Thickness in Silicon Nitride," *J. Am. Ceram. Soc.,* **77** [4] 911-14 (1994).

10. H. Gu, X. Pan, R.M. Cannon, and M. Rimle, "Dopant Distribution in Grain-Boundary Films in Calcia-Doped Silicon Nitride Ceramics," *J. Am. Ceram. Soc.,* **81** [12] 3125-35 (1998).

11. A. Tanaka, K. Igashira, H.J. Kleebe, and M. Riihle, "High-Temperature Strength of Fluorine-Doped Silicon Nitride," *J. Am. Ceram. Soc*., **77** [1] 275-77 (1994).

12. G. Pezzotti, K. Ota, and H.J. Kleebe, "Grain-Boundary Relaxation in High-Purity Silicon Nitride," *J. Am. Ceram. Soc*., **79** [9] 2237-46 (1996).

13. G. Pezzotti, K. Ota, and H.J. Kleebe, "Viscous Slip along Grain Boundaries in Chlorine-Doped Silicon Nitride," *J. Am. Ceram. Soc*., **80** [9] 2341-8 (1997).

14. J. Kleebe and G. Pezzotti, "Grain-Boundary Wetting-Dewetting in z = I SiAlON Cerarnic," *J. Am. Ceram. Soc*., **85** [12] 3049-53 (2002).

15. I. Tsuge, K. Nishida, and M. Komatsu, "Effect of Crystallizing the Grain-Boundary Glass Phase on the High-Temperature Strength of Hot-Press Si_3N_4 Containing Y_2O_3," *J. Am. Ceram. Soc*., **58** [7-8] 323-26 (1975).

16. D.R. Clarke, F.F. Lange, and G.D. Schnittgrund, "Strengthening of a Sintered Silicon Nitride by a Post-Fabrication Heat Treatment," *J. Am. Ceram. Soc*., **65** [4] C-51-2 (1982).

17. G. Xu, H. Zhuang, W. Li, and F. Wu, "Microwave Sintering of α/β-Si_3N_4," *J. Eur. Ceram. Soc.*, **17** [8] 977-81 (1997).

18. Y.C. Kim, C.H. Kim, and D.K. Kim, "Effect of Microwave Heating on Densification and α→β Phase Transformation of Silicon Nitride," *J. Eur. Ceram. Soc.*, **17** [13] 1625-1630 (1997).

19. N. Claussen and J. Jahn, “Mechanical Properties of Sintered and Hot-Pressed Si_3N_4-ZrO_2 Composites,” *J. Am. Ceram. Soc.*, **61** [1-2] 94-95 (1978).

20. J.J. Thomas, R.J. Christensen, D.L. Johnson, and H.M. Jennings, “Nonisothermal Microwave Processing of Reaction-Bonded Silicon Nitride,” *J. Am. Ceram. Soc.*, **76** [5] 1384-86 (1993).

21. M.J. Jones, M.C. Valecillos, K. Hirao, and M. Toriyama, “Densification Behavior in Microwave-Sintered Silicon Nitride at 28 GHz,” *J. Am. Ceram. Soc.,* **84** [10] 2424-26 (2001).

22. D.L. Johnson, “Microwave Heating of Grain Boundaries in Ceramics,” *J. Am. Ceram. Soc*., **74** [4] 849-50 (1991).

23. H.J. Kleebe, W. Braue, and W. Luxem, "Densification Studies of SRBSN with Unstabilized Zirconia by Means of Dilatometry and Electron Microscopy," *J. Mater. Sci.,* **29** [5] 1265-75 (1994).

24. F.F. Lange, L.K.L. Falk, and B.I. Davis, “Structural Ceramics Based on Si_3N_4-ZrO_2 (+Y_2O_3) Compositions,” *J. Mater. Res*., **2** [1] 66-76 (1987).

25. L.K.L. Falk, and K. Rundgren, “Microstructure and Short-Term Oxidation of Hot-Pressed Si_3N_4/ZrO_2 (Y_2O_3) Ceramics,” *J. Am. Ceram. Soc*., **75** [1] 28-35 (1992).

26. H.J. Kleebe, W. Braue, H. Schmidt, G. Pezzotti, and G. Ziegler, "Transmission Electron Microscopy of Microstructures in Ceramic Materials," *J. Eur. Ceram. Soc.,* **16** [3] 339-51 (1996).

27. K.P. Plucknett and D.S. Wilkinson, "Microstructural Characterization of a Microwave-Sintered Silicon Nitride Based Ceramics," *J. Mater. Res*., **10** [6] 1387- 96 (1995).

28. M.N. Rahaman, *Ceramic Processing and Sintering*; pp. 673-76. Marcel Dekker, New York, 1995.

Chapter 5

Grain Morphology and Mechanical Properties

Abstract

The influence of various amounts of ZrO_2 as a secondary additive on the grain morphology and mechanical properties of microwave sintered Si_3N_4 with Y_2O_3 and MgO sintering aids has been investigated. The microstructures were correlated to mechanical properties. Microwave and conventionally sintered sample results were compared. ZrO_2 additions improved Vickers hardness; however, no significant variation in the fracture toughness was observed despite differences in microstructure. Overall, microwave sintered samples had a higher Vickers hardness, similar fracture toughness, finer grain microstructure structure and a narrower grain size distribution when compared to conventionally sintered samples. The addition of 2.5 % ZrO_2 narrowed the grain size distribution further in the case of microwave sintering.

5.1. Introduction

For more than four decades, the understanding of processing-microstructure–properties relationship has contributed to the recent progress in the production of various types of silicon nitride ceramics.[1] Fracture toughness, hardness, and strength are the three major properties that many researchers have tried to improve.[2] Property control of Si_3N_4 has been difficult due to the relatively complex microstructure developed during densification by liquid-phase sintering and the complicated interrelationships between the size and shape of the silicon nitride grains, distribution of the grain boundary phase, and the mechanical properties.[3,4] The multi-phase microstructure of elongated β-Si_3N_4 crystals embedded in an amorphous or partially crystalline grain boundary provides a great opportunity to optimize material properties for specific applications. Therefore, a detailed understanding of microstructural development is required in order to achieve the demanding mechanical and thermal properties.

The key to obtaining a high-strength silicon nitride material is a nearly defect - free, fine-grain microstructure with a specific grain size distribution and aspect ratio. Attempts to improve strength have been centered on achieving the fine microstructure with minimum defects while maintaining moderate fracture toughness. Large elongated grains are preferred for high-toughness materials, since crack bridgin is the major toughening mechanism. Large grains are necessary but not sufficient by themselves for

high toughness.[5] Interfacial bonding force between grains and glass phase is another key factor, and thus the chemistry of grain the boundary phase is also important. Appropriate starting powders, compositions and sintering methods are required to optimize the microstructure and properties. For instance, grain growth is promoted by high-temperature sintering (gas pressure sintering) and selecting suitable sintering additives which promote grain-growth. On the other hand, low-temperature sintering and a (hipping) grain growth inhibitor is necessary to obtain high-strength materials.[6] The materials currently used for real applications have fracture toughnesses in the range of 5-7 $MPa \cdot m^{1/2}$ and flexural strengths of 700-1100 MPa.[7]

The major toughening mechanisms operative in silicon nitride are (a) crack bridging by larger elongated grains, (b) frictional translation of partially separated grains, (c) frictional pull out of elongated grains, and (d) inclined reinforcement bending.[5] By changing the angle where the crack plane intercepts the longitudinal surface of the β-Si_3N_4 whisker, the distance of the crack propagated along the interface (debond length) could be measured. It is easier to deflect the crack further up the interface as the angle of incidence decreases. The relative energy to de-bond the interface is related to the structure and chemistry of the interfaces as affected by the composition of the oxynitride glass matrix. The maximum angle of crack-plane incidence for interfacial debonding, increases with a decrease in the N_2 content of the oxynitride glass with an Al_2O_3-Y_2O_3 ratio of one. This reflects a decrease in the energy for interfacial debonding with the decreased N_2 content of this oxynitride glass. Decreasing the Al_2O_3-Y_2O_3 ratio of the glass decreases the interfacial debonding energy in oxynitride glass with a fixed N_2 content.

The second set of studies involved tailoring the additives used for liquid-phase sintering of Si_3N_4 to alter the thermal expansion coefficient and Young's modulus of the glassy grain-boundary phase.[8] With the relatively low thermal expansion coefficient of β-Si_3N_4, the grain-boundary glass phase is subjected to residual tensile stresses at room temperature. As a result, fracture in the glass near the interface may be promoted, leading to the development of bridging of elongated β-Si_3N_4 grains. The fracture toughness of Si_3N_4 ceramics is increased with an increase in the thermal expansion coefficient of the grain-boundary phase, as represented by the selection of the additive

composition.[8] Improvement of fracture toughness in Si_3N_4 can also be attained by the alignment of large elongated β-Si_3N_4 grains by tape casting raw powders seeded with rod-like β- Si_3N_4 particles. A fracture toughness of 12 MPa·$m^{1/2}$ and a bending strength of 1.4 GPa were achieved in the direction perpendicular to the grain alignment.[9]

M. Hirota et al.[10] sintered silicon nitride using 28 GHz microwave frequency and reported a fracture toughness of 9 MPa·$m^{1/2}$. There have been reports on the use of ZrO_2 as a second phase in Si_3N_4 ceramic matrix composites to improve their room temperature strength, fracture toughness, and oxidation resistance.[11-14] Although mechanical properties of Si_3N_4–ZrO_2 have been previously studied by many researchers, no detailed study has been reported in the literature about the use of ZrO_2 as a secondary additive in the context of microwave sintering. Thus, the objective of the present work was to study the effect of ZrO_2 secondary additives on the mechanical properties of microwave sintered Si_3N_4 ceramics. In this chapter, the results of grain size analysis and mechanical properties such as indentation fracture toughness and Vickers hardness of both microwave sintered Si_3N_4 are presented. Results from microwave-sintered samples were compared to conventionally-sintered samples.

5.2 Experimental Procedure

Silicon nitride samples were prepared by ball milling α-Si_3N_4 powder (E10 grade, UBE Industries Ltd., Yamaguchi, Japan) with Y_2O_3 (Aldrich Chemical Company Inc., Milwaukee, WI, 99.99%), MgO (Aldrich Chemical Company Inc., Milwaukee, WI, 99.99%), and TZ3Y (3 mole% Y_2O_3 stabilized ZrO_2, (Tosoh Corporation, Tokyo, Japan, 99.99%). Four different compositions were prepared for this study. (i) 90 wt% Si_3N_4, 4 wt% MgO and 6 wt% Y_2O_3 designated as SN1; ii) 87.5 wt% Si_3N_4 with 4 wt% MgO, 6 wt% Y_2O_3, and 2.5 wt% ZrO_2 designated as SN2; iii) 86 wt% Si_3N_4 with 4 wt% MgO, 6 wt% Y_2O_3, and 4 wt% ZrO_2 designated as SN3; iv) 85 wt% Si_3N_4 with 4 wt% MgO, 6 wt% Y_2O_3, and 5 wt% ZrO_2 designated as SN4. The powders were ball milled in de-ionized water for 12 hours using high-wear-resistant ZrO_2 milling media (YTZ Grinding Media, Tosoh Corporation, Tokyo, Japan). Milled powders were dried, ground and sieved through a 75 micron mesh. Five grams of mixed powder were uniaxially die-

pressed at 30 MPa and then cold isostatically pressed at 200 MPa to form cylindrical green pellets of diameter 23 mm and thickness of 5 mm.

Microwave sintering was performed at 1650°C, 1700°C and 1750°C (the corrected temperatures based on numerical modeling results discussed in Chapter 2) at 0.1 MPa nitrogen pressure in an industrial microwave furnace having variable output power of 3 kW maximum. The heating rate was manually controlled with the aid of a computer, at 50°C/min, prior to the holding period at the peak temperature. Samples were allowed to cool to ambient temperature in the applicator. Conventional sintering of the samples was performed in a Centorr vacuum furnace with tungsten heating elements at 1650°C, 1700°C and 1750°C with a heating rate of 10°C/min. A green pellet was embedded in a Si_3N_4 powder bed contained in a BN crucible and sintered in continuously flowing nitrogen gas at 0.1 MPa.

The microstructures were evaluated from diamond polished and CF_4 plasma etched samples using Ceramic and Metals Divisions, ORNL, Oak Ridge, TN's facilities. Crystalline phases were identified using X-ray diffraction (XRD). The same specimens were used to measure Vickers indentation fracture toughness, under a load of 98N, using the equation of Antis et al:

$$K_c = 0.016\left(\frac{E}{H}\right)\left(\frac{P}{c^{3/2}}\right) \qquad (5.1)$$

where E is the Young's modulus, H is the hardness, P is the peak load and c is the crack length. The crack lengths were measured using optical microscope after making indents on the samples.

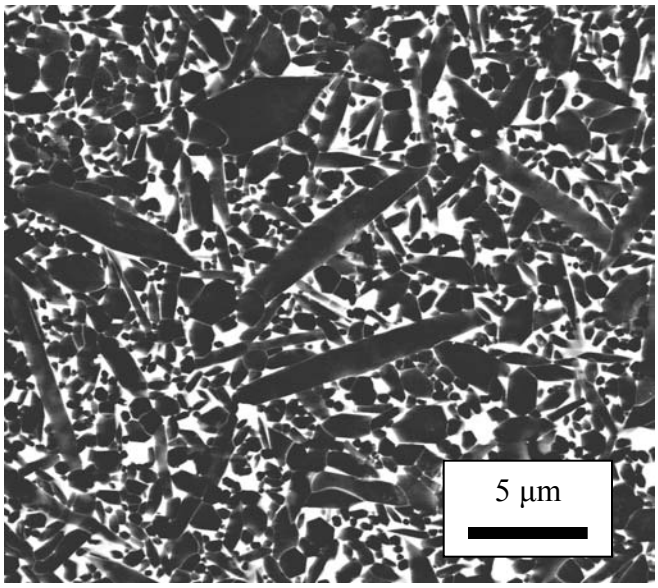

Figure 5.1 Example of a SEM micrograph (85 wt% Si_3N_4 with 4 wt% MgO, 6 wt% Y_2O_3, and 5 wt% ZrO_2, microwave sintered at 1750°C for 15 minutes) used for grain-size analysis.

Figure 5.1 shows one of the SEM micrographs used for grain-size analysis in the present study. Enlarged SEM micrographs were used to manually measure the length and width of individual grains by marking grain boundaries prior to measurement. These measurements were used for determination of the dimensional parameters which describe the individual β-Si_3N_4 grain morphology, such as length, width and aspect ratio. At least 2000 grains were measured for each sample to obtain reliable results. Since β-Si_3N_4 grains grow without impingement, they form ideal hexagonal prisms which can be characterized by length (L) and width (W). The width is defined as the distance between opposite but parallel planes and can be determined quiet accurately from arbitrary sectioned prisms, as shown in Figure 5.2. When the section is not parallel to the c-axis of the prism, the measured length is somewhat larger than the true length. Nevertheless, the error is small for aspect ratios larger than 2. In the present study, aspect ratio values more than 3 were used for plotting aspect ratios versus frequency % for silicon nitride samples containing various amounts of ZrO_2.

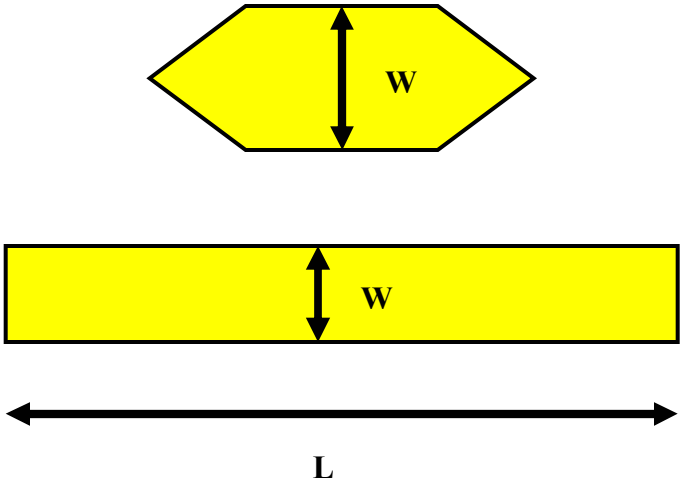

Figure 5.2 Grain size parameters as determined from specific grain sections.[15]

5.3 Results and Discussions

Figure 5.3 shows Vickers hardness values for microwave sintered Si_3N_4 samples containing 4 wt% MgO, 6 wt% Y_2O_3 and 0-5 wt% ZrO_2, as a function of temperature. In the case of samples sintered at 1650ºC for 15 minutes, the hardness increases with increasing ZrO_2 up to 2.5 wt% and thereafter decreases and again increases at 5 wt% ZrO_2. In contrast, at 1700ºC the hardness consistently increases with increasing ZrO_2 content. The sample sintered at 1750ºC shows an increase in hardness to 13 GPa when 2.5 wt% of ZrO_2 is added and similar hardness values at higher ZrO_2 levels. The ZrO_2 content had no significant effect on the hardness of conventionally-sintered samples regardless of the temperature, as shown in Table 5.1. The greater hardness of microwave- sintered samples is attributed to the finer grain microstructure (Figure 5.4.). Because of shorter sintering cycles and reduced thermal gradients, finer and uniform grain sizes can be obtained by microwave sintering. The greater uniformity in the microstructrue also results in reduced scatter in the mechanical properties.

Table 5.I Vickers Hardness and Fracture Toughness of Conventionally-Sintered Silicon Nitride Samples

Sample	VH (GPa)	Std.dev	FT(MP. $a^{1/2}$)	Std.Dev	E (GPa)
0wt%ZrO_2-1650	10.88	0.69	4.95	0.30	271
2.5wt%ZrO_2-1650	10.67	0.15	5.73	0.30	281
0wt%ZrO_2-1700	9.46	0.28	5.38	0.14	304
2.5wt%ZrO_2-1700	9.07	0.38	5.76	0.24	297
0wt%ZrO_2-1750	9.59	0.20	5.66	0.19	275
2.5wt%ZrO_2-1750	9.39	0.26	5.35	0.25	286

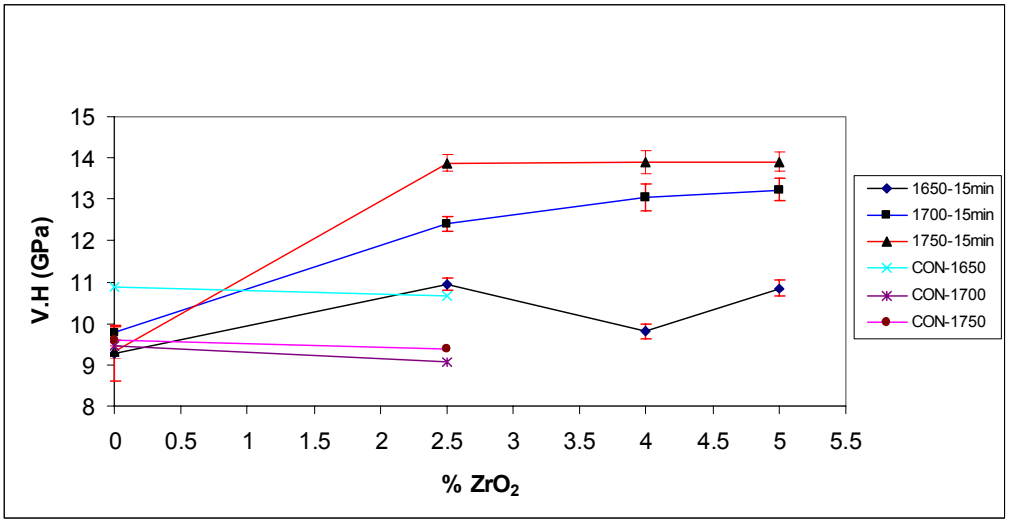

Figure 5.3. Vickers hardness of microwave sintered silicon nitride samples.

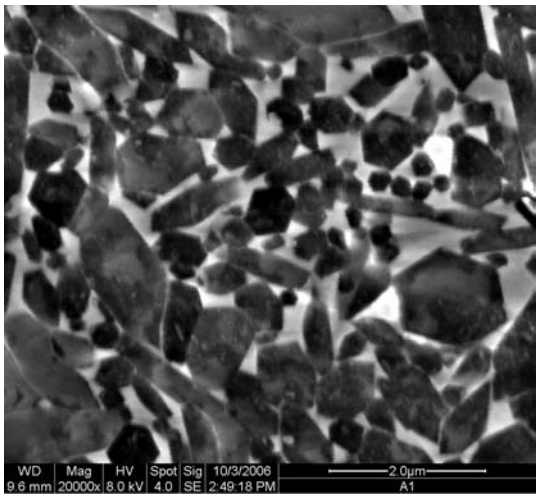

Figure 5.4 Fine grain-microstructure resulting from 85 wt% Si_3N_4 with 4 wt% MgO, 6 wt% Y_2O_3, and 5 wt% ZrO_2, microwave sintered at 1750°C for 15 minutes.

Figure 5.5 shows the indentation fracture toughness of microwave sintered samples at various temperatures, plotted as a function of ZrO_2 content. The overlapping error bars suggest ZrO_2 additions do not significantly influence the fracture toughness of both microwave and conventionally sintered samples.

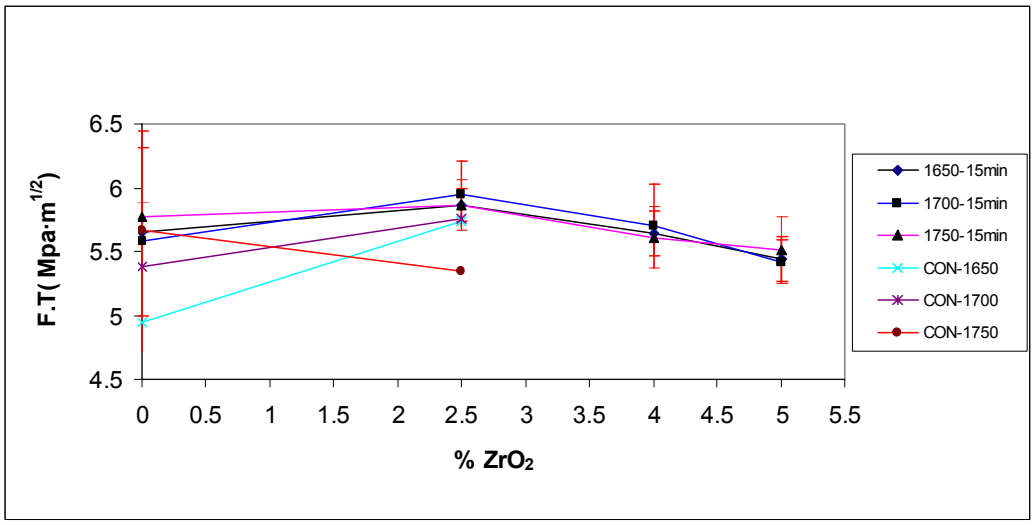

Figure 5.5. Fracture toughness of microwave-sintered silicon nitride samples.

Figure 5.6 shows the crack paths following Vickers indentation of Si_3N_4 samples SN1, SN2, SN3 and SN4, microwave sintered at three different temperatures, 1650ºC, 1700ºC and 1750ºC, respectively. The contribution from different toughening mechanisms will depend on the bonding strength between β-Si_3N_4 grains and the grain-boundary phase. A sufficiently weak boundary is a necessary requirement for bridging, pullout and crack deflection. Whether a crack propagates along an inclined β-Si_3N_4 grain boundary resulting in debonding, or through a β-Si_3N_4 grain, is dependent upon the ratio between the interface and the grain fracture energies, as well as the angle between the crack and the β-Si_3N_4 grains. It can be seen from this figure that the crack path is predominantly transgranular, with little crack deflection or interfacial debonding, thus implying strong bonding between the grain and grain-boundary glassy phase. Based on the results, it is deduced that despite the large β-Si_3N_4 grains, their effect on the fracture toughness is negligible, due to strong bonding between the grains and grain boundary.

A two factor statistical analysis of variance (Anova) was performed to study the effect of ZrO_2 on fracture toughness of conventional and microwave sintered samples. The Anova results indicated that ZrO_2 influenced the fracture toughness of microwave sintered samples, although the influence was very small. However, there was no significant influence of ZrO_2 in the case of conventional sintered samples as shown in the Anova computer results below.

Anova: Two-Factor Without Replication

SUMMARY	*Count*	*Sum*	*Average*	*Variance*
1650	2	10.68	5.34	0.3042
1700	2	11.14	5.57	0.0722
1750	2	11.01	5.505	0.04805
0	3	15.99	5.33	0.1279
2.5	3	16.84	5.613333	0.052233333

ANOVA

Source of Variation	*SS*	*df*	*MS*	*F*	*P-value*	*F crit*
Temperature	0.056233	2	0.028117	0.18495779	0.843912	19.00003
ZrO2 Wt%	0.120417	1	0.120417	0.792128056	0.467365	18.51276
Error	0.304033	2	0.152017			
Total	0.480683	5				

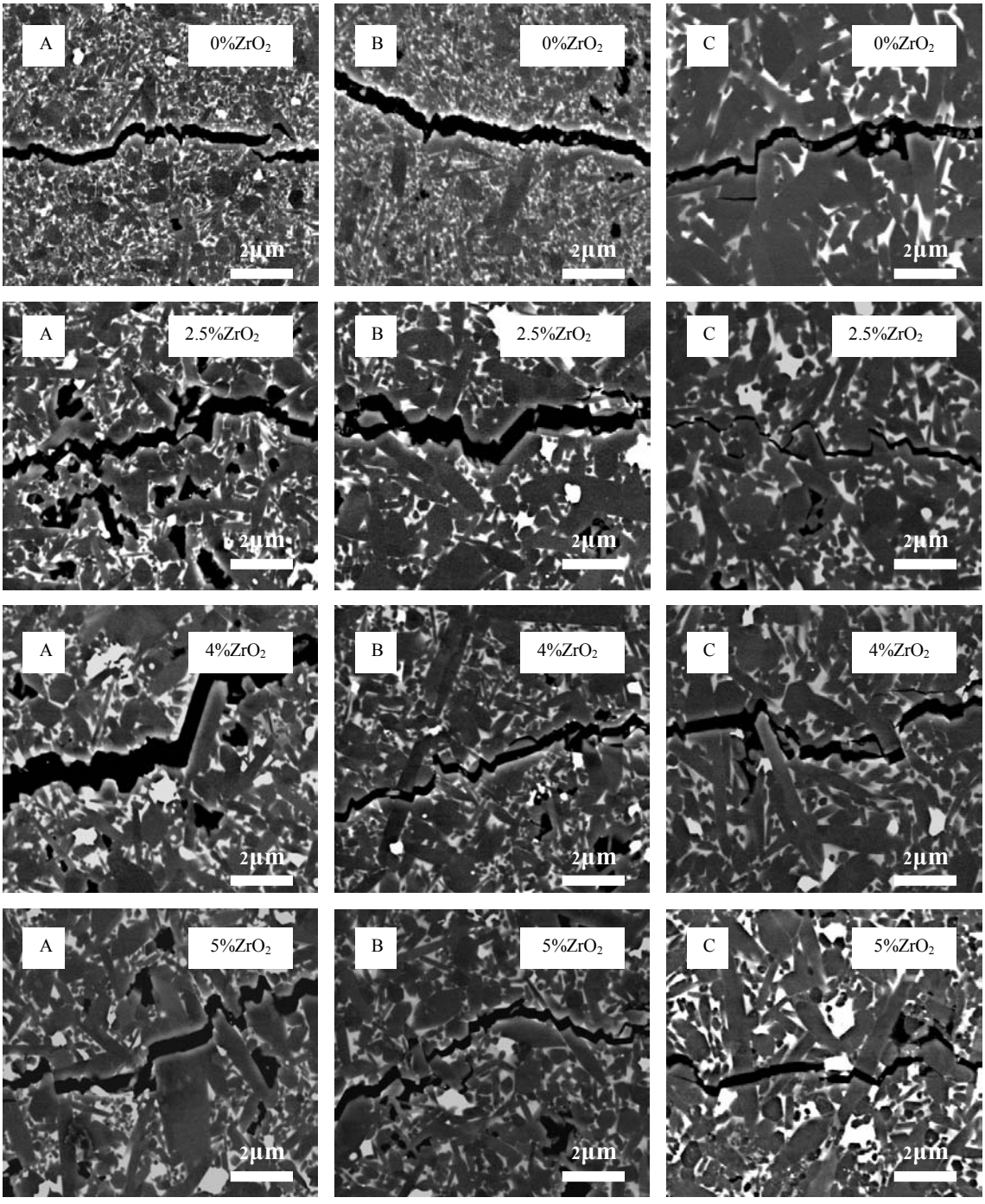

Figure 5.6. SEM images showing crack paths in microwave-sintered Si_3N_4 with MgO and Y_2O_3 as a function of ZrO_2 content (0 % ZrO_2 = SN1; 2.5 wt% ZrO_2 = SN2; 4 wt% ZrO_2 = SN3; and 5 wt% ZrO_2 = SN4) sintered at 1650ºC (A), 1700ºC (B) and 1750ºC (C) for 15 min in 0.1 MPa of nitrogen pressure.

The lower indentation fracture toughness of the samples is consistent with the argument that a smaller grain diameter would reduce toughening caused by crack deflection and bridging. The low fracture toughness of the samples is consistent with the crack-path observations from the SEM. Figure 5.7 shows the crack path following Vickers indentation of samples with compositions: (i) 90 wt% Si_3N_4 with 4 wt% MgO and 6 wt% Y_2O_3, designated as SN1, and ii) 87.5 wt% Si_3N_4 with 4 wt% MgO, 6 wt% Y_2O_3, and 2.5 wt% ZrO_2, designated as SN2. The samples were conventionally sintered at 1650ºC, 1700ºC and 1750ºC, respectively. Their crack paths reveal similar trends as previously observed in the microwave-sintered samples. Both transgranular and intergranular crack paths are evident.

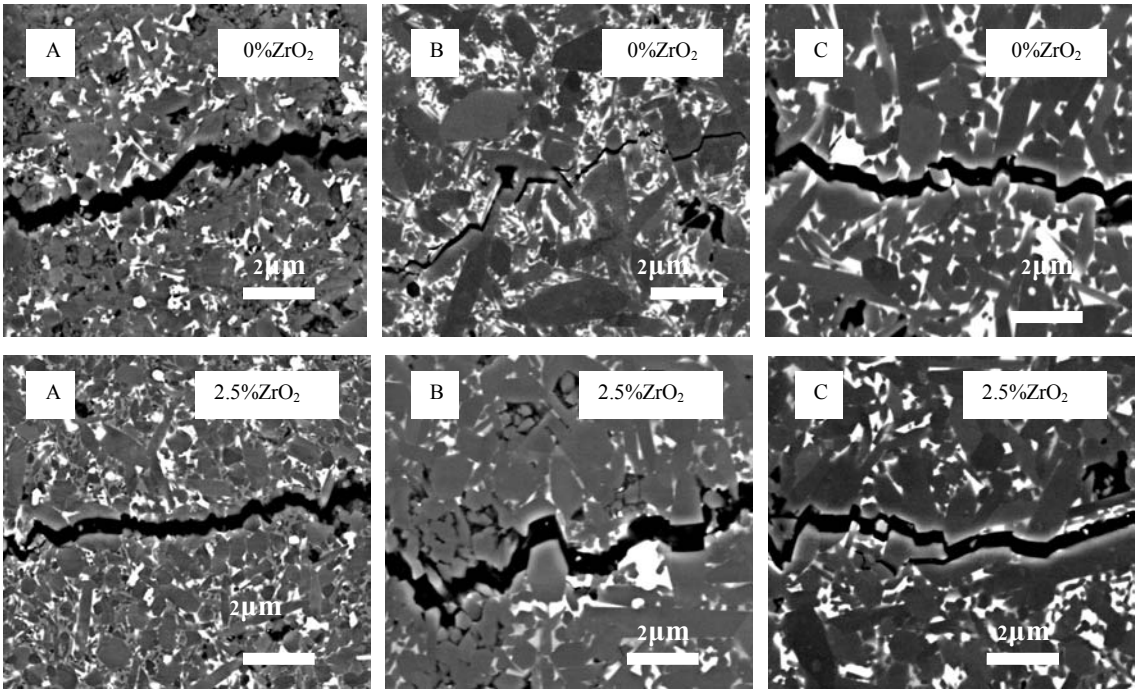

Figure 5.7. SEM images of conventionally-sintered Si_3N_4 with MgO and Y_2O_3 as a function of ZrO_2 content (0 wt% ZrO_2 = SN1; 2.5 wt% ZrO_2 = SN2) sintered at 1650ºC (A), 1700ºC (B) and 1750ºC (C) for 15 min in 0.1 MPa of nitrogen pressure.

Results of measured grain length, width and aspect ratios of microwave sintered samples with varying quantities of ZrO_2 are given in Figures 5.8-5.10. Grains were measured from ten enlarged SEM micrographs which were captured from different locations of the same sample. These measurements were used for determination of the two-dimensional parameters describing the individual β-Si_3N_4 grain morphology such as length, width and aspect ratio.

Figure 5.8 displays grain-length distributions of microwave-sintered samples at three different sintering temperatures. The blue, red, yellow and green color bars represent 0, 2.5, 4, and 5 wt% ZrO_2, respectively. At 1650ºC, 40% of grains in samples with less than 5 wt% ZrO_2 had a length of 1 μm. The percentage of 1 μm grains lowered to about 35% at 1700C. At 1750ºC, the sample that contains 0% ZrO_2 had two peaks (25%) with grains of 1 and 2 μm in length. The sample that contains 4 wt% ZrO_2 shows a larger number of 1 μm grains (35%) when compared to other samples at 1750ºC. All of the samples showed wider grain size distributions with grain length starting from 0.25 μm to 4.5 μm at all temperatures. These figures also show that less than 5% of the grains have a length greater than 3 μm.

Figure 5.9 shows grain-width distributions for microwave-sintered samples at three different temperatures. The sample with 0 % ZrO_2 had peaks at 0.25 μm and 0.75 μm, and all other samples had peaks at 0.25 μm and 0.50 μm. All samples exhibited a broad grain-width distribution at 1650ºC. With increasing sintering temperature, the grain width distribution narrowed and shifted towards the lower end of 0.25 μm, indicating a finer matrix of β-Si_3N_4 with reduced grain growth in the{100} prismatic crystal plane. In the case of the sample that contained 4 wt% ZrO_2, the number of grains increased from 39% to 69% when the sintering temperature increased from 1650ºC to 1750ºC. The experimental data clearly demonstrate, as expected, that the sintering temperature has a direct effect on the microstructure. At 1750ºC, the number of fine grains (0.25 μm) increased from 45% to 69% with increasing ZrO_2 addition from 0 wt% to 4 wt%, indicating it's possible to refine the microstructure by adding a lossy secondary additive. The maximum width of the grains is 1 μm.

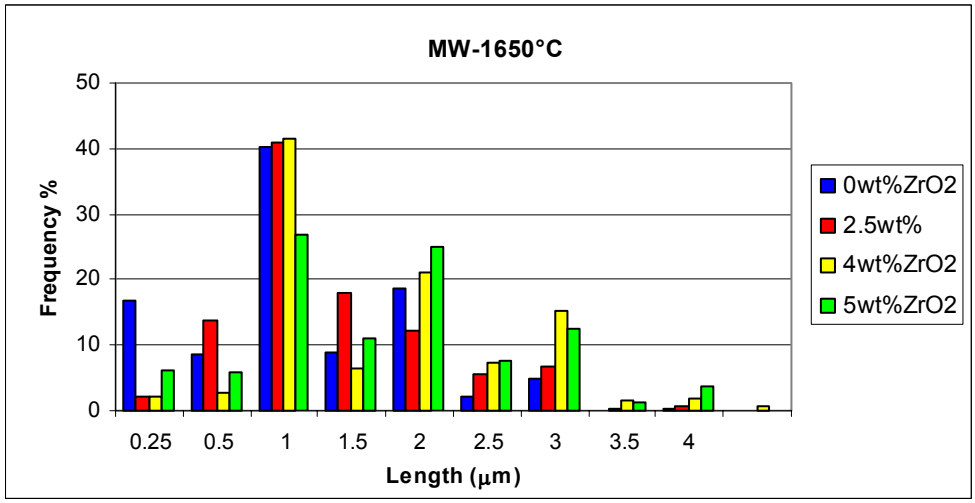

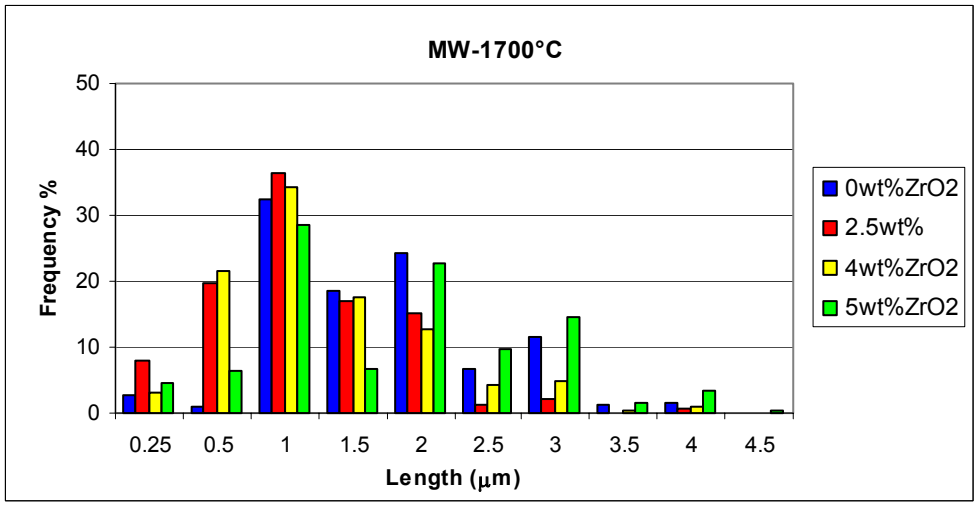

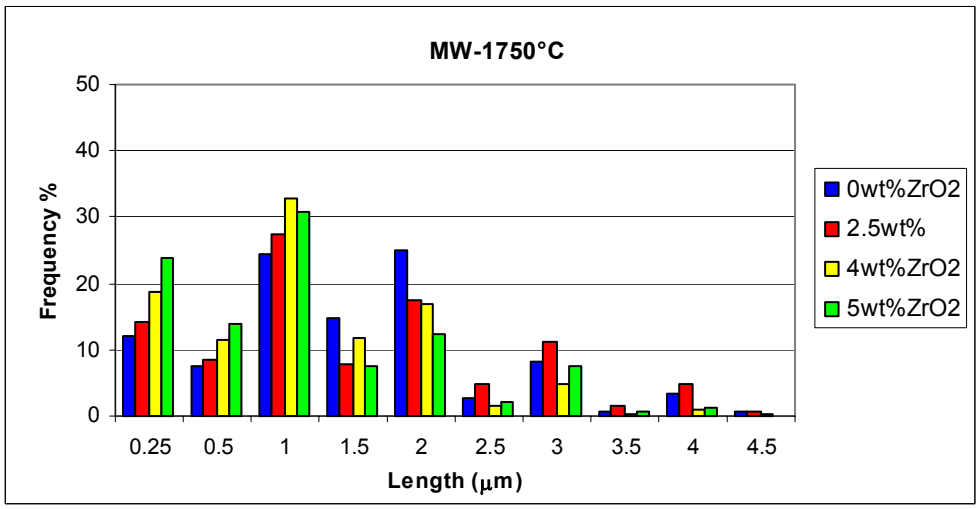

Figure 5.8. Grain length distributions of Si_3N_4 samples microwave sintered at 1650ºC, 1700ºC and 1750ºC.

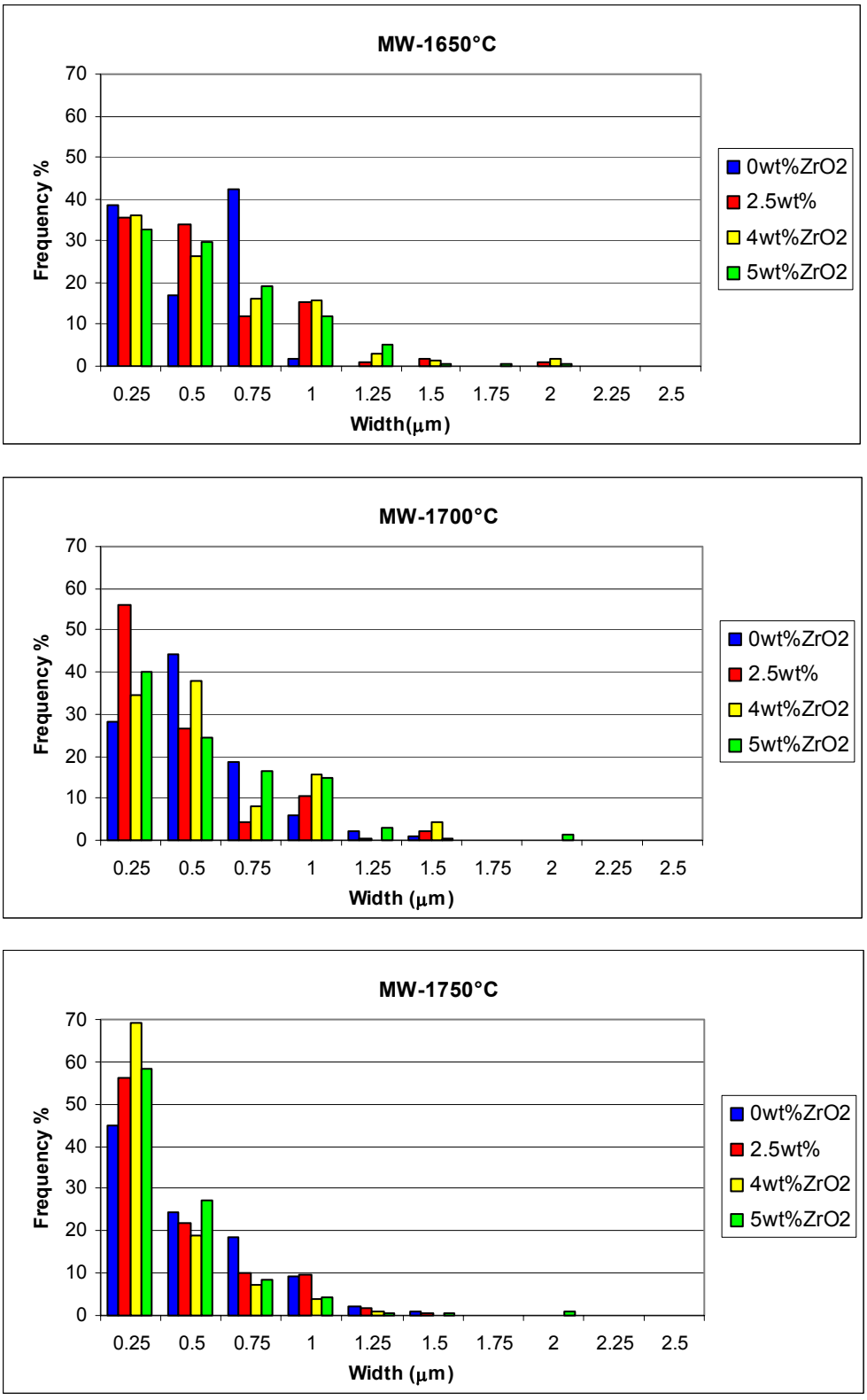

Figure 5.9. Grain width distributions of Si_3N_4 samples microwave sintered at 1650ºC, 1700ºC and 1750ºC.

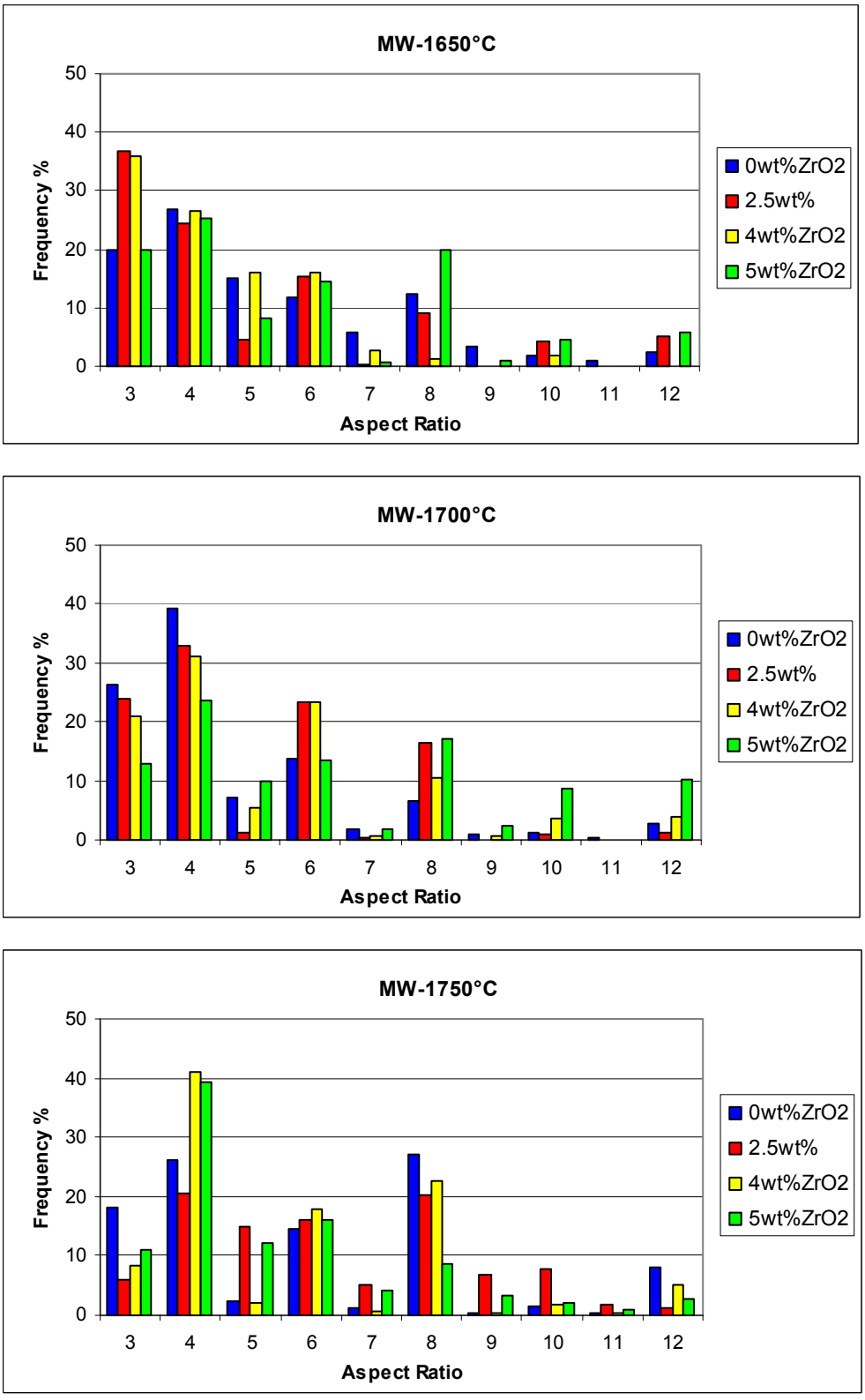

Figure 5.10 Aspect ratios of Si_3N_4 samples microwave sintered at 1650ºC, 1700ºC and 1750ºC.

Figure 5.11 shows grain-length distributions of the conventionally-sintered samples. Two peaks, with 38% grains with length of 1 μm and 25% of grains with 2 μm, resulted from sintering to 1650ºC. The length distribution became broader when the sintering temperature was increased from 1650ºC to 1750ºC. However, the change in grain-width distribution with increasing temperature is small, as evident in Figure 5.12. Two peaks where 30% of grains have widths of 0.25 or 0.5 μm are evident. Three major peaks with aspect ratios 4, 8, 12 are observed for samples containing 0 wt % ZrO_2. Approximately 33% of grains have aspect ratios between 4 and 8, while 10% have an aspect ratio of 12. In contrast, 25% of grains have an aspect ratio of 12 in the sample containing 2.5wt% ZrO_2. It is clearly evident from Figure 5.13 that the ZrO_2 addition had no significant influence on the grain-widths distribution in conventionally-sintered samples, unlike the effect observed in the case of microwave-sintered samples.

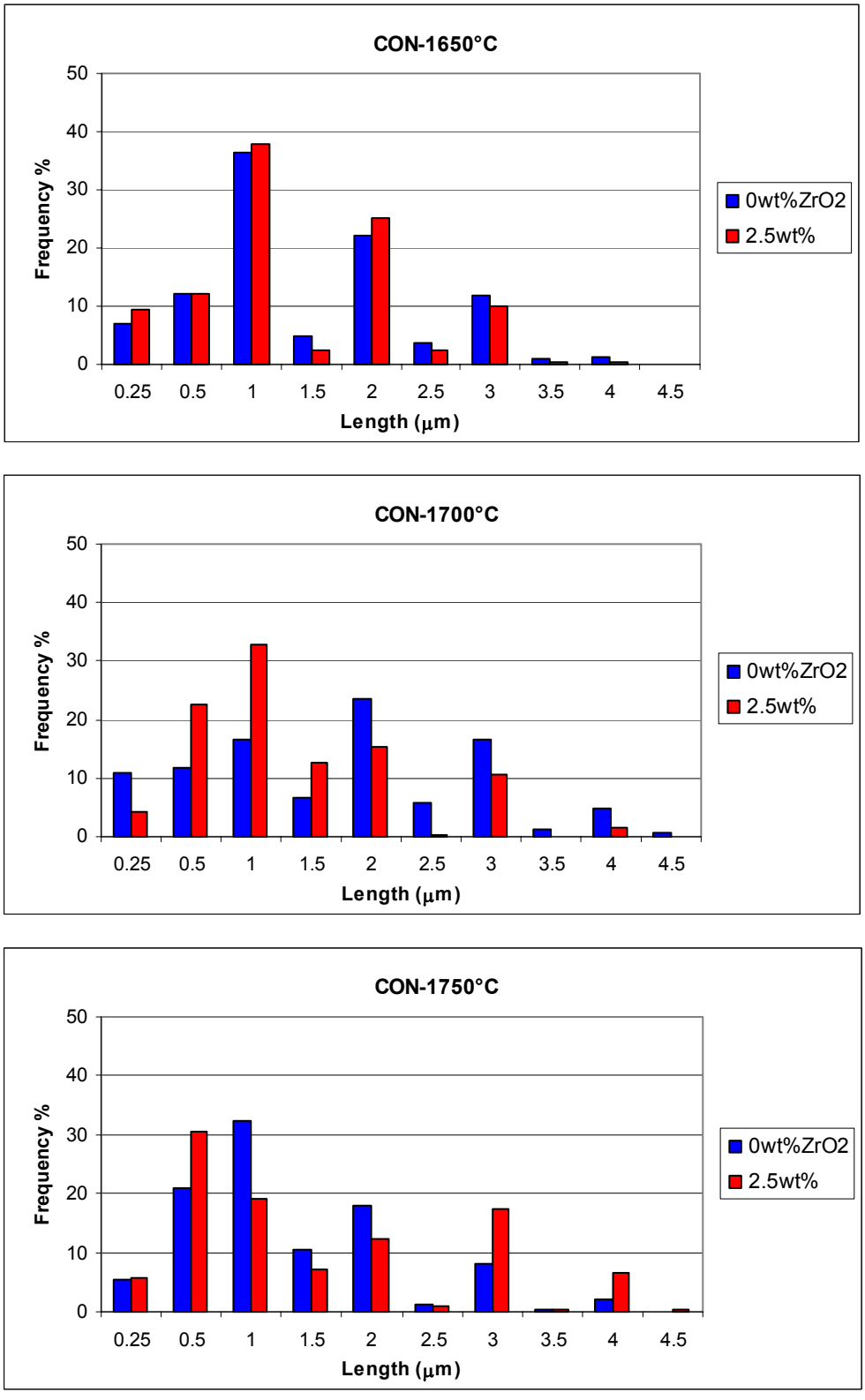

Figure 5.11. Grain length distributions of Si_3N_4 samples conventionally sintered at 1650ºC, 1700ºC and 1750ºC.

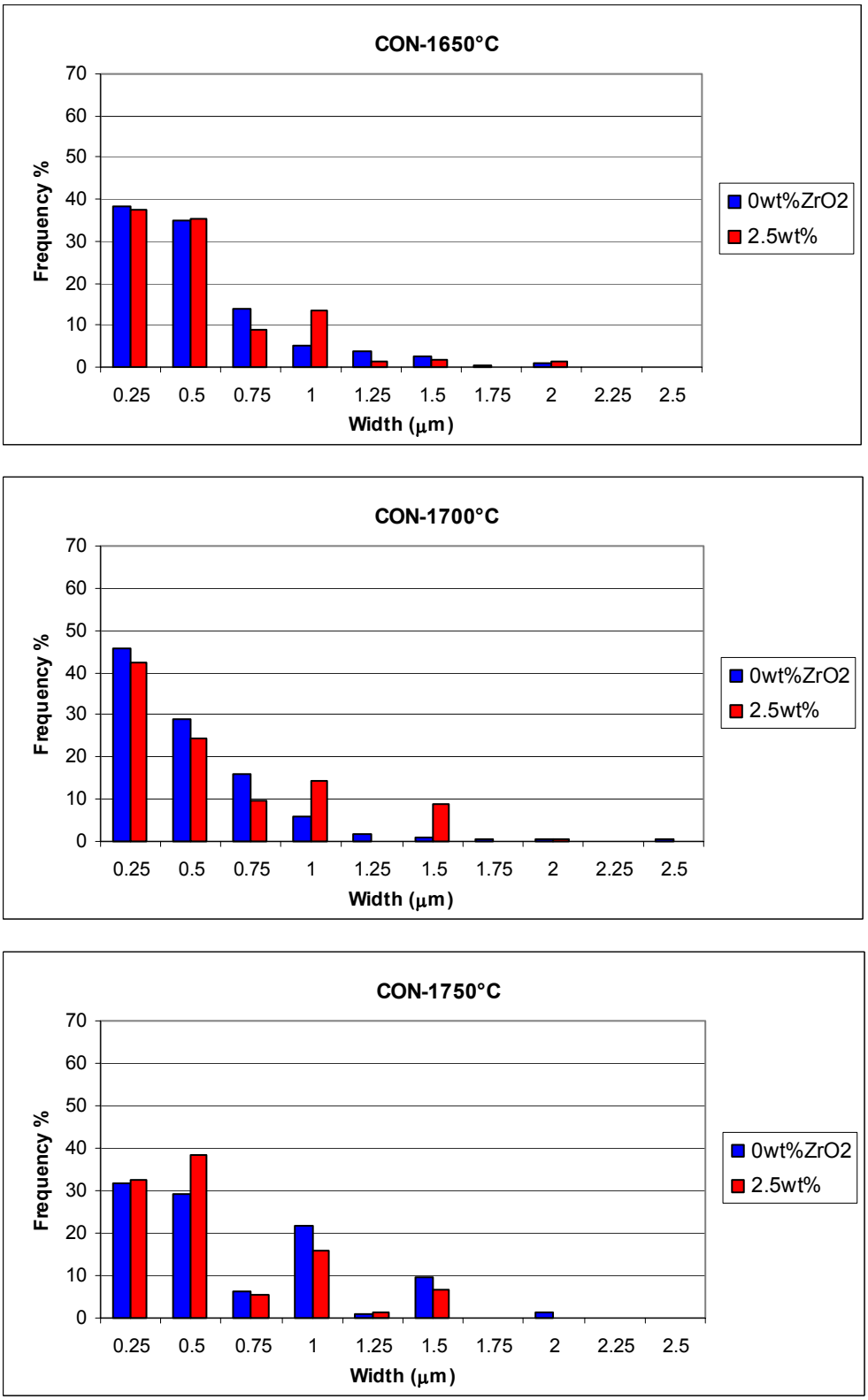

Figure 5.12. Grain width distributions of Si_3N_4 samples conventionally sintered at 1650ºC, 1700ºC and 1750ºC.

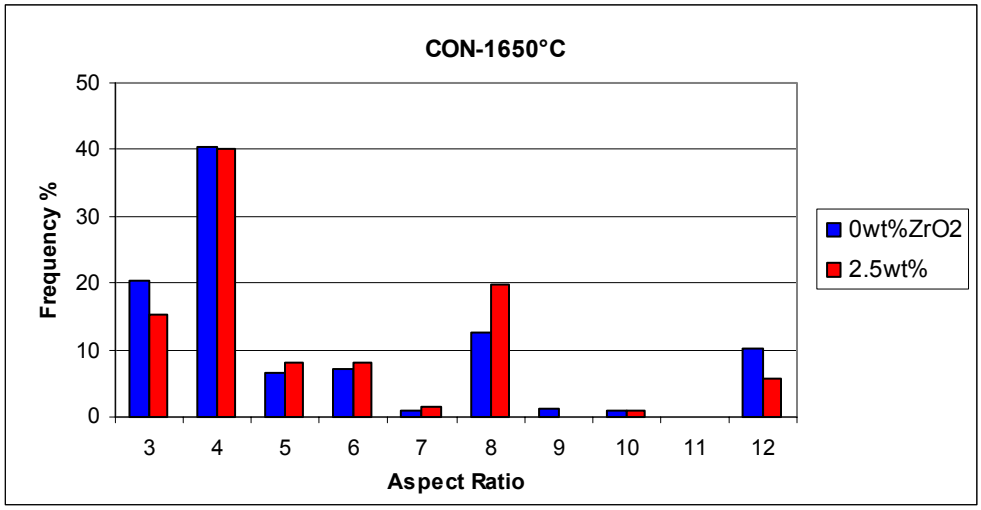

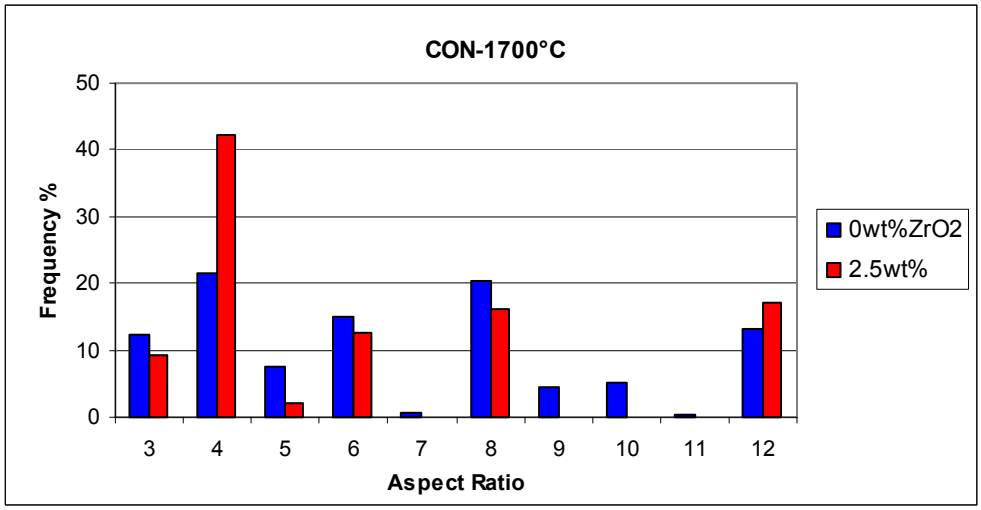

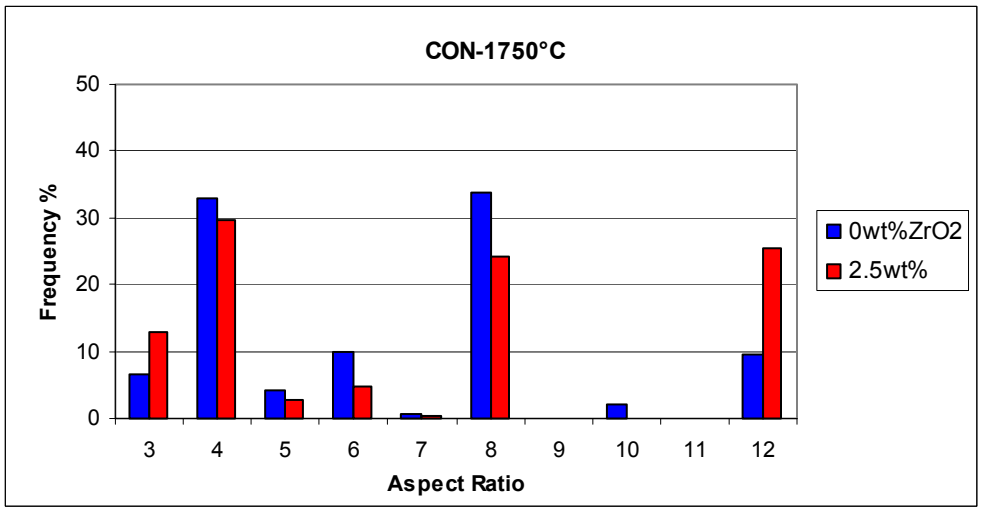

Figure 5.13 Aspect ratios of Si_3N_4 samples conventionally sintered at 1650ºC, 1700ºC and 1750ºC.

Figure 5.14 compares grains lengths of samples containing 0% ZrO_2 and sintered using microwave versus conventional techniques. Microwave-sintered samples have 6% more 2 μm grains than conventionally-sintered samples sintered at 1750ºC. The percentage of 2 μm grains increased from 19% to 26% when the temperature was increased from 1650 to 1750ºC. In the case of microwave-sintered samples, grains with 0.75 μm width reduced to 19% from 42%, and the highest peak shifted to 0.25 μm from 0.75 μm, when the sintering temperature was increased by 100ºC. The microwave-sintered samples exhibit a narrow width distribution at 1750ºC when compared to conventionally-sintered samples.

Both microwave and conventionally-sintered samples exhibit three major peaks with aspect ratios of 4, 8 and 12. Microwave sintered samples have 26-27% of grains with aspect ratios of 4 and 8. Conventionally-sintered samples contain 6% more grains with a similar aspect ratio and 8-9% with an aspect ratio of 12. A bimodal grain size distribution is also clearly evident in Figure 5.16. The frequency percentage of 2 μm length grains lowers from 25% to 18%, and 3 μm length grains reduce from 11% to 8%, when 2.5 wt% ZrO_2 is added to silicon nitride and sintering is done with microwave energy (Figure 5.17). However, the 4 μm long grains increase marginally.

Microwave sintered Si_3N_4 samples containing 2.5 wt% ZrO_2 developed a distinctly narrow grain-width distribution when the temperature was increased from 1650ºC to 1750ºC. In contrast, a broader grain-width distribution is evident in conventionally-sintered samples. The addition of ZrO_2 further reduced the number of grains with aspect ratios of 4 and 8 in both microwave and conventionally-sintered samples. However, the grains with an aspect ratio of 12 increased from 9% to 25% in the case of conventionally-sintered samples.

In summary, microwave sintering resulted in a finer, narrower distribution of grains when compared to conventional sintering. The addition of 2.5 wt% ZrO_2 had a pronounced effect on the development of the Si_3N_4 matrix microstructure. A bimodal grain size distribution is also clearly evident in both microwave and conventionally-sintered samples. The higher Vickers hardness value observed in the case of microwave-sintered samples with 2.5 wt of ZrO_2 corresponds to the fine-grain microstructure. Xin xu *et.al*[16] reported a Vickers hardness value of 18.3 GPa when nano sized β-Si_3N_4

crystals resulted from spark plasma sintering (SPS). In the literature, it is well established that the different planes of β-Si_3N_4 have different growth mechanisms.[17] The {001} basal plane growth is diffusion controlled, whereas the {100} prismatic plane is interface controlled. Due to the different growth mechanisms existing for different planes, the basal and primatic planes show different dependencies of the growth rate on over saturation. The basal planes {001}, have higher surface energies than primastic planes {100} and microwave sintering appears to support diffusion-controlled basal plane growth.

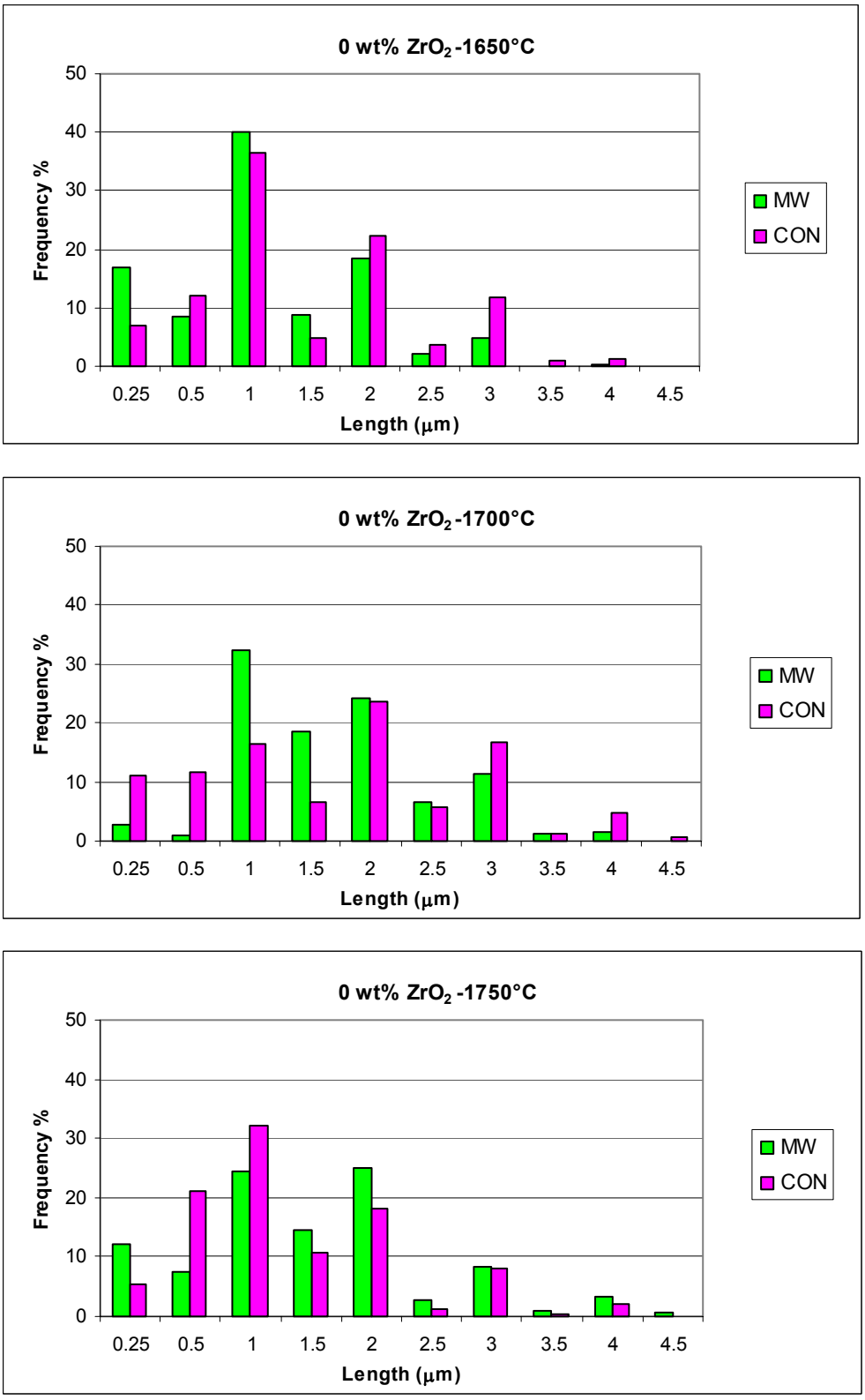

Figure 5.14. Grain-length distributions of microwave (MW) versus conventional (CON) sintered Si_3N_4 samples containing 0 wt% ZrO_2.

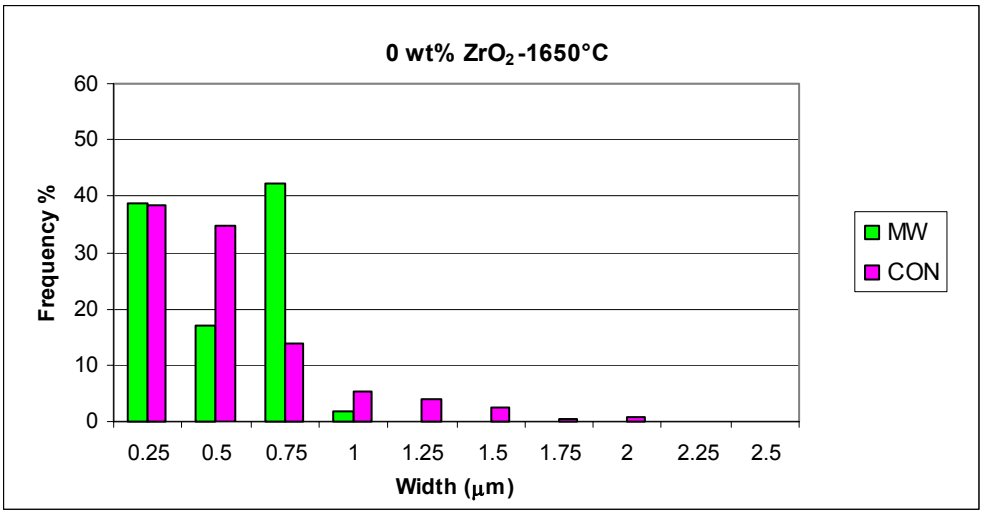

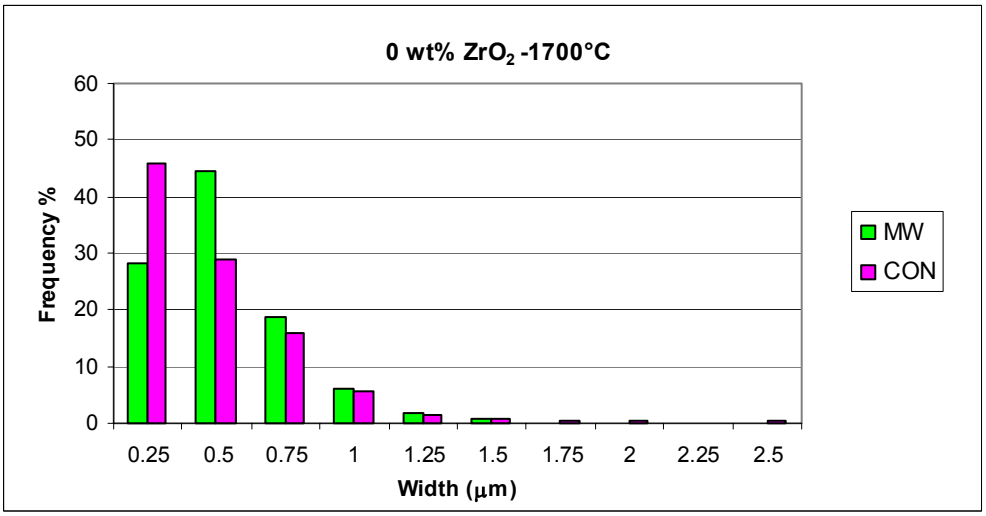

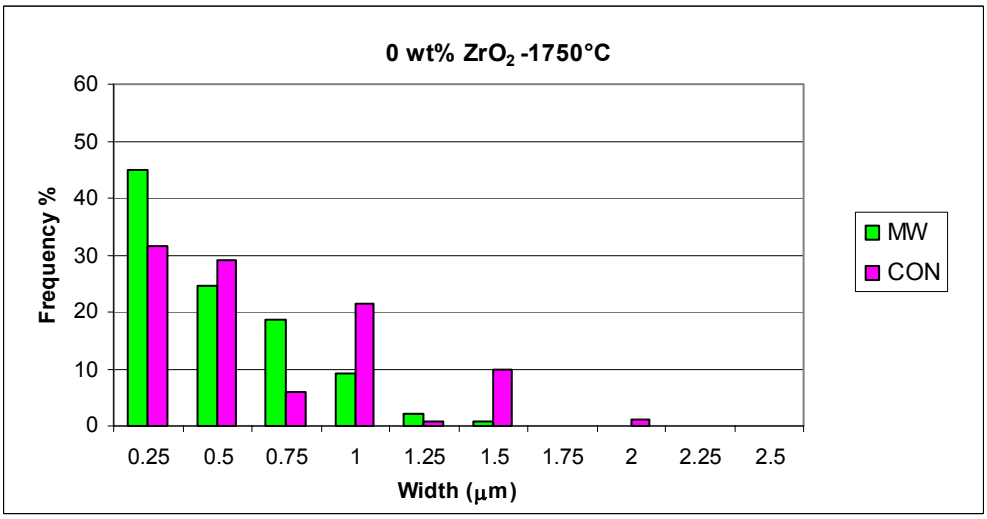

Figure 5.15. Grain-width distributions of microwave (MW) versus conventional (CON) sintered Si_3N_4 samples containing 0 wt% ZrO_2.

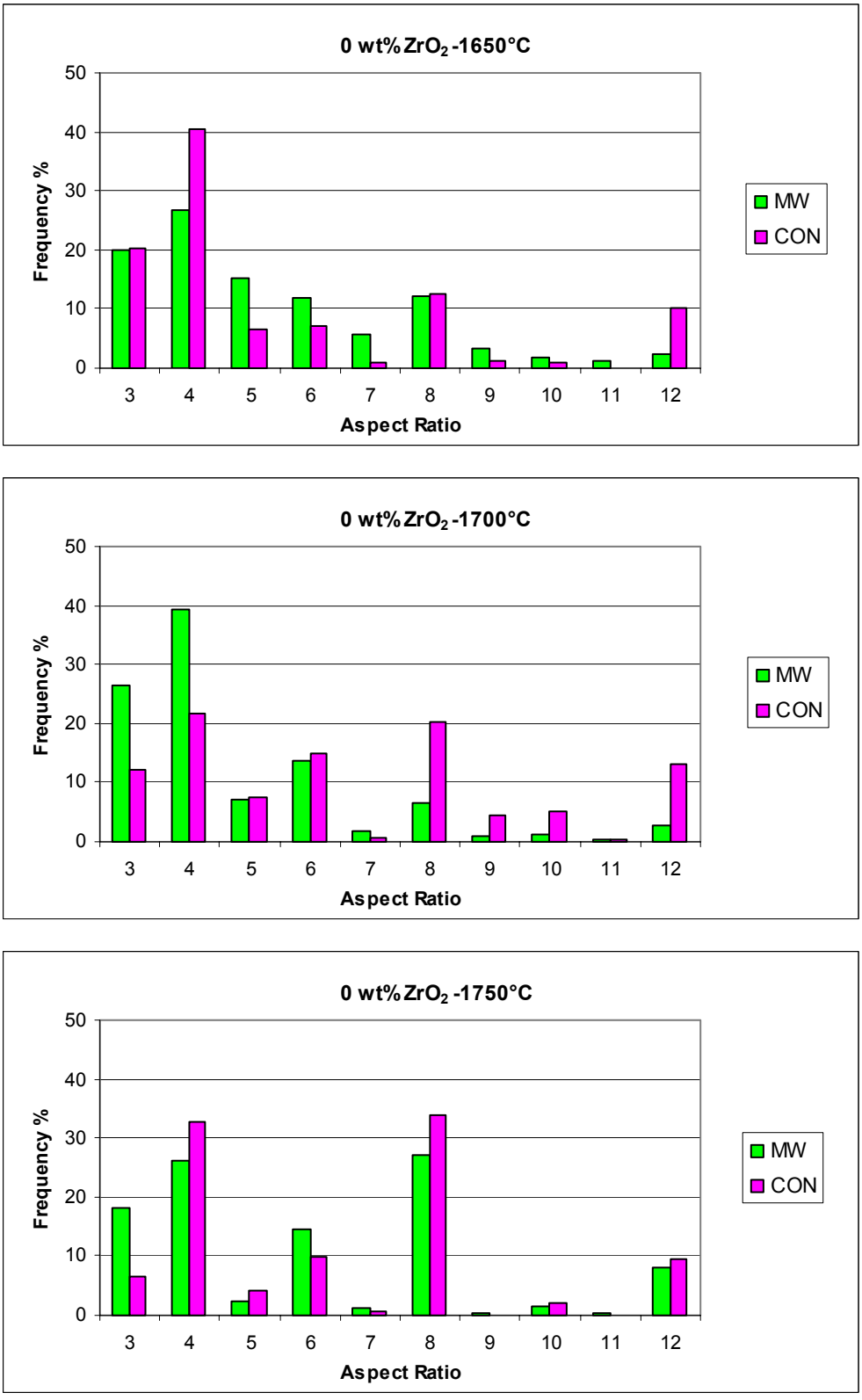

Figure 5.16. Aspect ratios of microwave (MW) versus conventional (CON) sintered Si_3N_4 containing 0 wt% ZrO_2.

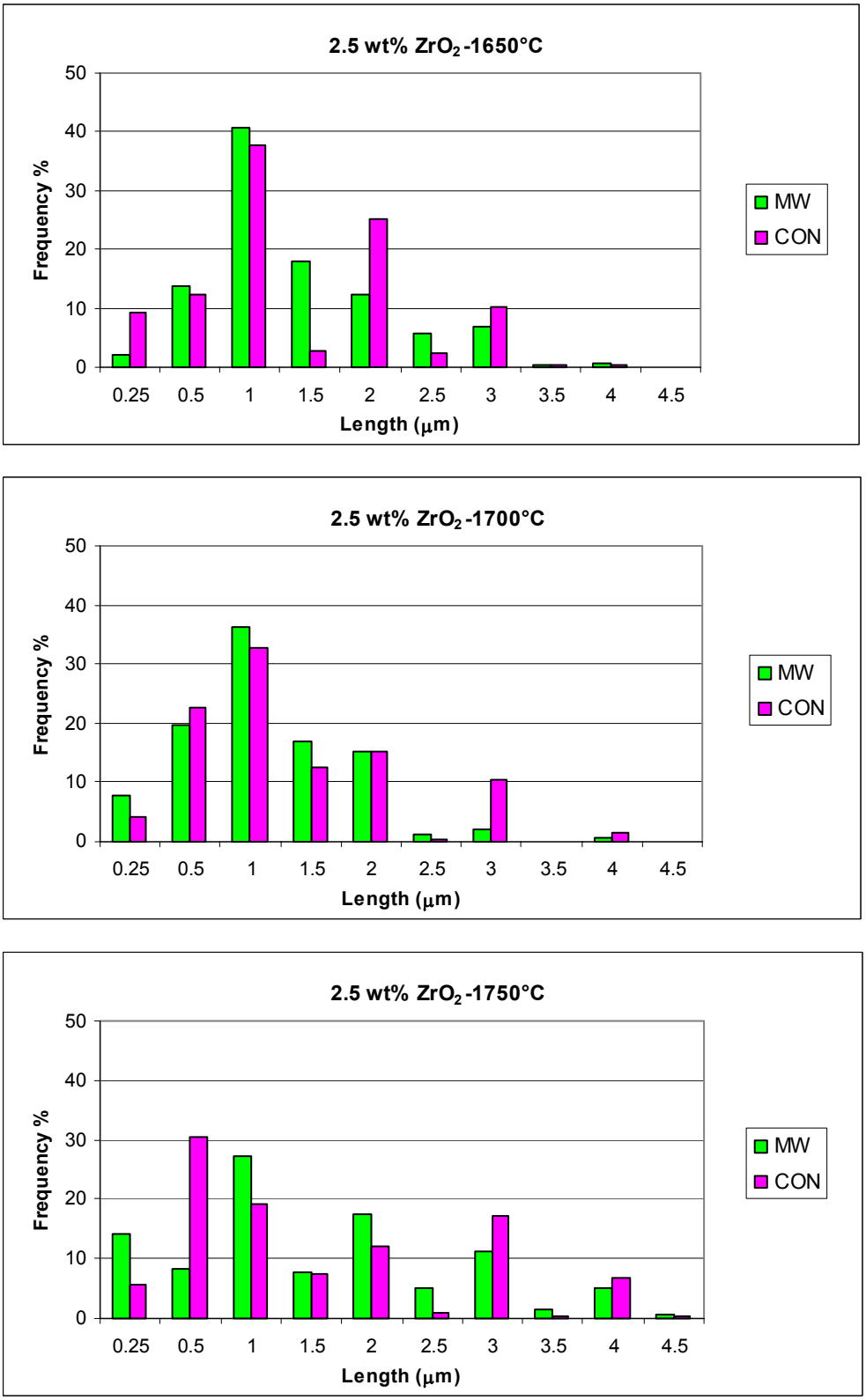

Figure 5.17. Grain-length distributions of microwave (MW) versus conventional (CON) sintered Si_3N_4 samples containing 2.5 wt% ZrO_2.

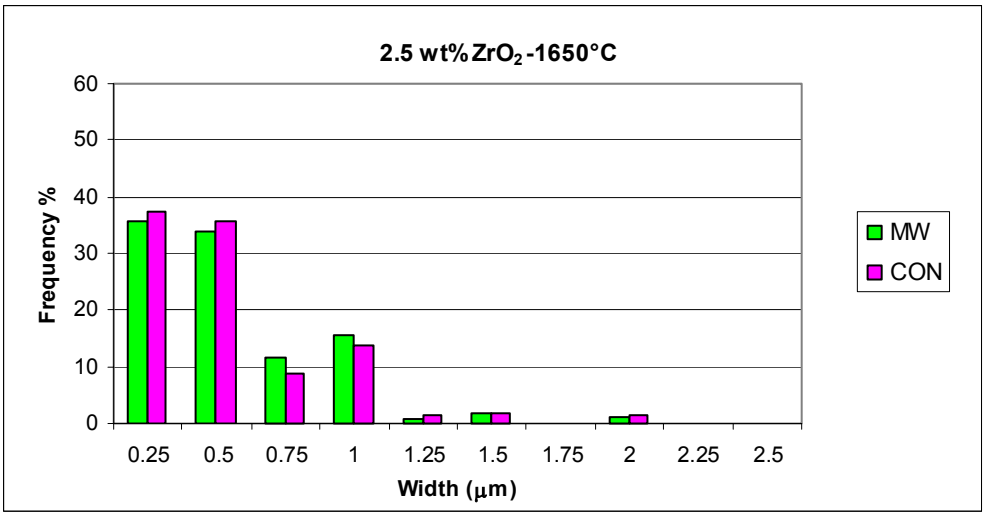

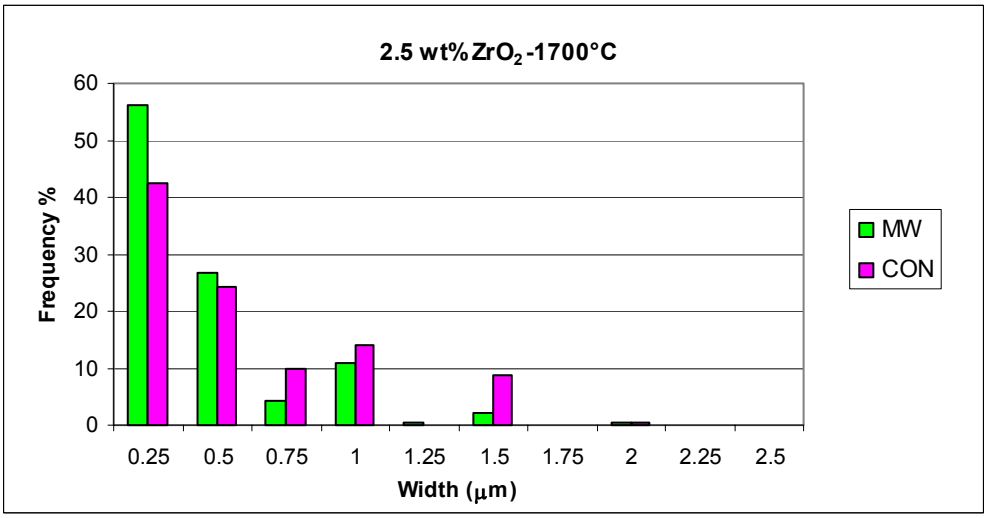

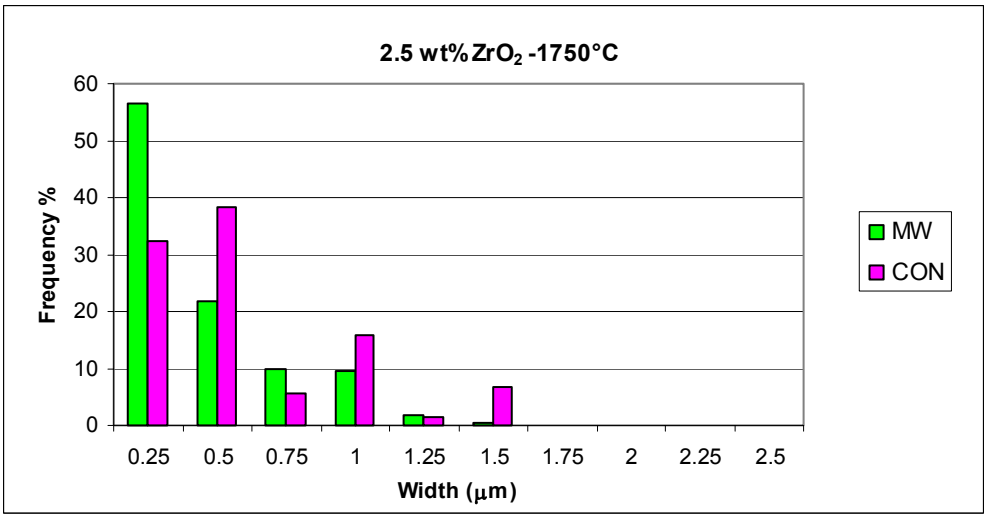

Figure 5.18. Grain-width distributions of microwave (MW) versus conventional (CON) sintered Si_3N_4 samples containing 2.5 wt% ZrO_2.

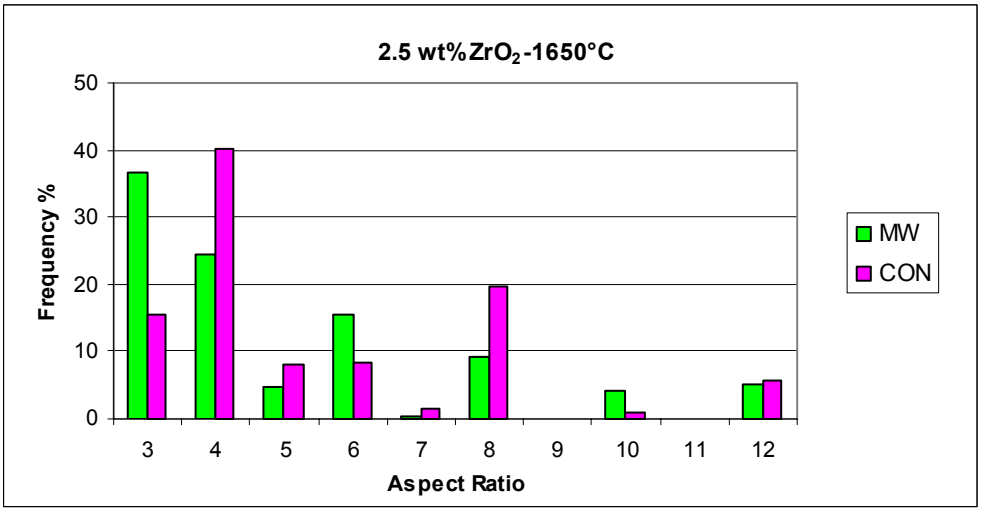

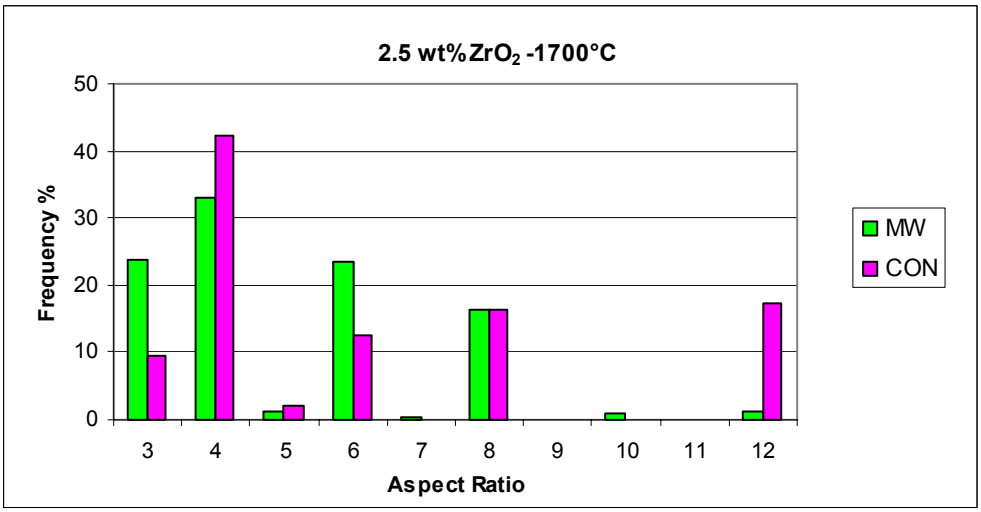

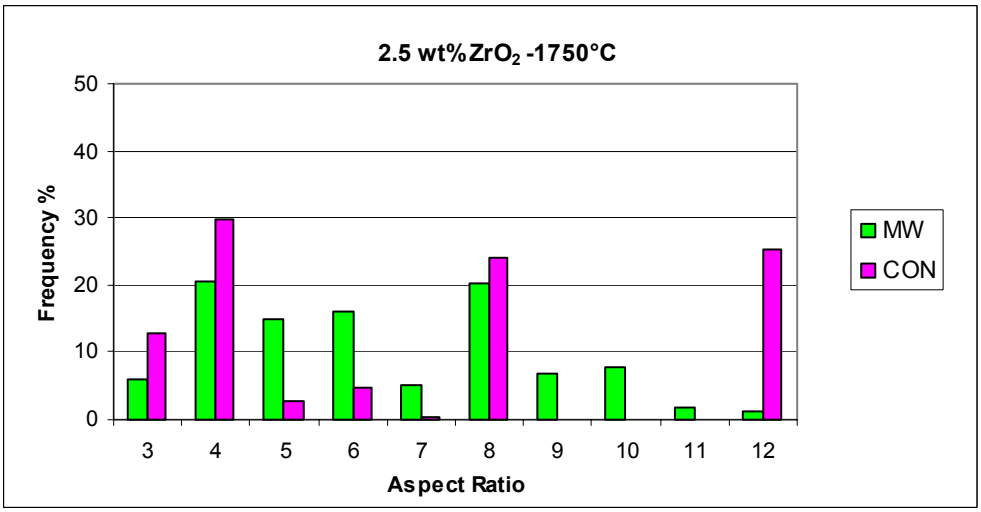

Figure 5.19. Aspect ratios of microwave (MW) versus conventional (CON) sintered Si_3N_4 containing 2.5 wt% ZrO_2.

5.4 Conclusions

ZrO_2 additions greatly increased the Vickers hardness of the microwave-sintered Si_3N_4 samples. The fracture toughness was relatively consistent despite differences in microstructure. This may be attributed to strong bonding between the grains and grain boundaries resulting in crack paths that were predominantly trans-granular, with little crack deflection. Additions of ZrO_2 produced fine grain β-Si_3N_4 with a narrow grain size distribution in the case of microwave-sintered samples. ZrO_2 had no significant influence on the grain size distribution of conventionally-sintered samples.

The enhanced Vickers hardness observed in the case of microwave-sintered samples with 2.5 wt% ZrO_2 is most likely due to the fine-grain microstructure development caused by the rapid heating rate of 50ºC/min versus 10ºC/min in the case of conventional sintering. Moreover, the volumetric heating produced by microwaves may influence the grain-growth kinetics.

5.5 References

1. F.L. Riley, "Silicon Nitride and Related Materials," *J. Am. Ceram. Soc.,* **83** [2] 245-65 (2000).

2. Q. Feng, S. Chockalingam, and D.A. Earl, "Microstructure of Microwave Sintered Silicon Nitride with Zirconia as Secondary Particulates," *J. Am. Ceram. Soc.,* **89** [12] 3770-77 (2006).

3. M.J. Hoffmann, "Analysis of Microstructural Development and Mechanical Properties of Si_3N_4 Ceramics," pp 87-100 in *Tailoring of Mechanical Properties of Si_3N_4 Ceramics*. Edited by M.J. Hoffmann, and G. Petzow. Kluwer Academic, Boston, MA, 1994.

4. Y. Tajima and K. Urashima, "Improvement of Strength and Toughness Silicon Nitride Ceramics," pp 101-109 in *Tailoring of Mechanical Properties of Si_3N_4 Ceramics.* Edited by M.J. Hoffmann, and G. Petzow. Kluwer Academic, Boston, MA, 1994.

5. P.F. Becher, S.L. Hwang, H.T. Lin, and T.N. Tiegs, "Microstructural Contributions to the Fracture Resistance of Silicon Nitride Ceramis," pp 87-100 in *Tailoring of Mechanical Properties of Si_3N_4 Ceramics.* Edited by M.J. Hoffmann and G. Petzow. Kluwer Academic, Boston, MA, 1994.

6. G.R. Terwilliger and F.F. Lange, "Pressureless Sintering of Si_3N_4, " *J. Mater. Sci*., **10** [2] 1169–74 (1975).

7. P.F. Becher, S.L. Hwang, and C.H. Hsueh "Using Microstructure to Attack the Brittle Nature of Silicon Nitride Ceramics," *Mater. Res. Bull.*, **20** [2] 23-27 (1995).

8. I. M. Peterson and T.Y. Tien, "Effect of the Grain Boundary Thermal Expansion Coefficient on the Fracture Toughness in Silicon Nitride," *J. Am. Ceram. Soc*., **78** [9] 2345-52 (1995).

9. K. Hirao and S. Kanzaki, "Processing Strategy for Producing Highly Anisotropic Silicon Nitride," *J. Am. Ceram. Soc*., **78** [6] 1687-90 (1995).

10. M. Hirota, M.E. Brito, K. Hirao, K. Watari, M. Toriyama, and T. Nagaoka, "Microwave Sintering of Silicon Nitride with Rare Earth Sesquioxide Additions," pp. 515-22 in *Microwaves: Theory and Application in Materials Processing IV*. Edited by D.E. Clark, W.H. Sutton, and D.A. Lewis. Materials Research Society, Pittsburgh, PA, 1997.

11. N. Claussen and J. Jahn, "Mechanical Properties of Sintered and Hot-Pressed Si_3N_4-ZrO_2 Composites," *J. Am. Ceram. Soc.*, **61** [1-2] 94-95 (1978).

12. F.F. Lange, L.K.L. Falk, and B.I. Davis, "Structural Ceramics Based on Si_3N_4-ZrO_2 (+Y_2O_3) Compositions," *J. Mater. Res*., **2** [1] 66-76 (1987).

13. L.K.L. Falk and K. Rundgren, "Microstructure and Short-Term Oxidation of Hot-Pressed Si_3N_4/ZrO_2 Ceramics," *J. Am. Ceram. Soc*., **75** [1] 28-35 (1992).

14. H.J. Kleebe, W. Braue, and W. Luxem, "Densification Studies of SRBSN with Unstabilized Zirconia by Means of Dilatometry and Electron Microscopy," *J. Mater. Sci.,* **29** [5] 1265-75 (1994).

15. M. Kramer, M.J. Hoffmann, and G. Petzow, "Grain Growth Studies of Silicon Nitride Dispersed in an Oxynitride Glass," *J. Am. Ceram. Soc.*, 7**6** [11] 2778-84 (1993).

16. X. Xu, T. Nishimura, N. Hirosaki, R.J. Xie, Y. Zhu, Y. Yamamoto, and H. Tanaka, "New Strategies for Preparing Nano Sized Silicon Nitride Ceramics," *J. Am. Ceram. Soc.*, **88** [4] 934-37 (2005).

17. M. Herrmann, I. Schulz, and I. Zalite, "Materials Based on Nano Sized β-Si_3N_4 Composite Powders," *J. Eur. Ceram. Soc.*, **24** [12] 3327-35 (2004).

CHAPTER 6

Conclusions

6.1 Summary

It is difficult to sinter pure Si_3N_4 in a multimode 2.45 GHz microwave furnace due to the material's low dielectric loss over the temperature range required for densification. The goal of this research was to investigate the effects of a lossy secondary additive, namely ZrO_2 stabilized with 3 mol% Y_2O_3, on densification, $\alpha \rightarrow \beta$ phase transformation, microstructural development, and mechanical properties of Si_3N_4 containing 4 wt% MgO and 6 wt% Y_2O_3 as primary liquid-forming sintering additives.

The main conclusions drawn from this work are:

(1) The $\alpha \rightarrow \beta$ transformation in the microwave-sintered samples studied is completed much earlier than densification, whereas a significant amount of α-Si_3N_4 remains in conventionally-sintered samples, even after heating to 1750ºC for 30 minutes. The enhanced $\alpha \rightarrow \beta$ phase transformation during microwave sintering is most likely due to the volumetric coupling of microwave power with the dielectrically lossy grain-boundary glassy phase, promoting dissolution of α–Si_3N_4 and nucleation of β-Si_3N_4. ZrO_2 additions enhanced densification during both microwave and conventional sintering. However, densification appears to be limited in microwave-sintered samples containing more than about 2.5 wt% ZrO_2, as surface porosity results from selective localized overheating and decomposition of ZrO_2-containing phases. This investigation demonstrated that it is possible to maximize the density by adjusting the amount of ZrO_2 and the microwave sintering temperature and time. Thus, microwave sintering can be used to simultaneously enhance $\alpha \rightarrow \beta$ phase transformation and densification.

(2) TEM results show the crystalline phases present after microwave sintering are mainly β-Si_3N_4 with minor N-Melilite. N-Melilite was formed by crystallization at multigrain junctions. TEM identified about 13 vol% Si-Y-Mg-O-N secondary phases on the grain boundaries and multigrain junctions. The existence of ZrO_2 particulates improved the microwave heating efficiency and enhanced densification. However, minor dissolution of ZrO_2 in the oxynitride liquid occurred during sintering. Both tetragonal and cubic Zr-rich phases were identified by SAD, which supports the existence of N-

stabilizing ZrO_2. Moreover, microwave sintering favored the formation of the Si-Mg-Y oxynitride liquid phase, and thus enhanced the dissolution of α-Si_3N_4. The thickness of the homophase boundary was measured to 3.4 nm.

(3) ZrO_2 additions increase the hardness of microwave sintered Si_3N_4 by facilitating the development of a fine-grained microstructure with few elongated grains. A 2.5 wt% ZrO_2 addition resulted in a Vickers hardness of 13.9 GPa at a sintering temperature of 1750ºC compared to 9.3 GPa for samples without ZrO_2. The fracture toughness did not significantly change with the ZrO_2 addition despite the differences in microstructure. The lack of any change in fracture toughness may be due to the strong bonding between the grain and grain boundary, as evidenced by a predominantly trans-granular crack path, with little crack deflection. The ZrO_2 addition produced a finer grain β-Si_3N_4 with a narrower grain size distribution in the case of microwave-sintered samples. The ZrO_2 addition had no significant influence in grain size distribution of conventionally-sintered samples. The enhanced hardness observed in the case of microwave-sintered samples with 2.5 wt% ZrO_2 is most likely due to the fine grain microstructure resulting from the rapid heating rate of 50ºC/min versus 10ºC/min in the case of conventional sintering. Moreover, the volumetric heating resulting from microwaves may have influenced the grain-growth kinetics.

(4) FDTD numerical simulations predict an increase in microwave power absorption in Si_3N_4 when the higher-dielectric-loss additives Y_2O_3 and ZrO_2 are added, resulting in an increase in sample temperature. FDTD simulations predict a 75-125^oC higher sintering temperature than the values measured experimentally using an optical radiation pyrometer. It was demonstrated that pure silicon nitride is transparent to 2.45 GHz microwaves, and its sintering takes place by coupling of the microwaves to the dielectrically lossy grain-boundary phase. Thus, temperature profiles required for successful sintering can be obtained by tailoring the dielectric properties of additives.

6.2 Recommendations for Future Work

Preliminary studies involving the development of a multi-layered graded structure, which consists of a central layer of 65 wt% α-Si_3N_4, 25 wt% 3 mol% Y_2O_3 stabilized ZrO_2, 6 wt% Y_2O_3 and 4 wt% MgO and top and bottom layer consists of 90 wt% α-Si_3N_4, 6 wt% Y_2O_3 and 4 wt% MgO demonstrated a indentation fracture toughness of 8.7 MPa·$m^{1/2}$ at the top layer. The experimental results suggest that it is worthwhile to further investigate a Si_3N_4 based multi-layered composite structure in detail. The thickness of the layers, additives compositions, sintering temperature and time could be tailored to enhance the mechanical properties such as fracture toughness and strength.

The sintering additives could be reduced through sol-gel coating of a more refractory glass composition, which is then subsequently re-crystallized to improve the high-temperature creep resistance properties.

The maximum operating temperature of existing temperature-dependent dielectric-property measurement systems are limited to 1450°C due to reactions between sample holders and the samples under study at temperatures above to 1450°C. Therefore the system needs to be improved to extend the measurement temperature range up to 2000°C. This will facilitate the real-time numerical simulations of power absorption and temperature distribution.

Appendix A. Vickers Hardness and Fracture Toughness Raw Data of Microwave-Sintered Silicon Nitride Samples

Table A.I. Vickers Hardness and Fracture Toughness of Microwave Sintered Sample at 1650°C - 0 wt%ZrO_2.

SID	#	D1	C1	C2	D2	C3	C4	D	V.H	C(1,2)	C(3.4)	C	E	F.T.
A1	1	198.00	105.00	107.00	198.00	110.24	132.33	198.00	9.28	205.00	220.29	212.64	284.40	5.604
	2	191.00	104.82	117.14	192.00	94.24	103.34	191.50	9.92	206.48	194.79	200.64	284.40	5.914
	3	201.00	201.00	203.00	183.00	120.35	118.28	192.00	9.87	302.50	210.82	256.66	284.40	4.098
	4	205.00	84.47	104.27	207.00	96.37	107.23	206.00	8.57	196.87	205.30	201.09	284.40	6.341
	5	201.00	106.94	95.85	202.00	111.59	118.41	201.50	8.96	201.90	216.00	208.95	284.40	5.855
	6	185.00	107.61	114.26	187.00	89.08	89.84	186.00	10.52	203.44	182.96	193.20	284.40	6.079
	7	198.00	108.88	105.08	197.00	100.08	104.91	197.50	9.33	205.98	201.00	203.49	284.40	5.972
	8	201.00	99.32	107.32	199.00	87.13	94.33	200.00	9.10	203.82	190.23	197.03	284.40	6.347
	9	210.00	201.00	213.00	207.00	117.47	118.49	208.50	8.37	312.00	221.48	266.74	284.40	4.201
	10	201.00	120.99	97.29	205.00	103.47	93.01	203.00	8.83	209.64	200.74	205.19	284.40	6.062
									9.27					**5.65**
									0.66					0.819

Table A.II. Vickers Hardness and Fracture Toughness of Microwave Sintered Sample at 1650°C - 2.5 wt%ZrO_2.

SID	#	D1	C1	C2	D2	C3	C4	D	V.H	C(1,2)	C(3.4)	C	E	F.T.
A2	1	181.06	108.33	113.55	179.71	87.82	98.75	180.39	11.18	201.47	183.14	192.31	296.40	6.061
	2	181.62	122.00	120.00	183.90	97.86	105.79	182.76	10.89	211.81	193.78	202.79	296.40	5.67
	3	182.12	113.00	110.00	180.13	100.41	102.48	181.13	11.09	202.56	191.51	197.04	296.40	5.868
	4	185.68	132.00	102.00	182.76	97.70	98.03	184.22	10.72	209.84	189.25	199.54	296.40	5.856
	5	180.98	112.00	111.00	182.80	98.92	112.70	181.89	11.00	201.99	197.21	199.60	296.40	5.779
	6	181.95	132.00	120.00	184.29	111.22	104.65	183.12	10.85	216.98	200.08	208.53	296.40	5.449
	7	182.00	116.00	115.00	182.34	107.53	111.43	182.17	10.96	206.50	200.65	203.58	296.40	5.619
	8	180.81	98.00	96.89	184.84	87.86	117.53	182.83	10.89	187.85	195.12	191.48	296.40	6.182
	9	180.98	111.00	102.40	183.44	110.20	98.08	182.21	10.96	197.19	195.86	196.53	296.40	5.926
	10	182.76	106.00	75.40	182.42	102.70	108.55	182.59	10.91	182.08	196.84	189.46	296.40	6.274
									10.95					**5.87**
									0.13					0.256

Table A.III. Vickers Hardness and Fracture Toughness of Microwave Sintered Sample at 1650°C- 4 wt%ZrO_2.

SID	#	D1	C1	C2	D2	C3	C4	D	V.H	C(1,2)	C(3.4)	C	E	F.T.
A3	1	195.19	140.00	138.00	188.23	132.00	142.00	191.71	9.90	236.60	231.12	233.86	298.30	4.819
	2	192.61	123.00	118.00	190.21	121.00	118.00	191.41	9.93	216.81	214.61	215.71	298.30	5.431
	3	190.25	98.00	114.00	193.54	112.00	114.00	191.90	9.88	201.13	209.77	205.45	298.30	5.857
	4	195.10	101.00	98.00	189.96	132.00	112.00	192.53	9.82	197.05	216.98	207.02	298.30	5.81
	5	196.37	113.00	124.00	191.64	98.00	114.00	194.01	9.67	216.69	201.82	209.25	298.30	5.761
	6	190.14	112.00	135.00	194.09	103.18	109.00	192.12	9.86	218.57	203.14	210.85	298.30	5.64
	7	192.45	107.00	125.00	193.12	110.00	112.00	192.79	9.79	212.23	207.56	209.89	298.30	5.699
	8	191.98	98.00	111.00	192.91	108.00	112.00	192.45	9.82	200.49	206.46	203.47	298.30	5.96
	9	194.64	103.22	88.14	193.67	145.00	138.00	194.16	9.65	193.00	238.34	215.67	298.30	5.51
	10	195.14	123.00	118.00	193.42	87.49	106.55	194.28	9.64	218.07	193.73	205.90	298.30	5.911
									9.80					**5.64**
									0.18					0.334

Table A.IV. Vickers Hardness and Fracture Toughness of Microwave Sintered Sample at 1650°C- 5 wt%ZrO_2

SID	#	D1	C1	C2	D2	C3	C4	D	V.H	C(1,2)	C(3.4)	C	E	F.T.
A4	1	186.00	121.85	95.79	188.00	124.69	117.28	187.00	10.40	201.82	214.99	208.40	260.60	5.222
	2	170.13	100.87	92.14	171.02	134.10	112.32	170.58	12.50	181.57	208.72	195.15	260.60	5.257
	3	185.00	109.57	87.01	187.00	125.24	102.95	186.00	10.52	190.79	207.60	199.19	260.60	5.559
	4	201.00	107.99	96.76	200.00	114.31	108.84	200.50	9.05	202.88	211.58	207.23	260.60	5.647
	5	183.00	105.07	91.80	184.00	123.38	105.58	183.50	10.81	189.94	206.48	198.21	260.60	5.525
	6	185.00	109.86	96.81	180.00	123.21	110.03	182.50	10.92	195.84	206.62	201.23	260.60	5.371
	7	190.00	107.91	98.03	198.00	117.95	118.80	194.00	9.67	197.97	217.38	207.67	260.60	5.446
	8	170.60	92.23	97.99	169.62	131.48	110.62	170.11	12.57	180.41	205.86	193.14	260.60	5.325
	9	170.09	102.15	104.94	170.00	127.62	95.36	170.05	12.58	188.59	196.49	192.54	260.60	5.347
	10	194.00	107.36	93.71	195.00	123.00	90.15	194.50	9.62	197.54	204.08	200.81	260.60	5.743
									10.86					**5.44**
									0.18					0.171

Table A.V. Vickers Hardness and Fracture Toughness of Microwave Sintered Sample at 1700°C-0 wt% ZrO_2

SID	#	D1	C1	C2	D2	C3	C4	D	V.H	C(1,2)	C(3.4)	C	E	F.T.
A5	1	166.06	107.15	101.18	168.68	111.13	105.08	167.37	12.99	187.20	192.45	189.82	282.30	5.596
	2	171.85	99.57	117.73	170.01	93.10	93.65	170.93	12.45	194.58	178.38	186.48	282.30	5.87
	3	167.75	101.77	103.81	165.67	113.92	116.16	166.71	13.09	186.67	197.88	192.27	282.30	5.468
	4	169.61	116.33	108.42	168.59	97.59	97.92	169.10	12.72	197.18	182.05	189.62	282.30	5.663
	5	164.96	109.69	107.06	170.33	130.89	106.43	167.65	12.95	190.86	203.83	197.34	282.30	5.288
	6	166.56	123.78	107.19	166.06	105.88	107.87	166.31	13.15	198.77	189.91	194.34	282.30	5.368
	7	168.38	99.66	108.67	169.91	103.43	110.79	169.15	12.72	188.36	192.07	190.21	282.30	5.638
	8	167.62	119.34	102.54	165.89	104.27	97.84	166.76	13.08	194.75	184.00	189.38	282.30	5.595
	9	166.48	102.49	89.04	165.38	108.71	103.51	165.93	13.21	179.01	188.80	183.90	282.30	5.818
	10	168.51	124.88	106.94	169.40	103.72	100.00	168.96	12.75	200.17	186.56	193.36	282.30	5.495
									9.77					**5.58**
									0.18					0.183

Table A.VI. Vickers Hardness and Fracture Toughness of Microwave Sintered Sample at 1700°C-2.5 wt% ZrO_2.

SID	#	D1	C1	C2	D2	C3	C4	D	V.H	C(1,2)	C(3.4)	C	E	F.T.
A6	1	169.15	111.13	111.63	174.27	109.73	92.00	171.71	12.34	195.96	188.00	191.98	290.00	5.721
	2	171.05	99.91	99.70	172.19	106.26	103.38	171.62	12.35	185.33	190.92	188.12	290.00	5.895
	3	169.57	107.45	106.13	169.31	101.14	87.43	169.44	12.67	191.58	178.94	185.26	290.00	5.956
	4	171.26	101.01	103.21	171.18	91.53	90.65	171.22	12.41	187.74	176.68	182.21	290.00	6.17
	5	171.73	83.83	97.97	172.95	98.39	110.66	172.34	12.25	176.77	191.00	183.88	290.00	6.126
	6	172.02	92.72	101.27	171.26	112.99	121.24	171.64	12.35	183.01	202.75	192.88	290.00	5.679
	7	175.70	79.26	86.16	171.64	110.92	123.99	173.67	12.06	170.56	203.28	186.92	290.00	6.023
	8	170.96	88.40	114.39	170.12	114.22	103.59	170.54	12.51	186.88	193.97	190.42	290.00	5.752
	9	171.39	102.11	100.38	168.21	97.92	88.91	169.80	12.62	186.94	177.52	182.23	290.00	6.118
	10	170.08	85.82	86.37	170.67	120.35	105.41	170.38	12.53	171.14	198.22	184.68	290.00	6.017
									12.41					**5.95**
									0.18					0.178

Table A.VII. Vickers Hardness and Fracture Toughness of Microwave Sintered Sample at 1700°C-4 wt% ZrO_2.

SID	#	D1	C1	C2	D2	C3	C4	D	V.H	C(1,2)	C(3.4)	C	E	F.T.
A7	1	172.02	112.61	121.49	170.08	120.48	110.87	171.05	12.44	203.06	200.72	201.89	319.70	5.549
	2	167.92	102.88	88.49	165.76	135.54	112.90	166.84	13.07	179.65	207.10	193.37	319.70	5.774
	3	165.34	108.46	89.80	169.78	121.33	113.24	167.56	12.96	181.80	202.18	191.99	319.70	5.861
	4	166.82	118.36	83.03	166.78	133.22	98.69	166.80	13.08	184.11	199.35	191.73	319.70	5.847
	5	167.45	98.94	96.95	165.76	132.24	110.96	166.61	13.11	181.67	204.48	193.08	319.70	5.779
	6	167.11	106.51	96.65	166.90	136.01	129.15	167.01	13.04	185.14	216.03	200.58	319.70	5.471
	7	168.13	113.03	93.90	171.85	139.35	106.18	169.99	12.59	187.53	208.69	198.11	319.70	5.673
	8	164.24	113.20	96.06	163.18	118.28	125.98	163.71	13.58	186.75	203.72	195.24	319.70	5.584
	9	165.08	103.17	109.82	165.59	110.41	108.04	165.34	13.31	189.04	192.02	190.53	319.70	5.85
	10	165.63	113.20	104.78	167.71	117.43	115.87	166.67	13.10	191.81	200.51	196.16	319.70	5.645
									13.03					**5.7**
									0.32					0.139

Table A.VIII. Vickers Hardness and Fracture Toughness of Microwave Sintered Sample at 1700°C-5 wt% ZrO_2.

SID	#	D1	C1	C2	D2	C3	C4	D	V.H	C(1,2)	C(3.4)	C	E	F.T.
A11	1	165.97	110.20	112.74	166.78	109.32	101.02	166.38	13.14	194.46	188.56	191.51	249.30	5.159
	2	164.70	87.06	88.19	163.94	87.62	84.28	164.32	13.47	169.98	167.92	168.95	249.30	6.149
	3	166.44	127.93	100.55	165.93	108.32	111.21	166.19	13.17	197.46	192.73	195.10	249.30	5.011
	4	171.94	72.06	78.93	166.65	90.02	92.41	169.30	12.69	161.47	174.54	168.00	249.30	6.389
	5	164.70	134.61	106.68	165.59	129.28	136.43	165.15	13.34	203.00	215.65	209.32	249.30	4.481
	6	166.98	115.87	112.82	166.10	125.09	119.63	166.54	13.12	197.84	205.41	201.62	249.30	4.78
	7	164.79	88.70	85.20	163.05	83.60	86.40	163.92	13.54	169.35	166.53	167.94	249.30	6.189
	8	164.96	111.21	115.36	164.96	119.42	122.43	164.96	13.37	195.77	203.41	199.59	249.30	4.807
	9	166.44	100.46	110.15	166.86	98.35	122.60	166.65	13.10	188.53	193.91	191.22	249.30	5.179
	10	164.15	87.22	98.02	164.32	88.87	82.26	164.24	13.49	174.70	167.73	171.21	249.30	6.024
									13.24					**5.42**
									0.25					0.698

Table A.IX. Vickers Hardness and Fracture Toughness of Microwave Sintered Sample at 1750°C-0 wt% ZrO_2.

SID	#	D1	C1	C2	D2	C3	C4	D	V.H	C(1,2)	C(3.4)	C	E	F.T.
A9	1	199.82	108.16	130.42	199.28	103.43	117.69	199.55	9.14	219.20	210.20	214.70	290.30	5.625
	2	197.51	102.17	102.29	196.11	117.90	111.11	196.81	9.39	200.99	212.56	206.77	290.30	5.869
	3	198.26	122.37	113.64	195.78	95.30	106.68	197.02	9.37	217.14	198.88	208.01	290.30	5.823
	4	195.90	98.88	104.36	197.34	118.15	119.58	196.62	9.41	199.57	217.54	208.55	290.30	5.789
	5	194.51	116.29	102.38	194.98	102.46	119.58	194.75	9.59	206.59	208.51	207.55	290.30	5.775
	6	195.99	113.05	99.26	200.29	111.15	104.07	198.14	9.27	204.15	207.76	205.95	290.30	5.944
	7	198.22	117.43	111.15	198.39	108.62	116.42	198.31	9.25	213.40	211.72	212.56	290.30	5.674
	8	196.45	101.03	96.18	196.08	115.79	118.82	196.27	9.45	196.83	215.35	206.09	290.30	5.882
	9	197.89	116.59	82.90	195.57	128.87	118.82	196.73	9.40	198.69	221.63	210.16	290.30	5.726
	10	200.16	119.37	123.80	203.54	106.60	115.20	201.85	8.93	221.67	212.67	217.17	290.30	5.593
									9.32					**5.77**
									0.13					0.115

Table A.X. Vickers Hardness and Fracture Toughness of Microwave Sintered Sample at 1750°C-2.5 wt% ZrO_2.

SID	#	D1	C1	C2	D2	C3	C4	D	V.H	C(1,2)	C(3.4)	C	E	F.T.
A10	1	161.44	97.78	68.70	163.35	108.29	115.16	162.40	13.80	163.96	193.40	178.68	280.90	5.931
	2	161.91	96.51	90.79	161.19	113.21	102.74	161.55	13.94	174.61	188.57	181.59	280.90	5.759
	3	159.41	111.43	93.20	162.25	118.76	111.51	160.83	14.07	182.02	196.26	189.14	280.90	5.393
	4	161.57	94.13	82.69	159.62	103.54	101.55	160.60	14.11	169.20	182.36	175.78	280.90	6.011
	5	161.06	77.05	84.77	161.02	107.74	108.46	161.04	14.03	161.44	188.61	175.03	280.90	6.066
	6	160.89	106.64	79.30	161.65	112.66	95.87	161.27	13.99	173.42	185.09	179.25	280.90	5.861
	7	163.77	100.79	95.15	162.63	116.13	96.17	163.20	13.66	179.86	187.47	183.66	280.90	5.719
	8	164.20	98.29	99.56	163.64	104.35	91.51	163.92	13.54	181.03	179.75	180.39	280.90	5.902
	9	161.78	81.12	78.20	162.03	129.57	94.26	161.91	13.88	160.55	192.93	176.74	280.90	6.01
	10	162.67	99.73	91.68	161.99	110.07	83.41	162.33	13.81	177.04	177.74	177.39	280.90	5.993
									13.88					**5.86**
									0.18					0.2

Table A.XI. Vickers Hardness and Fracture Toughness of Microwave Sintered Sample at 1750°C-4 wt% ZrO_2.

SID	#	D1	C1	C2	D2	C3	C4	D	V.H	C(1,2)	C(3.4)	C	E	F.T.
A11	1	162.08	100.08	97.67	161.19	117.81	110.96	161.64	13.93	179.92	194.98	187.45	291.30	5.594
	2	159.54	102.37	108.21	159.24	109.94	116.59	159.39	14.32	185.06	192.89	188.97	291.30	5.45
	3	162.88	97.50	95.43	165.55	105.12	100.93	164.22	13.49	177.91	185.80	181.85	291.30	5.948
	4	160.51	100.63	134.70	160.72	120.52	108.42	160.62	14.10	197.92	194.83	196.38	291.30	5.184
	5	160.13	109.94	93.90	161.74	115.95	119.38	160.94	14.05	181.99	198.54	190.26	291.30	5.447
	6	162.80	105.88	91.96	163.05	99.62	103.34	162.93	13.71	180.32	183.01	181.66	291.30	5.911
	7	159.84	100.00	92.51	162.04	114.60	113.12	160.94	14.05	176.18	194.88	185.53	291.30	5.657
	8	160.26	105.71	112.74	161.70	110.24	110.87	160.98	14.04	189.36	191.41	190.38	291.30	5.443
	9	168.59	100.84	108.67	160.26	107.32	96.32	164.43	13.46	189.05	181.95	185.50	291.30	5.781
	10	160.55	97.04	105.24	164.83	118.11	102.11	162.69	13.75	181.42	192.53	186.97	291.30	5.653
									13.89					**5.61**
									0.2919					0.235

Table A.XII. Vickers Hardness and Fracture Toughness of Microwave Sintered Sample at 1750°C- 5 wt% ZrO_2.

SID	#	D1	C1	C2	D2	C3	C4	D	V.H	C(1,2)	C(3.4)	C	E	F.T.
A12	1	158.00	97.12	124.00	164.57	110.00	123.00	161.29	13.99	189.56	198.79	194.17	270.50	5.102
	2	159.84	84.21	124.63	162.76	125.98	120.99	161.30	13.98	184.34	204.87	194.60	270.50	5.086
	3	161.06	121.62	96.02	161.27	102.45	102.58	161.17	14.01	189.35	183.15	186.25	270.50	5.427
	4	160.89	76.38	108.84	160.64	112.19	120.94	160.77	14.08	173.06	196.89	184.97	270.50	5.47
	5	162.33	90.35	87.13	162.50	100.97	108.25	162.42	13.79	169.91	185.86	177.88	270.50	5.86
	6	159.88	82.77	97.80	159.58	92.55	127.08	159.73	14.26	170.23	189.61	179.92	270.50	5.665
	7	160.00	104.31	103.26	161.57	90.86	116.50	160.79	14.07	183.79	184.47	184.13	270.50	5.508
	8	164.00	101.18	139.27	163.09	73.63	105.54	163.55	13.60	202.23	171.13	186.68	270.50	5.488
	9	165.00	95.05	90.90	160.17	92.34	108.29	162.59	13.76	175.48	180.40	177.94	270.50	5.863
	10	165.00	74.90	105.29	162.12	117.64	113.58	163.56	13.60	172.60	196.67	184.63	270.50	5.58
									13.91					**5.51**
									0.2169					0.265

Appendix B. Vickers Hardness and Fracture Toughness Raw Data of Conventional Sintered Silicon Nitride Samples

Table B.I. Vickers Hardness and Fracture Toughness of Conventionally Sintered Sample at 1650°C- 0 wt% ZrO_2.

SID	#	D1	C1	C2	D2	C3	C4	D	V.H	C(1,2)	C(3.4)	C	E	F.T.
B1	1	187.00	109.62	100.42	187.00	132.17	123.06	187.00	10.40	198.52	221.12	209.82	270.50	5.267
	2	190.00	115.60	118.01	188.00	157.22	153.88	189.00	10.19	211.81	249.55	230.68	270.50	4.617
	3	187.00	122.46	115.43	186.00	129.08	149.17	186.50	10.46	212.45	232.13	222.29	270.50	4.817
	4	180.00	122.56	121.53	181.00	134.93	126.11	180.50	11.17	212.05	221.02	216.53	270.50	4.849
	5	179.00	107.08	132.13	180.00	145.14	138.49	179.50	11.29	209.11	231.82	220.46	270.50	4.694
	6	179.00	115.17	85.80	179.00	160.32	146.54	179.00	11.36	189.99	242.93	216.46	270.50	4.811
	7	182.00	96.78	103.43	181.00	138.66	135.14	181.50	11.04	191.11	227.40	209.25	270.50	5.132
	8	170.00	113.61	102.46	174.00	151.93	129.54	172.00	12.30	193.04	227.74	210.39	270.50	4.825
	9	192.00	114.11	92.49	190.00	154.55	153.75	191.00	9.97	199.30	249.15	224.23	270.50	4.869
	10	188.00	107.16	85.33	182.00	127.93	108.39	185.00	10.63	190.25	209.16	199.70	270.50	5.611
									10.88					**4.95**
									0.69					0.301

Table B.II. Vickers Hardness and Fracture Toughness of Conventionally Sintered Sample at 1650°C- 2.5 wt% ZrO_2.

SID	#	D1	C1	C2	D2	C3	C4	D	V.H	C(1,2)	C(3.4)	C	E	F.T.
B2	1	184.27	72.61	80.92	186.77	127.64	109.41	185.52	10.57	168.90	211.91	190.41	280.90	6.159
	2	186.86	88.76	95.89	186.26	126.32	105.13	186.56	10.45	185.76	208.86	197.31	280.90	5.872
	3	181.26	84.78	91.94	183.04	133.19	122.34	182.15	10.97	178.99	219.29	199.14	280.90	5.654
	4	185.07	74.90	83.68	182.70	123.14	95.25	183.89	10.76	171.83	200.55	186.19	280.90	6.314
	5	185.20	95.89	98.94	187.45	119.33	126.58	186.33	10.48	190.02	216.68	203.35	280.90	5.605
	6	184.99	93.81	80.29	184.31	134.16	115.89	184.65	10.67	179.55	217.18	198.36	280.90	5.765
	7	186.64	110.98	104.15	181.85	130.18	118.18	184.25	10.72	200.89	215.11	208.00	280.90	5.357
	8	183.42	98.85	92.45	184.18	122.72	133.78	183.80	10.77	187.36	220.34	203.85	280.90	5.508
	9	183.17	116.36	99.87	185.20	101.44	128.78	184.19	10.72	199.70	207.71	203.71	280.90	5.526
	10	184.48	97.62	103.22	186.30	126.15	118.31	185.39	10.59	192.66	215.38	204.02	280.90	5.549
									10.67					**5.73**
									0.15					0.304

Table B.III. Vickers Hardness and Fracture Toughness of Conventionally Sintered Sample at 1700°C- 0 wt% ZrO_2.

SID	#	D1	C1	C2	D2	C3	C4	D	V.H	C(1,2)	C(3.4)	C	E	F.T.
B3	1	193.58	128.27	135.27	199.40	118.66	127.93	196.49	9.42	228.56	223.00	225.78	303.90	5.255
	2	197.42	128.27	132.49	194.17	117.35	109.55	195.80	9.49	229.09	210.54	219.81	303.90	5.451
	3	197.29	125.32	120.51	197.21	106.30	131.05	197.25	9.35	221.56	217.28	219.42	303.90	5.506
	4	192.11	131.09	122.70	188.78	123.59	119.41	190.45	10.03	222.95	215.89	219.42	303.90	5.316
	5	191.73	121.56	133.96	197.25	127.81	131.94	194.49	9.62	223.63	228.50	226.06	303.90	5.191
	6	204.46	134.05	120.76	194.76	122.53	104.36	199.61	9.13	229.64	210.83	220.23	303.90	5.541
	7	195.61	129.32	108.45	195.90	124.14	121.99	195.76	9.49	216.69	221.02	218.85	303.90	5.486
	8	199.45	118.61	123.50	202.52	121.65	137.50	200.99	9.01	220.78	230.84	225.81	303.90	5.374
	9	196.96	135.69	129.74	195.10	103.01	111.53	196.03	9.47	231.20	204.82	218.01	303.90	5.525
	10	195.40	115.07	136.41	193.50	134.76	128.14	194.45	9.62	223.44	228.20	225.82	303.90	5.199
									9.46					**5.38**

Table B.IV. Vickers Hardness and Fracture Toughness of Conventionally Sintered Sample at 1700°C- 2.5 wt% ZrO_2.

SID	#	D1	C1	C2	D2	C3	C4	D	V.H	C(1,2)	C(3.4)	C	E	F.T.
B4	1	195.86	110.69	97.49	198.64	112.46	110.69	197.25	9.35	202.02	210.90	206.46	296.50	5.959
	2	199.57	116.72	122.96	198.94	119.08	111.23	199.26	9.16	219.63	214.63	217.13	296.50	5.581
	3	198.90	119.67	114.65	198.14	110.60	133.83	198.52	9.23	216.61	221.29	218.95	296.50	5.491
	4	197.89	102.93	113.43	196.41	143.70	128.48	197.15	9.36	207.13	234.30	220.71	296.50	5.388
	5	211.42	120.13	115.75	212.81	101.03	106.13	212.12	8.09	223.65	209.99	216.82	296.50	5.954
	6	203.24	133.37	122.62	199.02	117.90	101.37	201.13	8.99	229.62	209.15	219.38	296.50	5.547
	7	202.48	108.24	115.20	202.73	116.63	110.22	202.61	8.86	212.96	214.79	213.88	296.50	5.805
	8	200.75	119.96	103.05	193.92	108.41	112.37	197.34	9.34	211.88	207.35	209.62	296.50	5.827
	9	193.84	103.52	100.73	203.75	109.88	107.02	198.80	9.21	199.05	210.33	204.69	296.50	6.084
	10	204.13	107.90	96.98	196.03	113.22	111.95	200.08	9.09	204.51	210.60	207.55	296.50	5.996
									9.07					**5.76**
									0.38					0.243

Table B.V. Vickers Hardness and Fracture Toughness of Conventionally Sintered Sample at 1750°C- 0 wt% ZrO_2.

SID	#	D1	C1	C2	D2	C3	C4	D	V.H	C(1,2)	C(3.4)	C	E	F.T.
B5	1	199.91	109.29	100.86	192.87	113.30	85.47	196.39	9.43	205.03	195.82	200.43	275.30	5.977
	2	197.63	107.19	104.19	192.95	126.41	107.73	195.29	9.54	204.51	213.55	209.03	275.30	5.58
	3	195.40	113.93	125.19	191.77	112.88	107.27	193.59	9.71	217.26	205.96	211.61	275.30	5.43
	4	192.83	118.40	119.08	192.91	106.51	96.81	192.87	9.78	215.16	198.12	206.64	275.30	5.607
	5	198.01	124.85	112.08	192.45	96.90	107.06	195.23	9.55	217.47	198.21	207.84	275.30	5.626
	6	197.42	108.11	123.21	196.28	104.66	98.46	196.85	9.39	214.37	199.70	207.04	275.30	5.706
	7	188.06	110.81	111.57	194.64	116.29	116.46	191.35	9.94	205.22	213.70	209.46	275.30	5.451
	8	192.91	116.29	108.75	192.66	108.16	91.04	192.79	9.79	208.98	195.93	202.45	275.30	5.779
	9	195.90	107.90	95.13	198.43	110.56	97.83	197.17	9.36	199.47	203.41	201.44	275.30	5.955
	10	194.39	109.42	99.93	198.98	129.41	114.14	196.69	9.41	201.87	221.27	211.57	275.30	5.519
									9.59					**5.66**
									0.20					0.192

Table B.VI. Vickers Hardness and Fracture Toughness of Conventionally Sintered Sample at 1750°C- 2.5 wt% ZrO_2.

SID	#	D1	C1	C2	D2	C3	C4	D	V.H	C(1,2)	C(3.4)	C	E	F.T.
B6	1	196.62	113.51	118.49	195.86	119.16	129.91	196.24	9.45	214.31	222.47	218.39	286.20	5.354
	2	197.93	123.50	128.40	199.99	126.96	113.51	198.96	9.19	224.92	220.23	222.57	286.20	5.275
	3	203.41	106.98	97.28	193.20	101.79	117.73	198.31	9.25	203.84	206.36	205.10	286.20	5.944
	4	193.25	125.15	103.64	201.43	128.31	114.27	197.34	9.34	211.02	222.01	216.51	286.20	5.454
	5	199.23	128.10	119.37	198.69	123.72	134.76	198.96	9.19	223.35	228.59	225.97	286.20	5.157
	6	193.04	119.71	122.79	200.92	128.27	116.84	196.98	9.38	217.77	223.02	220.39	286.20	5.301
	7	203.41	126.58	127.09	199.07	113.30	110.60	201.24	8.98	228.54	211.49	220.01	286.20	5.429
	8	190.42	133.92	119.96	195.06	138.73	126.12	192.74	9.79	222.15	229.96	226.05	286.20	4.993
	9	196.41	144.67	110.22	193.88	117.90	112.58	195.15	9.55	225.65	212.18	218.92	286.20	5.305
	10	193.25	130.04	110.69	192.91	118.15	128.31	193.08	9.76	216.99	219.69	218.34	286.20	5.269
									9.39					**5.35**
									0.26					0.248

Appendix C. Grain Size Distribution Raw Data of Grains of Microwave Sintered Silicon Nitride Samples

Table C.I. Length (L), Width (W) and Aspect Ratio (AR) of Grains of Microwave Sintered Sample at 1650°C- 0 wt%ZrO_2.

L	F	F%	W	F	F%	AR	F	F%
0.25	411	17	0.25	1531	39	3	285.0	20
0.5	208	9	0.5	679	17	4	385.0	27
1	982	40	0.75	1677	42	5	217.0	15
1.5	214	9	1	65	2	6	169.0	12
2	451	18	1.25	4	0	7	80.0	6
2.5	52	2	1.5	0	0	8	175.0	12
3	120	5	1.75	0	0	9	47.0	3
3.5	0	0	2	0	0	10	27.0	2
4	6	0	2.25	0	0	11	15.0	1
4.5	0	0	2.5	0	0	12	33.0	2

Table C.II. Length (L), Width (W) and Aspect Ratio (AR) of Grains of Microwave Sintered Sample at 1650°C- 2.5 wt%ZrO_2.

L	F	F%	W	F	F%	AR	F	F%
0.25	52	2	0.25	909	36	3	522.0	37
0.5	353	14	0.5	865	34	4	347.0	24
1	1041	41	0.75	299	12	5	66.0	5
1.5	456	18	1	392	15	6	220.0	15
2	310	12	1.25	20	1	7	5.0	0
2.5	143	6	1.5	45	2	8	130.0	9
3	172	7	1.75	0	0	9	1.0	0
3.5	7	0	2	23	1	10	60.0	4
4	13	1	2.25	0	0	11	1.0	0
4.5	0	0	2.5	0	0	12	71.0	5

Table C.III. Length (L), Width (W) and Aspect Ratio (AR) of Grains of Microwave Sintered Sample at 1650°C- 4 wt%ZrO_2.

L	F	F%	W	F	F%	AR	F	F%
0.25	30	2	0.25	536	36	3	177	18
0.5	43	3	0.5	396	26	4	408	43
1	620	41	0.75	238	16	5	61	6
1.5	95	6	1	237	16	6	95	10
2	315	21	1.25	42	3	7	5	1
2.5	110	7	1.5	19	1	8	95	10
3	226	15	1.75	0	0	9	2	0
3.5	21	1	2	27	2	10	44	5
4	27	2	2.25	0	0	11	1	0
4.5	7	0	2.5	0	0	12	69	7

Table C.IV. Length (L), Width (W) and Aspect Ratio (AR) of Grains of Microwave Sintered Sample at 1650°C- 5 wt%ZrO_2.

L	F	F%	W	F	F%	AR	F	F%
0.25	81	6	0.25	437	33	3	155.0	20
0.5	76	6	0.5	398	30	4	196.0	25
1	359	27	0.75	256	19	5	64.0	8
1.5	147	11	1	161	12	6	111.0	14
2	334	25	1.25	71	5	7	4.0	1
2.5	102	8	1.5	7	1	8	154.0	20
3	168	13	1.75	3	0	9	8.0	1
3.5	16	1	2	6	0	10	36.0	5
4	51	4	2.25	0	0	11	1.0	0
4.5	0	0	2.5	0	0	12	45.0	6

Table C.V. Length (L), Width (W) and Aspect Ratio (AR) of Grains of Microwave Sintered Sample at 1700°C- 0 wt%ZrO_2.

L	F	F%	W	F	F%	AR	F	F%
0.25	42	3	0.25	454	28	3	309	26
0.5	13	1	0.5	715	44	4	460	39
1	518	32	0.75	302	19	5	85	7
1.5	297	19	1	95	6	6	160	14
2	390	24	1.25	31	2	7	22	2
2.5	106	7	1.5	11	1	8	78	7
3	183	11	1.75	0	0	9	11	1
3.5	17	1	2	2	0	10	15	1
4	24	2	2.25	0	0	11	2	0
4.5	2	0	2.5	0	0	12	30	3

Table C.V. Length (L), Width (W) and Aspect Ratio (AR) of Grains of Microwave Sintered Sample at 1700°C- 2.5 wt%ZrO_2.

L	F	F%	W	F	F%	AR	F	F%
0.25	344	8	0.25	2490	56	3	619.0	24
0.5	872	20	0.5	1185	27	4	852.0	33
1	1610	36	0.75	183	4	5	31.0	1
1.5	753	17	1	476	11	6	605.0	23
2	674	15	1.25	11	0	7	6.0	0
2.5	52	1	1.5	92	2	8	425.0	16
3	91	2	1.75	0	0	9	2.0	0
3.5	6	0	2	8	0	10	20.0	1
4	23	1	2.25	0	0	11	1.0	0
4.5	2	0	2.5	0	0	12	28.0	1

Table C.VII. Length (L), Width (W) and Aspect Ratio (AR) of Grains of Microwave Sintered Sample at 1700°C- 4 wt%ZrO_2.

L	F	F%	W	F	F%	AR	F	F%
0.25	94	3	0.25	1070	34	3	319	21
0.5	666	21	0.5	1175	38	4	475	31
1	1064	34	0.75	244	8	5	82	5
1.5	550	18	1	487	16	6	358	23
2	398	13	1.25	4	0	7	10	1
2.5	133	4	1.5	127	4	8	158	10
3	155	5	1.75	0	0	9	9	1
3.5	5	0	2	1	0	10	57	4
4	28	1	2.25	0	0	11	1	0
4.5	0	0	2.5	0	0	12	58	4

Table C.VIII. Length (L), Width (W) and Aspect Ratio (AR) of Grains of Microwave Sintered Sample at 1700°C- 5 wt%ZrO_2.

L	F	F%	W	F	F%	AR	F	F%
0.25	93	5	0.25	800	40	3	160	13
0.5	128	6	0.5	490	24	4	294	24
1	571	29	0.75	330	16	5	124	10
1.5	132	7	1	296	15	6	169	14
2	455	23	1.25	59	3	7	22	2
2.5	196	10	1.5	8	0	8	210	17
3	292	15	1.75	0	0	9	30	2
3.5	33	2	2	22	1	10	106	9
4	69	3	2.25	0	0	11	1	0
4.5	7	0	2.5	0	0	12	125	10

Table C.IX. Length (L), Width (W) and Aspect Ratio (AR) of Grains of Microwave Sintered Sample at 1750°C- 0 wt%ZrO_2.

L	F	F%	W	F	F%	AR	F	F%-
0.25	275	12	0.25	1029	45	3	223	18
0.5	168	7	0.5	559	24	4	320	26
1	554	24	0.75	425	19	5	28	2
1.5	334	15	1	208	9	6	180	15
2	565	25	1.25	45	2	7	16	1
2.5	60	3	1.5	16	1	8	332	27
3	188	8	1.75	0	0	9	5	0
3.5	17	1	2	3	0	10	19	2
4	73	3	2.25	2	0	11	3	0
4.5	12	1	2.5	0	0	12	100	8

Table C.X. Length (L), Width (W) and Aspect Ratio (AR) of Grains of Microwave Sintered Sample at 1750°C- 2.5 wt%ZrO_2.

L	F	F%	W	F	F%	AR	F	F%
0.25	275	14	0.25	1056	56	3	52	6
0.5	161	8	0.5	409	22	4	178	21
1	529	27	0.75	187	10	5	128	15
1.5	150	8	1	177	9	6	138	16
2	337	17	1.25	33	2	7	43	5
2.5	96	5	1.5	8	0	8	175	20
3	215	11	1.75	2	0	9	60	7
3.5	28	1	2	3	0	10	67	8
4	96	5	2.25	0	0	11	15	2
4.5	9	0	2.5	0	0	12	10	1

Table C.XI. Length (L), Width (W) and Aspect Ratio (AR) of Grains of Microwave Sintered Sample at 1750°C- 4 wt% ZrO_2.

L	F	F%	W	F	F%	AR	F	F%
0.25	750	19	0.25	2784	69	3	195	8
0.5	464	12	0.5	767	19	4.00	969.0	41
1	1314	33	0.75	295	7	5.00	47.0	2
1.5	472	12	1	151	4	6	422.0	18
2	683	17	1.25	26	1	7	13.0	1
2.5	58	1	1.5	5	0	8.00	536.0	23
3	196	5	1.75	0	0	9.00	9.0	0
3.5	10	0	2	0	0	10.00	39.0	2
4	42	1	2.25	0	0	11.00	5.0	0
4.5	11	0	2.5	0	0	12.00	121.0	5

Table C.XII. Length (L), Width (W) and Aspect Ratio (AR) of Grains of Microwave Sintered Sample at 1750°C- 5 wt% ZrO_2.

L	F	F%	W	F	F%	AR	F	F%
0.25	1044	24	0.25	2502	58	3.00	218	11
0.5	600	14	0.5	1173	27	4.00	786	39
1	1347	31	0.75	366	9	5.00	243	12
1.5	329	8	1	181	4	6	320	16
2	539	12	1.25	27	1	7	82	4
2.5	91	2	1.5	17	0	8.00	175	9
3	324	7	1.75	1	0	9.00	63	3
3.5	21	0	2	28	1	10.00	44	2
4	46	1	2.25	0	0	11.00	20	1
4.5	4	0	2.5	2	0	12.00	52	3

Appendix D. Grain Size Distribution Raw Data of Grains of Conventional Sintered Silicon Nitride Samples

Table D.I. Length (L), Width (W) and Aspect Ratio (AR) of Grains of Conventional Sintered Sample at 1650°C- 0 wt%ZrO_2.

L	F	F%	W	F	F%	AR	F	F%
0.25	94	7	0.25	528	38	3	158.0	20
0.5	166	12	0.5	481	35	4	315.0	40
1	502	36	0.75	190	14	5	52.0	7
1.5	65	5	1	72	5	6	55.0	7
2	306	22	1.25	53	4	7	7.0	1
2.5	51	4	1.5	35	3	8	98.0	13
3	162	12	1.75	6	0	9	9.0	1
3.5	11	1	2	11	1	10	7.0	1
4	15	1	2.25	2	0	11	1.0	0
4.5	2	0	2.5	0	0	12	79.0	10

Table D.II. Length (L), Width (W) and Aspect Ratio (AR) of Grains of Conventional Sintered Sample at 1650°C- 2.5 wt%ZrO_2.

L	F	F%	W	F	F%	AR	F	F%
0.25	122	9	0.25	495	37	3	107.0	15
0.5	158	12	0.5	470	36	4	280.0	40
1	490	38	0.75	118	9	5	56.0	8
1.5	33	3	1	180	14	6	57.0	8
2	325	25	1.25	17	1	7	11.0	2
2.5	30	2	1.5	25	2	8	137.0	20
3	130	10	1.75	0	0	9	1.0	0
3.5	4	0	2	18	1	10	6.0	1
4	4	0	2.25	0	0	11	1.0	0
4.5	0	0	2.5	0	0	12	40.0	6

Table D.III. Length (L), Width (W) and Aspect Ratio (AR) of Grains of Conventional Sintered Sample at 1700°C- 0 wt%ZrO_2.

L	F	F%	W	F	F%	AR	F	F%
0.25	192	11	0.25	797	46	3	116	12
0.5	205	12	0.5	505	29	4	206	22
1	290	17	0.75	279	16	5	71	7
1.5	117	7	1	101	6	6	142	15
2	413	24	1.25	26	1	7	6	1
2.5	100	6	1.5	14	1	8	194	20
3	292	17	1.75	5	0	9	43	5
3.5	23	1	2	5	0	10	48	5
4	86	5	2.25	0	0	11	2	0
4.5	12	1	2.5	6	0	12	125	13

Table D.IV. Length (L), Width (W) and Aspect Ratio (AR) of Grains of Conventional Sintered Sample at 1700°C- 2.5 wt%ZrO_2.

L	F	F%	W	F	F%	AR	F	F%
0.25	97	4	0.25	889	42	3	109.0	9
0.5	510	23	0.5	510	24	4	488.0	42
1	739	33	0.75	205	10	5	24.0	2
1.5	284	13	1	296	14	6	145.0	13
2	346	15	1.25	2	0	7	1.0	0
2.5	10	0	1.5	187	9	8	188.0	16
3	236	10	1.75	0	0	9	1.0	0
3.5	0	0	2	11	1	10	1.0	0
4	33	1	2.25	0	0	11	1.0	0
4.5	0	0	2.5	0	0	12	198.0	17

Table D.V. Length (L), Width (W) and Aspect Ratio (AR) of Grains of Conventional Sintered Sample at 1750°C- 0 wt%ZrO_2.

L	F	F%	W	F	F%	AR	F	F%
0.25	141	5	0.25	818	32	3	65.0	7
0.5	540	21	0.5	748	29	4	320.0	33
1	827	32	0.75	157	6	5	42.0	4
1.5	272	11	1	555	22	6	95.0	10
2	464	18	1.25	20	1	7	7.0	1
2.5	29	1	1.5	252	10	8	331.0	34
3	210	8	1.75	2	0	9	1.0	0
3.5	8	0	2	28	1	10	19.0	2
4	57	2	2.25	0	0	11	1.0	0
4.5	0	0	2.5	0	0	12	94.0	10

Table D.VI. Length (L), Width (W) and Aspect Ratio (AR) of Grains of Conventional Sintered Sample at 1750°C- 2.5 wt%ZrO_2.

L	F	F%	W	F	F%	AR	F	F%
0.25	105	6	0.25	598	32	3	100	13
0.5	562	30	0.5	706	38	4	231	30
1	352	19	0.75	104	6	5	20	3
1.5	134	7	1	292	16	6	38	5
2	225	12	1.25	26	1	7	2	0
2.5	14	1	1.5	125	7	8	188	24
3	319	17	1.75	0	0	9	1	0
3.5	4	0	2	0	0	10	1	0
4	123	7	2.25	0	0	11	1	0
4.5	6	0	2.5	0	0	12	198	25